CCL Report 2006-12

LES of Sooting Flames

Hossam El-Asrag and Suresh Menon

Computational Combustion Laboratory
School of Aerospace Engineering
Georgia Institute of Technology
270 Ferst Drive
Atlanta, Georgia 30332-0150
http://www.ccl.gatech.edu

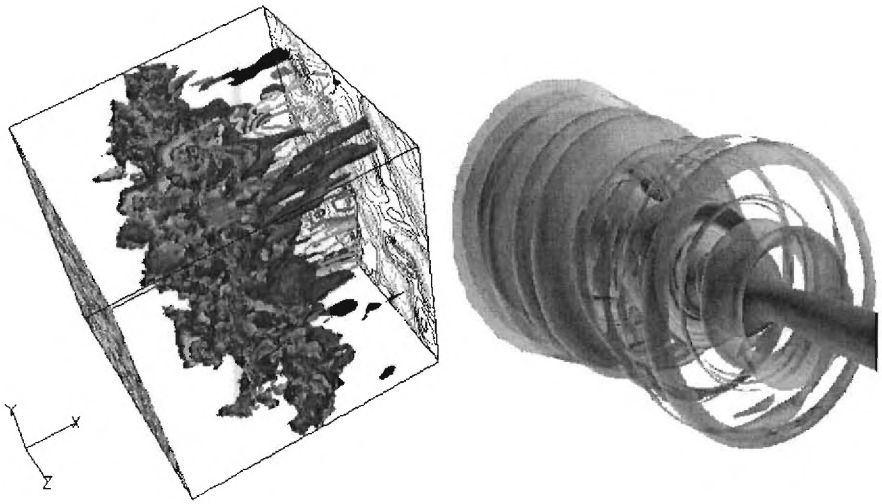

Sponsored by: *Army Research Office*
Contract Number: *DAAD19-03-1-0049*
Date: *December 2006*

Contents

List of Figures

List of Tables

Nomenclature

Roman Symbols

C_{EBU}	model coefficient for the Eddy Break-Up model
C_ϵ	model coefficient for subgrid dissipation
C_λ	scalar diffusivity
C_ν	model coefficient for turbulent viscosity
a	speed of sound
c_p	specific heat at constant pressure per unit mass
c_v	specific heat at constant volume per unit mass
D	mass diffusivity
D^{sgs}	dissipation of turbulent kinetic energy
Da	Damkohler number
E	total energy per unit mass
e	internal energy per unit mass
$\mathbf{F}$, $\mathbf{F}'$	flux vectors
$\mathbf{G}$, $\mathbf{G}'$	flux vectors
H	total enthalpy per unit mass
J	Jacobian of the coordinate system transformation
k	turbulent kinetic energy
Ka	Karlovitz number
L	characteristic length
l_m	mixing length scale
Le	Lewis number
Mw	molecular weight
Ns	total number of species
N_s	soot number density
P	production of turbulent kinetic energy
Pr	Prandtl number
$\mathbf{Q}$, $\mathbf{Q}'$	state vector
q_i	heat flux
Re	Reynolds number
R_u	universal gas constant
r	spatial position
S	rate of strain
s	spatial coordinate along the LEM line
t	time
U, V, W, u_i	Cartesian velocity vector components
u'	rms velocity
u'_{sgs}	subgrid scale turbulence intensity
$V_{i,m}$	diffusion velocity of species m
X	mole fraction
Y	mass fraction

Greek Symbols

β	Collision frequency
γ	ratio of specific heats
δ_{ij}	Kronecker delta
ϕ	equivalence ratio
η	Kolmogorov length scale
λ	stirring frequency
μ	dynamic viscosity
ν	kinematic viscosity
μ_k	Stoichiometric coefficient
ρ	density
$\dot{\Omega}$	heat release rate

Subscripts

i, j, k	Cartesian tensor indices or species indices
iv	inviscid
cyl	cylindrical
car	cartesian
F	laminar
LEM	quantity at the LEM level
LES	quantity at the LES level
k	chemical index
ref	reference
n	time step index
t, T	turbulent quantity
u	unburned
∞	quantity at infinity downstream
v	viscous

Superscripts

0	reference quantity
LEM	quantity at the LEM level
sgs	subgrid scale
$stir$	stirring
$test$	test filter scale
$'$	Reactants
$''$	Products

Units

mm	1 millimeter = 10^{-3} m
$mmHg$	1 mm Mercury = 0.001333 bar
nm	1 nanometer = 10^{-9} m
μm	1 micrometer = 10^{-6} m
$\dot{A}$	1 $\dot{A}$ngström = 10^{-10} m
k	kelvin

Other Symbols

∂	partial derivative operator
∇	gradient operator
$\nabla\cdot$	divergence operator
$\sum$	summation operator
$\prod$	product operator
Δ	difference operator
$\tilde{}$	Favre spatial filter
$\langle\ \rangle$	test filter
$\bar{}$	space average
$'$, $''$	fluctuating quantity

Abbreviations

CFD	Computational Fluid Dynamics
CMC	Conditional Moment Closure
CFL	Courant-Friedrichs-Lewy number
CO	Carbon monoxide
DNS	Direct Numerical Simulation
DVODE	Double precision Variable Coefficients Ordinary Differential Equations solver
EBU	Eddy Break-Up Model
EDC	Eddy Dissipation Concept
H/C	Hydrogen to Carbon
HC	Hydrogen Carbon
ISAT	In Situ Adaptive Tabulation
LDKM	Localized Dynamic k-equation Model
L.H.S.	Left Hand Side
LEM	Linear-Eddy Mixing model
LES	Large-Eddy Simulation
MOM	Method of Moments
MOMIC	Method of Moments with Interpolative Closure
MPI	Message Passing Interface
MIN	Minimum
NOx	Nitrogen Oxides
ODE	Ordinary Differential Equation

R.H.S.	Right Hand Side
PAHs	Polycyclic Aromatic Hydrocarbons
PDE	Partial Differential Equation
PDF	Probability Distribution Function
FD	Finite Difference
FDF	Filtered Density Function
RANS	Reynolds Averaged Navier - Stokes
SOx	Sulfur Oxide
TKE	Turbulent Kinetic Energy
rms	Root Mean Square, variance

Large Eddy Simulation of Sooting Flames

Hossam El-Asrag and Suresh Menon
School of Aerospace Engineering
Georgia Institute of Technology
Atlanta, Georgia 30332

Annual Report for the period July-December 2006

Submitted to
Army Research Office
Contract: DAAD19-03-1-0049
December 30, 2006

Abstract

Soot prediction in realistic systems is one of the most challenging problems in theoretical and applied combustion. Soot formation as a chemical process is very complicated and not fully understood up to the moment. The major difficulty stems from the chemical complexity of the soot formation processes as well as its strong coupling with the other thermochemical and fluid processes that occur simultaneously. Soot is a major byproduct of incomplete combustion, having a strong impact on the environment, as well as the combustion efficiency. Therefore, it needs to be predicted in realistic configurations in an accurate and yet computationally efficient way. In the current study, a new soot formation subgrid model is developed and reported here. The new model is designed to be used within the context of the Large Eddy Simulation (LES) framework, combined with Linear Eddy Mixing (LEM) as a subgrid combustion model. The final model can be applied equally to premixed and non-premixed flames over any required geometry and flow conditions in the free, the transition, and the continuum regimes. The soot dynamics is predicted using a Method of Moments approach with Lagrangian Interpolative Closure (MOMIC) for the fractional moments. Since, no prior knowledge of the particles distribution is required, the model is generally applicable. The effect of radiation is introduced as an optically thin model. As a validation the model is first applied to a non-premixed non-sooting flame, then a set of canonically premixed flames. Finally, the model is validated against a non-premixed jet sooting flame. Good results are predicted with reasonable accuracy.

1 Introduction and Background

Pollutant emissions control and prediction are currently a major concern in industry. The major combustion-generated pollutants are, matter particulates (soot), unburned hydrocarbons (UHC), CO, NOx, SOx and greenhouse gases (GHGs). Extensive research has been conducted to investigate the source of most of these pollutants, with a lesser extent on UHC and soot emissions. NOx is mainly generated in the high temperature stoichiometric regions, while CO is formed due to either local extinction or incomplete combustion. On the other hand, soot as a carbonaceous particulate forms from gas-phase processes in fuel rich regimes due to the incomplete combustion of hydrocarbons. The particulate diameter can range from the order of nm for the primary particles up to $10\mu m$ for soot aggregates ([1]). This wide range of particle sizes can coexist at the same time inside the combustor and different approaches have to be implemented to track the particle history. For instance, the Thermophoretic forces, generated by the temperature gradients, and the soot particle diffusion treatment in the free molecular regime are different from those in the continuum and the transition regimes ([2]).

Typical fuels used in gas turbine engines (JetA, JP-8, etc) usually have high H/C ratio, which is the main constitutes of soot particulate, and hence high soot tendency. The presence of particulates in gas turbine engine can severely affect the lifetime of the turbine blades by colliding with and causing geometrical damage, and this in turn, will increase the cost of periodic maintenance. However, soot formation can be helpful to enhance contrail formation and tactical visibility of aircrafts at the same time. In addition, soot strongly affect other pollutants (NOx, CO) emission within the same combustor. For instance, [3] mentioned that at low-engine power conditions, the production rate is maximum for CO and UHC and minimum for soot and nitrogen oxides . On the other hand, at high power condition, soot and NOx are produced in very high proportions, while CO and UHC are suppressed. The effect of soot on other pollutants is very important and so far has not been adequetly studied up to this time. Furthermore, after soot is generated and transported to another region of different compositions, it can alter the concentrations of other species by surface growth and oxidation processes. As a result, the local equivalence ratio is altered together with the temperature and the heat release profiles ([4]). Moreover, flame visibility and structure are found to be affected by soot formation (black smoke) as well ([5]).

Soot is a highly emissive particulate, which enhances radiation and heat transfer. In gas turbine engines, soot thermal radiation strongly affects the flame and combustion process. [6] estimated the fractional energy losses from radiation to be as high as 30 % for coflow diffusion flames. This thermal energy losses reduces the combustion efficiency and the maximum available chemical energy for mechanical work. Moreover, the radiation effect contributes to the thermal loads of the combustor liners and the turbine blades. On the other hand, the high emissivity of soot can be useful to enhance the heat transfer to the required loads in gas furnaces. Recently, soot was also found to be a primary cause of greenhouse effect ([7]). In addition to the above mentioned properties, soot particulates such as PAHs absorb carcinogenic materials, there by pose health hazardous to human beings, when they find their way to the respiratory system. As a result, soot particulate emissions is subjected to stringent regulations by the US Environmental Protection Agency (EPA), implying that soot physics needs to be studied and understood from the practical point of view.

In the current section, first the historical background on soot modeling and formation hypothesis is introduced. Next, the current experimental and numerical status of soot modeling in turbulent flames will be summarized. Finally, an overview of turbulent combustion modeling will be presented.

2 Soot Formation and Modeling

Soot formation and modeling is one of the least investigated and understood combustion areas. This is due to the complexity of the process, or the uncertainty in the chemical pathway, and the uncertainty about the coupling of these processes with fluid dynamics, heat transfer and turbulence. The next subsections show a brief historical background for the work done related to soot formation and modeling. Following that, the current status of soot modeling will be briefly reviewed.

2.1 Historical View

Historically, first paper that discussed the formation of carbon black in flames was published in 1957 by [8] in the journal Combustion and Flame. Following that, the first paper published by the Combustion Institute was in the eleventh symposium in 1967 by Homman and Wagner, who first discussed the mechanisms of carbon formation in premixed flames. They examined both acetylene and benzene flames at a pressure of 20 $mmHg$ (0.03 bar), and observed that the hydrocarbon formation (PAHs) starts few centimeters downstream of the oxidation layer. These PAHs are found to be more stable kinetically than the smaller hydrocarbons, which oxidize at the end of the oxidation zone. Observing the rate of formation of these hydrocarbons, they concluded that components like C_6H_2 and C_8H_2 takes a major role in the path of conversion of acetylene and benzene to PAHs.

Another work at the same symposium studied the radiation emitted from a sooting flame ([9]). However, no clear view was proposed for the soot formation process. The authors explained the soot formation process based on the spectroscopic analysis of the flame, and proposed the first known soot formation path, although without any physical evidence. The mechanism involves first cracking of the fuel, followed by dehydrogenation and polymerization of the hydrocarbons, and finally agglomeration of the soot particles. It was further found that the soot particles are composed of a 4% by weight hydrogen, with a carbon to hydrogen ratio of $H/C = 0.5$. Also, the decomposition of the higher saturated hydrocarbons occur at a temperature around $1000C$.

[10] claimed that polymers are formed from acetylene, which decompose to soot particles, while other higher hydrocarbon components like vinyl acetylene has a minor role in soot formation. In the following year, Chakraborty and Long published four papers ([11, 12, 13, 14]). These papers were the first few papers to discuss soot formation and PAHs kinetics in diffusion flames. They especially discussed the effects of adding additives on soot formation in ethylene and ethane flames, and its effect on soot formation.

[15] investigated the formation of carbon in a well-stirred reactor. The critical C/O ratio for soot inception was observed and compared to Bunsen-Type flames. He observed that as the preheat temperature increases, this value decreases. For ethylene, a value of C/O=0.679

is tabulated. [16] proposed a model for soot formation based on the idea that positive ions such as $C_nH_n^+$ acts as soot nuclei, and these particles ionize during surface growth and agglomeration. The soot nuclei, estimated to be around 20-30 A, pertains there positive sign until they reach a certain size, and during this period a repulsion force exists at the surface to prevent coagulation. It was also stated that after coagulation starts, an aggregation chain like process is activated as a result of a dipole electric attraction process.

[17] investigated soot formation by combustion of an atomized liquid fuel. He showed that soot formed by the combustion of the large droplets is controlled by the relative velocity between the droplet and the combustion air. His results, suggests that this process can be avoided by extinction of the small flames when a certain critical relative velocity is reached between the fuel droplet and the air, which can be controlled through injection method. It was found that this extinction velocity increases with the square root of the droplet diameter and the oxygen concentration, and decreases considerably if the oxygen concentration falls. An interesting conclusion is that the recirculation of the combustion gases reduces oxygen concentration, extinction velocity and soot formation.

Another early soot formation mechanism that resembles greatly the current model was proposed by [18] using an experimental investigation on a flat acetylene-oxygen flame at low pressure. They gave an early definition for surface growth, coagulation and aggregation processes, with relative particle sizes. Their observations can be summarized as follows:

(a) The clusters formed at the early and the intermediate stages of coagulation are in spherical form and switch to a chainlike structure in the flame tail.

(b) The particle diameter distribution starts as a log-normal distribution at the early stages of soot formation and then asymptote to a Gaussian distribution at the flame tail and in the later stages.

(c) The particle number density increases rapidly during the early stages (through nucleation), and then decreases due to coagulation.

(d) Nucleation rate occurs rapidly, while coagulation is relatively slow. Also, the surface growth rate increases then decreases in the late stages.

[19] investigated soot behavior in a turbulent C_2H_2 free jet flame. This paper was among the first papers that discussed the effect of turbulence on soot formation. Magnussen observed that large soot aggregates are formed inside the turbulent eddies, that engulf them. These turbulent eddies break down to smaller ones that burned away, according to the energy cascade theory. Thus, larger soot particles exist only in the larger eddies, where the residence time is large. In addition, turbulence creates inhomogeneity that carries the soot particles away from the regions of higher oxygen concentration. In the subsequent papers [20] developed a soot model for turbulent flames. The model states that soot formation takes place in two stages, involving the formation of the soot nuclei which subsequently form the soot particle. For the nucleation process the model used the [21] nucleation model. After computing the soot mass concentration from the nucleation rate and the soot particle formation rate, the soot combustion rate is expressed from an EDC model in terms of the dissipation rate ϵ and the turbulent kinetic energy k. The above model assumes that the

rate of formation of soot depends on the mixing between the eddies that contain soot and other eddies that contain oxygen. However, it neglects the previous observation that soot is formed inside the eddies ([19]).

The model is applied to a turbulent acetylene/air diffusion flame and comparison with the experiment showed good agreement. Later, [22] extended the work by using the same above EDC model on a turbulent acetylene diffusion flame, and conducted a parametric study to investigate the effect of Reynolds number, fuel preheating, and fuel dilution on soot formation. They noticed as the Reynolds number increases the soot concentration decreases, while the peak location remains in the same location. As the Reynolds number increases, the turnover time is reduced and the residence time for soot formation is reduced as well. They also observed that the fuel preheating and dilution reduces soot mass concentration. By analyzing the probability density function and the flatness factor, they showed that, the higher the Reynolds number, the more homogeneous is the soot mass distribution will be.

[23] investigated soot formation for methane-oxygen premixed flames and concluded that the first step towards soot formation in methane flames is the production of acetylene, with ethane and ethylene as an intermediates. Subsequently, the reactions of acetylene lead to the formation of benzene, PAH and poly acetylenes. The peak of acetylene is found to lag the peak of the higher hydrocarbon intermediates. They proposed that the rate of change of the number density is proportional to the square of the number density. Recently, this model is derived from the aerosol master equation by [24].

[25] showed that the soot composition as mainly carbon with up to 10 mole percent hydrogen, as well as traces of other elements. The soot particle nucleus is estimated to be about $20 - 30\ nm$ in diameter (that corresponds to about 10^6 carbon atoms). Soot formed in the temperature range of 1000 to 2500 C and is preceded by the formation of unsaturated hydrocarbons such as acetylenes and PAHs, which are thermodynamically and kinetically more stable than paraffines and olefines. These unsaturated hydrocarbons act as the main precursor for soot formation. Usually, the soot formation steps need time (order of *msec*) to create the soot particles. Wagner noted that the critical C/O ratio for soot formation varied with the fuel type. For instance ethylene flames starts sooting at a C/O ratio of about 0.6 for flat premixed flames. In addition, as pressure increases, the soot yield increases but the critical value remains the same.

Other detailed soot reviews are, [26], [27], [28] on soot nucleation, and [29] on the soot formation in diesel engines. [27] discussed the unresolved problems in SO_x, NO_x, and soot control in combustion. In particular, he emphasized that an applicable practical soot emission model did not exist, and discussed the nature of the soot particle, its general composition, and the C/O critical ratio. [30] suggested that the temperature and the fuel structure are the most important factors in soot formation, and that the soot tendency is reversed for aliphatics between premixed and diffusion flames. The reason being that in premixed flames there is always a competition between the rate of soot oxidation and the rate of pyrolysis and soot growth, while in diffusion flames such a competition does not exist. Levy summarized the soot formation steps as:

(a) The oxidative pyrolysis of the aromatic rings to give rise to unsaturated hydrocarbons.

(b) Following the formation of the radical species from the oxidative pyrolysis is the transformation of these radicals to a soot nuclei, which is the first particle to appear. This

particle is in the range $200 - 300$ A. However, a major question at this step is how the first soot nuclei are formed. Whether acetylene, benzene or PAHs is the soot precursor is still not certain as well. Other review (e.g: [28]) explained that the soot nucleation is an ionic processes rather than a chemical chain mechanistic problem.

(c) Three other processes are responsible for the soot mass growth. They are the surface growth, coagulation and aggregation. Surface growth occurs by attack of species on the soot surface. Still the type of these species and the reaction on the surface is questionable. Coagulation is affected by particle to particle collision and aggregation is the coalescence of these particles into chains.

(d) Finally, the oxidation of the soot particle. Many formulas exist for soot oxidation, the most notable one being the Nagle and Strickland-Constable's semi-empirical formula ([31]).

Another remarkable review by [32] (although 20 years old) is considered one of the most recent review papers. However, the most and first comprehensive collection of papers related to soot in all aspects was collected in a book edited by Bockhorn in 1994 ([33]).

2.2 Current Status

A lot of experimental and theoretical work has been conducted in the last 20 years. Experimental work has been conducted on soot formation in methane flames by Moss for premixed turbulent flames ([34]), and in confined turbulent jet diffusion flames ([35]). Recently, [36, 37] and [38] have conducted experimental work on turbulent non-premixed ethylene/air flames.

Numerical studies include the early work by [20] on turbulent combustion modeling with an emphasis on soot formation, [39] used CMC to simulate methane - air jet diffusion flames, [40] used LEM approach to study aerosol dynamics in engine exhaust plumes. Recently, [41] used detailed NO_x mechanism combined with MOM to predict the interaction among soot, thermal radiation and NO_x formation in non-premixed flames. A good review for available soot models till 1997, is given by [42].

Generally, a detailed chemical kinetics model is needed to capture the chemistry and the flow physics accurately, which is usually hard to be implemented in realistic configurations such as gas turbines or internal combustion engines. For such configurations, the operating conditions usually imply a high Reynolds number, which in turn, leads to a wide range of length and time scales.

The coupling between turbulence and soot formation is still not well understood. Several approaches have been used in the past to predict soot in realistic configurations as gas turbines, gas flares, and internal combustion engines. For instance, the laminar flamelet approach used by [43, 44, 45], allows the usage of a detailed chemical mechanism but is not suitable for turbulent flames at high Reynolds numbers. Since, it assumes fast chemistry limit and that the Kolmogorov scale is larger than the flamelet thickness. However, both are incorrect in a general combustion condition, where different flame regimes and high turbulent levels can coexist. Recently, the transported PDF method ([46]) was used to predict soot in a turbulent ethylene/air flame. Although the methodology permits a more accurate turbulent-

kinetics interaction, it has the disadvantage of modeling the molecular mixing, which is very vital to mix reactants together, and neglecting the unsteady effects.

[47] conducted experimental research on a slightly sooting methane oxygen flames. They concluded that particle inception is primarily controlled by the internal arrangement of polymers that lead to the formation of the first soot nuclei. These polymers are composed of aromatic compounds with 2-3 condensed rings connected to aliphatic and oxygen bonds. Regardless, the inception process is still not fully understood.

Soot formation process in premixed H/C flames is considered to occur as follows. The hydrocarbon fuel is oxidized to give small hydrocarbon radicals. Radicals combine to give acetylene as a soot precursor. Acetylene adds carbon atoms to other unsaturated radicals to form aromatic rings. All the forgoing processes occur in the molecular length scales in the order of 0.5 nm ([33]). Afterward, the large aromatic structures start to coagulate to form the primary soot particles. Once the primary particles are formed they start surface growth by picking up molecules and radicals from the gas phase. As a consequence, the rate of soot formation is attributed to the radical reactions rather than to the ionic reactions. While surface growth controls the soot concentration, coagulation controls the soot size. The soot primary particles coagulate to form a chain like aggregates if the residence time is high enough. Finally, all the above processes occur simultaneously with soot oxidation and destruction.

Soot precursors can be either acetylene, polyacetylene, allene, butadiene or PAHs ([28]). However, experimental ([26]), thermodynamic ([48]) and kinetic ([49]) evidence supports the that PAHs as the main soot precursor. [50] proposed a four step model based on PAHs as the precursor. The initial step is the formation of the first aromatic ring in an aliphatic system (acetylene), followed by planar PAHs growth, particle nucleation, and finally particle growth by coagulation into chain like aggregates. This model will be extremely useful, when we have a well suited reduced mechanism that can predict PAHs, which is not available now (as far as the author's knowledge). The first aromatic ring formation in non-aromatic fuels (no ring structure) was described as follows: The pathway starts with vinyl C_2H_3 addition to acetylene C_2H_2 to form vinyl-acetylene. Afterwards, the first aromatic ring is formed by acetylene addition to n-C_4H_3, which is formed by H abstraction of vinyl-acetylene. At low temperature, acetylene is added to n-C_4H_5 to give benzene. However, [51] suggested that benzene is formed by combination of propargyl radicals rather than the n-isomers, as Frenklach suggested. Frenklach used the method of moment as a lumping technique to describe the PAHs growth ([50]). The kinetics of the infinite sequence of PAHs growth reactions were described by a small number of differential equations developed for the moments of the PAHs distribution. This method is utilized here in a different way, as will be discussed later.

[52] introduced a simplified semi-empirical model for soot nucleation and surface growth. The model is based on benzene and acetylene as indicator in the flame structure for soot nucleation and surface growth. This model used several experimental data obtained from counterflow diffusion flames ([53]), and has the advantage of generality and independence of initial fuel type. Moreover, the use of acetylene as an indicative for soot location requires less number of species to be included in the mechanism, which reduces the computational cost. Acetylene has proven to give good agreements in both methane and ethylene flames by [54] and [55]. [56] suggested that soot surface growth due to absorption of acetylene on the

particle surface to be first order in acetylene concentration and linear function in the soot surface area as will be shown later.

Most of the work mentioned above used a similar model to connect the soot chemistry to the flow dynamics, where two transport equations for the soot mass fraction and number density are solved simultaneously with the conservation of mass, momentum, and energy ([39]).

The following section will summarize most of the above mentioned turbulent combustion models used for soot modeling in turbulent flames. Also, a general overview of turbulent combustion modeling will be presented, with an emphasis on the models suitable for Large Eddy Simulation (LES).

3 Turbulent Combustion Modeling

One of the most active research areas that are still open for further improvements is the simulation of reactive flows in realistic configurations. For the reaction to occur, the reactants have to be mixed together. These mixing only occur at small molecular length scales. In numerical approaches like LES and RANS, only large energetic scales are resolved (only the mean flow in RANS calculations), while small scales (mentioned earlier) need to be modeled. The resolution of these scales are very hard to achieve numerically, within the available computational limits. Consequently, the combustion source term is modeled. The modeling of this term is complicated by its nonlinearity in addition to the complex interaction between turbulent transport and combustion heat release. For instance, a two-way coupling between turbulence and combustion exists. Turbulence enhances mixing and causes the flame to wrinkle, which increases its surface area. As the flame surface area increases, more reaction surface will be available. On the other hand, combustion releases heat, which causes instabilities in the flow that enhance transition to turbulence. Moreover, for non-premixed flames, as turbulence increases, the mixing rate increases and the flame length needed to consume the fuel decreases, and the flame became more compact and shorter. A shorter flame, allows for a more compact combustor design, less material and mechanical requirements. Many turbulent combustion models reviews and text books has been introduced ([57, 58, 59, 60, 61]). A brief discussion and review will be introduced here as well. In the next subsections, we will introduce some length and time scales that will be used in the discussion of the combustion models.

3.1 Time and length scales

Three time scales are most important for combustion applications. The residence time scale τ_{res}, which is defined as the time taken by a fluid element to move between two locations. This time scale is governed by the local fluid velocity U and length L, which might be considered as the combustor dimension or the distance between two grid points $\overline{\Delta}$:

$$\tau_{res} = \frac{\overline{\Delta}}{U} \tag{1}$$

The second time scale is the mixing time scale τ_{mix}. This time scale is different than the diffusion time scale due to molecular mixing. For turbulent flows, it can be identified by the

turbulent intensity $u^{'}$ (computed from the subgrid turbulent kinetic energy), and integral length scale l (defined in the next section) as:

$$\tau_{mix} = \frac{l}{u^{'}} \tag{2}$$

In a more physical sense, this is the time scale needed for an eddy to make a complete turnover. Where the eddy is defined as a macroscopic entity, in which the microscopic elements all behave in the same manner [62].

Finally, the chemistry time scale τ_c, which is species dependent. For a species Y_k the chemical time scale can be calculated from:

$$\tau_{c,k} = \frac{\rho Y_k}{|\dot{\omega}_k|} \tag{3}$$

Where, $\dot{\omega}_N$ is the species consumption rate and ρ is the mixture density. However, for premixed flames the above chemistry time scale is usually difficult to estimate and another characteristic time scale is identified based on the laminar unstrained flame speed S_F and thickness δ_F by:

$$\tau_F = \frac{\delta_F}{S_F} \tag{4}$$

The relation between these three time scales identify the mode of combustion with respect to flow dynamics. Three modes are identified for chemistry. Frozen chemistry, occurs when $\tau_c >> \tau_{res}$. This flow usually characterizes nonreactive situations, where the mixing time τ_{mix} is very large to achieve mixing or combustion. The other limit is the chemical equilibrium limit, where $\tau_c << \tau_{res}$. This type of flow is characterized by fast mixing that allow chemistry to occur independent of the flow dynamics. The reaction rate in this case is infinite and occurs instantaneously. In-between these two limits the finite rate chemistry becomes important, where the chemical and mixing time scales are comparable (for example during ignition and initial mixing process).

Three length scales used in the subsequent sections are also introduced here (although many other exist). The integral length scale, l, which represents the mean size of the energy containing non-universal large eddies. This mean size depends on the boundary conditions and is geometry dependent. Its magnitude is usually of the same order as the size of the combustor. Mathematically, the integral length scale at location x and time t can be represented in terms of the correlation between two points $R_{i,j}(r, x, t)$, separated by a distance r as follows:

$$l(x,t) = \frac{1}{R(o,x,t)} \int_0^\infty R(r,x,t)dr \tag{5}$$

Where $R(r,x,t) = \langle u_i^{'}(x+r,t)u_j^{'}(x,t)\rangle$ is the correlation between the root mean square (r.m.s) velocity $u_i^{'}$ at two points separated by distance r. Another important length scale is the Kolmogorov length scale η. This length scale represents, theoretically, the smallest possible fluid dynamics length scale, at which the turbulent kinetic energy is completely dissipated to internal energy. This length scale also characterize the dissipation range, where the flow field is locally isotropic. At this range the dynamic viscosity ν is significant in addition to the dissipation rate ϵ. Accordingly, by dimensional analysis η can be approximated

in terms of the energy dissipation ϵ as:

$$\eta = \frac{\nu^{3/4}}{\epsilon^{1/4}} \tag{6}$$

The integral and the Kolmogorov length scales are related by:

$$\frac{l}{\eta} \approx Re_l^{3/4} \tag{7}$$

Where, $Re_l = \frac{u^{'}l}{\nu}$ is the Reynolds number based on the integral length scale. The third length scale is related to the flame thickness δ_F, which usually give an indication of the reaction zone thickness (or inner layer) $\delta_{RZ} \approx 0.1\ \delta_F$. The combination of these length scales determine the combustion regime for both premixed ([63]) and non-premixed ([39]) flames. Another non-dimensional numbers, used for identifying the flame regime in premixed flames, are the Damkohler number and the Karlovitz number. The former, is the ratio between the mixing and the chemical time scales defined as ([63]):

$$Da = \frac{\tau_{mix}}{\tau_F} = \frac{S_F l}{\delta_F u^{'}} \tag{8}$$

Where, δ_F and S_F are the laminar flame thickness and speed, respectively. Finally, the ratio between the chemical characteristic time scale and smallest turbulence time scale (based on the Kolmogorov time scale) is known as the Karlovitz number.

$$Ka = \frac{t_F}{t_\eta} = \frac{\delta_F v_\eta}{S_F \eta} \tag{9}$$

Where, v_η is the velocity based on the Kolmogorov length and time scale. The next section will summarize the most known combustion models used in the field of turbulent combustion. Most of these models are originally designed for RANS calculations and are eventually extended for LES.

3.2 Laminar Chemistry Model

This model assumes that turbulence effect on chemistry is negligible and only molecular diffusion controls mixing. In other words, the chemistry time scale is very large in comparison to the turbulent time scale:

$$\begin{aligned} &\tau_c >> \tau_{mix} \\ &Da << 1 \\ &Ka >> 1 \end{aligned} \tag{10}$$

Under the above conditions, the laminar reaction rate is much smaller than the rate due to mixing, and laminar chemistry controls the reaction process. As indicated by the above assumptions, this model is an oversimplification for turbulent flows, as it considers no turbulence effect on chemistry, and that the reactants are readily mixed. Hence, the production/destruction rate for the $k-th$ species molar concentration $[C_k] = \frac{\rho Y_k}{M w_k}$ is simply calculated from:

$$\begin{aligned} &\tfrac{d[C_k]}{dt} = \\ &\textstyle\sum_{l=1}^{N_T} \left[\left(\mu^{"}_{k,l} - \mu^{'}_{k,l}\right) k_{f,l} \prod_{j=1}^{Ns} [C_j]^{\mu^{'}_{j,l}} + \left(\mu^{'}_{k,l} - \mu^{"}_{k,l}\right) k_{b,l} \prod_{j=1}^{Ns} [C_j]^{\mu^{"}_{j,l}} \right] \end{aligned} \tag{11}$$

In the above equation, $k_{f,l}$, $k_{b,l}$ are the forward and the backward reaction rates of the $l-th$ reaction, respectively. Also, $\mu'_{k,l}$ and $\mu''_{k,l}$ are the stoichiometric coefficients of the reactants and products of the $l-th$ reaction, respectively. The number of reactions is N_r and the number of species is N_s.

3.3 Eddy Breakup and Eddy Dissipation Concept Models

The other limit occurs, when the mixing time is very high in comparison to the chemical time scale. Chemical reaction is governed by the mixing rate. The following conditions must be satisfied:

$$\begin{aligned} &\tau_c << \tau_{mix} \\ &Da >> 1 \\ &Re_t >> 1 \end{aligned} \tag{12}$$

This concept was first introduced by [64], and modified by [20]. The model assumes that the chemical time scale τ_c is much smaller than the mixing time scale τ_{mix}. Spalding based his argument on the energy spectrum cascade theory in the inertial range, where energy is transformed from the large to the molecular scales. Using the scaling laws in this regime the chemical time scale can be represented as $\tau_c = \frac{k}{\epsilon}$, where k is the turbulent kinetic energy and ϵ is the dissipation rate. Both k and ϵ can be obtained for a turbulent model such as k-ϵ for RANS studies. Accordingly, he defined the turbulent mean reaction rate of products $\bar{\omega}_p$ of products for EBU model as:

$$\bar{\omega}_p = \bar{\rho} C_{EBU} \frac{\epsilon}{k} \left(\bar{Y}_P^{"2}\right)^{1/2} \tag{13}$$

Here, $\bar{Y}_P^{"2}$ is the variance of the product mass fraction and C_{EBU} is a calibration constant for EBU. [20] modified the EBU, by replacing the variance by the mean mass fraction to introduce EDC model. The model takes the minimum between the production rate of the reactants deficient species (taken as fuel Y_F in lean flames and oxygen Y_O for rich one) and the product species as:

$$\bar{\omega}_p = \frac{\epsilon}{k} \bar{\rho}\ min\left(C_{1EBU}\bar{Y}_F, C_{2EBU}\frac{\bar{Y}_P}{1+\mu}\right) \tag{14}$$

The above formulation involves a set of constants (C_{1EBU}, C_{2EBU}) that are not universal and need to be specified. However, the above formulations assume that turbulence control the mixing process all the time for a one step global mechanism $(Y_F + \mu Y_O \longrightarrow (1+\mu)Y_P)$. In general conditions, both limits (turbulent mixing and molecular mixing) can exist. Hence, the model can be reformulated as follows:

$$\bar{\omega}_p = min\left[\dot{\omega}_p^{ck}, \dot{\omega}_p^{mix}\right] \tag{15}$$

Here, $\dot{\omega}_p{}^{c.k} = Mw_p \frac{d[C_p]}{dt}$ is the production rate of the Y_p species based on chemical kinetics as shown in Eq. (11), and $\dot{\omega}_p{}^{mix}$ is the production rate based on mixing and is calculated from Eq. (14).

The above formulation is more adequate for premixed flames. For non-premixed flames the species concentrations are simply replaced by a conserved scalar as the mixture fraction. [65] introduced a modification based on the EBU and the EDC models as:

$$\bar{\omega_R} = -\frac{1}{2}\bar{\rho}\frac{Y_F}{1 - Z_st}\chi_{st}P(\tilde{Z}_{st}) \tag{16}$$

Where, Y_F, χ_{st}, and $P(\tilde{Z}_{st})$ are the fuel mass fraction in the fuel stream, the scalar dissipation rate, and the PDF of the mixture fraction conditioned at the stoichiometric value $X = X_{st}$, respectively. In general, the EBU or EDC model over predicts the production rates in regions of high strain rate, for example in the shear layer and near the wall. In addition, it assumes that all the chemical processes are controlled by mean quantities, which is not correct, since the chemical process is mainly controlled by the small unresolved scales. The above formulations can be modified easily for LES applications, by replacing the turbulent kinetic energy by the subgrid kinetic energy k_{sgs}, which is solved simultaneously with the space filtered equations in LES.

3.4 Laminar Flamelet Concept

[66, 67] introduced the laminar flamelet concept, which states that the chemical reaction occurs in an asymptotically thin layers called flamelets. Inside these flamelets the laminar chemistry assumption is valid, and mixing or turbulent transport has no effect. Inherently, the flamelet model includes three important assumptions:

- Large Da number (or equivalently short chemical time scale).
- The reaction zone thickness is smaller than the Kolmogorov length scale.
- The statistics of the reactive scalars can be identified based on the statistics of non-reactive scalars that represent the flame location.

Based on these assumptions the turbulent eddies can never penetrate the thin reaction zone and chemistry is mainly controlled by the chemical kinetics. In addition, the reactive scalars and the non-reactive scalar are convected by the same speed.

In the flamelet concept, the flame is considered as a thin propagating sheet that is identified as an iso-surface of a conserved scalar variable. In non-premixed flames this scalar is the mixture fraction, while in premixed flames it can be either the progress variable ([63]) or a flame iso-surface tracking variable G. For non-premixed flames, the mixture fraction equation is solved first as:

$$\rho\frac{\partial Z}{\partial t} + \rho v \cdot \nabla Z = \nabla \cdot (\rho D \nabla Z) \tag{17}$$

Where Z is the mixture fraction and D is the molecular diffusivity coefficient. Following that the flame surface is identified by $Z = Z_{st}$, where Z_{st} is the stoichiometric mixture fraction. Next, a general flamelet reactive species ψ_i equation can be solved in the mixture fraction space as:

$$\rho\frac{\partial \psi_i}{\partial t} + \frac{\rho}{Le_i}\frac{\chi}{2}\frac{\partial {\psi_i}^2}{\partial Z^2} = \dot{\omega}_i \tag{18}$$

In the above formulation, the scalar dissipation χ, considered as an inertial range invariant, has to be related to the mixture fraction Z. [63] identified this relation as:

$$\chi = 2D_t|\nabla Z|^2 \tag{19}$$

In the above equation D_t is the eddy diffusivity. For LES the above relations are solved as follows ([68]. First, the dissipation rate is computed from the filtered mixture fraction as $\widetilde{\chi} = 2D_t(\nabla\widetilde{Z})^2$, where the eddy diffusivity is computed from $D_t = (C_z\overline{\Delta})^2\widetilde{S}$. The constant C_z can be determined dynamically and the Favré filtered stain rate is $\widetilde{S} = |\widetilde{S_{ij}}\widetilde{S_{ij}}|^{1/2}$. Finally, the scalar variance can be computed from $\widetilde{Z'^2} = C_\nu\overline{\Delta}(\nabla\widetilde{Z})^2$. Inherently, in the above formulation a constant time scale is assumed, which is equivalent to assuming that the production and dissipation of the scalar variance are balanced ([68]). However, this assumption is not necessarily true under general turbulent conditions.

Two categories of the flamelet model are identified, the steady flamelet model ([69]), which assumes that the flame structure is in steady state by neglecting the time derivative in Eq. (18), and the unsteady flamelet model ([70]). The steady state assumption, is inaccurate if the chemistry is not fast enough. In the unsteady flamelet model Eq. (18) is solved simultaneously with the LES equations. Examples, of the unsteady flamelet models are the Lagrangian Flamelet Model (LFM) ([70]) and the Eulerian Flamelet Model ([71]). The later model is more superior over the former, since the LES and the flamelet equation are fully coupled and the effect of the resolved turbulence fluctuations on the scalar dissipation rate is included. However, both of them will be expensive for complex chemistry.

Another LES approach is the flamelet/progress variable method ([72]). In this method, a transport equation for a progress variable is solved with the LES equation, combined with a steady flamelet library. However, in both models (progress variable and scalar dissipation) a presumed PDF is needed to find the filtered mass fraction from the flamelet library. The progress variable formulation shows better results regarding unsteady phenomena as extinction and re-ignition ([68]).

In premixed flames, the method is termed level-set approach ([73],[63]), or the G-equation model. Where the flame sheet iso-surface is represented by the level-set function G, which might represent a scalar as temperature or progress variable, and is described as:

$$\rho\frac{\partial G}{\partial t} + \rho u_i\frac{\partial G}{\partial x_i} = \rho s_d|\nabla G| \tag{20}$$

Here, s_d is the displacement speed of the flame element. If the flame surface is given as $G = G^*$, the fresh mixture is defined by $G > G^*$ and the burnt gases are identified as $G < G^*$. In LES, [74] derived the filtered G equation as:

$$\frac{\partial\bar{\rho}\tilde{G}}{\partial t} + \frac{\partial\bar{\rho}\tilde{u}_i\tilde{G}}{\partial x_i} = -\rho s_T|\nabla\tilde{G}| - \frac{\partial G_i^{sgs}}{\partial x_i} \tag{21}$$

where the unresolved transport term G_i^{sgs} is modeled as follows (using a gradient diffusion assumption ([75]) :

$$G_i^{sgs} = \bar{\rho}\left[\widetilde{u_iG} - \tilde{u}\tilde{G}\right] = -\frac{\bar{\rho}\nu_t}{Sc}\nabla\tilde{G} \tag{22}$$

where, Sc is the turbulent Schmidt number and ν_t is the turbulent eddy vicoscity, respectively. The turbulent flame speed in Eq. (21) S_T can be modeled as:

$$\left(\frac{S_T}{S_F}\right)^n = 1 + \alpha\left(\frac{\bar{u}'}{S_F}\right)^n \tag{23}$$

Here, S_F is the laminar flame speed, $n = 2$, α is an adjustable parameter, and $u' = \frac{3}{2}\sqrt{k_{sgs}}$ is the subgrid turbulence intensity. However, [76, 68] provides a new filtering technique that conserves the nature of the level-set variable.

3.5 Artificially Thickened Flames

For completeness, the artificially thickened flame model will be overviewed here. In order to be able to resolve the thin flame thickness in premixed flames on the LES grid level, [77] introduced the flame thickening concept, where the thermal diffusivity is scaled by a factor (F) and the flame thickness will be increased by the same factor. From laminar premixed flame theories:

$$\begin{aligned} S_F &\propto \sqrt{D_{th}B} \\ \delta_F &\propto \frac{FD_{th}}{S_F} \end{aligned} \tag{24}$$

Where, B is called a pre-exponential value. As a result of this the interaction of turbulence with chemistry is altered by the variation of the Da number value. In other wards, as the flame is thickened, it became less sensitive to the turbulent effects.

3.6 Conditional Moment Closure

This concept is mainly derived for non-premixed flames by [78] for RANS calculations. Bilger argued that the fluctuations of the reactive scalars are accompanied by fluctuations in the mixture fraction. Consequently, the reactive scalars are conditioned on the mixture fraction for non-premixed flames and the progress variable for premixed flames. The general methodology of Conditional Moment Closure (CMC) is summarized in the following bullets:

- Starting from the $k-th$ species Y_k conservation equations as:

$$\rho\frac{\partial Y_k}{\partial t} + \rho\vec{v}\cdot\vec{\nabla}Y_k = \vec{\nabla}\cdot\left(\rho D_k\vec{\nabla}Y_k\right) + \dot{\omega}_k$$

- Bilger replaces every reactive scalar by a conditional mean plus a conditional fluctuations:

$$Y_k = \bar{\psi}_k\left(Z;x,t\right) + \psi_k'\left(Z;x,t\right)$$

  Where Z is the mixture fraction and the conditional mean is defined as ([61]):

$$\bar{\psi}_k\left(Z;x,t\right) = \int_0^1 Y_k\ P\left(Y_k|Z;x,t\right)$$

  Here, $P\left(Y_k|Z;x,t\right)$ is the conditional PDF. The following assumptions are taken:

- The conditional turbulent transport is negligible.

- The higher moments of the chemical source term can be neglected.
- The conditional velocity can be replaced by the mean unconditioned velocity. The following equation is then derived as ([78]):

$$\langle \rho | Z \rangle \frac{\partial \bar{\psi}_k}{\partial t} + \bar{v} \cdot \nabla \bar{\psi}_k = \langle \rho | Z \rangle \tilde{\chi}_Z \frac{\partial^2 \bar{\psi}_k}{\partial Z^2} + \omega_k \left(\langle Y_k | Z \rangle \right)$$

  In the above equation all the Z subscripts indicates the mixture fraction space. The values $\langle \rho | Z \rangle$ and $\langle Y_k | Z \rangle$ indicates the density and the scalar conditioned on the mixture fraction Z. The scalar dissipation is computed from $\tilde{\chi}_Z = \langle \rho \chi | Z \rangle / \langle \rho | Z \rangle$.

- For the PDF $P(Y_i | Z; x, t)$ either the transport PDF equation is used or a presumed shape is utilized.

The CMC was used for soot prediction in RANS calculations ([79]). [80] reformulated the CMC for LES applications, where the number of independent spatial coordinates are reduced by integrating the reactive scalar transport equation in one direction. However, some issues regarding CMC boundary conditions and numerical efficiency is still under investigation ([81]).

3.7 PDF Methods

In the PDF transport methods, a transport equation for the joint PDF between the velocity and the scalars $\Phi(v_i, \psi_j : x_i, t)$ are derived from the Navier Stokes equations ([82]). This joint PDF equation includes all the relevant information to the moments of the velocities v_i and the scalars ψ_j (temperature, mixture fraction and species concentration). However, it includes no information for the scalars gradients ([63]). Accordingly, the PDF transport equation represents the variation in the physical space x_i, the velocity space v_i, and the scalar field space ψ_j. Hence, the PDF transport equation is a multidimensional equation that has $7 + Ns$ dimensions, where, Ns is the number of scalars to be solved. The PDF method has been used extensively for RANS calculations then modified afterwards for LES applications ([83]).

In the transport equation for the joint PDF, the chemical reaction source term, the local rate of convection of the joint PDF in the physical space, and the transport by the pressure forces and the body forces in the velocity space are closed terms. Therefore, these terms are exact and require no closure, which is the powerful point in the PDF methods. However, the molecular mixing in the scalar space, the transport of the PDF by shear stresses, and the fluctuating pressure gradient in the velocity space are all unclosed terms and require closure. Since the PDF equation is multidimensional it is very expensive to be solved by finite volume or finite difference methods. Therefore, PDF methods use the Lagrangian Monte Carlo technique, which is found to increase the memory requirements only linearly with the problem dimension ([82]).

To illustrate the PDF method the transport equation is written as follows ([82]):

$$\underbrace{\frac{\partial \rho \Phi}{\partial t} + \nabla \cdot (\rho v \Phi)}_{\mathrm{I}} + \underbrace{\left(\rho g - \nabla \bar{P}\right) \cdot \nabla_v \Phi}_{\mathrm{II}} + \underbrace{\sum_{i=1}^{N_s} \frac{\partial}{\partial \psi_i} \left[\omega_i \Phi\right]}_{\mathrm{III}} = \underbrace{\text{Molecular mixing and transport by shear stresses and pressure fluctuations}}_{IV} \tag{25}$$

where $\Phi(v, \psi, x, t)$ is the joint PDF, N_s is the number of reactive scalars, ψ_i denotes $i-th$ scalar, $\bar{P}$ is the mean pressure, and the subscript v denotes the velocity space, respectively.

The Monte Carlo hybrid algorithm can be summarized as follows:

- The physical domain is descritized by finite volume or finite difference methods and the mean equations of the conservation of mass, momentum, and energy (i.e. RANS or LES) are solved on the physical grid.
- A number of particles N is specified to represent the whole domain.
- Each particle N_j (where j is the particle index) is characterized by a position $x^{(j)}$ and a velocity $v^{(j)}$ in the physical space and a corresponding value of the reactive scalars that it represents.
- The first term I in Eq. (25) is modeled as :

  $$x^{(j)}(t + \Delta t) = x^{(j)}(t) + v^{(j)} \Delta t$$

  Where Δt is the integration time step (should be small enough for numerical stability and accuracy of calculation).
- The second term II in Eq. (25) is represented by :

  $$v^{(j)}(t + \Delta t) = v^{(j)}(t) + \left(g - \nabla \frac{\bar{P}}{\rho}\right) \Delta t$$

  Where $\bar{P}$ is the mean pressure in the physical space. The above equation represents the transport of the particle in the Lagrangian space by the pressure and the body forces.
- The third term on the L.H.S. III in Eq. (25) is represented by the change in composition of the scalar by:

  $$\psi_i^{(j)}(t + \Delta t) = \psi_i^{(j)}(t) + \left(\frac{\omega_i^{(j)}}{\rho^{(j)}}\right) \Delta t$$

  The above equation represents the change of the value of the scalar ψ_i of the lagrangian particle j by reaction.

- The terms on the R.H.S IV has to be modeled by any known stochastic Lagrangian mixing models as the Langevin model, the Interaction by Exchange model (IEM) or the Coalescence-Dispersion (C-D) methods [84].

The drawback of the above formulation is the statistical error of the Lagrangian Monte Carlo method, which is inversely proportional to the initial number of particles. In addition to modeling the molecular mixing as mentioned before. Finally, the PDF hybrid method in the above formulation assumes that the different physical processes in the PDF transport equation are additive in time, so that each effect on the particle velocity can be computed independently.

3.8 Filtered Density Function

The Filtered Density Function (FDF), first proposed by [85] for LES calculations and then developed by [86] and [87]. The transport equation of FDF is derived by space filtering the joint PDF transport equation. The resulting equation contains unclosed terms similar to Eq. (25) that need closure. Again, the Monte Carlo simulation methodology is used to close these terms (transport by shear stresses, pressure forces, and molecular mixing) using one or a combination of the famous mixing models like the generalized Langevin model (GLM) ([86, 83, 88]).

For closure of the unclosed terms in FDF, Monte Carlo simulation is used, where particles are tracked in a Lagrangian sense and a two way coupling is done between the filtered field and the particles. The LES filtered equations for mass, momentum, and energy are solved on a finite volume grid and the mean values are computed, as the mean pressure, velocity components, subgrid kinetic energy, and dissipation. Next, the information is transferred from the grid cell centers to the Monte Carlo particles by interpolation techniques ([89]). The information is transferred back from the particles to the grid points by ensemble averaging. FDF has the advantage of comprising all the low and high moments information on the subgrid level, which give it superiority over the conventional LES combustion subgrid models described above. [86] assessed the consistency and convergence of the Monte Carlo Procedure by comparing the FDF results with a second order LES-FD and to a DNS results for a temporal mixing layer. The FDF results show superior results over the second order LES-FD at some locations, which is attributed to the accuracy errors in the LES-FD procedure that does not exist in the Lagrangian methodology. However, there are some issues that is currently under investigation and we summarize them here:

- There is a redundancy issue with hybrid schemes, some variables are computed by the FDF Lagrangian solver, other by the Eulerian solver, and other by both. The consistency between these variables need to be checked ([88]).

- Molecular mixing is mainly a subgrid phenomena, FDF as a PDF methodology requires closure for these terms. Several mixing models are proposed that depend on the filtered mean values for closing such term.

- The numerical error by the interpolation techniques between the grid points and the particle locations needs to be probably assessed. [86] used a second order interpolation for 3D flows and fourth order interpolation for 2D flows.

- The mixing time in FDF needs to be modeled based on solving two extra equations for the mass fraction mean and variance ([89]).
- In FDF, the number of particles mass weight inside each cell is adjusted to the current LES cell mass by a splitting-clustering technique, this generates numerical diffusion in the composition space. In this methodology particles that have mass larger than the cell mass average is split, while lighter particles are clustered ([89]).
- Since the particle location and velocity are random variables, the stochastic nature of the particle scheme leads to numerical instabilities ([90]). This instability decreases by increasing the number of tracked particles, which increases the computational and memory requirements.
- The continuity conservation in FDF is questionable ([89]), since the interpolation technique leads to velocity errors and the particles number is finite and are allowed to move freely in the domain. However, [91] claimed that if the particles are initially distributed uniformly, they will remain uniform during the simulation if continuity is satisfied.
- To avoid numerical instabilities and divergence in the numerical scheme due to transport of data from the stochastic particle domain to the deterministic Eularian domain, [89] used an indirect transfer of information by solving an enthalpy transport equation. The source term in the enthalpy equation is computed from the particles density and then LES scheme is updated based on this.

3.9 Linear Eddy Mixing and Combustion Model

The Linear Eddy Mixing model developed by Kerstein ([92, 93, 94, 95, 96, 97, 98]) will be prescribed here. LEM as a subgrid combustion model for LES calculations is called LEMLES.

In LEMLES, models at the resolved scales are avoided altogether. Instead, scalar evolution is modeled by a combined Eulerian-Lagrangian approach that captures both the large and the small scale processes correctly. All processes occurring below the LES grid scale, such as reaction-diffusion, heat release, volumetric expansion, and turbulent stirring by the small-scales (i.e., scales below the grid scale $\overline{\Delta}$) are simulated within each LES cells on a one-dimensional domain (the LEM domain). The large-scale transport (by the LES resolved mass transport) of the subgrid scalar fields across LES cells is modeled by a Lagrangian advection process that ensures exact mass conservation ([99, 100, 101]). A brief literature review of LEM will be introduced next, followed by the justification of choosing LEMLES as the current combustion and mixing model for soot predictions.

LEM has been extensively validated and applied to a variety of turbulent combustion problems in both the premixed and the non-premixed regimes. Menon and Kerstein ([102]) applied LEM for a premixed flame propagating in a statistically steady turbulent flow field in the wrinkled flamelet regime. The molecular diffusion and finite rate processes are replaced with a flame propagation model based on the G-equation methodology (GLEM). The domain considered was a longitudinal line along the turbulent flame brush, which is propagating with a constant flame speed and is subjected to turbulent stirring. The turbulent flame speed was found to be linearly dependent on the turbulent fluctuations, and that the flame surface

is fractal from the integral length scale down to the Kolmogorov scale or the Gibson length scale.

Different studies has been conducted to diffusion jet flames. [103] conducted a study on a hydrogen-argon-air jet diffusion flame. The LEM domain in this case represents the jet centerline. The study investigates the effect of molecular transport on the chemistry-turbulence interactions. The Lewis number and differential diffusion were found to impact the heat release rate in the near field, affecting the buoyancy of the jet and the air entrainment downstream. [104] used LEM to predict the mixing of a conserved scalar in a turbulent shear layer. The scalar field PDF shows a good agreement with the DNS data.

[105] used LEM to compare between a detailed full chemical mechanism and a reduced mechanism for H_2-air combustion with NO formation for a non-premixed, turbulent jet flame. Good agreement is achieved, with some deviations for the radical species. The LEM domain was represented by a vertical line that is convected downstream. The work concluded that the effect of Lewis number counteracts the preferential diffusion effect on lowering the temperature. Furthermore, the chemical kinetics effect is found to be dominant close to the nozzle jet, while the flow is more transport controlled downstream, where the flame reaches an equilibrium state. A similar configuration was used previously by [106] to predict NOx formation in a jet hydrogen-air flame.

[107] utilized LEM to construct a joint-pdf to close the chemistry term in the PDF moments equations. The derived PDF assumes that the PDF of scalars can be expressed as a function of its lower moments for a decaying homogeneous turbulence. In addition, the general turbulence reacting flow scalar PDF can be approximated by the decaying homogeneous turbulence PDF tabulated by using LEM. The resulting joint-PDF was function of the progress variable and the mixture fraction. The model was applied to a RANS calculation of a turbulent, round jet flame. It showed good agreement with the pre-assumed PDFs and the experimental data.

[75, 108] compared the one-dimensional stand-alone LEM and DNS to capture the premixed flame structure, and to study the effect of Lewis number and turbulent intensity. They included the effect of finite rate chemistry and the effect of heat release. Good qualitative agreement is achieved with DNS. The model confirms the linear relation between the turbulent intensity, and the turbulent flame speed. In comparison with DNS, only the stationary state LEM data can be quantitatively comparable to DNS, while the transient data can be compared only qualitatively. Hence, different LEM realizations were simulated and the average was taken over time and space. In addition, to simulate a freely propagating DNS flame with a stationary LEM one, an observation window is fixed to the propagating flame with defined boundaries to represent the LEM domain.

[99, 100] used LEM as a subgrid model for LES applications. They were the first to use the Lagrangian transport scheme to model the scalar advection through the LES cells. The model was applied to study premixed flames in the flamelet regime. Comparison with the conventional LES and DNS results shows the superiority of LEM subgrid model in capturing the flame structure, the flame turbulence interaction and the counter-gradient diffusion effects. The G-equation model was used to captured the transition from wrinkled flamelet to corrugated flamelet in three dimensional stagnation point premixed flame. More recently, [109, 110] investigated the LEM subgrid model for a set of 3D and 1D premixed flames in the thin reaction zone using single step chemistry. The statistics show good agreement with the

DNS data. The flame structure and surface area were captured accurately, to demonstrate the ability of LEMLES in such high turbulent regime. [111] compared between the filtered G-equation and LEMLES in a dump combustor. For different lean equivalence ratios, the two models show different flame length and structure. The difference was attributed to the more accurate prediction of the vortex breakdown by LEMLES. More recently,([112]) LEMLES was used to simulate a non-premixed and partially premixed flame in a swirl, bluff body stabilized flame. Results were compared to experimental and all the flow features were captured reasonably. The results demonstrate the capability of LEMLES to handle such complex flows.

In the current Thesis LEM is chosen as the combustion and mixing model. As mentioned earlier, for combustion to occur the reactants have to mix at the molecular levels at the unresolved scales. In LEM the mixing, diffusion, and reaction processes are solved for exactly, without any filtering or closure requirements. Consequently, all the mixing closure problems in other models (as PDF and FDF) are all avoided. In addition, from the above discussions, for premixed flames, LEM can be employed in all the combustion regimes, while other methodologies, as the flamelet model, can only operate at regimes, where the smallest turbulent eddy is larger than the reaction zone thickness. Moreover, LEM allows the usage of relatively complex mechanisms to predict pollutants as NOx, CO ([113]), and soot ([114]). Hence, LEM was found to be currently the most universal and flexible model to be employed to predict soot for LES calculations.

The following section will present the Thesis technical objectives. In section V, the governing equations, the numerical approach, and the elements of the proposed model will be shown in details. Next, the numerical implementation will be discussed in Section VI. Afterwards, the last three sections will be devoted for the results in premixed and non-premixed configurations for both sooting and non-sooting flames, and finally the the conclusions and the recommendations.

4 Technical Objectives

In this chapter the technical objectives of the current Thesis, the challenges, and the proposed road map to achieve the goals are presented. The general goal of the current work is to develop a soot subgrid model for LES calculations. This subgrid model should be characterized by the following features:

1. Applicable to all combustion regimes in premixed and non-premixed flames without any ad-hoc changes.
2. The model should be flexible to absorb all future changes of its components.
3. Suitable for highly turbulent unsteady flames and complex configuration.
4. Computationally efficient and reasonably accurate.
5. The model should cure all the shortcomings in the current models, such as neglecting the effect of unresolved turbulence fluctuations, unsteady effects, and physical coupling between acoustic, turbulence flame interaction, on soot formation.
6. The model should account for the basic physical processes involving soot such as diffusion, thermophoresis, soot dynamics, and radiation.

In order to achieve the above goals, the following questions have to be answered:

1. Which numerical approach is suitable and what type of subgrid models and closures will be associated with it (chapter III).
2. What are the physical processes that will be accounted for in the soot model.
3. Are there any numerical issues that will arise by incorporating these soot models with the other existing combustion and closure models or not.
4. How will the chemistry closure be encountered and how will it affect the soot model and the choice of the fuel/type and the mechanism used.
5. Are there any experimental data for turbulent flames that match the choice of the fuel type for validation.

As a consequence of the former discussion at the end of chapter (I), LEMLES is found to be the most suitable numerical approach to achieve the first and the second goals. Therefore, the LES formulation will be implemented, combined with the LEM for combustion closure and LDKM for momentum closure. The formulation is compressible and Favré averaged.

The physical soot processes that need to be accounted for are soot nucleation, surface growth, coagulation, aggregation, thermal radiation, soot transport by diffusion and thermophoresis. In order to achieve flexibility, each of these components are attached to LEM in the from of independent modules. For each module, the most efficient models in the literature are picked up to perform the required functionality.

In order, to reduce the computational effort a low carbon content fuel (ethylene) is chosen, and a recently reduced mechanism form the literature is used to close the chemistry. Few

experimental data are found in the literature, the most recent one is picked up to validate our results.

In the validation method, we started by studying a set of canonical premixed flames, to examine the model physics and its qualitative behavior. Then we examined LEMLES without soot in a non-premixed configuration and compared it with the experiment. Then finally, the model was validated against a non-premixed ethylene/air jet flame.

5 Mathematical Formulation and Numerical Approach

In this chapter the flow governing equations and the numerical approach used together with the subgrid closures of the filtered equations, will be presented. The last section of the chapter is devoted to show the proposed model components in details.

5.1 Governing Equations

The fluid dynamics and mechanics era starts, when the French physicist Louis Navier and the Irish mathematician Gabriel Stokes derived the governing equations of motion simultaneously about a century ago. No exact analytical closed form solution has been found yet to solve such equations. One of the difficulties is that the inflow boundary conditions are randomly time dependent, and a deterministic solution is nearly impossible. Since then, the science of CFD has evolved progressively to find a numerical solution for such equations under different forms and conditions. The Navier-Stokes equations describes the conservation of mass, momentum and energy, where all the fluid physical processes are implicitly included inside. The full reactive compressible Navier Stokes equations can be written in different forms in terms of either the primitive variables or the conservative variables. The latter can be written as well in either the strong or the week conservative form. The balance equations are composed of the mass conservation equation, the energy conservation equation (the first law of thermodynamics) and the vector momentum equation (Newton's second law).

The fluid is assumed Newtonian, which means that the viscous forces are linearly proportional to the velocity gradient and all the fluid elements are in the continuum regime . The derivation of the governing equations can be found in general text books ([115]). The general reacting compressible Navier Stokes equations, for a multi-species, multi-diffusion flow with no body force for mass, momentum, energy, and species conservation are:

$$\begin{aligned}
&\tfrac{\partial \rho}{\partial t} + \tfrac{\partial \rho u_i}{\partial x_i} = 0 \\
&\tfrac{\partial \rho u_i}{\partial t} + \tfrac{\partial}{\partial x_j}\Big[\rho u_i u_j + p\delta_{ij} - \tau_{ij}\Big] = 0 \\
&\tfrac{\partial \rho E}{\partial t} + \tfrac{\partial}{\partial x_i}\Big[\Big(\rho E + p\Big)u_i + q_i - u_j\tau_{ji}\Big] = 0 \\
&\tfrac{\partial \rho Y_k}{\partial t} + \tfrac{\partial}{\partial x_j}\Big[\rho Y_k\left(u_j + V_{i,k}\right)\Big] = \dot{w}_k, k = 1, Ns
\end{aligned} \tag{26}$$

The first equation, derived using an Eulerian approach, is the continuity equation, which states that the rate of change of density (first term) is balanced by the net rate of mass flux per unit volume (second term) passing out of the control surface surrounding the control volume (for a single phase formulation without source terms). In the second equation, the first term represents the rate of variation of the a fluid element momentum passing through the control volume per unit volume, while the second, third and fourth terms represent the rate of momentum lost or gained by convection, normal surface forces and shear forces per unit volume, respectively. Similarly, the first term in the energy equation is the rate of variation of total energy per unit volume, the second, third, and fourth terms are the rate of change of energy by convection and by work done by surface forces (pressure), heat addition by conduction, convection or radiation, and work done by shear stresses on the control surface. Finally, the species conservation equation represents the balance, between

the rate of variation of the $k-th$ species mass per unit volume, by the rate of variation by species convection (second term on left hand side) , molecular diffusion (third term on left hand side) and mass production by combustion (term on the right hand side).

In the above equations, ρ is the density, p is the thermodynamic pressure, u_i is the velocity vector, and i is the Einstein summation index over the three coordinates. The total energy per unit mass E is given on the macroscopic level as the summation of internal energy, kinetic energy and potential energy (neglected for current applications) as:

$$E = e + \frac{u_k u_k}{2} \tag{27}$$

Here, e is the internal energy given as the sum of the sensible enthalpy and the chemical stored energy as:

$$e = \sum_{k=1}^{Ns} Y_k h_k - \frac{P}{\rho} \tag{28}$$

where, the species enthalpy per unit mass is calculated from the thermal equation of state as:

$$h_k = \Delta h^0_{f,k} + \int_{T_{ref}}^{T} c_{p,k}(T) dT \tag{29}$$

Here $h^0_{f,k}$ is the standard heat of formation of the k^{th} species at the temperature T^{ref} and $c_{p,k}$ is the k^{th} species specific heat at constant pressure. The standard state is defined by $P_{ref} = 1\ atm$ and $T_{ref} = 300\ K$. The specific heat capacity and the heat of formation are calculated by solving each species curve fit polynomial ([116]) at a given temperature as a thermally perfect model.

In Eq. (26), q_i is the heat flux vector that contains contributions from the thermal conduction, diffusive enthalpy flux, Dufour heat flux, and radiation heat flux and is given by:

$$q_i = -\kappa \frac{\partial T}{\partial x_i} + \rho \sum_{k=1}^{Ns} h_k Y_k V_{i,k} + R_u T \sum_{k=1}^{Ns} \sum_{n=1}^{Ns} \left(\frac{X_n D_{T,k}}{M w_k D_{k,n}} \right) (V_{i,k} - V_{i,n}) + q_R \tag{30}$$

In the above formulation, X_n is the molar concentration of the n^{th} species, $D_{T,k}$ and $D_{k,n}$ are the thermal diffusivity and the molecular binary diffusivity between the k^{th} and n^{th} species, respectively. While Fourier's law is used to represent heat transfer by conduction, where κ is the thermal conductivity. The radiation term is considered here as an optically thin model (shown later).

The viscous stress tensor for a continuous, isotropic, Newtonian linear fluid element is given by:

$$\tau_{ij} = \mu \left(\frac{\partial u_i}{\partial x_j} + \frac{\partial u_j}{\partial x_j} \right) - \frac{2}{3} \mu (\frac{\partial u_k}{\partial x_k}) \delta_{ij} \tag{31}$$

Here, the first term in brackets is the strain rate by velocity gradients and the second term represents the deformation of the surface boundaries by dilatation or compressibility

effect. The δ_{ij} is the Kronecker function, where $\delta_{ij} = 1$ for $i = j$ and $\delta_{ij} = 0$ for $i \neq j$. In the former equation, μ is the kinematic viscosity coefficient computed from the Sutherland law as:

$$\frac{\mu}{\mu_{ref}} = (T/T_{ref})^{3/2} \frac{T_{ref} + T_s}{T_s + T} \tag{32}$$

where μ_{ref} is the reference viscosity at T_{ref} and $T_s = 110.4K$.

In the species mass conservation equation (Eq. 26), the mass reaction rate per unit volume and the species mass fraction are $\dot{w}_m$ and Y_m, respectively. For a general reaction r in a set of Nr reactions, the reaction equation is given by:

$$\sum_{k=1}^{Ns} \nu'_{k,r} M_k \rightarrow \sum_{k=1}^{Ns} \nu''_{k,r} M_k \tag{33}$$

Where, $\nu'_{k,r}$ is the stoichiometric coefficients of the reactants, $\nu''_{k,r}$ is the stoichiometric coefficients of the products, M_k is an arbitrary specification for the $k-th$ species and N_s is the total number of species. Arrhenius states that species will not react until they possess energy greater than a certain threshold amount symbolled as E_a, and the reaction rate of these species is generally proportional to the exponential Boltzman factor ($exp^{\frac{-E_a}{R_u T}}$), where the constant of proportionality includes the effects of molecular collision and the orientation of the molecules during collision represented by the steric factor. Hence, the $k-th$ species mass reaction rate per unit volume is given as:

$$\dot{w}_k = Mw_k \sum_{r=1}^{Nr} \left(\nu''_{k,r} - \nu'_{k,r} \right) A_r T^{\alpha_r} e^{\frac{-E_{ar}}{R_u T}} \pi_{n=1}^{Ns} \left(\frac{X_k P}{R_u T} \right), \quad k = 1, Ns \tag{34}$$

In Eq. (34), Mw_k is the molecular weight of the $k-th$ species, A_r, α_r, and E_{ar} are the Arrhenius constants for the $r-th$ reaction, X_k is the molar fraction of the $k-th$ species. From conservation of mass the sum over all the species should vanish:

$$\sum_{k=1}^{Ns} \dot{w}_k = 0 \tag{35}$$

The heat release rate $\dot{\Omega}$ can be expressed as:

$$\dot{\Omega} = -\sum_{k=1}^{N_s} h_k \dot{w}_k \tag{36}$$

Where h_k is the specific enthalpy given by Eq. (29). The diffusion velocity for the $k-th$ species in the $j-th$ direction is approximated by the Fick's law as:

$$V_{j,k} = -(D_k/Y_k) \frac{\partial Y_k}{\partial x_j} \tag{37}$$

where, D_k is the k^{th} species molecular diffusion coefficient.

The mass conservation can be represented by:

$$\sum_{k=1}^{Ns} Y_k = 1 \tag{38}$$

$$\sum_{k=1}^{Ns} V_{i,k} = 0, \quad i = 1, 2, 3. \tag{39}$$

The above set of equations (Eq. 26) are $5 + Ns$ equations in $6 + Ns$ variables. To close the picture, the pressure p is determined from the equation of state for a perfect gas mixture.

$$P = \rho T \sum_{k=1}^{N_s} \frac{Y_k R_u}{M w_k} \tag{40}$$

Here T is the temperature and R_u is the universal gas constant. The next section will represent the numerical approach used to solve the above set of equations.

5.2 Numerical Approach

Solving the Navier Stokes equations is faced with many challenges. For instance, the variation of the boundary and initial conditions by turbulence makes the problem indeterministic, with no unique solution. In addition, as the Reynolds number increases, the inertia forces increase more than the viscous forces and more length and time scales are introduced in the system. As a result, the computational cost to resolve all these length scales increases approximately as Re^3. While the large length scales are boundary dependent and hence non-universal, the small isotropic length scales decrease as $Re^{-3/4}$. Knowing that the Re in a typical gas turbine is in the range of a million, huge computational resources are needed to solve the complete flow field features. Unfortunately, the current computational resources cannot yet meet these demands. As a consequence, simple problems, where the boundary conditions are more deterministic at low and moderate Reynolds number can only be resolved. Solving the above equations without any modelling is termed as Direct Numerical Simulation (DNS), which is limited to low Reynolds numbers flows. Since turbulence is a transient phenomenon, we also need to capture the variation of the flow field with time. Other modeling approaches are then introduced to make the above equations more tractable. The Reynolds Average Navier stokes equations (RANS) are derived by averaging the original balance equations over time and solving for the mean properties only. However, in case we are interested in transient processes as flame instability, ignition or flame quenching, RANS lacks the ability to resolve for such transient phenomena. On the other hand, Large Eddy Simulation (LES) resolves all the non-universal length scales above a specified cut-off value and models the small universal one on the subgrid level. LES is still on its way to gain the complete trust of the computational community. However, in the near future it is expected to be the main computational tool with the anticipated development of computational resources. As a spatially filtered technique, LES is capable of capturing unsteady features that are derived mainly by the large energetic scales. However, for reactive problems the small scales that are responsible for the mixing of the reactants are not resolved and need to be

modeled. LES is found to be sensitive to the subgrid models used in addition to the filter width and the type, which means the solution is implicitly dependent on the filter features. This dependency can be resolved using dynamic approaches to compute the subgrid length and velocity scales ([117]). For a review of LES for turbulent combustion the recent review by [68] is highly recommended. In the current work, LES is chosen as the numerical approach. The next sections describe the derivation of the LES equations and there subgrid closure.

5.2.1 LES Filtered Governing Equations.

The LES equations are derived by using Favré spatial filtering approach ([118]), where the flow variable f are decomposed into super-grid (solved) $\widetilde{f}$ and subgrid (unsolved) f'' components. According to Favré averaging, the spatial filtering for a flow variable f is defined as:

$$\widetilde{f}(x_i,t) = \int f(x_i',t)G_f(x_i,x_i')dx_i' \tag{41}$$

where G_f is the filter kernel defined over the entire domain. As a consequence, the supergrid components are determined by:

$$\widetilde{f} = \frac{\overline{\rho f}}{\overline{\rho}} \tag{42}$$

The filter used is the top hat filter G_f, whose value is based on the local cell size (i.e., $\Delta x, \Delta y, \Delta z$) and is defined as:

$$G_f\left(\vec{x},\vec{x'}\right) = \begin{cases} \frac{1}{\bar{\Delta}} & |\vec{x}-\vec{x'}| < \frac{\bar{\Delta}}{2} \\ 0 & otherwise \end{cases} \tag{43}$$

Applying the Favré averaging over the entire Navier Stokes equations, the resultant LES equations can be introduced as follows ([119]):

$$\begin{aligned}
&\tfrac{\partial \overline{\rho}}{\partial t} + \tfrac{\partial \overline{\rho}\widetilde{u_i}}{\partial x_i} = 0 \\
&\tfrac{\partial \overline{\rho}\widetilde{u_i}}{\partial t} + \tfrac{\partial}{\partial x_j}\left[\overline{\rho}\widetilde{u_i}\widetilde{u_j} + \overline{p}\delta_{ij} - \overline{\tau_{ij}} + \tau_{ij}^{sgs}\right] = 0 \\
&\tfrac{\partial \overline{\rho}\widetilde{E}}{\partial t} + \tfrac{\partial}{\partial x_i}\left[\left(\overline{\rho}\widetilde{E} + \overline{p}\right)\widetilde{u_i} + \overline{q_i} - \widetilde{u_j}\overline{\tau_{ji}} + H_i^{sgs} + \sigma_i^{sgs}\right] = 0 \\
&\tfrac{\partial \overline{\rho}\widetilde{Y_k}}{\partial t} + \tfrac{\partial}{\partial x_j}\left[\overline{\rho}\widetilde{Y_k}\widetilde{u_j} - \overline{\rho D_k}\tfrac{\partial \widetilde{Y_k}}{\partial x_j} + \Phi_{j,k}^{sgs} + \Theta_{jk}^{sgs}\right] = \overline{\rho}\widetilde{\dot{w}_k}, \qquad k = 1, Ns
\end{aligned} \tag{44}$$

Here, $\widetilde{u_i}$ is the i-th filtered velocity component, $\overline{\rho}$ is the filtered density and $\overline{p}$ is the filtered pressure, which is computed from the filtered equation of state: $\overline{p} = \overline{\rho}R_u \sum_{k=1}^{N_s}\left(\frac{\widetilde{Y_k}\widetilde{T}}{Mw_k} + T_k^{sgs}\right)$. Here, $\widetilde{T}$ is the filtered temperature, and $\widetilde{Y_k}$ is the filtered k^{th} species mass fraction. The $\widetilde{Y_k}$ in the above relation are obtained from the subgrid closure, as described later and is subjected to the mass conservation condition $\sum_1^{N_s}\widetilde{Y_k} + \widetilde{Y_s} = 1.0$ and $\widetilde{Y_s}$ is the soot filtered mass fraction.

The filtered total energy per unit mass is defined as $\widetilde{E} = \widetilde{e} + \frac{1}{2}\widetilde{u_k}^2 + k^{sgs}$, where $k^{sgs} = \frac{1}{2}\left[\widetilde{u_k u_k} - \widetilde{u_k}\widetilde{u_k}\right]$ is the subgrid kinetic energy, and $\widetilde{e}$ is the filtered internal energy per unit

mass given as the sum of the sensible enthalpy and the chemical stored energy as $\widetilde{e} = \sum_{k=1}^{N_s} \widetilde{Y_k h_k} - \overline{p}/\overline{\rho}$. The species enthalpy is calculated from the thermal equation of state: $\widetilde{h_k} = \Delta h^0_{f,k} + \int_{T_{ref}}^{T} c_{p,k}(\widetilde{T}) d\widetilde{T}$. Also, $c_{p,k}$ is the specific heat at constant pressure for the k^{th} species. The filtered viscous shear stress is approximated using the filtered velocity as: $\overline{\tau_{ij}} = \bar{\mu}\Big(\partial\widetilde{u_i}/\partial x_j + \partial\widetilde{u_j}/\partial x_i\Big) - \frac{2}{3}\bar{\mu}\Big(\partial\widetilde{u_k}/\partial x_k\Big)\delta_{ij}$. The filtered heat flux is defined as (after neglecting the Dufour heat flux):

$$\overline{q_i} = -\overline{\kappa}\frac{\partial\widetilde{T}}{\partial x_i} + \overline{\rho}\sum_{k=1}^{N_s}\widetilde{h_k}\overline{D_k}\frac{\partial\widetilde{Y_k}}{\partial x_i} + 4\ a_{over}\ \sigma\left(\widetilde{T}^4 - \widetilde{T_{ref}}^4\right) + \sum_{k=1}^{N_s} q_{ik}^{sgs} \tag{45}$$

Here, $\overline{\kappa}$ and $\overline{D_k}$ are the mean thermal mixture conductivity and molecular diffusion of the k-th species, respectively. An optically thin radiation model ([120]) is employed here, where σ is the Stefan Boltzmann constant, and the overall Plank mean absorption coefficient is defined as $a_{over} = 266.0\widetilde{f_v}\widetilde{T} + 0.1\left(\widetilde{X_{CO_2}} + \widetilde{X_{H_2O}}\right)$. Where $\widetilde{X_{CO_2}}$ and $\widetilde{X_{H_2O}}$ are the filtered mole fractions for the CO_2 and H_2O, respectively.

The filtered LES equations contain many subgrid terms, denoted by the superscript sgs, that require closure. These terms represent the effect of the unresolved motion on the resolved field. The subgrid terms τ_{ij}^{sgs}, H_i^{sgs}, σ_i^{sgs}, T_k^{sgs} and q_{ik}^{sgs} are respectively, the subgrid shear stress, the subgrid heat flux, the subgrid viscous stress, the subgrid temperature species correlation and the subgrid heat flux via turbulence fluctuation. These terms are defined as ([119]):

$$\begin{aligned}
\tau_{ij}^{sgs} &= \overline{\rho}\Big[\widetilde{u_i u_j} - \widetilde{u_i}\widetilde{u_j}\Big] \\
H_i^{sgs} &= \overline{\rho}\Big[\widetilde{Eu_i} - \widetilde{E}\widetilde{u_i}\Big] + \Big[\overline{pu_i} - \overline{p}\widetilde{u_i}\Big] \\
\sigma_i^{sgs} &= \widetilde{u_j\tau_{ji}} - \widetilde{u_j}\overline{\tau_{ji}} \\
T_k^{sgs} &= \Big[\widetilde{Y_k T} - \widetilde{Y_k}\widetilde{T}\Big]/Mw_k \\
q_{ik}^{sgs} &= \Big[\overline{h_k D_k \partial Y_k/\partial x_i} - \widetilde{h_k}\widetilde{D_k}\partial\widetilde{Y_k}/\partial x_i\Big] + \Big[4.0 a_{over}\sigma\left(\overline{T}^4 - \widetilde{T}^4\right)\Big]
\end{aligned} \tag{46}$$

The next subsections will show the closure for the forgoing terms.

5.2.2 Momentum Equation Closure

In the current section the momentum equation subgrid closure is represented. Many studies have been performed on this issue most of them utilize the Kolmogorov hypothesis, which states that at high Reynolds number the small scale structures are isotropic and independent of the mean flow, and that large scale energetic structures cascade down to the small scale one, where they are dissipated by viscous and thermal dissipation effects. These assumptions acquire a high Reynolds number turbulent flow field. In addition, the turbulent-viscosity hypothesis introduced by Boussinesq states that the devatoric part of the Reynolds stress tensor is proportional to the mean strain rate. Although the turbulent viscosity hypothesis has the disadvantage of assuming the anisotropy tensor to be aligned with the mean strain rate tensor, it has been widely used and has proven to give reasonable physical results.

Many subgrid models exist for closure of the subgrid shear stress that combine the foregoing ideas. In order to utilize the turbulent viscosity hypothesis a characteristic mixing length L_{mix} and velocity V_{mix} have to be determined, such that $\nu_T \propto C_\nu L_{mix} V_{mix}$. Usually, the length scale is specific to the problem dimensions (i.e., $\bar{\Delta}$), however, many models emerged to compute the velocity scale. For instance, the Smagorinsky model ([121]) assumes equilibrium between the turbulent kinetic energy dissipation and production rates to obtain a relation between the characteristic velocity and the resolved strain rate, such that $\nu_T = \overline{\Delta}^2 (2\widetilde{S_{ij}}\widetilde{S_{ij}})^{1/2}$. Strictly speaking, the above formulation assumes no backscattering ([91]) and is valid only in the dissipation range and therefore we will need to solve the entire inertial range in the super-grid scale. Thus, higher resolution at high Reynolds number is required.

In the current study, an approach developed before ([122, 123, 74]), which is more suitable for high Reynolds number and complex flows, is implemented. In this method the velocity scale is derived using k^{sgs} by solving the transport equation for the subgrid kinetic energy, while the characteristic length scale is taken as the grid resolution $\bar{\Delta}$. In order to relax the equilibrium assumption embedded in other subgrid models, the transport equation formally derived for k^{sgs} is solved along with the rest of the LES equations. By this way, the cutoff between the resolved and the unresolved scales can be shifted towards the inertial range, which allows the usage of a coarse grid over the entire domain. In addition, in this way the effect of the resolved turbulent fluctuations effect is taken into account at the subgrid scale. The ability of this model has been demonstrated and tested extensively in the past ([122, 123, 119, 74]).

The k^{sgs} transport equation model is given by:

$$\frac{\partial \overline{\rho} k^{sgs}}{\partial t} + \frac{\partial}{\partial x_i}\left(\overline{\rho}\widetilde{u_i} k^{sgs}\right) = P^{sgs} - D^{sgs} + \frac{\partial}{\partial x_i}\left(\frac{\overline{\rho}\nu_T}{\sigma_T}\frac{\partial k^{sgs}}{\partial x_i}\right) \tag{47}$$

Here, the subgrid kinetic energy is defined as $k^{sgs} = \frac{1}{2}\left[\widetilde{u_k^2} - \widetilde{u_k}^2\right]$, and σ_T is a subgrid Prandtl number, assumed to be unity. In the above equation, P^{sgs} and D^{sgs} represent the production and dissipation of the subgrid kinetic energy, respectively. These terms are modelled as follow:

$$P^{sgs} = -\tau_{ij}^{sgs}\frac{\partial \widetilde{u_i}}{\partial x_j} \tag{48}$$

$$D^{sgs} = C_\epsilon \overline{\rho}(k^{sgs})^{3/2}/\overline{\Delta} \tag{49}$$

The subgrid stress using k^{sgs} model is then obtained as:

$$\tau_{ij}^{sgs} = -2\overline{\rho}\nu_T\left(\widetilde{S_{ij}} - \frac{1}{3}\widetilde{S_{kk}}\delta_{ij}\right) + \frac{2}{3}\overline{\rho}k^{sgs}\delta_{ij} \tag{50}$$

where the subgrid eddy viscosity is given by

$$\nu_T = C_\nu (k^{sgs})^{1/2}\overline{\Delta} \tag{51}$$

The two model coefficients C_ν and C_ϵ are obtained using a Localized Dynamic K-Equation (LDKM) approach as part of the solution ([123]). This dynamic approach has been used

quite successfully in many of the past non-reacting and reacting studies ([123, 74]). The advantage of the dynamic model is to eliminate the dependency of the solution on the filter properties ([117]). The dynamic model is based on the scale similarity notion, which states that if different turbulent flows follow scale similarity, the models that describe them should behave similarly at different scales ($\overline{\Delta}$). [124] conducted experiment for turbulent jets at high Re, and observed that the subgrid tress τ_{ij}^{sgs} at the grid filter level $\overline{\Delta}$ is self similar to what is called the Leonard's stress $L_{ij} = \left(\langle\overline{\rho}\widetilde{u_i}\widetilde{u_j}\rangle - \frac{\langle\overline{\rho}\widetilde{u_i}\rangle\langle\overline{\rho}\widetilde{u_i}\rangle}{langle\overline{\rho}\rangle}\right)$ at the test filter level $\langle\Delta\rangle = 2\overline{\Delta}$. Consequently, if the subgrid shear stress and test subgrid kinetic energy at the test filter are denoted as $\langle\tau_{ij}^{sgs}\rangle$, and $k_{test} = \frac{1}{2}[\frac{\langle\overline{\rho}\widetilde{u_k}\widetilde{u_k}\rangle}{\langle\overline{\rho}\rangle} - \frac{\langle\overline{\rho}\widetilde{u_k}\rangle\langle\overline{\rho}\widetilde{u_k}\rangle}{\langle\overline{\rho}\rangle\langle\overline{\rho}\rangle}]$, respectively, the shear stress and the Leonard's stress at the test filter level can be related as follows:

$$\langle\tau_{ij}^{sgs}\rangle = \langle C_L\rangle L_{ij} \tag{52}$$

where, $\rangle\tau_{ij}^{sgs}\rangle$ is computed with a similar expression as Eq. (50), with all variables computed at the test filter level as:

$$\langle tau_{ij}^{sgs}\rangle = -2\langle\overline{\rho}\rangle\nu_T\Big(\langle\widetilde{S_{ij}}\rangle - \frac{1}{3}\langle\widetilde{S_{kk}}\rangle\delta_{ij}\Big) + \frac{2}{3}\overline{\rho}k_{test}\delta_{ij} \tag{53}$$

By equating Eq. (53) with Eq. (52) and noting that $\mu = C_\nu(k_{test})^{1/2}\langle\Delta\rangle$, the model expression for C_ν is finally computed from ([123]):

$$C_\nu = -\frac{(\langle C_L\rangle L_{ij} - \frac{2}{3}\langle\overline{\rho}\rangle\ k_{test}\delta_{ij})}{2\langle\overline{\rho}\rangle\sqrt{k_{test}}\langle\Delta\rangle(\langle\widetilde{S_{ij}}\rangle - \frac{1}{3}\langle\widetilde{S_{kk}}\rangle\delta_{ij})} \tag{54}$$

Noting that the above system is over-determined, the least square method is used to solve for C_ν ([125]). A similar approach is used to calculate the dissipation coefficient, where the following relation is utilized:

$$D^{sgs} = -\frac{\tau_{ij}^{sgs}}{\overline{\rho}}\frac{\partial\widetilde{u_j}}{\partial x_i} \tag{55}$$

The following relation is derived [123]:

$$C_\epsilon = \frac{\langle\Delta\rangle(\overline{\mu} + \mu_t)}{\langle\overline{\rho}\rangle\ k_{test}^{3/2}}\left[\langle\widetilde{T_{ij}}\frac{\partial\widetilde{u_j}}{\partial x_i}\rangle - \widehat{\widetilde{T_{ij}}}\frac{\widehat{\partial\widetilde{u_j}}}{\partial x_i}\right] \tag{56}$$

Here, $\mu_t = \overline{\rho}\nu_t$ and the tensor $\widetilde{T_{ij}}$ is defined as $-2\Big(\widetilde{S_{ij}} - \frac{1}{3}\widetilde{S_{kk}}\delta_{ij}\Big) + \frac{2}{3}k^{test}\delta_{ij}$, while $\widehat{\widetilde{T_{ij}}}$ indicates evaluation at the test-filter level.

5.2.3 Energy Equation Closure

The closure for the subgrid heat flux is achieved using an eddy viscosity model. Such a closure is acceptable since the small-scales primarily provides dissipation for the energy transferred from the large scales. Assuming that an eddy viscosity ν_T is prescribed from Eq. (51), these subgrid fluxes can be approximated as:

$$H_i^{sgs} = -\nu_T\frac{\partial\widetilde{h}}{\partial x_i} \tag{57}$$

However, the subgrid terms T_k^{sgs}, q_{ik}^{sgs} and σ_i^{sgs} are found to be negligible and neglected hereafter ([126]). It is to be mentioned that the radiation subgrid effect is included implicitly on the subgrid level as will be discussed later in addition to the filtered radiation flux as discussed in Eq. (45).

Since we are not resolving the species equations on the supergrid level, the subgrid diffusion mass flux (Θ_{jm}^{sgs}) closure will not be considered here, however a similar eddy viscosity hypothesis can be used for closure.

5.3 Combustion Closure

Physically, scalar mixing, combustion and heat release occur at the small-scales, however, in conventional LES, the small-scales are not resolved. Therefore, these scales have to be modeled in combustion problems. Modeling of these subgrid processes at the filtered level involve models that may not be applicable for all conditions. The current available combustion models were discussed in chapter I. Here, the LEM approach used will be presented.

5.3.1 LEM Approach

In LEMLES, the gas phase species conservation equations are not spatially filtered as the other LES equations. Rather, the exact unfiltered equations are solved using a two-step Eulerian-Lagrangian approach, and then the resulting scalar fields are ensembled averaged in each LES cell to recover the LES-resolved species mass fractions, $\widetilde{Y}_k$ (that is used in the LES-resolved energy and state equations). This approach eliminates most of the closure problems for the filtered species equations. LEM simulate all the physical subgrid processes at their relevant time scales. A general conservation equation for a scalar Φ can be written as:

$$\underbrace{\rho\frac{\partial \Phi}{\partial t}}_{\text{Eulerian Time Dervative}} + \underbrace{\rho u_i \frac{\partial \Phi}{\partial x_i}}_{\text{Advection}} - \underbrace{\frac{\partial}{\partial x_i}\left[\rho D_\Phi \frac{\partial \Phi}{\partial x_i}\right]}_{\text{Molecular Diffusion}} = \underbrace{\dot{\omega}_\Phi}_{\text{chemical source term}} \tag{58}$$

where D_Φ is the molecular diffusion of the scalar Φ. The scalar evolution is tracked using a two scale numerical approach, namely the large scale processes, that represent the convection by eddies larger than the filtered scales, and the small scale processes, that represent the transport by molecular diffusion, advection by unresolved small scales and chemical reaction. The two-step approach can be described mathematically by decomposing total velocity field into the LES-resolved velocity, $\widetilde{u}_i$, the LES-resolved subgrid fluctuations $\left(u_i^{'}\right)^R$ at the cell face and the unresolved subgrid fluctuations, $\left(u_i^{'}\right)^S$. Thus, a general decomposition of the velocity field can be written as

$$u_i = \widetilde{u}_i + \left(u_i^{'}\right)^R + \left(u_i^{'}\right)^S \tag{59}$$

Using this relation Eq. (58) can be rewritten as:

$$\underbrace{\rho\frac{\partial\Phi}{\partial t}}_{\text{Eulerian time dervative}} + \underbrace{\rho\left(\widetilde{u}_i+\left(u_i^{'}\right)^R\right)\frac{\partial\Phi}{\partial x_i}}_{\text{Advection by filtered and resolved large scales}} + \underbrace{\rho\left(u_i^{'}\right)^S\frac{\partial\Phi}{\partial x_i}}_{\text{Advection by unresolved scales}} - \underbrace{\frac{\partial}{\partial x_i}\left[\rho D_\Phi\frac{\partial\Phi}{\partial x_i}\right]}_{\text{molecular Diffusion}} = \underbrace{\dot{\omega_\Phi}}_{\text{chemical source term}} \tag{60}$$

Now, to describe how these two-scale approach is applied inside the LEM model, we have to consider the LEM domain first. The LEM domain is simply a one dimensional line that is embedded inside the LES cell. This one dimensional line has no specific spatial orientation. Physically it is aligned along the maximum scalar gradient or normal to the flame front ([100]). The domain length can also be approximated by the width of the LES cell Δ. The LEM resolution is usually determined to resolve all the length scales down to the smallest one. Being a 1D line, LEM makes the computational effort affordable to resolve the Kolmogorov length scale. For reactive problems, usually the reaction zone has to be resolved at least by 4-5 points. So, if the flame thickness is δ_F and the reaction zone thickness is 0.1 δ_F, the LEM resolution required will be $min\left(\eta, 0.02\delta_F\right)$, where the 0.02 factor ensures that the inner layer is resolved by 5 points.

The general theme of LEM is summarized as follow. The large scale advection is modelled by a Lagrangian tracking. The molecular diffusion is calculated deterministically by Ficikian Law, while the small scale advection is modelled by a stochastic Monte Carlo approach. By this way LEM preserves a mechanistic distinction between the two processes that govern turbulent transport. The fluid motion, which arranges the scalar filed without changing the concentration and the molecular diffusion that transfers scalars from one cell to another.

5.3.2 LEM Governing Equations

Using a similar approach to Eq (58), the unfiltered k^{th} species equation can be written as:

$$\rho\frac{\partial Y_k}{\partial t}+\rho\left[\widetilde{u}_i+\left(u_i^{'}\right)^R+\left(u_i^{'}\right)^S\right]\frac{\partial Y_k}{\partial x_i}-\frac{\partial}{\partial x_i}\left[\rho D_k\frac{\partial Y_k}{\partial x_i}\right]=\dot{\omega}_k \tag{61}$$

Equation (61) is split and solved by the two-scale procedure, where the large scale processes are separated as:

$$\frac{Y_k^*-Y_k^n}{\Delta_{t_{LES}}}=-\left[\widetilde{u}_i+\left(u_i^{'}\right)^R\right]\frac{\partial Y_k^n}{\partial x_i} \tag{62}$$

and the small scale processes are integrated along the LEM domain:

$$\left(Y_k^{n+1}-Y_k^*\right)=\int_t^{t+\Delta t_{LES}}-\frac{1}{\rho}\left[\left[\rho\left(u_i^{'}\right)\right]^S\frac{\partial Y_k^n}{\partial x_i}-\frac{\partial}{\partial x_i}\left[\rho D_k\frac{\partial Y_k}{\partial x_i}\right]-\dot{\omega}_k\right]dt^{'} \tag{63}$$

Here, the superscript n indicates the LES time level, Δt_{LES} is the LES time-step, D_k is the k^{th} species diffusion coefficient, and $\dot{\omega}_k$ is the k^{th} species (unfiltered and therefore exact)

production or destruction rate. Equation (62) represents the 3D advection of the scalar field modelled by a Lagrangian transport of the subgrid mass across the LES cells ([127]), and the integrand in Eq. (63) represents the LEM subgrid model, which is solved locally inside each LES cell.

In the subgrid implementation of Eq. (63) the species equation (along with a similar equation for the subgrid temperature ([93]) and the soot-related equations) are solved on a 1D domain that is aligned in the direction of the maximum scalar gradient. Within this 1D domain, the subgrid LEM equations take the following form:

$$\rho_{LEM}\frac{\partial Y_{k,LEM}}{\partial t^s} = F_k^{stir} + \frac{\partial}{\partial s}\left[\rho_{LEM} D_k \frac{\partial Y_{k,LEM}}{\partial s}\right] + \dot{\omega}_k \qquad k = 1, \ldots N_s \tag{64}$$

$$\underbrace{\frac{\partial T_{LEM}}{\partial t^s}}_{\text{Eulerian time derivative}} = \underbrace{-\frac{1}{\overline{C_p}}\sum_{k=1}^{N_s} C_{p,k} Y_{k,LEM} V_k \frac{\partial T_{LEM}}{\partial s}}_{\text{diffusion of heat by species Fickian diffusion}} + \underbrace{\frac{1}{\rho_{LEM}\overline{C_p}}\frac{\partial}{\partial s}\left(\overline{\kappa}\frac{\partial T_{LEM}}{\partial s}\right)}_{\text{heat conduction}}$$
$$+ \underbrace{\frac{a_{over}\sigma\left(T_{LEM}^4 - T_o^4\right)}{\rho_{LEM}\overline{C_p}}}_{\text{heat radiation}} - \underbrace{\frac{1}{\rho_{LEM}\overline{C_p}}\sum_{k=1}^{N_s} h_k \dot{\omega}_k M w_k}_{\text{heat release by chemical reaction}} + F_T^{stir} \tag{65}$$

In the above equations, $Y_{k,LEM}$ and T_{LEM} are the k-th species mass fraction and the field temperature on the subgrid level, respectively.

The 1D line (s) resolution in LEM is chosen to resolve all the turbulent scales below $\overline{\Delta}$ (e.g., down to the Kolmogorov length scale η if required). Here, F_k^{stir} and F_T^{stir} in Eqs. (64 and 65) represent $-\left[\rho\left(u_i^{'}\right)\right]^S \frac{\partial Y_k^n}{\partial x_i}$ in Eq. (63) and $-\left[\rho\left(u_i^{'}\right)\right]^S \frac{\partial T}{\partial x_i}$, which are the subgrid stirring effect on the species (including soot), and the temperature fields, respectively. The pressure is assumed constant inside the LEM domain, which is an assumption valid only in case we have no steep pressure gradients in the subgrid level (e.g. shocks). A thermally perfect gas is assumed and the pressure and density on the subgrid level is computed from:

$$P_{LEM} = P_{LES} \tag{66}$$

$$\rho_{LEM} = \frac{P_{LEM}}{T_{LEM}\sum_{k=1}^{Ns} Y_k^{LEM}\frac{R_u}{Mw_k}} \tag{67}$$

Here, ρ_{LEM} is the subgrid mixture density and R_u is the universal gas constant.

5.3.3 Stirring by Subgrid unresolved scales

The stirring process is modelled by a stochastic rearrangements process ([93, 95, 97]) that represents the action of a turbulent eddy (below $\overline{\Delta}$) on the scalar field. These stochastic rearrangements are instantaneously statistically independent events that conserves the scalar field but alters the gradient only and simulate the action of a compressive strain on a scalar field. The stirring is implemented as a sequence of events that maps a spatial segment

of the concentration field onto itself. This stochastic process is named triplet mapping. Since, summing the scalar field is linear initially $\psi(x) = x$, the scalar field is compressed by a factor of three, to produce three copies of the original filed. These three copies are rearranged together, with the middle one being mirror inverted with respect to the others as shown in Fig. 1. Figure 1 shows an illustration for the LEM domain with respect to the LES cell and the mapping event before and after stirring. Mathematically, applying the above mapping sequence to the segment $[x_o, x_o + l]$ at time t_o, transforms $\psi(x, t_o)$ to $\hat{\psi}(x, t_o)$ according to:

$$\hat{\psi}(x, t_o) = \begin{cases} \psi(3x - 2x_o, t_o) & x_o \leq x \leq x_o + \frac{l}{3} \\ \psi(-3x + 4x_o + 2l, t_o) & x_o + \frac{l}{3} \leq x \leq x_o + \frac{2l}{3} \\ \psi(3x - 2x_o - 2l, t_o) & x_o + \frac{2l}{3} \leq x \leq x_o + l \\ \psi(x, t_o) & otherwise \end{cases} \tag{68}$$

where, l is the domain length, x_o is the start position of the eddy mapping event and t_o is the stirring time. Compressing the line into three copies, requires the number of grid points to be multiple of three. To simulate a complete eddy at least 6 points are needed. To illustrate the mapping events, assume we have 9 LEM cells, as shown in Fig. 2. Triplet mapping divides this line into three sections each is composed of 3 cells. Then applying the first equality to the first three cells we should get:

$$\hat{\psi}(x_o, t_o) = \psi(x_o, t_o)\hat{\psi}(x_1, t_o) = \psi(x_4, t_o)\hat{\psi}(x_2, t_o) = \psi(x_7, t_o) \tag{69}$$

In general the sequence for an initially $3k$ cells are 1,4,7,....$3k-8$,$3k-5$, $3k-2$,$3k-1$,$3k-4$,...,.$3k-3$,$3k$. Doing this rearrangement, the mapping causes only discontinuities for the scalar gradient but not for the scalar itself. The triplet mapping can also be regarded as a random walk of a fluid element with a turbulent diffusivity D_T ([96]).

[128] mentioned that in the inertial range (where the inertial forces are dominant over the viscous forces) the Kolmogorov rate of energy transfer from eddies of size l to the smaller eddies (down to the Kolmogorov length scale) is proportional to $l^{4/3}$. [96] used this 3D inertial scaling turbulence law to drive the properties that govern the mapping event. As a consequence, the 3D physical effect is included in the stirring events, even though we are solving on a 1D line. Three quantities govern the stirring event: the eddy size, its location within the subgrid domain, and the stirring frequency. However, the event location x_o is chosen randomly from a uniform distribution within the 1D domain. If $x_o > L_{LEM} - l$ then the eddy will go beyond the LEM line length and the event has to be truncated. The stirring frequency is computed from a Poisson process with a rate λL_{LEM}, where λ is the event-frequency. Knowing that the eddy size can possibly lie in-between the LES filter grid width Δ and the Kolmogorov length scale η (i.e., in the range $\eta < l < \overline{\Delta}$), the eddy size is sampled randomly from a PDF of eddy sizes given by $f(l)$. [94] argued that λ and $f(l)$ are function of five parameters, namely D_T the fluid element diffusivity, L_{LEM} the LEM domain length, η the smallest possible eddy size, l the current eddy size and p the inertial scaling law power. The turbulent diffusivity induced by segments in the size range (η, Δ) is given by ([129]):

$$D_T = \frac{2}{27}\lambda \int_{\eta}^{\overline{\Delta}} l^3 f(l)\, dl \tag{70}$$

Since, D_T is proportional to 4/3 in the inertial range as mentioned before (in the previous paragraph), $f(l)$ will be proportional to l to the power of $4/3 - 4 = -8/3$ from Eq. (70) and the pdf of the eddy size is given by:

$$f(l) = \left(\frac{5}{3}\right) \frac{l^{-8/3}}{\eta^{\frac{5}{3}} - \overline{\Delta}^{\frac{5}{3}}} \tag{71}$$

The derivation of the above PDF is done as follows:

- From the previous discussion $f(l)$ should be proportional to l^{p-4}, where $p = 4/3$ in this case. Assume $f(l) = Al^{p-4}$.
- Utilizing the mathematical fact that $\int_{-\infty}^{\infty} f(l) = 1.0$, and by setting the integration limits in-between $\overline{\Delta}$ and η (since it will be zero everywhere else). The constant A will be:

$$A = \frac{3-p}{\eta^{3-p} - \overline{\Delta}^{3-p}} \tag{72}$$

- Plugging A into $f(l) = Al^{p-4}$ and setting $p = 4/3$ we finally get Eq. (71).

Here, $\eta = N_\eta \overline{\Delta} Re_{\overline{\Delta}}^{-3/4}$, and $Re_{\overline{\Delta}} = u^{'}\overline{\Delta}/\nu$ is the local subgrid turbulent Reynolds number, where $u^{'} = \sqrt{2k^{sgs}/3}$ is the subgrid turbulence intensity. Also, N_η is an empirical constant that reduces the effective range of scale between the integral length scale and η, but does not change the turbulent diffusivity ([93]). Finally, the event rate λ is calculated by combining Eqs. (71 and 70) ([93]):

$$\lambda = \frac{\nu Re_{\overline{\Delta}}}{C_\lambda \overline{\Delta}^3} \frac{[\frac{\overline{\Delta}}{\eta}]^{\frac{5}{3}} - 1}{1 - [\frac{\eta}{\overline{\Delta}}]^{\frac{4}{3}}} \tag{73}$$

The subgrid stirring time scale is then obtained as:

$$\Delta t_{stir} = 1/\lambda\overline{\Delta} \tag{74}$$

The two empirical constants N_η and C_λ have to be determined. The first parameter N_η is found to be in the range $1 - 13$ ([130, 131]). In the current work it is fixed to 5 according to past studies ([132]). The second parameter C_λ was computed before by comparing the turbulent flame speed to the Pocheau flame speed model to DNS data under unity Lewis number assumption ([130]) in the flamelet regime. [109] used value of $C_\lambda = 15$ in the thin reaction zone regime, which is used here ([99]).

5.3.4 Volumetric Expansion

Heat release in the subgrid LEM domain results in volumetric expansion that is also included in the LEM as an increase in the subgrid domain volume. Since the pressure is constant, increasing the temperature will decrease the density and the LEM cells will expand. For strict mass conservation, each LEM cell that has been burned (partially or fully) is increased volumetrically. [133, 134, 100] expand each cell in the 1D domain by $\Delta V_{LEM,i}^{n+1} = \rho_i^n / \rho_i^{n+1}$, where $\Delta V_{LEM,i}^{n+1} = (\Delta s)^3$ is the change in the volume of the i-th LEM cell, and ρ_i^n and ρ_i^{n+1} are respectively, the density of the i-th cell at two successive time steps and Δs is local LEM cell length. A generalized approach will allow the subgrid LEM domains to vary from LES cell to cell but this can make proper load balancing in a simulation cumbersome. Therefore, for computational expediency ([134]), the LEM domain is regrided after the large-scale advection to retain a uniform grid spacing. However, to maintain the initial number of LEM cells the number of cells that exceeds the initial amount is truncated. This regriding operation introduces some spurious diffusion for the scalars, that is proven to have a negligible effect ([111]) since only a small number of LEM cells are involved. In addition, ([133]) argued that the truncated amount is from the burned side, and that will not affect the flame speed, since volumetric expansion is decoupled from the diffusion reaction equation.

5.3.5 Advection by Large Scales

Once the subgrid processes have evolved within each LES cell, large-scale transport of the scalar fields is implemented using a Lagrangian approach to solve Eq. 62 ([134, 100]). This approach transports the subgrid LEM fields across the LES cell faces in such a way to ensure mass conservation on the subgrid and the supergrid level. [100] tested the splicing scheme for convection of a square face and outward burning of a circular flame. The scheme shows accurate propagation in all direction. The splicing technique uses the filtered velocity magnitude and direction at the LES cell face to compute the amount of masses needed to be advected between the LEM domains in different LES cells, in such a way to conserve mass. The sufficiently small LES time step ensures that mass is transported form one LES cell to an adjacent one only, without crossing to other cells. This reduces the complexity of the problem. The algorithm for splicing can be summarized here as follows:

- Since LES scheme is a cell centered scheme, the filtered velocity values are known only at the cell center. The velocities at the cell faces are computed by a second order interpolation from the cell centers (shown in the following chapter).
- The resolved mass fluxes are computed at the LES cell face. The computation of these mass fluxes is alsp described in the next chapter.
- The direction of the mass fluxes is set equal to the direction of the filtered velocity field.
- Hence, the magnitude m_{LES} and the direction of the mass to be spliced is determined from the above two steps.

- The Influx is given a positive sign and the out-flux is given a negative sign along each coordinate direction.
- The fluxes are sorted in an ascending order, so that the lowest negative (largest out-flux) will be first and the highest positive(largest influx) will be last.
- For each LES cell, the equivalent number of LEM cells that contain the required mass to be transported is computed. The LEM cell mass is computed as $\rho_{LEM}V_{LEM}$, and the number of cells to be spliced is $N_{spliced} = \frac{m_{LES}}{\rho_{LEM}V_{LEM}}$. If the number of cells contains a fraction from an LEM cell it will be transformed as a fraction to the other cells to preserve continuity.
- An upwind like scheme is implemented to update the fluxes ([100]). The largest out-flux is fluxed out from the right end of the LEM domain and the largest influx from the surrounding LES cells is convected into the leftmost LEM cell. Following that, the lower order influx and out-flux masses are convected.

Figures 3, 4 and 5 illustrates the splicing operation in a two dimensional environment. First, the equivalent fluxes at each face is computed from LES ($F1$,$F2$,$F3$ and $F4$) , then this fluxes are arranged with the lowest negative first. Next the LEM cells corresponding to each flux value is calculated for each LEM line. Finally, the influx masses are convected to the neighboring LEM domain from the left and the out-flux from the last LEM cell from the right.

5.3.6 Fractional Step Method

LEM follows a fractional step method to simulate each physical process concurrently at its relevant time step. Figure 6 shows the general flow chart for the LEM subroutine. The inputs to the LEM solver are the LES time step, the subgrid turbulence intensity $u^{'} = \sqrt{2k_{sgs}/3}$, the filter width $\bar{\Delta}$ and the filtered scalar values, $\widetilde{P_{LES}}$, $\widetilde{Y_{LES}}$ and $\widetilde{u_i}$. First, the mass fluxes across the LES cell faces are exchanged. Next, the one dimensional reaction-diffusion-stirring subroutine are solved for the subgrid scale processes. This is followed by the volumetric expansion and the splicing across the LES cell faces. Lastly, the coupled large scale and small scales values are averaged over the LEM cells to be passed to the LES domain. Consequently, the filtered values for the scalars that include the species, temperature or any other scalars are computed as:

$$\widetilde{\Phi} = \frac{\sum_{i=1}^{N_{LEM}} \rho_{i,LEM}\Phi_i}{\sum_{i=1}^{N_{LEM}} \rho_{i,LEM}} \tag{75}$$

where, i is the index of the LEM cell and Φ_i is the local value of the scalar at the $i-th$ cell.

The reaction-diffusion-stirring subroutine flow chart is shown in Fig. 7. First, the LEM domain is initialized from the previous time step data. Next, a loop starts over the LES cells, where the relevant time scales are computed first based on the inputs discussed in the last paragraph. The stirring time t_{stir} is computed from Eq. (74), while the diffusion time step is computed from:

$$\Delta t_{diff} = \frac{C_{diff} * \Delta s_{LEM}^2}{D_{max}} \tag{76}$$

Here, C_{diff} is a stability factor taken as 0.25, D_{max} is the maximum molecular diffusion coefficient computed over all the species at the local temperature, and Δs_{LEM} is the grid spacing between LEM cells. The parameters T_{nexts} and T_{nextg} are set to t_{stir} and t_{diff}, respectively. The chemistry time step is computed as well, either by the DVODE solver, or by other means. In the current study, the chemistry time step is computed to match the acetylene reaction with the DVODE solver within a maximum of 5% error. Next, over each LES cell, the LES integration time step is divided by the minimum time step calculated for stirring and diffusion to figure out how many stirrings and diffusion should occur per time step. As the number of stirrings and diffusion time step per LES time step is specified, a loop is started over each cell. If the stirring time is smaller than the diffusions time, triplet mapping is performed to simulate the scaler mixing in the subgrid level. Otherwise, the one dimensional solver of the energy and species equations is turned on. The stirring and diffusion time concurrently occur till the LES integration time is reached.

5.4 Soot Dynamic Model

Prediction of soot formation and transport in unsteady turbulent flames is very challenging because both realistic chemical kinetics for gas and soot is required, and flow-chemistry interaction over a wide range of spatial and temporal scales has to be resolved. In the past, several steady state approaches have been used to predict soot in realistic turbulent configurations. A good review of available soot models till 1997 is given in [42]. In general, past soot models can be classified into two general categories. The first one solves two transport equations for the soot volume fraction and number density in conjunction with other simplified turbulent models. The second category either uses a prescribed soot probability density function (PDF) distribution or solves the transport moment equations for the soot PDF. [44], [135, 43] used the laminar flamelet approach combined with the soot mass fraction and the number density transport equations to approximate the soot chemistry to study a low turbulent buoyant fire and an axisymmetric turbulent methane-air jet flames at elevated and atmospheric pressure. This was one of the first available databases on turbulent sooting methane-air flames that is based on the current understanding of the physics of soot formation.

[79] used the same soot transport equations with the CMC approach to study turbulent methane jet flames ([43]). They used a detailed hydrocarbon mechanism and obtained good agreement with measurements. [136] applied a detailed soot model along with a joint transported PDF equation of the mixture fraction, enthalpy and soot volume fraction to study an ethylene-air jet flame. They found that most of the soot is formed around 1400 K and for such a flame, the correlation between the mixture fraction and the soot volume fraction is very weak.

Recently, [137]developed a hybrid model that uses a Lagrangian Monte Carlo solution of the joint scalar PDF of the mixture fraction, soot number density and volume fraction combined with an Eulerian solution of the turbulent flow field. The model used the laminar flamelet-state relationship for the gas phase properties. The model shows good temperature

agreements with under prediction for the soot volume fraction along the centerline. The results shows that the radiation effect is to increase the predictable soot volume fraction. This may be due to the reduction in temperature, which reduces the oxidation rate. [138] developed a soot model that combines the $k-\epsilon$ model for the turbulent flow field with the stretched laminar flamelet approach for a detailed kerosene/air mechanism. They used two soot inception models, one based on acetylene and another based on the formation of aromatic rings. They concluded that the acetylene model significantly under predicts the soot volume fraction, which indicates the importance of the aromatic species as an intermediate species in such flame types.

Another PDF based transport study was done by [139]. In this study, a skeletal n-heptane chemistry model with an assumed log-normal soot size distribution is applied in the KIVA-3V code. [46] used the method of moments (MOM) combined with a joint-scalar transport PDF to predict the soot properties for two ethylene turbulent flames with full chemistry. They showed that increasing the number of statistical moments included improves the results. Good agreement with the experimental data is shown as well.

All of the above cited models were primarily steady state approaches. So far, very few studies have simulated truly unsteady turbulent sooting flames. As noted earlier, an approach using LES is developed and applied here to a canonical turbulent premixed flame and to a non-premixed flame. The next section describes the Method of Moments approach, following that the proposed soot subgrid model will be discussed.

5.4.1 Method of Moments

The Method of Moments with interpolative closure (MOMIC) is based on the idea that the knowledge of all the moments is equivalent to knowing the distribution function itself ([140]). The model utilizes the MOM to predict the population dynamics of an ensemble of particles that undergo simultaneous nucleation, coagulation and surface growth, and finally agglomeration. The moment equations can be derived starting from the Smoluchowski master equation for the time evolution of particle population:

$$\frac{dN_{s,1}}{dt} = -\sum_{j=1}^{\infty} \beta_{1,j} N_{s,1} N_{s,j}$$

$$\frac{dN_{s,i}}{dt} = \frac{1}{2}\sum_{j=1}^{i-1} \beta_{j,i-1} N_{s,j} N_{s,i-j} - \sum_{j=1}^{\infty} \beta_{i,j} N_{s,i} N_{s,j}, i = 2, \ldots \infty \tag{77}$$

Here, $N_{s,i}$ is the number density of the spherical particles of class size i and $\beta_{i,j}$ is the collision frequency between two class size particles i and j. The moment equations are derived by

expanding Eq. (77) as follows:

$$\begin{aligned}
\frac{dN_{s,1}}{dt} &= -N_{s,1}\sum_{j=1}^{\infty}\beta_{1,j}N_{s,j} \\
\frac{dN_{s,2}}{dt} &= -N_{s,2}\sum_{j=1}^{\infty}\beta_{2,j}N_{s,j} + \frac{1}{2}\beta_{1,1}N_{s,1}N_{s,1} \\
\frac{dN_{s,3}}{dt} &= -N_{s,3}\sum_{j=1}^{\infty}\beta_{3,j}N_{s,j} + \frac{1}{2}\left(\beta_{1,2}N_{s,1}N_{s,2} + \beta_{2,2}N_{s,2}N_{s,2}\right) \\
\frac{dN_{s,4}}{dt} &= -N_{s,4}\sum_{j=1}^{\infty}\beta_{4,j}N_{s,j} + \frac{1}{2}\left(\beta_{1,3}N_{s,1}N_{s,3} + \beta_{2,2}N_{s,2}N_{s,2} + \beta_{3,1}N_{s,3}N_{s,1}\right) \\
&\vdots \\
\frac{dN_{s,\infty}}{dt} &= \ldots
\end{aligned} \tag{78}$$

By adding the similar components of each equation vertically we get:

$$\frac{d\sum_{i=1}^{\infty}N_{s,i}}{dt} = -\sum_{i=1}^{\infty}N_{s,i}\sum_{j=1}^{\infty}\beta_{i,j} + \frac{1}{2}\sum_{i=1}^{\infty}\sum_{j=1}^{i-j}\beta_{j,i-j}N_{s,j}N_{s,i-j} \tag{79}$$

By utilizing the following mathematical formula:

$$\sum_{i=1}^{\infty}\sum_{j=1}^{i-1}N_{s,j}N_{s,i-j} = \sum_{i=1}^{\infty}\sum_{j=1}^{\infty}N_{s,i}N_{s,j} \tag{80}$$

we finally obtain the following expression:

$$\frac{d\sum_{i=1}^{\infty}N_{s,i}}{dt} = -\frac{1}{2}\sum_{i=1}^{\infty}\sum_{j=1}^{\infty}\beta_{i,j}N_{s,i}N_{s,j} \tag{81}$$

Then by defining the $r-th$ moment as:

$$M_r = \sum_{i=1}^{\infty}m_i^r N_{s,i} \tag{82}$$

Here, m_i is the mass of the soot particles of class size i. We get the $zero-th$ moment $M_o = \sum_{i=1}^{\infty}N_{s,i}$:

$$\frac{dM_o}{dt} = -\frac{1}{2}\sum_{i=1}^{\infty}\sum_{j=1}^{\infty}N_{s,i}N_{s,j} \tag{83}$$

Similar argument can be used to derive the rest of the moment equations. Here, we will derive the first moment rate only for illustration. The first moment is defined as $M_1 = \sum_{i=1}^{\infty}m_i N_{s,i}$.

By multiplying Eqs. (78) by m_i we get:

$$\frac{dm_1 N_{s,1}}{dt} = -m_1 N_{s,1} \sum_{j=1}^{\infty} \beta_{1,j} N_{s,j}$$

$$\frac{dm_2 N_{s,2}}{dt} = -m_2 N_{s,2} \sum_{j=1}^{\infty} 2\beta_{2,j} N_{s,j} + \frac{1}{2} 2\beta_{1,1} m_1 N_{s,1} N_{s,1}$$

$$\frac{dm_3 N_{s,3}}{dt} = -m_3 N_{s,3} \sum_{j=1}^{\infty} 3\beta_{3,j} N_j + \frac{1}{2} \left(3\beta_{1,2} N_{s,1} N_{s,2} m_1 + 3\beta_{2,2} N_{s,2} N_{s,2} m_1\right)$$

$$\vdots$$

$$\vdots$$

$$\frac{dN_{s,\infty}}{dt} = \ldots \tag{84}$$

Again, by summing vertically and assuming spatially homogeneous, particles, i.e: ($m_i = im_1$), the following expression is obtained:

$$\frac{d\sum_{i=1}^{\infty} im_1 N_{s,i}}{dt} = -\sum_{i=1}^{\infty} im_1 N_{s,i} \sum_{j=1}^{\infty} \beta_{i,j} + \frac{1}{2} \sum_{i=1}^{\infty} im_1 \sum_{j=1}^{i-j} \beta_{j,i-j} N_{s,j} N_{s,i-j} \tag{85}$$

From the relation given by Eq. (80), the following formula is induced:

$$\sum_{i=1}^{\infty} im_1 \sum_{j=1}^{i-j} \beta_{j,i-j} N_{s,j} N_{s,i-j} = \sum_{i=1}^{\infty} \sum_{j=1}^{\infty} \beta_{j,i} N_{s,i} N_{s,j} (i+j) m_1 \tag{86}$$

By substitution in Eq. (85), the following expression is obtained:

$$\frac{d\sum_{i=1}^{\infty} im_1 N_{s,i}}{dt} = -\sum_{i=1}^{\infty} im_1 N_{s,i} \sum_{j=1}^{\infty} \beta_{i,j} + \frac{1}{2} \sum_{i=1}^{\infty} im_1 \sum_{j=1}^{\infty} im_1 \beta_{j,i} N_{s,j} N_{s,i} + \frac{1}{2} \sum_{i=1}^{\infty} im_1 \sum_{j=1}^{\infty} jm_1 \beta_{j,i} N_{s,j} N_{s,i} \tag{87}$$

By replacing i with j in the last expression as a dummy index we get:

$$\frac{dM_1}{dt} = 0 \tag{88}$$

The above derivation includes the coagulation effect only. By adding the other physical soot processes, the soot moment equations can be expressed as follows ([141]):

$$\frac{dM_0}{dt} = R_0 + C_0. \tag{89}$$

$$\frac{dM_1}{dt} = R_1 + C_1 + S_1. \tag{90}$$

$$\frac{dM_2}{dt} = R_2 + C_2 + S_2. \tag{91}$$

...

$$\frac{dM_r}{dt} = R_r + C_r + S_r. \tag{92}$$

where $M_r = \sum_{i=1}^{\infty} m_i^r N_{s_i}$ is the r^{th} moment of the soot particle distribution, defined by the mass m_i of the individual primary particles and the number density N_{s_i} of the soot particles of size class i. The terms R_r, C_r and S_r are the moment rates that count for nucleation, coagulation and surface growth respectively. All the above rates must be added with their relevant sign.

The zero moment (r = 0) represents the number density N_s defined by the number of soot particles per unit volume of the mixture. The second moment represents the total mass of soot particles m_s per unit volume. The third and the fourth moments are proportional to the particle mass distribution function skewness and kurtosis, respectively. Accordingly, the soot mass fraction can be computed by $Y_s = M_1/\rho$, where ρ is the mixture density at a given instant. The soot volume fraction is given by $f_v = (\rho Y_s)/\rho_{soot}$, where ρ_{soot} is the soot density, taken as 1.8 g/cm^3 here. Hence, according to the above relations, prediction of only the first three moment differential equations should be sufficient to predict the soot mass fraction.

The application of the above terms depends greatly on what regime we are working in, which depends on the local pressure and temperature values. The soot nuclei diameter ranges between $200 - 400$ A, while the soot aggregates can be in the order of μm. Hence, the coupling between the soot particles and the fluid dynamic scales has to be considered over all this wide range. To determine the working regime, the Knudsen number Kn is calculated as:

$$Kn = \frac{2\lambda}{D_s} \tag{93}$$

where D_s is the average soot particle diameter computed from MOM, and λ is the mean free path of the fluid defined by:

$$\lambda = \left(\sqrt{2}\pi\sigma_g^2 N\right)^{-1} \tag{94}$$

Here, σ_g is the collision diameter of the fluid molecules, and N is the number density of the gas ([2]). When the Knudsen number is $<< 1$, the mean free path is much smaller than the particle diameter and the continuum regime formulation has to be adapted. On the other hand, if the Knudsen number is $>> 1$ the free molecular implementation is required. In between these two extremes is the transition regime. For most of the high pressure and combustion applications, the free molecular regime is found to be dominant.

The above formulation is valid for the coalescent limit, when all the particles in the coagulating ensemble are assumed spherical. After a certain transient period, the soot particle diameter exceed a certain threshold, after which coalescent collisions are not physical anymore, and the soot particles start to agglomerate and take on a fractal dimension. Under these conditions, the moments will also be function of the primary number of particles in addition to the mass of the particles. This regime is termed aggregation of soot particles and will be discussed in Section. (5.4.8). The following subsections introduce how each soot process is tracked within the MOMIC for different flow regimes (i.e., in the free, continuum and transition regimes).

5.4.2 Nucleation of Primary Particles

Generally speaking, several theories have been proposed to address the soot precursor, which include polyacetylene, ionic species, PAHs or acetylene. These chemical products are stable kinetically and once they are formed they need a huge amount of energy to decompose to there initial elements ([26]). The majority of the soot community support PAHs as a main soot precursor ([142]). However, the formation of PAHs requires the presence of acetylene for formation of the first aromatic ring, as mentioned before. As a result, in the current study acetylene is taken as the soot precursor. Acetylene is predicted here by a reduced ethylene/air mechanism developed at Princeton University ([143]). The details of this mechanism will be given later. However, the reaction rates are modified here by the soot nucleation, surface growth and oxidation rates according to the Lindstedt model ([52]).

Particle nucleation is the process of transition of gas-phase species to solid particles. However, this is the least understood process in soot formation. Based on PAHs as soot precursor, soot nucleation is formed by two simultaneous processes, one of them is the clustering of PAHs species together by collision to form dimers and trimer's of PAHs, and the other one is the individual growth of the PAHs species by gas phase chemical reactions ([142]). However, the use of acetylene as an indicative species for soot formation has proven to give good results with methane ([144]) and ethylene flames ([54]). Accordingly, the nucleation reaction of soot particles is expressed based on the Lindstedt model ([52]) as:

$$C_2H_2 \rightarrow^n 2C + H_2 \tag{95}$$

And the nucleation rate k_n in dimensions $\frac{kmol}{m^3 s}$ is given by:

$$k_n = 0.63x10^4 exp\left(-\frac{21000.0}{T}\right)[C_2H_2] \tag{96}$$

The above reaction rate states that the soot monomer is composed of two carbon atoms. Therefore as long as two carbon atoms come together a soot nuclei will be formed. Finally, the rate of moment variation by the soot nucleation is assumed in both coalescent and non-coalescent limits as follows for zero-th moment:

$$R_0 = \kappa \frac{k_n N_{av}}{C_\epsilon} \tag{97}$$

For higher moments (r$\geq$1)the nucleation rate is computed from:

$$R_r = R_0 \left(M_c / N_{av} * C_\epsilon\right)^r \tag{98}$$

Here, κ is a calibration constant taken as unity for the present work, but may need to be adjusted, k_n is the rate constant of nucleation computed, as in Eq. (96) ([79]), $C_\epsilon = 60$ is the minimum number of initial soot particles (C) required for nucleation, M_c is the molecular weight of a carbon atom, and N_{av} is the avogadro's number. This model assumes that the

nucleation effect is controlled by the nucleation rate of the carbon atoms by acetylene, and that the mass moments grow linearly as nucleation adds more particles to the mixture. Other studies incorporate similar assumptions as well ([139]).

5.4.3 Surface Growth

While nucleation controls the number of primary particles and coagulation controls the evolution of the number density, surface growth controls the number amount of carbon mass deposited on the soot particle surface ([142]). Surface growth is defined as the process of mass deposition or abstraction on the soot particle surface by gas-phase chemical species. This process controls the soot mass fraction and volume fraction, but it has no effect on the number density. [56, 145] indicate that, for premixed flames the surface growth rate is a first order kinetic function in acetylene. Accordingly, the surface growth is expressed by ([79]):

$$C_2H_2 \rightarrow^g 2C + H_2 \tag{99}$$

The surface growth reaction rate k_s is expressed as a first order function of acetylene and soot surface area ([52]):

$$k_s = 0.75x10^3 exp\left(-\frac{12100}{T}\right) As_i[C_2H_2] \tag{100}$$

where, As_i is the surface area of the particle of size i, with dimensions $\left[\frac{1}{m}\right]$ computed from

$$As_i = \pi d_p^2 N_{s,i} \tag{101}$$

and the particle diameter can be written as follows:

$$d_p = \left(\frac{6.0M_2}{\pi\rho_{soot}M_1}\right)^{1/3} \tag{102}$$

The oxidation of soot by OH and O_2 is considered and assumed to proceed, as follows ([52]):

$$C + \frac{1}{2}O_2 \rightarrow CO \tag{103}$$

$$C + OH \rightarrow CO + H \tag{104}$$

and the oxidation rate Kox_r is expressed as

$$k_{ox} = 7.15x10^2\sqrt{(T)}exp\left(-\frac{19800}{T}\right) As_i[O_2] + 0.36\sqrt{(T)}As_i[OH] \tag{105}$$

In the above equations, T is the temperature in Kelvin predicted by the LEM model, $[C_2H_2]$, $[O_2]$ and $[OH]$ are the acetylene, oxygen and hydroxyl molar concentration respectively computed from the reduced ethylene mechanism, respectively ([143, 146]).

In the MOMIC method, the surface growth rate can be expressed ([141]) in the coalescent limit as follows:

$$S_r = \pi \left(\frac{6}{\pi\rho}\right)^{2/3} \frac{k_s - k_{ox}}{\Delta m} M_0 \sum_{k=0}^{r-1} \Delta m^{r-k} \mu_{r+2/3}, r = 1, 2, 3, \cdots \tag{106}$$

Here, As_i is the surface area of the particle of size i, calculated from Eq. (101), Δm is the mass increment from one size bin to another. In other words, if a particle of size m_i gains Δm by mass deposition on its surface it will be transferred to the mass bin $i+1$ and μ_r is the r^{th} size moment defined as:

$$\mu_r = \frac{M_r}{M_o} \tag{107}$$

The above equation (Eq. 106) is derived utilizing the following mathematical formulation:

$$\frac{dN_{s,1}}{dt} = -\frac{k_s N_{s,1} s_1}{\Delta m} \tag{108}$$

$$\frac{dN_i}{dt} = -\frac{k_s}{\Delta m} \left(N_{s,i-1} s_{i-1} - N_{s,i} s_i\right) \tag{109}$$

The above differential equations states that the rate of variation of the number density is linear function of the particle surface area, s_i and, the growth rate per unit area, k_s. Multiplying the above equation by m^r and taking the summation over all the class sizes, Eq. (106) is retrieved.

5.4.4 Coagulation

Originally, the Smoluchowski equation ([147]) describes the time evolution of particle population y coagulation. The coagulation term in the moments equation is modelled based on Eqs (77). Following the discussion on section (5.4.1) the particle population equations are rewritten in the moment form by Frenklach et al., as follows ([148, 24, 141]).

$$C_o = -\frac{1}{2} \left(\sum_{i=1}^{\infty} \sum_{j=1}^{\infty} m_i^k \beta_{ij} Ns, iNs, j \right) \tag{110}$$

$$C_r = \frac{1}{2} \sum_{k=1}^{r-1} \begin{pmatrix} r \\ k \end{pmatrix} \left(\sum_{i=1}^{\infty} \sum_{j=1}^{\infty} m_i^k m_j^{r-k} \beta_{ij} N_{s,i} N_{s,j} \right) r = 2, 3, ... \tag{111}$$

where, β is the collision coefficient, $N_{s,i}$ is the number density and m_i is the average mass of particles of class size i. The above equations are the same for all the three regimes (i.e., continuum, free, and transition). However, modeling the collision coefficient will be different for each regime ([149]). Since the collision frequency is function of the number density it is computationally expensive and cannot be solved on a closed form. In past studies ([148]) a constant value for the collision frequency is assumed. However, MOMIC method allows a more accurate description of this term ([141]), which saves a lot of computational time with a reasonable modeling accuracy. The next three subsections will introduce the moment equations in the continuum, free molecular and transition regimes in the coalescent limit, respectively .

5.4.5 Continuum regime

For the continuum regime ($Kn << 1$) the collision coefficient for coalescent collisions of spherical particles is given by the following equation ([149]):

$$\beta_{ij}^{c} = K_c \left(\frac{C_i}{m_i^{\frac{1}{3}}} + \frac{C_j}{m_j^{\frac{1}{3}}} \right) \left(m_i^{\frac{1}{3}} + m_j^{\frac{1}{3}} \right) \tag{112}$$

K_c is given by ([150]):

$$K_c = \frac{2k_B T}{3\mu} \tag{113}$$

Here, μ is the gas viscosity, and C is the Cunningham slip correction factor and can be expressed as $C = 1 + 1.257Kn$ ([151]). By substituting Eq. (112) in Eq. (111) we get:

$$C_o^c = K_c \left[1 + \mu_{1/3}\mu_{-1/3} + K_c^{'} \left(\mu_{-1/3} + \mu_{1/3}\mu_{-2/3} \right) \right] M_o^2 \tag{114}$$

$$\begin{array}{l} C_r^c = \\ \frac{1}{2} K_c \sum_{k=1}^{r-1} \binom{r}{k} \left[2\mu_k \mu_{r-k} + \mu_{k+1/3}\mu_{r-k-1/3} + \mu_{k-1/3}\mu_{r-k+1/3} \right] M_o^2 + \frac{1}{2} K_c \sum_{k=1}^{r-1} \binom{r}{k} \\ K_c^{'} \left(\mu_{k-1/3} + \mu_{r-k}\mu_{-2/3} + \mu_k \mu_{r-k-1/3} + \mu_{k+1/3}\mu_{r-k-2/3} + \mu_{k-2/3}\mu_{r-k+1/3} \right) M_o^2 \end{array} \tag{115}$$

Here $K_c^{'} = 2.5146\lambda \left(\frac{\pi \rho_s}{6} \right)^{1/3}$, ρ_s is the soot particle density and λ is the free molecular path ([151]). The above equations include fractional reduced moments (e.g, $\mu_{-2/3}$), which need to be solved to close the system. These fractional moments are obtained by Lagrangian interpolation in-between the whole moments $0, 1, 2, 3, ...$ It also indicates that extrapolation is needed for the $r_{max} + 1/3$ moment, where r_{max} is the number of moments solved. The validity and accuracy of the interpolation technique is discussed by [141] and [150]; it is shown that the logarithm of the fractional moment is linear with the moment order after $r = 3$, with excellent accuracy between the exact method from the master equation and the MOMIC interpolation technique. In the current study, we solve only up to the 4^{th} moment since we are interested only in the zeroth and first three moments. The positive fractional moments are computed by Lagrangian interpolation among the whole moments logarithms as:

$$log\left(\mu_p\right) = L_p\left(log\mu_o, log\mu_1, ...log\mu_{max}\right) \tag{116}$$

While the negative fractional moments was found sufficient to be interpolated among the first three moments ([141]):

$$log\left(\mu_p\right) = L_p\left(log\mu_o, log\mu_1, log\mu_2\right) \tag{117}$$

where L_p is the Lagrangian interpolation operator. For a data of N points, the Lagrangian interpolation fits the data with a polynomial of degree $N - 1$. For instance, if we have an original set of data $Y_i = f(x_i)$, where i varies from 1 to N, the final fitted polynomial can be expressed as:

$$P(x) = \sum_{k=1}^{N} L_k(x) Y_k \tag{118}$$

where L_k is the Lagrangian coefficient computed from:

$$L_k(x) = \frac{(x - x_1)(x - x_2) \ldots\ldots (x - x_n)}{(x_k - x_1)(x_k - x_2) \ldots\ldots (x_k - x_n)} \tag{119}$$

By solving for the fractional moments and substituting into Eqs. (114 and 115), the equations will be function of the whole moments that are known at each time step.

By interpolation, the negative fractional moments are expressed as:

$$\begin{aligned} \mu_{-1/2} &= \mu_o^{15/8} \mu_1^{-10/8} \mu_2^{3/8} \\ \mu_{-1/6} &= \mu_o^{91/72} \mu_1^{-26/72} \mu_2^{7/72} \end{aligned} \tag{120}$$

While some of the fractional positive moments are given by the following:

$$\begin{aligned} \mu_{1/2} &= \mu_o^{5/16} \mu_1^{15/16} \mu_2^{-5/16} \mu_3^{1/16} \\ \mu_{3/2} &= \mu_o^{-1/16} \mu_1^{9/16} \mu_2^{9/16} \mu_3^{-1/16} \\ \mu_{1/6} &= \mu_o^{935/1296} \mu_1^{561/1296} \mu_2^{-255/1296} \mu_3^{55/1296} \\ \mu_{7/6} &= \mu_o^{-55/1296} \mu_1^{1155/1296} \mu_2^{231/1296} \mu_3^{-35/1296} \\ \mu_{5/6} &= \mu_o^{91/1296} \mu_1^{1365/1296} \mu_2^{-195/1296} \mu_3^{-35/1296} \\ \mu_{11/6} &= \mu_o^{35/1296} \mu_1^{231/1296} \mu_2^{1155/1296} \mu_3^{-55/1296} \\ \mu_{13/6} &= \mu_o^{35/1296} \mu_1^{-195/1296} \mu_2^{1365/1296} \mu_3^{91/1296} \\ \mu_{15/6} &= \mu_o^{91/1296} \mu_1^{-405/1296} \mu_2^{1215/1296} \mu_3^{405/1296} \end{aligned}$$

5.4.6 Free Molecular Regime

For the free molecular regime, $Kn >> 1$, and the mean free path is much larger than the travelling particle diameter. This regime characterizes low density fluids at high temperature levels. In this regime, the collision coefficient can be calculated from ([149]):

$$\beta_{ij}^{f} = K_f \sqrt{\left(\frac{1}{m_i} + \frac{1}{m_j}\right)} \left(m_i^{\frac{1}{3}} + m_j^{\frac{1}{3}}\right)^2 \tag{121}$$

and K_f is given by

$$K_f = \epsilon \sqrt{\frac{6 k_B T}{\rho}} \left(\frac{3}{4\pi\rho}\right)^{\frac{1}{6}} \tag{122}$$

where ϵ is the Van Der Waals enhancement factor. [152], performed a study on the effect of ϵ at different pressures. They showed that this factor ranges from 1.333 and 2.0. They also mentioned that the small aerosol particles are highly affected by this factor, since it mainly represents the Van-Der Waals forces, which contribute to the particle size distribution. The substitution of Eq. (121) into Eq. (111) leads to the following equation is obtained:

$$C_r^f = \sum_{i=1}^{\infty}\sum_{j=1}^{\infty}\left(m_i+m_j\right)^{1/2} m_i^{1/2} m_j^{1/2}\left(m_i^{1/3}+m_j^{1/3}\right)^2 N_i N_j \tag{123}$$

Since the expansion of the term $(m_i + m_j)^{1/2}$ will be infinite, [141] used a double interpolation procedure for the MOMIC. First a grid functions f_l, where l ranges form 0 to the maximum moment equation r_{max} is solved. These grid functions are defined as:

$$f_l^{x,y} = \sum_{i=1}^{\infty}\sum_{j=1}^{\infty}\left(m_i+m_j\right)^{1/2} m_i^x m_j^y\left(m_i^{1/3}+m_j^{1/3}\right)^2 N_i N_j m_i^{1/2} m_j^{1/2} \tag{124}$$

As a result, the coagulation terms in the free molecular regime can be expressed as:

$$\begin{aligned} C_o^f &= \frac{1}{2}K_f M_o^2 f_{1/2}^{0,0} \\ C_r^f &= \frac{1}{2}K_f M_o^2 \sum_{k=1}^{r-1}\binom{r}{k} f_{1/2}^{k,r-k} \end{aligned} \tag{125}$$

Utilizing the identity that $\mu_r = \frac{\sum_{i=1}^{\infty} m^r N_i}{\sum_{i=1}^{\infty} N_i}$ and by substituting into the grid functions in Eq.(124) we can get $f_l^{x,y}$ in terms of the reduced moments only. Hence, the whole grid functions are given as:

$$\begin{aligned} f_o^{0,0} &= \left(2\mu_{1/6}\mu_{-1/2} + 2\mu_{-1/6}^2\right) M_o^2 \\ f_o^{1,1} &= \left(2\mu_{7/6}\mu_{1/2} + 2\mu_{5/6}^2\right) M_o^2 \\ f_o^{1,2} &= \left(\mu_{7/6}\mu_{3/2} + \mu_{1/2}\mu_{13/6} + 2\mu_{5/6}\mu_{11/6}\right) M_o^2 \\ f_o^{1,3} &= \left(\mu_{7/6}\mu_{5/2} + \mu_{1/2}\mu_{19/6} + 2\mu_{5/6}\mu_{17/6}\right) M_o^2 \\ f_o^{1,4} &= \left(\mu_{7/6}\mu_{7/2} + \mu_{1/2}\mu_{25/6} + 2\mu_{5/6}\mu_{23/6}\right) M_o^2 \\ f_o^{2,2} &= 2\left(\mu_{13/6}\mu_{3/2} + 2\mu_{11/6}^2\right) M_o^2 \\ f_o^{2,3} &= \left(\mu_{13/6}\mu_{5/2} + \mu_{3/2}\mu_{19/6} + 2\mu_{11/6}\mu_{17/6}\right) M_o^2 \end{aligned} \tag{126}$$

$$\begin{aligned} f_1^{0,0} &= \left(2\mu_{7/6}\mu_{-1/2} + 4\mu_{5/6}\mu_{-1/6} + 2\mu_{1/2}\mu_{1/6}\right) M_o^2 \\ f_1^{1,1} &= \left(2\mu_{13/6}\mu_{1/2} + 4\mu_{11/6}\mu_{5/6} + 2\mu_{3/2}\mu_{7/6}\right) M_o^2 \\ f_1^{1,2} &= \left(2\mu_{13/6}\mu_{3/2} + 4\mu_{11/6}\mu_{11/6} + 2\mu_{5/2}\mu_{7/6} + \mu_{1/2}\mu_{19/6} + \mu_{1/2}\mu_{19/6}\right) M_o^2 \\ f_1^{1,3} &= \left(2\mu_{13/6}\mu_{5/2} + \mu_{3/2}\mu_{19/6} + 2\mu_{11/6}\mu_{17/6} + \mu_{7/2}\mu_{7/6} + \mu_{1/2}\mu_{25/6} + 2\mu_{5/6}\mu_{23/6}\right) M_o^2 \\ f_1^{1,4} &= \left(2\mu_{13/6}\mu_{7/2} + \mu_{3/2}\mu_{25/6} + 2\mu_{11/6}\mu_{23/6} + \mu_{9/2}\mu_{7/6} + \mu_{1/2}\mu_{31/6} + 2\mu_{5/6}\mu_{29/6}\right) M_o^2 \\ f_1^{2,2} &= \left(2\mu_{19/6}\mu_{3/2} + 2\mu_{13/6}\mu_{5/2} + 4\mu_{17/6}\mu_{11/6}\right) M_o^2 \\ f_1^{2,3} &= \left(2\mu_{19/6}\mu_{5/2} + 2\mu_{17/6}\mu_{17/6} + 2\mu_{7/2}\mu_{13/6} + \mu_{3/2}\mu_{25/6} + 2\mu_{11/6}\mu_{23/6}\right) M_o^2 \end{aligned} \tag{127}$$

$$
\begin{aligned}
f_2^{0,0} &= \left(2\mu_{13/6}\mu_{-1/2} + 4\mu_{11/6}\mu_{-1/6} + 2\mu_{3/2}\mu_{1/6} + 4\mu_{7/6}\mu_{1/2} + 4\mu_{5/6}^2\right) M_o^2 \\
f_2^{1,1} &= \left(2\mu_{19/6}\mu_{1/2} + 2\mu_{5/2}\mu_{7/6} + 4\mu_{17/6}\mu_{5/6} + 4\mu_{13/6}\mu_{3/2} + \mu_{11/6}^2\right) M_o^2 \\
f_2^{1,3} &= \left(2\mu_{19/6}\mu_{5/2} + 2\mu_{13/6}\mu_{7/2} + 2\mu_{17/6}\mu_{17/6} + 2\mu_{11/6}\mu_{23/6}\right) \\
&+ \left(\mu_{9/2}\mu_{7/6} + \mu_{13/6}\mu_{1/2} + 2\mu_{5/6}\mu_{29/6}\right) M_o^2 \\
f_2^{1,4} &= \left(\mu_{19/6}\mu_{7/2} + \mu_{25/6}\mu_{5/2} + 2\mu_{17/6}\mu_{23/6} + 2\mu_{13/6}\mu_{9/2} + 2\mu_{31/6}\mu_{3/2} + 4\mu_{11/6}\mu_{29/6}\right) \\
&+ \left(\mu_{11/2}\mu_{7/6} + \mu_{37/6}\mu_{1/2} + 2\mu_{35/6}\mu_{5/6}\right) M_o^2 \\
f_2^{2,2} &= \left(2\mu_{25/6}\mu_{3/2} + 2\mu_{7/6}\mu_{13/6} + 4\mu_{23/6}\mu_{11/6}4\mu_{19/6}\mu_{5/2} + 4\mu_{17/6}^2\right) M_o^2 \\
f_2^{2,3} &= \left(3\mu_{25/6}\mu_{5/2} + 3\mu_{7/2}\mu_{19/6} + 2\mu_{23/6}\mu_{17/6} + 2\mu_{29/6}\mu_{11/6} + 4\mu_{17/6}\mu_{23/6} + \mu_{9/2}\mu_{13/6}\right) \\
&+ \left(\mu_{3/2}\mu_{31/6}\right) M_o^2
\end{aligned}
\tag{128}
$$

Afterwards, the fractional grid functions $f_{1/2}^{x,y}$ are interpolated by Lagrangian technique between the whole grid function values as:

$$
f_{1/2}^{x,y} = f_o^{3/8} f_1^{3/4} f_2^{-1/8} \tag{129}
$$

5.4.7 Transition Regime

The transition regime demarcation value is usually vague in the literature. However, in this study, the range in-between $Kn = 1$ and $Kn = 0.1$ is taken as the boundary values between the continuum and the free molecular regimes. In the transition regime, the collision frequency is usually expressed in the form of empirical formula of Fuchs ([149]). This formula is hard to implement in the MOMIC. As a result, [153] suggested to use the harmonic mean to approximate the coagulation rate in this regime, which is also implemented here and is given as follows:

$$
C_r^T = \frac{C_r^f C_r^c}{C_r^f + C_r^c} \tag{130}
$$

where C_r^f is the corresponding value at the free molecular regime from Eq. (123) and C_r^c is the corresponding value at the continuum regime from Eqs. (114 and 115).

5.4.8 Soot Aggregation

The previous sections describe the soot development in the coalescent limit, where the particles after coagulating are still in the spherical configuration. Physically, after an initial period of coagulation, aggregation starts to activate and chain like structures are formed. The idea here is to start with the coalescent limit model described above until a critical average diameter d^* is reached. Afterwards, the aggregation limit will be activated ([141]). The aggregate structure is composed primarily of spherical particles that obey the fractal relationship.

$$
n = k_f \left(\frac{2R_g}{d_p}\right)^{D_f} \tag{131}
$$

where n is the number of primary particles that can be determined from the coalescent limit, R_g is the radius of gyration of an aggregate , d_p is the diameter of primary particles, D_f is

the fractal dimension (taken as 1.8 here), and k_f is the fractal prefactor. At the aggregation limit the particle distribution is function of mass moments and number of primary particles n. Frenklach introduced a new moment function P_r for n:

$$P_r = \sum_{j=1}^{\infty} n_i^r N_i \tag{132}$$

where the moments P_r can be calculated from

$$\begin{array}{l} \frac{dP_1}{dt} = R_1 \\ \frac{dP_r}{dt} = R_r + H_r \cdot \quad r = 2\ 2, 3, ... \end{array} \tag{133}$$

where R_r is the inception rate computed as before.

$$R_r = \kappa M_r \frac{K_r}{\rho_{soot}} \tag{134}$$

H_r is the aggregate coagulation contribution given by:

$$H_r = \frac{1}{2} \sum_{k=1}^{r-1} \begin{pmatrix} r \\ k \end{pmatrix} \left(\sum_{i=1}^{\infty} \sum_{j=1}^{\infty} n_i^k n_j^{r-k} \beta_{ij} N_i N_j \right) \tag{135}$$

Here, β_{ij}^a is the collision of the aggregates. Similar to the coalescent limit, in the free molecular regime the aggregate coagulation is:

$$H_r^f = \frac{1}{2} K_f M_o^2 h_{1/2}^r$$

Defining the reduced aggregation moments as $\pi_r = \frac{H_r}{H_o}$, the grid function $h_{1/2}^r$ is given by:

$$\begin{array}{l} h_{1/2}^r = \sum_{k=o}^{l} \binom{l}{k} \sum_{q=1}^{r-1} \binom{r}{q} \left(\mu_{k+1/6} \pi_{q+2/D_f - 2/3} X \mu_{l-k-1/2} \pi_{r-q} + \right) + \\ \left(2\mu_{k-1/6} \pi_{q+1/D_f - 1/3} X \mu_{l-k-1/6} \pi_{r-q+1/D_f - 1/3} + \mu_{k-1/2} \pi_q X \mu_{l-k-1/6} \pi_{r-q+2/D_f - 2/3} \right) \end{array} \tag{136}$$

For the continuum regime of aggregate coagulation we have the following expression:

$$\begin{array}{l} H_r^c = \frac{1}{2} K_c \sum_{k=1}^{r-1} \binom{r}{k} \\ \left[2\pi_k \pi_{r-k} \mu_{1/3} \pi_{k+1/D_f - 1/3} X \mu_{-1/3} \pi_{r-k+1/3-1/D_f} + \mu_{-1/3} \pi_{k-1/D_f + 1/3} X \mu_{1/3} \pi_{r-k-1/3+1/D_f} \right] M_o^2 + \\ \frac{1}{2} K_c K_c' \sum_{k=1}^{r-1} \binom{r}{k} \\ \left[\mu_{-1/3} \pi_{k+1/3-1/D_f} \pi_{r-k} + \mu_{-1/3} \pi_{r-k+1/3-1/D_f} \pi_k + \mu_{1/3} \pi_{k-1/3+1/D_f} \mu_{-2/3} \pi_{r-k+2/3-2/D_f} \right] + \\ \frac{1}{2} K_c K_c' \sum_{k=1}^{r-1} \binom{r}{k} \left[\mu_{-2/3} \pi_{k+2/3-2/D_f} \mu_{1/3} \pi_{r-k-1/3+1/D_f} \right] M_o^2 \end{array} \tag{137}$$

The agglomeration critical diameter d^*, after which agglomeration starts is given by [154] and is taken here as $d^* = 10nm$. While the particles are agglomerating they still undergoing coagulation simultaneously. But at this time the coagulating particles are function of the number of primary particles and the mass as well. The set of Eqs (133) is solved simultaneously with the coagulation equations in the non-coalescent limit, which will take the form:

$$\frac{dM_r^a}{dt} = R_r + C_r^a + S_r^a. \tag{138}$$

In this case the surface growth rate will be given with a similar formula to Eq. (106)as:

$$S_r^a = \pi \left(\frac{6}{\pi\rho}\right)^{2/3} \frac{Ks_r - Kox_r}{\Delta m} M_0^2 \sum_{k=0}^{r-1} \Delta m^{r-k} \mu_{r+2/3}\pi_{1/3}, r = 1, 2, 3, \cdots \tag{139}$$

and the grid function for the coagulation rate in the free molecular regime will be given as:

$$\begin{array}{l} f_l^{x,y} = \sum_{i=1}^{l} \binom{l}{k} \mu_{x+k+1/6}\pi_{2/D_f-2/3}\mu_{y+l-k-1/2} + \\ 2\mu_{x+k-1/6}\pi_{1/D_f-1/3}\mu_{y+l-k-1/6}\pi_{1/D_f-1/3} + \mu_{y+l-k+1/6}\pi_{2/D_f-2/3}\mu_{x+k-1/2} \end{array} \tag{140}$$

In the continuum regime the $r-th$ coagulation rates $C_r^{c,a}$ in the non-coalescent limit are given by:

$$\begin{array}{l} C_o^{c,a} = K_c \left[1 + \mu_{1/3}\pi_{1/D_f-1/3}\mu_{-1/3}\pi_{-1/D_f+1/3}\right] M_o^2 + \\ K_c K_c^{'} \left[\mu_{-1/3}\pi_{-1/D_f+1/3} + \mu_{1/3}\mu_{-2/3}\pi_{1/D_f-1/3}\pi_{2/D_f-2/3}\right] M_o^2 \end{array} \tag{141}$$

$$\begin{array}{l} C_r^{c,a} = \frac{1}{2} K_c \sum_{k=1}^{r-1} \binom{r}{k} \\ \left[2\mu_k\mu_{r-k} + \mu_{k+1/3}\pi_{1/D_f-1/3}\mu_{r-k-1/3}\pi_{-1/D_f+1/3} + \mu_{k-1/3}\pi_{-1/D_f+1/3}\mu_{r-k+1/3}\pi_{1/D_f-1/3}\right] M_o^2 + \\ \frac{1}{2} K_c \sum_{k=1}^{r-1} \binom{r}{k} K_c^{'} \left(\mu_{k-1/3}\pi_{-1/D_f+1/3}\mu_{r-k} + \mu_k\mu_{r-k-1/3}\pi_{-1/D_f+1/3}\right) M_o^2 \\ K_c^{'} \left(+\mu_{k+1/3}\mu_{r-k-2/3}\pi_{1/D_f-1/3}\pi_{-2/D_f+2/3} + \mu_{k-2/3}\mu_{r-k+1/3}\pi_{-2/D_f+2/3}\pi_{1/D_f-1/3}\right) M_o^2 \end{array} \tag{142}$$

In the transition regime a similar treatment is done to the coalescent limit.

5.4.9 Soot Diffusion and Thermophoresis

Several theories have been developed to account for soot transport by Brownian diffusion and thermophoretic forces ([2, 155]). As a soot particle is created, it is subjected to a drag force by the surrounding fluid due to the relative motion between them. In addition, in reacting flow with high temperature gradients, the particles are subjected to a force in the opposite direction of the temperature gradient ([156]). Numerical and experimental studies ([155]) found that the thermophoretic forces counteract the drag forces on the particle. In the continuum regime, where the Knudsen number is much smaller than unity, several theories has been developed to compute the drag force on the particle, starting from the simplified Stokes formula developed in 1851 for drag over a sphere. Here, we use the more generalized Knudsen and Weber formula ([157]), where the drag force is given by:

$$F_D = \frac{6\pi\mu RV}{1 + Kn\left[A + Bexp\left(-E/Kn\right)\right]} \tag{143}$$

In the above equation, V is the relative particle velocity. A, B, and E are constants taken as 1.099, 0.518, and 0.425, respectively ([158]). [159] showed that for Brownian diffusion the coefficient of particle diffusivity is given by $D_s = k_B T/k_d$, where the drag coefficient is defined as $k_d = F_D/V$ and k_B is the Boltzman constant. In the free molecular regime, where

the soot particles are very small relative to the fluid mean free path, the particle diffusivity model developed by [2, 158] is used here. The model accounts for different modes of reflection of the molecules from the particle surface. The two extremes are specular scattering, where the reflection angle is equal to the incidence angle, and diffuse scattering, where the reflection angle is random, and the reflection velocity is Maxwellian. Accordingly, the particle diffusion coefficient is given by:

$$D_s = \frac{3}{8}\sqrt{\frac{k_B T}{2\pi m_r}}\frac{1}{N_f R_d^2 \Omega_{avg}^{1,1}} \tag{144}$$

Here, k_B is the Boltzmann constant, R_d is the particle radius and $\Omega_{avg}^{1,1}$ is the reduced collision integral given by:

$$\begin{array}{l}\Omega_{avg}^{1,1} = \Omega_d^{1,1} + Kn\left(0.9\Omega_d^{1,1} + 0.1\Omega_s^{1,1}\right)(1+Kn) \\ \left(0.9Kn\left(\Omega_d^{1,1} - \Omega_s^{1,1}\right)/\left[1+(R/2.5)^{15}\right]\right)/(1+Kn)\end{array} \tag{145}$$

In the above equation the reduced collision integral for the scattering and the diffusive limits are calculated from:

$$\begin{array}{l}\Omega_d^{(1,1)} = 1 + \frac{\pi}{8} + \left[1.072 + \frac{2.078}{T^{*1/4}} + \frac{1.261}{T^{*1/2}}\right]\frac{\sigma}{R} + \left[3.285 - \frac{8.872}{T^{*1/4}} + \frac{5.225}{T^{*1/2}}\right]\left(\frac{\sigma}{R}\right)^2 \\ \Omega_s^{(1,1)} = 1 + \left[0.316 + \frac{1.47}{T^{*1/4}} + \frac{0.476}{T^{*1/2}}\right]\frac{\sigma}{R} + \left[1.53 - \frac{5.013}{T^{*1/4}} + \frac{4.025}{T^{*1/2}}\right]\left(\frac{\sigma}{R}\right)^2\end{array} \tag{146}$$

Here, σ is the collision diameter, $T^* = k_B T/\epsilon$ is the reduced temperature, and ϵ is the potential energy well depth taken as 98.4 $watt/m^2/k^4$ for the mixture and 33.3 $watt/m^2/k^4$ for the soot ([158]). The thermophoretic force and velocity are neglected in the continuum regime. In the free molecular regime the thermophoretic velocity is computed from:

$$V_T = \left(1 - \frac{6}{5}\frac{\Omega_{avg}^{1,2}}{\Omega_{avg}^{1,1}}\right)\frac{\kappa \nabla T}{N_f K_B T} \tag{147}$$

Here, $\Omega_{avg}^{1,2}$ is computed from a similar expression to Eq. (145).

5.5 Subgrid LEM-MOMIC

In earlier studies ([75, 100, 110]), the subgrid mixing and combustion model, LEM has been validated against experimental and DNS data for similar canonical but non-sooting premixed flames in the flamelet and in the thin reaction zone regimes. In this section, the extensions of LEM to account for sooting flames are described.

To predict soot accurately, the soot particle size distribution function (PSDF) has to be known spatially and temporally. Several approaches have been used to predict soot dynamics. For simple monodisperse cases, log-normal or Gaussian distribution have been used ([139]). In the more complicated polydisperse case other methods have been developed. For example, sectional method ([160]), where the particle size range is divided into discrete intervals inside each of which the aerosol master equation is solved (under the assumption of exponential growth of the particle size at the sections boundaries), is often used. Stochastic methods ([161, 162]) are used as well for laminar flames, where the time evolution of the

soot number density is solved using a stochastic algorithm such as the Monte Carlo method. Although very accurate, these methods are known to be computationally very expensive and are not considered here for LES applications.

MOMIC method (Described in section 5.4.1) developed by [148] is based on solving the moments of the PSDF instead of the PSDF itself. This method is computationally efficient and also accurate. Therefore, it is used in the present approach. In particular, the Method of Moment (MOM) using Interpolative Closure (MOMIC) ([141]) is utilized. MOM is based on the idea that the knowledge of all the moments is equivalent to knowing the distribution function itself. MOMIC has the advantage of not requiring a priori knowledge for the PSDF. Hence, it is generally applicable for polydisperse cases and requires solving only a limited (e.g., first few moments) set of differential equations for the time evolution of PSDF moments ([151]), which makes this approach very cost effective.

5.5.1 Model Overview

Here, we implement the MOMIC approach within the existing subgrid mixing and combustion (LEMLES) model. Details of the original LEMLES, and the LEM-MOMIC soot model components are schematically shown in Figs. 8 and 9.

Figure 8 shows the modules of the LEM-MOMIC subgrid model. The model is designed to be flexible to handle any future changes of its components. LEM is the core turbulent mixing and reaction diffusion model and it is combined with an optically thin radiation model and the soot MOMIC model that accounts for the different soot formation processes such as nucleation, oxidation, surface growth, coagulation and aggregation. To allow for general applications, the soot particle thermophoresis ([155]) and diffusion ([2]) are also included in the transport equation of the soot mass fraction.

The chemistry model is a reduced multi-step, multi-species ethylene/air mechanism ([143]) combined with the four step acetylene based soot model ([52]). In addition, in situ adaptive tabulation (ISAT) ([163]) is used to reduce the simulation time significantly. ISAT retrieves pre-stored values of the scalars (species and temperature) within a specified ellipsoid error of tolerance. ISAT allows the speed up of the computation of the order of 30 times faster than direct integration ([164]).

A schematic diagram of the complete soot chemistry path used here is shown in Fig. 9. The soot nucleus is assumed to be composed of two carbon (c) atoms. After the combustion process, acetylene and other hydrocarbon radicals are produced. Acetylene is decomposed to give a soot nucleus and hydrogen. Soot nuclei collide together to coalesce and produce larger soot particles. At the same time, oxidative attack of oxygen and hydroxyl continue to interact with the soot surface and reduce the soot particle mass by oxidizing carbon atoms to CO and H radicals. After a certain transient period the soot particle diameter exceed a certain threshold, after which coalescent collision is not physical anymore and the soot particles start to agglomerate and take on a fractal dimension. These features are qualitatively and quantitatively incorporated in an LEM-MOMIC closure, as described below.

5.5.2 Governing Equations

In LEM-MOMIC the governing equations are rewritten as:

$$\rho_{LEM}\frac{\partial Y_{k,LEM}}{\partial t^s} = F_k + \frac{\partial}{\partial s}\left[\rho_{LEM} D_k \frac{\partial Y_k}{\partial s}\right] + \dot{\omega}_k \qquad k = 1, \ldots N_s \tag{148}$$

$$\rho_{LEM}\frac{\partial Y_s}{\partial t^s} = F_s + \frac{\partial}{\partial s}\left[\rho_{LEM}\left(D_s\frac{\partial Y_s}{\partial s} - V_T Y_s\right)\right] + \dot{\omega}_s \tag{149}$$

$$\frac{\partial T_{LEM}}{\partial t^s} = -\frac{1}{\overline{C_p}}\sum_{k=1}^{N_s} C_{p,k} Y_{k,LEM} V_k \frac{\partial T_{LEM}}{\partial s} + \frac{1}{\rho_{LEM}\overline{C_p}}\frac{\partial}{\partial s}\left(\overline{\kappa}\frac{\partial T}{\partial s}\right) + a_{over}\sigma\left(T^4 - T_o^4\right) - \frac{1}{\overline{\rho C_p}}\sum_{k=1}^{N_s} h_k \dot{\omega}_k M w_k + F_T \tag{150}$$

In the above equations, Y_k and Y_s are the k-th species and soot mass fraction, respectively, which are subjected to the mass conservation condition $\sum_1^{N_s}\widetilde{Y_k} + \widetilde{Y_s} = 1.0$. The soot molecular diffusivity and thermophoretic velocity are denoted by D_s and V_T, respectively. The calculation of these terms are explained in Eqs. (144) and (147) in section (5.4.9).

The 1D line s resolution in LEM-MOMIC is chosen to resolve all the turbulent scales below $\overline{\Delta}$ (e.g., down to the Kolmogorov length scale, η). Here, F_k, F_T, F_s and F_{M_r} in Eq. (151) represent $-\left[\rho\left(u_i^{'}\right)\right]^S \frac{\partial Y_k^n}{\partial x_i}$ in Eq. (63), the subgrid stirring effect on the species (including soot), and a similar term in the temperature and the moment fields, respectively.

In the coalescent limit, where the soot particles are assumed to conserve the spherical shape after collision, the following equation for the r-th moment M_r are included in the subgrid model.

$$\frac{\partial M_r}{\partial t^s} = R_r + C_r + S_r + F_{M_r}, r = 0, 1, 2, 3.... \tag{151}$$

The terms R_r, C_r and S_r are, the nucleation, the coagulation (in the coalescent limit) and the surface growth effect on the $r-$moment equation, respectively. Whenever the soot particle exceeds a critical diameter, taken here as 25 nm ([150]), the particles start to aggregate to form a chain like structures of fractal dimension $D_f = 2.0$ ([165]). Then, Eq. (151) is replaced by:

$$\frac{\partial P_r}{\partial t^s} = R_r + Ca_r + H_r + Sa_r + F_{M_r}, r = 0, 1, 2, 3.... \tag{152}$$

Here, H_r, Ca_r, and Sa_r are respectively, the aggregation rate, the coagulation rate, and the surface growth rate in the non-coalescent limit, and P_r is the $r-th$ mass moments after aggregation. The derivation of these terms is given in [141, 150], and therefore, only a brief description is given here. In the current implementation, F_{M_r} effect is neglected, while the soot mass fraction stirring F_s in Eq. (149) is implemented only if the Stokes number defined as $St = \rho d_p/\Delta t_{LES}$ is small enough, so that the soot particles can be stirred by the turbulent eddies. Here, d_p is the average soot particle diameter.

5.5.3 Chemical Kinetics

For realistic predictions of soot physics, a relatively detailed mechanism is essential (here, we study ethylene-air flames). In addition, it is necessary to define what gas specie is indicative of soot precursor. Although PAHs, benzene and acetylene all have been proposed ([28]), we consider acetylene as the key gas species for soot inception. This choice is motivated in part by past observations in ethylene-air premixed flames ([166]), that acetylene is the main precursor, which determines the mass of the soot formed in the inception stage. Another study by [167], concluded that most of the soot particle mass comes from C_2H_2 through two main possible paths: the direct addition of acetylene to the soot growing particle and by the addition of acetylene to PAHs, which eventually becomes the soot nuclei. The choice of the acetylene based model is due to the unavailability of a computationally efficient reduced PAHs based soot and the associated chemical mechanism. However, the simulation strategy can easily include any future development in the kinetics models.

Therefore, in the present effort we combine an acetylene based four-step soot model ([52]) that describes nucleation, surface growth, and oxidation with a reduced but multi-step ethylene-air kinetics model. Two kinetics mechanisms for ethylene-air are studied here: a 16-step, 20 species mechanism (MECH-A) and a 15-step, 19 species mechanism (MECH-B) ([143]). Although, the accuracy of the two mechanisms is proven to be the same ([143]), MECH-B is computationally more efficient and is accompanied by a detailed binary diffusivity library for the gas phase species. As a result, (MECH-B) was the mechanism to be used for the final validation case.

The reduced mechanism developed by [143] at Princeton University is summarized here. The detailed mechanism for ethylene oxidation by [168] is the starting mechanism for both the reduced mechanisms. The reduction is guided by densely sampled reaction states, spanning the present parameter range of study, from perfectly stirred reactors (PSR) and auto-ignition, which are respectively representative applications of high- to intermediate-, and low- to intermediate-temperature chemistries. By applying the theory of directed relation graph ([143]), 26 important participating species, namely H_2, H, O, O_2, OH, H_2O, HO_2, H_2O_2, C, CH, CH_2, CH_2*, CH_3, CH_4, CO, CO_2, HCO, CH_2O, CH_3O, C_2H_2, C_2H_3, C_2H_4, C_2H_5, $HCCO$, CH_2CO, CH_2CHO, were identified. Two additional species, C_2H_6 and C_3H_6, were retained in the skeletal mechanism in order to lower the reduction error in flame speeds under fuel rich conditions. The final skeletal mechanism, therefore, consists of 28 species and 167 reactions. By further using computational singular perturbation ([146]), ten species, C, CH, CH_2, CH_2*, HCO, CH_3O, C_2H_3, C_2H_5, $HCCO$, and CH_2CHO, were found to be in quasi steady state.

For the current studies, MECH-A is employed in a thermally perfect model with diffusion coefficients determined by using species dependent constant Lewis number. For a more general application, MECH-B is used with proper binary diffusion coefficients. It was found ([143]) that the diffusion coefficient of some species can be approximated by another species in the mechanism. Thus, by grouping the species with similar diffusion coefficients, only a 9x9 binary diffusion coefficient matrix needs to be calculated in the evaluation of mixture average diffusion coefficients for all the species, resulting in approximately an 80% reduction in CPU time (when compared to the full evaluation). It is noted that while MECH-B is only smaller than the 16-step mechanism ([143]) by only one species, the number of elementary

reactions involved is reduced by about 20%, which is approximately the fraction of CPU time saved in the evaluation of the chemical reaction source terms.

The four-step soot model used in the current study is ([52, 169, 170]):

$$C_2H_2 \rightarrow^n 2C + H_2 \tag{153}$$

$$C_2H_2 \rightarrow^g 2C + H_2 \tag{154}$$

$$C + \frac{1}{2}O_2 \rightarrow CO \tag{155}$$

$$C + OH \rightarrow CO + H \tag{156}$$

Equation (153) states that the soot monomer is composed of two carbon atoms. Therefore, as long as two carbon atoms come together a soot nucleus is formed. Equation (154) states that the soot reactivity is proportional to the local surface particle area per unit volume and first order in acetylene concentration. The oxidation of the soot particles by OH and O_2 species is prescribed by Eqs. (155) and (156) ([169, 170]).

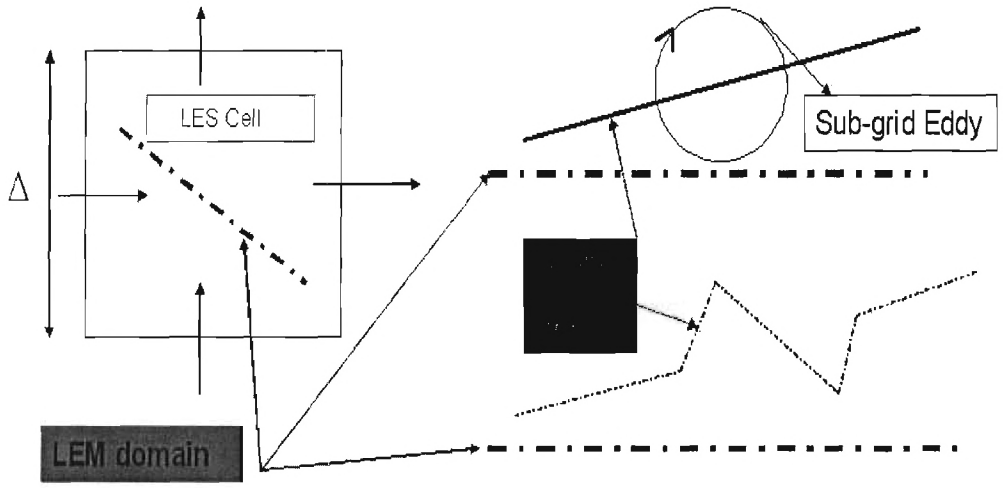

Figure 1: Illustration of LEM domain and mapping event (the arrows corresponds to mass flux advection across the LES boundaries).

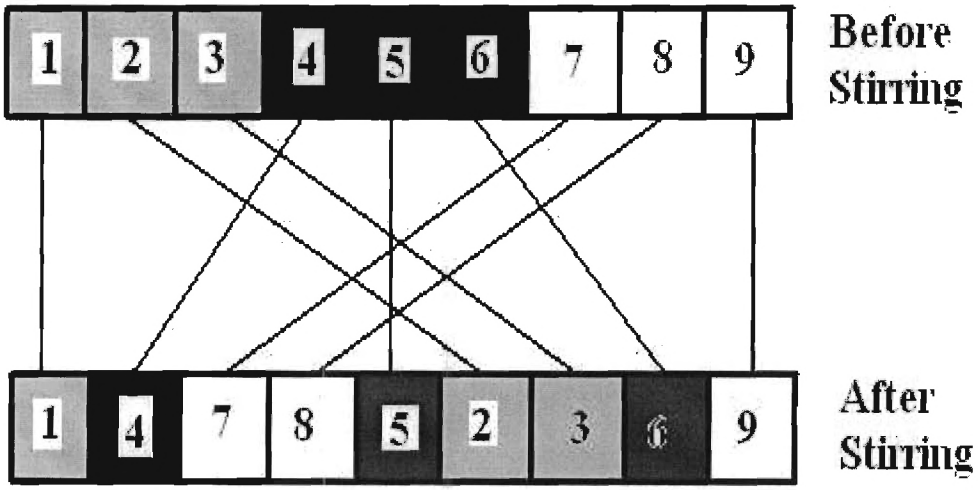

Figure 2: Effect of triplet mapping on the LEM domain.

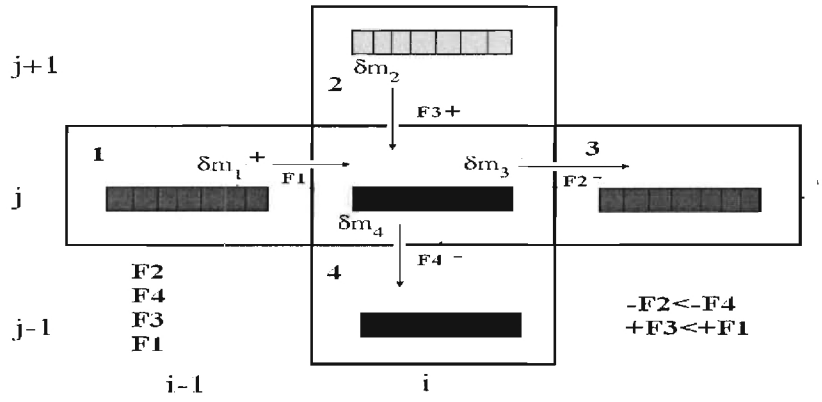

Figure 3: Before splicing, fluxes magnitude and direction is computed then arranged in an ascending order, F1, F2, F3, F4 are the transported mass fluxes and δm_i is the amount of LEM mass transported.

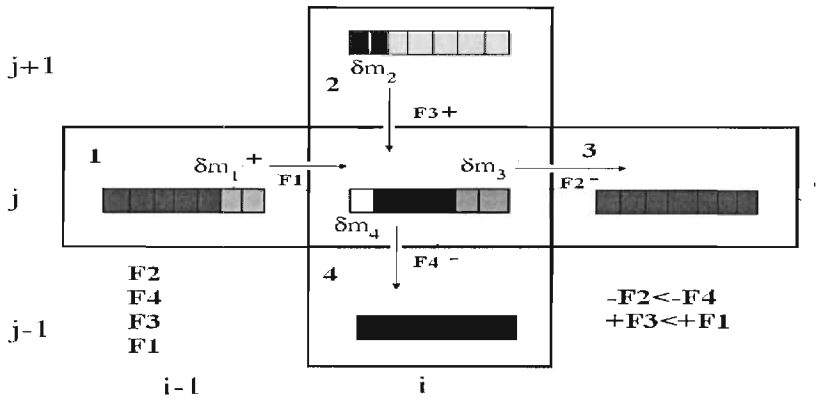

Figure 4: The equivelant LEM cells to the influx-outflux masses are computed.

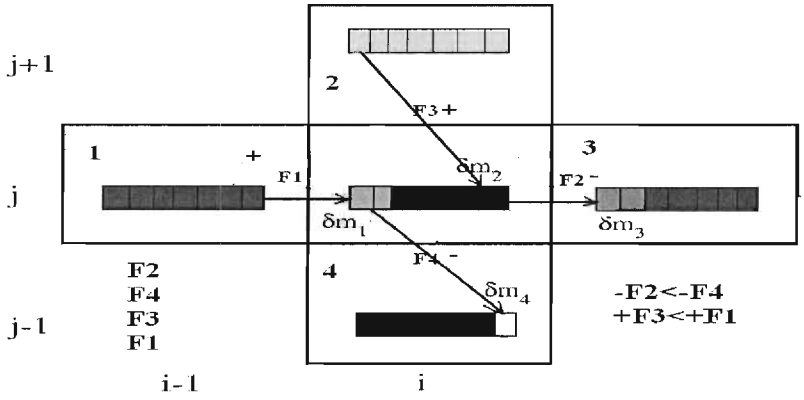

Figure 5: The LEM cells are spliced.

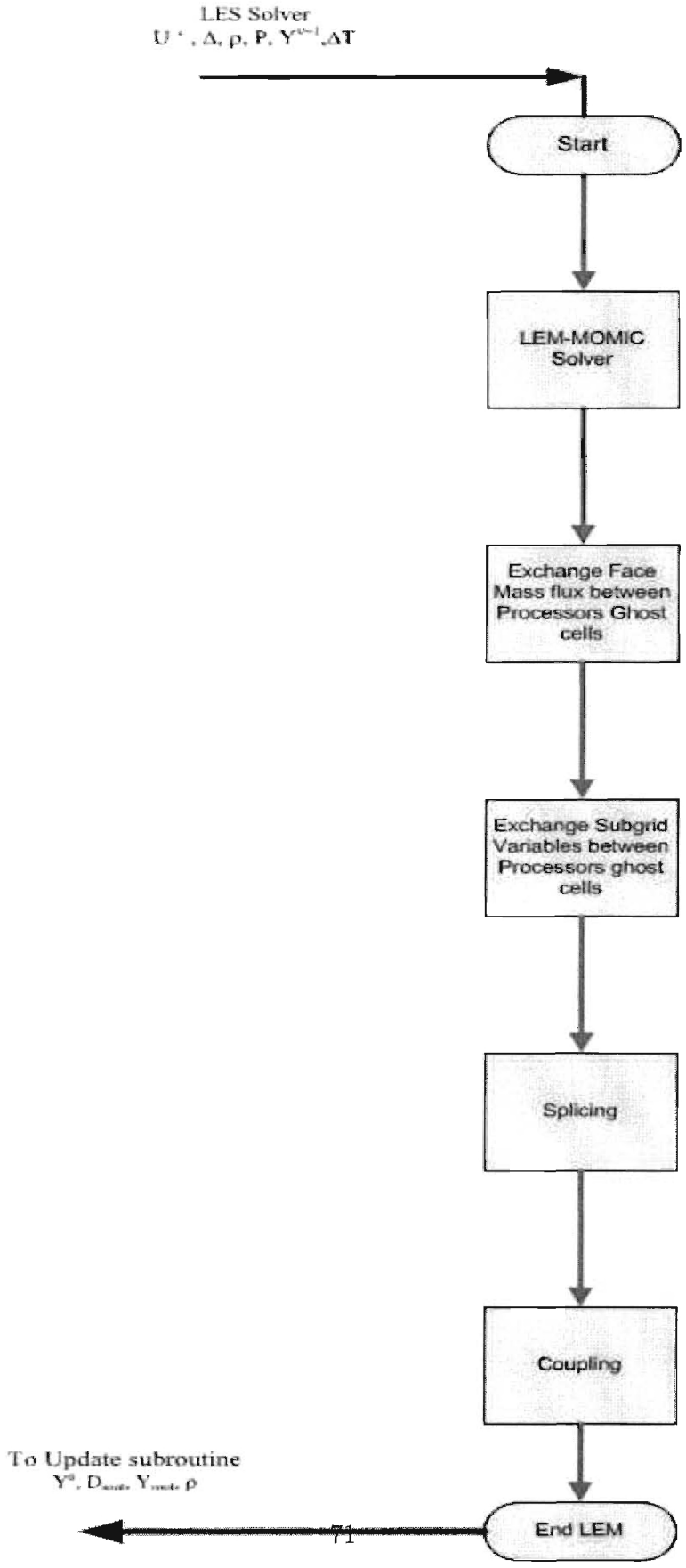

Figure 6: General flow chart for the LEM solver within LES

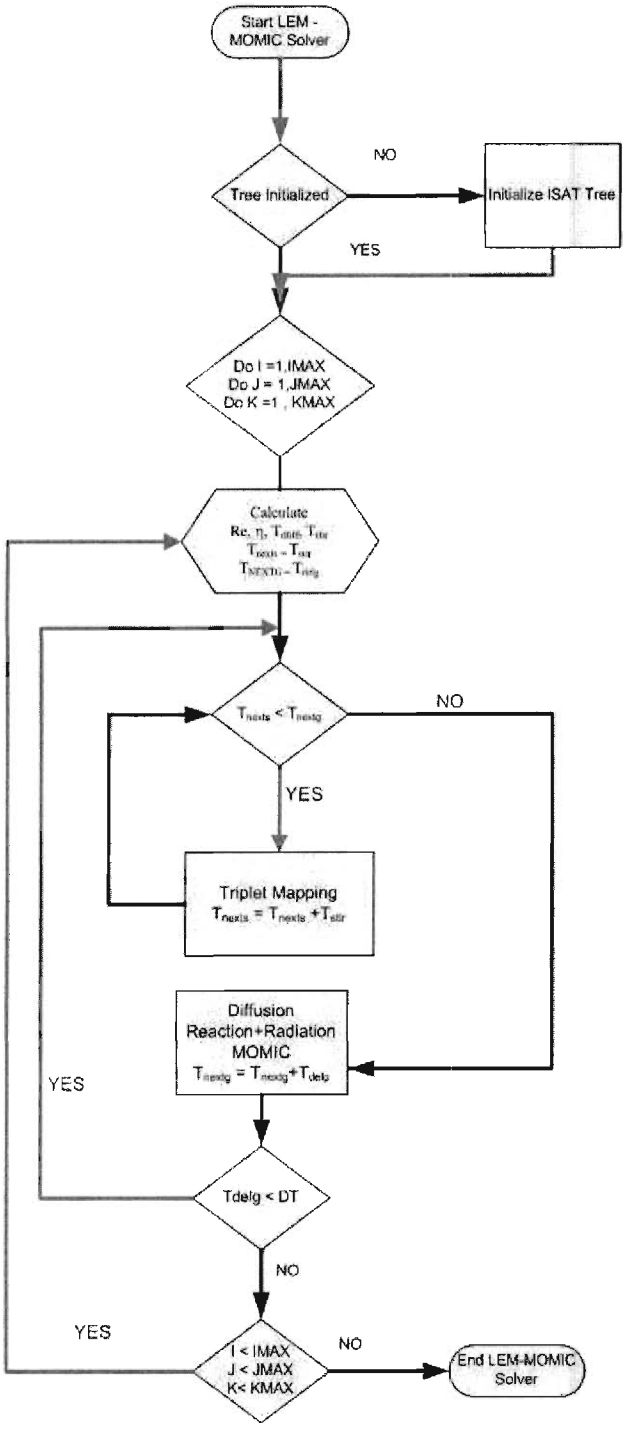

Figure 7: Flow chart for the LEM solver

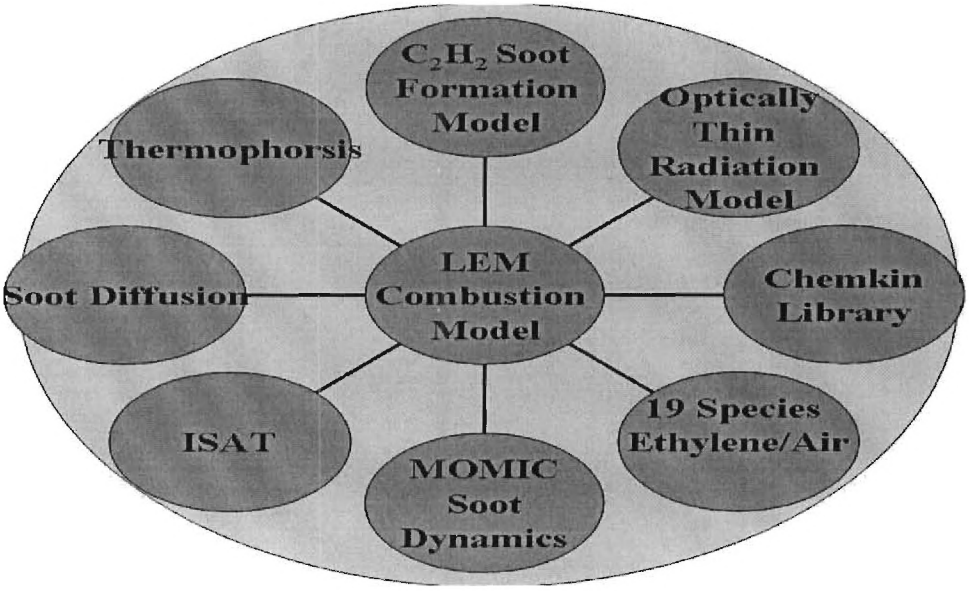

Figure 8: Schematic diagrams for the LEM-MOMIC soot model.

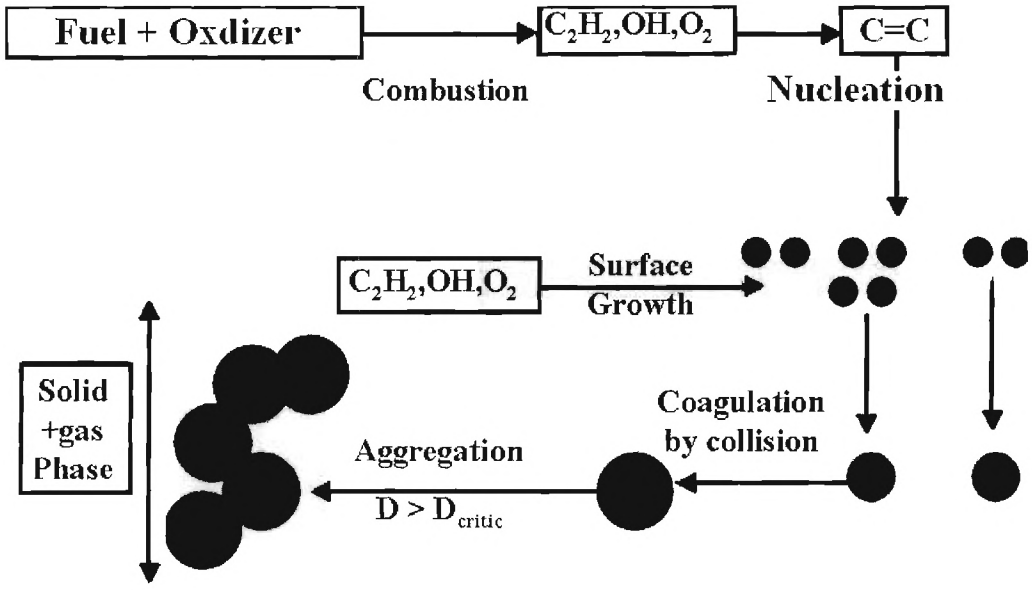

Figure 9: Schematic diagrams for the Soot formation and dynamic model.

6 Numerical Formulation and Implementation

In the previous section the LES equations were introduced, along with the closure of the momentum and energy equations. In this chapter the numerical implementation and scheme used to solve the governing equations are shown. Next we will introduce some numerical issues regarding the chemical time step and the type of gird used.

6.1 Conservative Form

The Navier Stokes equations in the strong conservative form are written as:

$$\frac{\partial}{\partial t}\left[Q\right] + \frac{\partial}{\partial x}\left[F_{IV} - F_V\right] + \frac{\partial}{\partial y}\left[G_{IV} - G_V\right] + \frac{\partial}{\partial z}\left[H_{IV} - H_V\right] = \Phi \tag{157}$$

Here, Q is the vector of conservative variables , F_{IV}, G_{IV}, and H_{IV} are the inviscid fluxes in the x y and z directions, respectively, while, F_V, G_V, and H_V are the viscous fluxes in the x y and z directions, respectively. The vector Q and the source term Φ are given as:

$$\mathbf{Q} = \begin{bmatrix} \rho \\ \rho U \\ \rho V \\ \rho W \\ \rho E \\ \rho Y_k \end{bmatrix} \quad \mathbf{\Phi} = \begin{bmatrix} 0 \\ 0 \\ 0 \\ 0 \\ 0 \\ \dot{\omega}_k \end{bmatrix} \tag{158}$$

The inviscid fluxes F_{IV}, G_{IV}, and H_{IV} are given as:

$$F_{IV} = \begin{bmatrix} \rho U \\ \rho UU + P \\ \rho VU \\ \rho WU \\ \rho \left(E + \frac{P}{\rho}] \right) U \\ \rho Y_k U \end{bmatrix}$$

$$G_{IV} = \begin{bmatrix} \rho V \\ \rho UV \\ \rho VV + P \\ \rho VW \\ \rho \left(E + \frac{P}{\rho} \right) V \\ \rho Y_k V \end{bmatrix} \tag{159}$$

$$H_{IV} = \begin{bmatrix} \rho W \\ \rho UW \\ \rho VW \\ \rho WW + P \\ \rho \left(E + \frac{P}{\rho} \right) W \\ \rho Y_k W \end{bmatrix}$$

And the viscous fluxes F_V, G_V, and H_V are given as:

$$
\begin{aligned}
F_V &= \begin{bmatrix} 0 \\ \tau_{xx} \\ \tau_{xy} \\ \tau_{xz} \\ (U\tau_{xx} + V\tau_{yx} + W\tau_{xz} + q_x)\, U \\ \rho Y_k V_{1,k} \end{bmatrix} \\
G_V &= \begin{bmatrix} 0 \\ \tau_{xy} \\ \tau_{yy} \\ \tau_{yz} \\ (U\tau_{xy} + V\tau_{yy} + W\tau_{yz} + q_y)\, U \\ \rho Y_k V_{2,k} \end{bmatrix} \\
H_V &= \begin{bmatrix} 0 \\ \tau_{xz} \\ \tau_{yz} \\ \tau_{zz} \\ (U\tau_{xz} + V\tau_{yz} + W\tau_{zz} + q_z)\, U \\ \rho Y_k V_{3,k} \end{bmatrix}
\end{aligned}
\tag{160}
$$

In the forgoing equations, U, V, and W are the velocity components in the x, y, and z directions, respectively. The diffusion velocity in the $i-th$ direction for the Y_k species is $V_{i,k}$ and the total energy per unit mass is E. The pressure P and the density ρ are related by the perfect gas equation of state as discussed in the previous chapter. Utilizing the symmetry, the shear stress tensor has nine components that can be represented as:

$$
\begin{aligned}
\tau_{xx} &= 2\mu\frac{\partial U}{\partial x} - \tfrac{2}{3}\mu\left(\frac{\partial U}{\partial x} + \frac{\partial V}{\partial y} + \frac{\partial W}{\partial z}\right) \\
\tau_{xy} = \tau_{yx} &= \mu\left(\frac{\partial U}{\partial y} + \frac{\partial V}{\partial x}\right) \\
\tau_{xz} = \tau_{zx} &= \mu\left(\frac{\partial U}{\partial z} + \frac{\partial W}{\partial x}\right) \\
\tau_{yy} &= 2\mu\frac{\partial V}{\partial y} - \tfrac{2}{3}\mu\left(\frac{\partial U}{\partial x} + \frac{\partial V}{\partial y} + \frac{\partial W}{\partial z}\right) \\
\tau_{zy} = \tau_{yz} &= \mu\left(\frac{\partial V}{\partial z} + \frac{\partial W}{\partial y}\right) \\
\tau_{zz} &= 2\mu\frac{\partial W}{\partial z} - \tfrac{2}{3}\mu\left(\frac{\partial U}{\partial x} + \frac{\partial V}{\partial y} + \frac{\partial W}{\partial z}\right)
\end{aligned}
\tag{161}
$$

The heat flux in the $i-th$ direction is q_i and is given by Eq. (30) in chapter II. The numerical implementation will be described in the following section.

6.2 Numerical Implementation

The above set of equations are nonlinear Partial Differential Equations (PDEs) that need to be solved numerically. The first major approximation is to approximate the continuum

nature of these PDEs into a discrete domain, called a mesh or a grid. This discrete domain solution tends to the continuum solution as the grid spacing goes to zero. Accordingly, the first step to solve the Navier Stokes equations is to specify the solution domain and the boundary conditions for such domain. Afterwards, this domain is discretized into a set of points or cells in which the governing equations are solved. Two types of grids exist, the structured grid, where the grid points are aligned on a Cartesian domain along the three axis and the unstructured grid, where the grid points are organized on specific shapes that do not coincide with specific coordinates. Here, we implement our code on a curvilinear structured grid, which simplifies the grid generation and the domain discretization greatly and conform smoothly with the boundaries.

However, the Cartesian grid can best describe rectangular or square domains, where there is no curvatures at the boundaries. Unfortunately, the real domains have nonuniform boundaries like nozzles, spherical domains and gas turbine blades. To solve this problem we can interpolate at the boundaries, which introduces a lot of numerical errors at sensitive places. The other choice is to convert the physical nonuniform space into a computational uniform one. This transformation, simply creates a new set of generalized coordinates that are function of the Cartesian physical coordinates but are body fitted. Figure 10 shows a two dimensional physical domain, where the boundaries are not aligned with the coordinates direction. In this case, the body fitted coordinate ζ is aligned along the body surface, η along the circumference directions and ξ is normal to the body plane. By transformation, the computational plane will look as in Fig. 11. Two types of grids are used in the current work, the curvilinear algebraic single domain grid for premixed flames applications and the butterfly two domain grid for the non-premixed cases. The later type of grid will be discussed in more details in the next section.

6.3 Butterfly Grid

The two domain grid or the butterfly grid is composed of an inner Cartesian grid around the centerline and an outer cylindrical grid surrounding it. The outer grid is shown in Fig. 12. Three locations at constant I,J,K are plotted together in the axial, radial and circumferential directions. A more detailed view of the inner Cartesian grid is shown in Fig. 13. This approach has two advantages with respect to regular one domain grids: first, it avoids the excessive mesh refinement at the centerline, which can restrict the computational time step greatly and degrade the computational efficiency. Second, it allows more flexibility for the processors distribution in parallel computation, where load balancing is important. As shown, the two grids are smooth and are designed such that on the LES level no special interpolation or treatment is needed to message pass the information between the processors. However, on the LEM domain some adjustments ([171]) have to be done to exchange the fluxes. As discussed in the last chapter, LEM splicing is done using the resolved mass fluxes at the cell face of the LES cell. These fluxes are computed as follows on the boundary between the two domains:

- First assume that the cylindrical grid has only 8 points in the circumferential direction ($i.e. Kmax_{cyl} = 8$. As mentioned before the first grid point is adjusted at one of the Cartesian domain corners.

- The four corners circumferential position of the Cartesian domain with respect to the cylindrical domain are specified as follows:

$$K1 = 1.0 * (Kmax_{cly} - 1)/8.0$$
$$K2 = 3.0 * (Kmax_{cly} - 1)/8.0$$
$$K3 = 5.0 * (Kmax_{cly} - 1)/8.0$$
$$K4 = 7.0 * (Kmax_{cly} - 1)/8.0$$

  Then for our example this corners will be k=1,3,5, and 7.

- At the ghost cells in the radial direction$(-1, -2, 0)$, which are inside the Cartesian domain the fluxes are equated as follows: If $K1 + 1 < k < K2$ then:

$$\begin{aligned} F_{j,cyl} &= F_{k,car} \\ F_{k,cyl} &= F_{j,car} \end{aligned} \tag{162}$$

  Where, $F_{j,cyl}$ is the flux in the j direction for the cylindrical grid and $F_{j,car}$ is the flux in the j direction for the Cartesian domain. Similar definition can be extracted for the i and k directions. If $K2 + 1 \leq k \leq K3$ then:

$$\begin{aligned} F_{j,cyl} &= F_{j,car} \\ F_{k,cyl} &= -F_{k,car} \end{aligned} \tag{163}$$

  If $K3 + 1 < k < K4$ then:

$$\begin{aligned} F_{j,cyl} &= -F_{k,car} \\ F_{k,cyl} &= -F_{j,car} \end{aligned} \tag{164}$$

  If $K4 + 1 < k < K1$ then:

$$\begin{aligned} F_{j,cyl} &= -F_{j,car} \\ F_{k,cyl} &= F_{k,car} \end{aligned} \tag{165}$$

  These fluxes and grid are shown in the schematic in Fig. 14.

The cylindrical domain is named domain I and the inner grid is domain II. In constructing the two domain grid the following points have to be considered:

- The transition between the two grids should be as smooth as possible to avoid any numerical oscillations between the two grids.

- First the inner Cartesian grid is constructed with the the axis z-y arranged as in Fig. 14. Then the cylindrical grid as $+ve$ z clockwise and $+ve$ y to the outward direction.

- The $Kmax_{car}$ value has to be chosen such that $(Kmax_{cyl} - 1)/8$ is an integer value. The relation between the two is:

$$Kmax_{cyl} = 4(Kmax_{car} - 1) + 1$$

  That ensures that both grids share the same ghost cells, for smooth communication. The $Kmax_{car}$ is an odd number with minimum value of 3.

- The point $j = 0$, $k = 0$ is the upper right corner of the Cartesian grid. For the outer grid $k = 0$ should be in the middle of the lower surface of the cartesian grid. Other arrangements may be possible, but this one is found to avoid any conflictions between the two grids.

6.4 Generalized Coordinates

The transformation process preserves the nature of the governing equations ([172]). The Navier stokes equations in its general form is a mixed parabolic elliptic PDE. The transformation process allows us to cluster the grid points at the places of high gradients, which it makes the application of the boundary conditions easier and more accurate.

The transformation process starts by expressing the generalized coordinates (τ, ζ, η, ξ) in terms of the cartesian coordinates (t, x, y, z) in time and space as:

$$\begin{aligned} \tau &= t \\ \zeta &= \zeta(t, x, y, z) \\ \eta &= \eta(t, x, y, z) \\ \xi &= \xi(t, x, y, z) \end{aligned} \tag{166}$$

By reversing the role of independence we get:

$$\begin{aligned} t &= \tau \\ x &= x(\tau, \zeta, \eta, \xi) \\ y &= y(\tau, \zeta, \eta, \xi) \\ z &= z(\tau, \zeta, \eta, \xi) \end{aligned} \tag{167}$$

Then, the derivatives in the physical domain are expressed in terms of the derivatives in the computational domain as:

$$\begin{aligned} \frac{\partial}{\partial t} &= \frac{\partial}{\partial \tau} \\ \frac{\partial}{\partial x} &= \zeta_x \frac{\partial}{\partial \zeta} + \eta_x \frac{\partial}{\partial \eta} + \xi_x \frac{\partial}{\partial \xi} \\ \frac{\partial}{\partial y} &= \zeta_y \frac{\partial}{\partial \zeta} + \eta_y \frac{\partial}{\partial \eta} + \xi_y \frac{\partial}{\partial \xi} \\ \frac{\partial}{\partial z} &= \zeta_z \frac{\partial}{\partial \zeta} + \eta_z \frac{\partial}{\partial \eta} + \xi_z \frac{\partial}{\partial \xi} \end{aligned} \tag{168}$$

In Eq. (168) the metrics (ζ_t, η_t, ξ_t, ζ_x, η_x, ξ_x, ζ_y, η_y, ξ_y, ζ_z, η_z, ξ_z) have to be determined. These metrics are function of the derivatives at the physical space and have to be determined numerically. In matrix form the relation between the derivatives at the physical and the computational domain can be expressed as:

$$\begin{bmatrix} dt \\ dx \\ dy \\ dz \end{bmatrix} = \begin{bmatrix} 1 & 0 & 0 & 0 \\ x_\tau & x_\zeta & x_\eta & x_\xi \\ y_\tau & y_\zeta & y_\eta & y_\xi \\ z_\tau & z_\zeta & z_\eta & z_\xi \end{bmatrix} \begin{bmatrix} d\tau \\ d\zeta \\ d\eta \\ d\xi \end{bmatrix} \tag{169}$$

By reversing the role of independence we get:

$$\begin{bmatrix} d\tau \\ d\zeta \\ d\eta \\ d\xi \end{bmatrix} = \begin{bmatrix} 1 & 0 & 0 & 0 \\ \zeta_t & \zeta_x & \zeta_y & \zeta_z \\ \eta_t & \eta_x & \eta_y & \eta_z \\ \xi_t & \xi_x & \xi_y & \xi_z \end{bmatrix} \begin{bmatrix} dt \\ dx \\ dy \\ dz \end{bmatrix} \tag{170}$$

Be speculating Eqs (169 and 170) we conclude that:

$$\begin{bmatrix} 1 & 0 & 0 & 0 \\ \zeta_t & \zeta_x & \zeta_y & \zeta_z \\ \eta_t & \eta_x & \eta_y & \eta_z \\ \xi_t & \xi_x & \xi_y & \xi_z \end{bmatrix} = \begin{bmatrix} 1 & 0 & 0 & 0 \\ x_\tau & x_\zeta & x_\eta & x_\xi \\ y_\tau & y_\zeta & y_\eta & y_\xi \\ z_\tau & z_\zeta & z_\eta & z_\xi \end{bmatrix}^{-1} \tag{171}$$

Based on the above identity, the metrics can be computed from:

$$\begin{aligned}
\zeta_x &= J\left(y_\eta z_\xi - y_\zeta z_\eta\right) \\
\zeta_y &= J\left(x_\xi z_\eta - x_\eta z_\xi\right) \\
\zeta_z &= J\left(x_\eta y_\xi - x_\xi y_\eta\right) \\
\eta_x &= J\left(y_\xi z_\zeta - y_\zeta z_\xi\right) \\
\eta_y &= J\left(x_\zeta z_\xi - x_\xi z_\zeta\right) \\
\eta_z &= J\left(x_\xi y_\zeta - x_\zeta y_\xi\right) \\
\xi_x &= J\left(y_\zeta z_\eta - y_\eta z_\zeta\right) \\
\xi_y &= J\left(x_\eta z_\xi - x_\zeta z_\eta\right) \\
\xi_z &= J\left(x_\zeta y_\eta - x_\eta y_\zeta\right) \\
\zeta_t &= -\left(x_t \zeta_x + y_\tau \zeta_y + z_\tau \zeta_z\right) \\
\eta_t &= -\left(x_t \eta_x + y_\tau \eta_y + z_\tau \eta_z\right) \\
\xi_t &= -\left(x_t \xi_x + y_\tau \xi_y + z_\tau \xi_z\right)
\end{aligned} \tag{172}$$

In Eq. (172) the terms x_η,x_ζ, x_ξ, y_η,y_ζ, y_ξ, z_η, z_ζ, z_ξ can be calculated easily by differencing locally in the generalized coordinates. The Jacobian J is defined by:

$$J = \frac{1}{x_\zeta\left(y_\eta z_\xi - y_\xi z_\eta\right) - x_\eta\left(y_\zeta z_\xi - y_\xi z_\zeta\right) + x_\xi\left(y_\zeta z_\eta - y_\zeta z_\eta\right)} \tag{173}$$

By applying the above definitions to Eq. (157) we finally get the generalized coordinate form as:

$$\begin{aligned}
&\frac{\partial}{\partial \tau}\left[\bar{Q}\right] + \frac{\partial}{\partial \zeta}\bar{F_{IV}} + \frac{\partial}{\partial \eta}\bar{G_{IV}} + \frac{\partial}{\partial \xi}\bar{H_{IV}} - \\
&\frac{\partial}{\partial \zeta}\bar{F_V} - \frac{\partial}{\partial \eta}\bar{G_V} - \frac{\partial}{\partial \xi}\bar{H_V} = \bar{\phi}
\end{aligned} \tag{174}$$

Where, the fluxes and the conservative variables are defined in the computational domain as:

$$\begin{aligned}
\bar{Q} &= \frac{Q}{J} \\
\bar{E_{IV}} &= \frac{1}{J}\left(\zeta_t Q + \zeta_x E_{IV} + \zeta_y E_{IV} + \zeta_z G_{IV}\right) \\
\bar{F_{IV}} &= \frac{1}{J}\left(\eta_t Q + \eta_x E_{IV} + \eta_y E_{IV} + \eta_z G_{IV}\right) \\
\bar{F_{IV}} &= \frac{1}{J}\left(\xi_t Q + \xi_x E_{IV} + \xi_y E_{IV} + \xi_z G_{IV}\right) \\
\bar{E_V} &= \frac{1}{J}\left(\zeta_t Q + \zeta_x E_V + \zeta_y E_V + \zeta_z G_V\right) \\
\bar{F_V} &= \frac{1}{J}\left(\eta_t Q + \eta_x E_V + \eta_y E_V + \eta_z G_V\right) \\
\bar{F_V} &= \frac{1}{J}\left(\xi_t Q + \xi_x E_V + \xi_y E_V + \xi_z G_V\right) \\
\bar{\phi} &= \phi
\end{aligned} \tag{175}$$

Expanding the above equations will give the final computational form of the Navier Stokes equations:

$$\bar{\mathbf{Q}} = \begin{bmatrix} \frac{\rho}{J} \\ \frac{\rho U}{J} \\ \frac{\rho V}{J} \\ \frac{\rho W}{J} \\ \frac{\rho E}{J} \\ \frac{\rho Y_k}{J} \end{bmatrix} \quad \bar{\mathbf{\Phi}} = \begin{bmatrix} 0 \\ 0 \\ 0 \\ 0 \\ 0 \\ \omega_k \end{bmatrix} \tag{176}$$

The inviscid fluxes $\bar{F_{IV}}$, $\bar{G_{IV}}$, and $\bar{H_{IV}}$ are given as:

$$
\begin{aligned}
\bar{F_{IV}} &= \frac{1}{J}\begin{bmatrix} \rho\tilde{U} \\ \rho\tilde{U}U + \zeta_x P \\ \rho\tilde{U}V + \zeta_y P \\ \rho\tilde{U}W + \zeta_z P \\ \rho\left(E + \frac{P}{\rho}\right)\tilde{U} \\ \rho Y_k \tilde{U} \end{bmatrix} \\
\bar{G_{IV}} &= \frac{1}{J}\begin{bmatrix} \rho\tilde{V} \\ \rho\tilde{V}U + \eta_x P \\ \rho\tilde{V}V + \eta_y P \\ \rho\tilde{V}W + \eta_z P \\ \rho\left(E + \frac{P}{\rho}\right)\tilde{V} \\ \rho Y_k \tilde{V} \end{bmatrix} \\
\bar{H_{IV}} &= \frac{1}{J}\begin{bmatrix} \rho\tilde{W} \\ \rho\tilde{W}U + \xi_x P \\ \rho\tilde{W}V + \xi_y P \\ \rho\tilde{W}W + \xi_z P \\ \rho\left(E + \frac{P}{\rho}\right)\tilde{W} \\ \rho Y_k \tilde{W} \end{bmatrix}
\end{aligned}
\tag{177}
$$

While the viscous fluxes $\bar{F_V}$, $\bar{G_V}$, and $\bar{H_V}$ are given as:

$$\bar{F_V} = \frac{1}{J}\begin{bmatrix} 0 \\ \zeta_x\tau_{xx} + \zeta_y\tau_{xy} + \zeta_z\tau_{xz} \\ \zeta_x\tau_{yx} + \zeta_y\tau_{yy} + \zeta_z\tau_{yz} \\ \zeta_x\tau_{zx} + \zeta_y\tau_{zy} + \zeta_z\tau_{zz} \\ (U_j\tau_{ij} - q_i)\,\zeta_i \\ \zeta_x\left(\rho Y_k V_{1,k}\right) + \zeta_y\left(\rho Y_k V_{2,k}\right) + \zeta_z\left(\rho Y_k V_{3,k}\right) \end{bmatrix}$$

$$\bar{G_V} = \frac{1}{J}\begin{bmatrix} 0 \\ \eta_x\tau_{xx} + \eta_y\tau_{xy} + \eta_z\tau_{xz} \\ \eta_x\tau_{yx} + \eta_y\tau_{yy} + \eta_z\tau_{yz} \\ \eta_x\tau_{zx} + \eta_y\tau_{zy} + \eta_z\tau_{zz} \\ (U_j\tau_{ij} - q_i)\,\eta_i \\ \eta_x\left(\rho Y_k V_{1,k}\right) + \eta_y\left(\rho Y_k V_{2,k}\right) + \eta_z\left(\rho Y_k V_{3,k}\right) \end{bmatrix} \tag{178}$$

$$\bar{H_V} = \frac{1}{J}\begin{bmatrix} 0 \\ \xi_x\tau_{xx} + \xi_y\tau_{xy} + \xi_z\tau_{xz} \\ \xi_x\tau_{yx} + \xi_y\tau_{yy} + \xi_z\tau_{yz} \\ \xi_x\tau_{zx} + \xi_y\tau_{zy} + \xi_z\tau_{zz} \\ (U_j\tau_{ij} - q_i)\,\xi_i \\ \xi_x\left(\rho Y_k V_{1,k}\right) + \xi_y\left(\rho Y_k V_{2,k}\right) + \xi_z\left(\rho Y_k V_{3,k}\right) \end{bmatrix}$$

Where the contravarient velocities are defined as:

$$\begin{aligned} \tilde{U} &= \zeta_x U + \zeta_y V + \zeta_z W \\ \tilde{V} &= \eta_x U + \eta_y V + \eta_z W \\ \tilde{W} &= \xi_x U + \xi_y V + \xi_z W \end{aligned} \tag{179}$$

The energy fluxes in Eq. (178) are expanded as follows:

$$\begin{aligned} &(U_j\tau_{ij} - q_i)\,\zeta_i = \zeta_x\left(U\tau_{xx} + V\tau_{xy} + W\tau_{xz} - q_x\right) + \zeta_y\left(U\tau_{yx} + V\tau_{yy} + W\tau_{yz} - q_y\right) + \\ &\zeta_z\left(U\tau_{zx} + V\tau_{zy} + W\tau_{zz} - q_z\right) \\ &(U_j\tau_{ij} - q_i)\,\eta_i = \eta_x\left(U\tau_{xx} + V\tau_{xy} + W\tau_{xz} - q_x\right) + \eta_y\left(U\tau_{yx} + V\tau_{yy} + W\tau_{yz} - q_y\right) + \\ &\eta_z\left(U\tau_{zx} + V\tau_{zy} + W\tau_{zz} - q_z\right) \\ &(U_j\tau_{ij} - q_i)\,\eta_i = \xi_x\left(U\tau_{xx} + V\tau_{xy} + W\tau_{xz} - q_x\right) + \xi_y\left(U\tau_{yx} + V\tau_{yy} + W\tau_{yz} - q_y\right) + \\ &\xi_z\left(U\tau_{zx} + V\tau_{zy} + W\tau_{zz} - q_z\right) \end{aligned} \tag{180}$$

The heat fluxes are given by:

$$\begin{aligned} q_x &= -\kappa\left[\zeta_x\frac{\partial T}{\partial\zeta} + \eta_x\frac{\partial T}{\partial\eta} + \xi_x\frac{\partial T}{\partial\xi}\right] \\ q_y &= -\kappa\left[\zeta_y\frac{\partial T}{\partial\zeta} + \eta_y\frac{\partial T}{\partial\eta} + \xi_y\frac{\partial T}{\partial\xi}\right] \\ q_z &= -\kappa\left[\zeta_z\frac{\partial T}{\partial\zeta} + \eta_z\frac{\partial T}{\partial\eta} + \xi_z\frac{\partial T}{\partial\xi}\right] \end{aligned} \tag{181}$$

Finally, the species diffusivity fluxes are expressed as:

$$\begin{aligned} V_{1,k} &= -\frac{D_k}{Y_k}\left[\zeta_x \frac{\partial Y_k}{\partial \zeta} + \eta_x \frac{\partial Y_k}{\partial \eta} + \xi_x \frac{\partial Y_k}{\partial \xi}\right] \\ V_{2,k} &= -\frac{D_k}{Y_k}\left[\zeta_y \frac{\partial Y_k}{\partial \zeta} + \eta_y \frac{\partial Y_k}{\partial \eta} + \xi_y \frac{\partial Y_k}{\partial \xi}\right] \\ V_{3,k} &= -\frac{D_k}{Y_k}\left[\zeta_z \frac{\partial Y_k}{\partial \zeta} + \eta_z \frac{\partial Y_k}{\partial \eta} + \xi_z \frac{\partial Y_k}{\partial \xi}\right] \end{aligned} \tag{182}$$

6.5 Numerical Formulation

As mentioned earlier, the governing equations are discretized over a selected domain, over which the boundary conditions are identified. the main approach usually used for discretization ([115]) is the finite difference method. In the finite difference approach, the derivatives are approximated by algebraic equations, which have to be solved only at the discrete grid points. Usually, the Taylor series expansion is used to drive the finite difference equations. The resulting set of algebraic equations involve a truncation error (T.E.), which is the numerical difference between the exact PDE and the resulting algebraic equation. The higher the order of the T.E. (smaller value), the more exact the finite difference approximation will be, and the more computational effort (mathematical operations) will be needed. However, this rule is not general for all schemes. For very coarse grids, it will be useless to use a higher order scheme, since the order of magnitude is defined as the grid size approaches zero. Generally, the error source in the resulting finite difference expression (FDE) can arise from:

(a) The truncation error (T.E) as discussed above.

(b) Since the resulting solution is stored in memory locations in the computer, these memory locations have limited number of digits to be stored. Hence usually very small or very large numbers are rounded to the machine limits. This round-off error sometimes can be significant, when the problem involves numbers of extremely large or small magnitudes. In addition, the accumulation of these errors with time has an effect too. The round-off error increases with the mesh size, while the T.E decreases as the grid is more refined.

(c) Expressing the continuum equations on a discretized domain, leads to an error known as the discretization error, which is the difference of the final solution between the PDE and FDE expression. This type of error can be regarded as a sum of the other known errors.

(d) Numerical errors also may rise due to inaccurate presentation of the boundary conditions (BC) or the initial conditions (IC). This type of error is not represented in some numerical approaches as will be discussed later.

The known methods to drive the derivatives expressions are Taylor expansion, polynomial fitting, integral methods and finite volume approach. However, these methods can be classified as either conservative or non-conservative Finite Difference Expression (FDE). The conservative schemes are those which maintain the applicability of the conservation laws even after the discretization processes. These schemes eliminate most of the above errors,

except for the round-off error. The finite volume approach in one of the forgoing mentioned schemes.

In the finite-volume method the conservation laws are applied to a finite control volume in space. Hence, all the conservation properties are maintained exactly at the final FDE form, like mass, momentum and energy conservation across the selected control volume boundaries.

6.6 The Finite Volume Approach

In the finite-volume approach the domain is divided into a set of control volumes (cells) rather than single grid points. The grid point can be considered to be set at the cell center in cell-centered scheme. The control volumes are set to match the boundaries exactly. By recasting the governing equations in the divergent form we get:

$$\frac{\partial \vec{\bar{Q}}}{\partial t} + \vec{\nabla} \cdot \vec{\psi} = \vec{\bar{\Phi}} \tag{183}$$

Here, Q, $\vec{\psi}$, and $\vec{\phi}$ are the conservative variables, the fluxes and the source term vectors, respectively. The above divergent formulation represents the strong conservative form. The flux vector is defined as:

$$\vec{\psi} = \left(\bar{F_V} - \bar{F_{IV}}\right)\vec{i} + \left(\bar{G_V} - \bar{G_{IV}}\right)\vec{j} + \left(\bar{H_V} - \bar{H_{IV}}\right)\vec{k} \tag{184}$$

where, i, j, and k are the unit vectors in the three orthogonal coordinates and F, G, H are given by Eqs, (177 and 178). By volumetric integration over a control volume V for Eq. (183):

$$\int\int\int_V \frac{\partial \vec{Q}}{\partial t} dV + \int\int\int_V \vec{\nabla} \cdot \vec{\psi} dV = \int\int\int_V \vec{\Phi} dV \tag{185}$$

Now recalling green theorem (divergence theorem) that states:

$$\int\int\int_V \left(\vec{\nabla} \cdot \vec{\psi}\right) dV = \int\int_A \vec{\psi} \cdot d\vec{A} \tag{186}$$

Here, A is the control volume surface area. hence, Eq. (185) can be written as:

$$\int\int\int_V \frac{\partial \vec{Q}}{\partial t} dV + \int\int_A \vec{\psi} \cdot dA = \int\int\int_V \vec{\Phi} dV \tag{187}$$

For a general arbitrary cell with volume dV and center $(i,\ j,\ k)$ the integral of the flux over the six cell faces can be written as:

$$\begin{aligned} \frac{\partial \vec{\bar{Q}}}{\partial t} dV \ + \ & \left(\vec{\psi} \cdot \hat{n} dA\right)_{i+1/2,j,k} + \left(\vec{\psi} \cdot \hat{n} dA\right)_{i-1/2,j,k} + \\ & \left(\vec{\psi} \cdot \hat{n} dA\right)_{i,j+1/2,k} + \left(\vec{\psi} \cdot \hat{n} dA\right)_{i,j-1/2,k} + \\ & \left(\vec{\psi} \cdot \hat{n} dA\right)_{i,j,k+1/2} + \left(\vec{\psi} \cdot \hat{n} dA\right)_{i,j,k-1/2} = \bar{\Phi} dV \end{aligned} \tag{188}$$

Where the unit normal to the cell control volume surface is denoted as $\hat{n}$. For instance, in the ζ direction for the face defined by $(i+1/2, j, k)$, $\hat{n}$ will be defined as:

$$\hat{n} = \frac{\nabla\zeta}{|\nabla\zeta|} = \frac{\zeta_x i + \zeta_y j + \zeta_z k}{|\nabla\zeta|} \tag{189}$$

The only term needed, to be able to compute Eq. (188) numerically, is the surface area of each cell face dA. For a cell face $ABCD$ shown in the arbitrary cell in Fig. (15), the surface area will:

$$dA = \frac{1}{2}|\left(\vec{r}_{AC} X \vec{r}_{BD}\right) + \left(\vec{r}_{BC} X \vec{r}_{CD}\right)| \tag{190}$$

Where, $\vec{r}_{AC} = \vec{r}_A - \vec{r}_C$. By expanding and use vector product relationships, we finally get:

$$dA = \frac{|\nabla\zeta|}{J} \tag{191}$$

And the flux on the face $(i+1/2, j, k)$ will be expressed as:

$$\begin{array}{l} \psi'_{i+1/2,j,k} = \left(\vec{\psi}\cdot\hat{n}dA\right)_{i+1/2,j,k} = \\ \frac{1}{J}\left[\left(\bar{F_{IV}} - \bar{F_V}\right)\zeta_x + \left(\bar{G_{IV}} - \bar{G_V}\right)\zeta_y + \left(\bar{H_{IV}} - \bar{H_V}\right)\zeta_z\right]_{i+1/2,j,k} \end{array} \tag{192}$$

By similar analysis for the fluxes on the other cell faces we finally get the finite volume representation for the governing equations as:

$$\begin{array}{l} \frac{\partial\vec{Q}}{\partial t}dV_{i,j,k} + \left(\psi'_{i+1/2,j,k} - \psi'_{i-1/2,j,k}\right) + \left(\psi'_{i,j+1/2,k} - \psi'_{i,j-1/2,k}\right) + \\ \left(\psi'_{i,j,k+1/2} - \psi'_{i,j,k-1/2}\right) = \phi dV_{i,j,k} \end{array} \tag{193}$$

In the above formulation the area factor is implicitly represented as in Eq. (192) and the negative sign is for the cell faces in the negative coordinates direction.

6.7 Numerical Scheme

Generally, there are three types of numerical schemes, explicit methods, implicit methods and hybrid schemes. The explicit methods are easier in implementation , but less stable and require a small integration time step to avoid growth of numerical errors. Implicit methods, are more stable and can withstand a larger time step than the explicit techniques but are more complicated from the implementation point of view. The hybrid method use a mix between the implicit and the explicit numerical schemes. In the explicit methods the derivatives at the current time step are expressed as a function of the previous known data at the previous step, while in the implicit methods the derivatives are expressed in term of the current step unknown values and a set of equations are solved together to find the final values at the current index. Although, the explicit schemes are less stable and require smaller integration time step, it is used to be an excellent candidate for reactive flow problems, where the integration is limited by the small chemical time step anyway. In addition, the explicit schemes are simpler and require less computational time per step.

6.7.1 MacCormak Scheme

The integration scheme chosen here is the MacCormak explicit method. We will discuss here the formulation and the pros and cons of the method. MacCormak first introduced his predictor corrector method in 1969 as one of the most famous and known schemes. The method uses a predictor step that is discretized using either (backward or forward) differencing followed by another corrector step that will be in the reverse order of the predictor step. The idea is to eliminate the bias due to one sided first order differencing to end up with a second order scheme in time and space ([173]). So, the equation first are integrated to an intermediate time step to yield a predicted value for the dependent variables, then the order is reversed and a corrector value is computed. These type of schemes are also known as multi-step or time split methods. Now by rewriting Eq. (193):

$$\begin{aligned}&\frac{\partial \bar{Q}_{i,j,k}}{\partial t} dV_{i,j,k} + \left(\vec{\psi}\cdot\hat{n}dA\right)_{(i+1/2,j,k)} - \left(\vec{\psi}\cdot\hat{n}dA\right)_{(i-1/2,j,k)} + \left(\vec{\psi}\cdot\hat{n}dA\right)_{(i,j+1/2,k)} \\ &- \left(\vec{\psi}\cdot\hat{n}dA\right)_{(i,j-1/2,k)} + \left(\vec{\psi}\cdot\hat{n}dA\right)_{(i,j,k+1/2)} - \left(\vec{\psi}\cdot\hat{n}dA\right)_{(i,j,k-1/2)} = \phi dV_{i,j,k}\end{aligned} \tag{194}$$

we observe from the above equation that the flux values ψ at the cell faces are needed. However, the finite volume formulation only provides the cell centers value (i,j,k). Many methods can be used to solve this problem. [174] used a fourth order interpolation between the cell. If we denote the forward interpolation by the superscript + and the backward by − then the fluxes according to Nelson scheme is given by (we will drop the $^-$and $'$ sign from now on):

$$\begin{aligned}\vec{\psi}^{+}_{i+1/2,j,k} &= \tfrac{1}{6}\left(2\vec{\psi}_i + 5\vec{\psi}_{i+1} - \vec{\psi}_{i+2}\right) \\ \vec{\psi}^{-}_{i+1/2,j,k} &= \tfrac{1}{6}\left(-\vec{\psi}_{i-1} + 5\vec{\psi}_i + 2\vec{\psi}_{i+1}\right)\end{aligned} \tag{195}$$

Although more accurate, this $4-th$ order scheme is less stable and requires the time step to be 50% less than the required second order step. Here, simple extrapolation from the cell centers are used for fluxes at the cell face:

$$\begin{aligned}\vec{\psi}^{+}_{i+1/2,j,k} &= \vec{\psi}_{i+1,j,k} \\ \vec{\psi}^{-}_{i+1/2,j,k} &= \vec{\psi}_{i,j,k} \\ \vec{\psi}^{+}_{i,j+1/2,k} &= \vec{\psi}_{i,j+1,k} \\ \vec{\psi}^{-}_{i,j+1/2,k} &= \vec{\psi}_{i,j,k} \\ \vec{\psi}^{+}_{i,j,k+1/2} &= \vec{\psi}_{i,j,k+1} \\ \vec{\psi}^{-}_{i,j,k+1/2} &= \vec{\psi}_{i,j,k} \\ \vec{\psi}^{+}_{i-1/2,j,k} &= \vec{\psi}_{i,j,k} \\ \vec{\psi}^{-}_{i-1/2,j,k} &= \vec{\psi}_{i-1,j,k} \\ \vec{\psi}^{+}_{i,j-1/2,k} &= \vec{\psi}_{i,j,k} \\ \vec{\psi}^{-}_{i,j-1/2,k} &= \vec{\psi}_{i,j-1,k} \\ \vec{\psi}^{+}_{i,j,k-1/2} &= \vec{\psi}_{i,j,k} \\ \vec{\psi}^{-}_{i,j,k-1/2} &= \vec{\psi}_{i,j,k-1}\end{aligned} \tag{196}$$

Recalling, Eq. (184) and collecting the viscous and unviscid fluxes together as:

$$\begin{aligned}\vec{F} &= \left(\vec{F}_{IV} - \vec{F}_V\right) \\ \vec{G} &= \left(\vec{G}_{IV} - \vec{G}_V\right) \\ \vec{H} &= \left(\vec{H}_{IV} - \vec{H}_V\right)\end{aligned} \tag{197}$$

Using Eq. (196), the forward (+) predictor step can be written as:

$$\begin{aligned}&\vec{Q}^*_{i,j,k} = \vec{Q}^n_{i,j,k} - \\ &\tfrac{\Delta t}{\Delta V_{i,j,k}}\left[\left(\vec{F}^n_{i+1} - \vec{F}^n_i\right)\tfrac{\zeta_x}{J} + \left(\vec{G}^n_{i+1} - \vec{G}^n_i\right)\tfrac{\zeta_y}{J} + \left(\vec{H}^n_{i+1} - \vec{H}^n_i\right)\tfrac{\zeta_z}{J}\right] - \\ &\tfrac{\Delta t}{\Delta V_{i,j,k}}\left[\left(\vec{F}^n_{j+1} - \vec{F}^n_j\right)\tfrac{\eta_x}{J} + \left(\vec{G}^n_{j+1} - \vec{G}^n_j\right)\tfrac{\eta_y}{J} + \left(\vec{H}^n_{j+1} - \vec{H}^n_j\right)\tfrac{\eta_z}{J}\right] - \\ &\tfrac{\Delta t}{\Delta V_{i,j,k}}\left[\left(\vec{F}^n_{k+1} - \vec{F}^n_k\right)\tfrac{\xi_x}{J} + \left(\vec{G}^n_{k+1} - \vec{G}^n_k\right)\tfrac{\xi_y}{J} + \left(\vec{H}^n_{k+1} - \vec{H}^n_k\right)\tfrac{\xi_z}{J}\right]\end{aligned} \tag{198}$$

Where the $*$ sign indicates the predictor value for the dependent variables, and n is the value at the last time step. The backward corrector step then can be written as:

$$\begin{aligned}&\vec{Q}^{n-1}_{i,j,k} = \tfrac{1}{2}\left(\vec{Q}^n_{i,j,k} + \vec{Q}^*_{i,j,k}\right) + \\ &-\tfrac{\Delta t}{2\Delta V_{i,j,k}}\left[\left(\vec{F}^n_i - \vec{F}^n_{i-1}\right)\tfrac{\zeta_x}{J} + \left(\vec{G}^n_i - \vec{G}^n_{i-1}\right)\tfrac{\zeta_y}{J} + \left(\vec{H}^n_i - \vec{H}^n_{i-1}\right)\tfrac{\zeta_z}{J}\right] - \\ &\tfrac{\Delta t}{2\Delta V_{i,j,k}}\left[\left(\vec{F}^n_j - \vec{F}^n_{j-1}\right)\tfrac{\eta_x}{J} + \left(\vec{G}^n_j - \vec{G}^n_{j-1}\right)\tfrac{\eta_y}{J} + \left(\vec{H}^n_j - \vec{H}^n_{j-1}\right)\tfrac{\eta_z}{J}\right] - \\ &\tfrac{\Delta t}{2\Delta V_{i,j,k}}\left[\left(\vec{F}^n_k - \vec{F}^n_{k-1}\right)\tfrac{\xi_x}{J} + \left(\vec{G}^n_k - \vec{G}^n_{k-1}\right)\tfrac{\xi_y}{J} + \left(\vec{H}^n_k - \vec{H}^n_{k-1}\right)\tfrac{\xi_z}{J} +\right]\end{aligned} \tag{199}$$

Choosing the forward-backward sequence for the corrector predictor method, can affect greatly the one-sided differencing bias. One method to avoid this ([175]) is to compute the flux derivatives in a certain way. The rule is that the derivatives inside the flux have to be computed in the opposite direction if in the same direction and central if it is in the cross directions. For instance, let us focus on the flux F in the i direction $\vec{F}$. In the predictor step this flux is forward differenced in the $i-th$ direction. Recalling that this flux vectors is equal to:

$$\vec{F} = \tfrac{1}{J}\begin{bmatrix} \rho\tilde{U} & & \\ \left(\rho\tilde{U}U + \zeta_x P\right) & - & \left(\zeta_x\tau_{xx} + \zeta_y\tau_{xy} + \zeta_z\tau_{xz}\right) \\ \left(\rho\tilde{U}V + \zeta_y P\right) & - & \left(\zeta_x\tau_{yx} + \zeta_y\tau_{yy} + \zeta_z\tau_{yz}\right) \\ \left(\rho\tilde{U}W + \zeta_z P\right) & - & \left(\zeta_x\tau_{zx} + \zeta_y\tau_{zy} + \zeta_z\tau_{zz}\right) \\ \left(\rho\left(\rho E + P\right)\tilde{U}\right) & - & \left(\left(U_j\tau_{ij} - q_i\right)\zeta_i\right) \\ \left(\rho Y_k\tilde{U}\right) & - & \left(\zeta_x\left(\rho Y_k V_{1,k}\right) + \zeta_y\left(\rho Y_k V_{2,k}\right) + \zeta_z\left(\rho Y_k V_{3,k}\right)\right) \end{bmatrix} \tag{200}$$

where the shear stress in the $i-th$ direction is expressed as :

$$\tau_{xx} = \tau_{xx} = 2\mu\frac{\partial U}{\partial x} - \frac{2}{3}\mu\left(\frac{\partial U}{\partial x} + \frac{\partial V}{\partial y} + \frac{\partial W}{\partial z}\right) \tag{201}$$

The derivatives in the $i-th$ direction will be expressed as:

$$\frac{\partial U}{\partial x} = \frac{\left(U_{i,j,k} - U_{i-1,j,k}\right)}{\Delta x} \tag{202}$$

While the cross stream derivatives are computed as:

$$\begin{aligned} \frac{\partial V}{\partial y} &= \frac{\left(V_{i,j+1,k} - V_{i,j-1,k}\right)}{2\Delta y} \\ \frac{\partial W}{\partial z} &= \frac{\left(W_{i,j,k+1} - W_{i,j,k-1}\right)}{2\Delta z} \end{aligned} \tag{203}$$

All other derivatives will be done in a similar fashion to the above set of equations.

For completeness, a brief description of how the code computes the fluxes by the MacCormak's scheme is presented in Appendix A.

6.7.2 Characteristic Boundary Conditions

Partial differential equations (PDE) are classified according to the behavior of the characteristic curves. The characteristic curves originally represents the various possible solutions of the PDE. For instant, let us consider the general solution for the PDE is given by $\phi(x, y)$, this represents a surface in space that may vary with time. The curves that constitute this space are the characteristic curves. There are three main types of PDEs. Elliptic, hyperbolic and parabolic. In hyperbolic PDEs the characteristics are all real and the problem is essentially an initial value problem. In the elliptic case the characteristics are imaginary and propagate in all directions and the problem will be a boundary value problem. A classical method for solving the hyperbolic equations is the method of characteristics. Along the characteristic lines, the PDE is reduced to an ODE, which can easily be integrated to obtain the desired solution.

Generally, there are four types of boundary conditions:

- Dirichlet boundary condition. If the dependent variables along the boundary is specified.
- Neumann boundary condition. If the normal gradient of the dependent variable along the boundary is specified.
- Robin boundary condition. If the imposed boundary conditions are a linear combination of Neumann and Dirichlet types.
- Mixed boundary condition. If along the boundary the conditions are Dirichlet at a portion and Neumann at another.

For a n dimensional vector $\vec{Q}(\vec{X}, t)$ in volume V, the general behavior of Q is described by the governing equations, the initial conditions and the boundary conditions. The boundary conditions can be defined as the information needed to completely specify $\frac{\partial Q}{\partial t}$, and which cannot be obtained from information inside the computational domain. For hyperbolic systems, as the system of Euler equations, the number of boundary conditions required at a given point on the boundary ranges from 0 up to the number of independent variables and may vary with time and position as the solution evolves. If the boundary conditions

are determined by specifying the derivative value only and not the value itself, then by this way the time integration of the main equations is decoupled from the boundaries behavior. For example, the initialization of the velocity at the wall is set to zero and the boundary conditions set the derivative with time to zero.

Following [176, 177], the main idea here is to convert the hyperbolic equations into wave modes or equations that propagates at a definite characteristic velocity, and to treat the Navier Stokes equations, which are mixed elliptic hyperbolic as a pure hyperbolic system. The characteristic velocities usually are functions of local space and time and represent the solutions of an eigenvalue problem ([176]). By diagonalizing the line coordinate direction with time, a multidimensional boundary problem can be treated more easily as one-dimensional. In addition, along a certain direction the derivatives in the other directions can be lumped in one constant. The eigenvalues can be determined using the following equation $|(A^k - \lambda I)|$, where, $A^k = P^{-1}Q^k$ and P is the transformation matrix between the conservative and the primitive variables while Q^k is the transformation matrix between the flux and the solution vector in the k direction.

The boundary conditions used here are the Navier Stokes Characteristic Boundary Conditions (NSCBC) introduced by [176]. For well posedness two types of boundary conditions must be specified at each boundary based on the local flow conditions. The physical boundary conditions that are specified from outside the computational domain and the numerical boundary conditions that takes information from the inside of the computational domain. From the approximations of the NSCBC that the treatment of the ingoing and outgoing way is approximated by an inviscid like boundary conditions. Therefore, the waves associated with diffusion processes are neglected. The one sided differencing of the equations at the boundaries using an upwind scheme does not affect the whole central scheme order. Although, the Navier Stokes equation are mixed parabolic-hyperbolic, the NSCBC assumes that these equations behave in a hyperbolic way most of the time. The characteristic velocities at the boundaries are given as;

$$\begin{aligned} \lambda_1 &= u_i - a \\ \lambda_2 &= u_i \\ \lambda_3 &= u_i \\ \lambda_4 &= u_i \\ \lambda_5 &= u_i + a \end{aligned} \tag{204}$$

Where, a is the acoustic propagation speed, u_i is the flow velocity in the $i-th$ direction, (λ_1 and λ_5) are the sound wave propagation velocities in the $i-th$ direction, λ_2 is the convective velocity at which the entropy waves will travel in the $i-th$ direction, and (λ_3 and λ_4) are the velocities at which the cross stream waves (both sound and entropy) will propagate in the $i-th$ direction. If the flow is supersonic (i.e $a \leq u$), then all the characteristic waves velocities are travelling with the mean mean velocity direction and wave is propagating from left to right (assuming mean flow is from left to right). If these wave is coming from the inflow (left) then it will be a physical boundary condition (determined from outside the domain). If it is at the outflow section then it will be a numerical boundary condition (determined by the inner domain). For subsonic flow the first wave will propagate opposite to the mean flow

direction and the reverse will happen. The amplitude of these waves are defined as:

$$\begin{aligned} L_1 &= \lambda_1 \left(\frac{\partial P}{\partial x_1} - \rho a \frac{\partial U_1}{\partial x_1} \right) \\ L_2 &= \lambda_2 \left(a^2 \frac{\partial P}{\partial x_1} - \frac{\partial U_1}{\partial x_1} \right) \\ L_3 &= \lambda_3 \frac{\partial U_2}{\partial t} \\ L_4 &= \lambda_4 \frac{\partial U_3}{\partial t} \\ L_5 &= \lambda_5 \left(\frac{\partial P}{\partial x_1} - \rho a \frac{\partial U_1}{\partial x_1} \right) \end{aligned} \tag{205}$$

And the $\vec{d}$ that represents the derivatives along the 1D line is defined as:

$$\vec{d} = \begin{pmatrix} \frac{1}{a^2}\left[L_2 + \frac{1}{2}\left(L_5 + L_1\right)\right] \\ \frac{1}{2}\left(L_5 + L_1\right) \\ \frac{1}{2\rho a}\left(L_5 - L_1\right) \\ L_3 \\ L_4 \end{pmatrix} \tag{206}$$

The following subsections will give a brief review of the NSCBC implementation.

6.7.3 Subsonic Inflow

For subsonic inflow (four+Ns) physical boundary conditions are specified and one numerical from the characteristic equations. All the physical boundary conditions will have the subscript *inlet* hereafter. For subsonic inflow we will have $four + Ns$ waves coming from the outflow and one wave from inside. Hence, the inflow conditions are described as follows:

$$\begin{aligned} U_{i,j,k} &= U_{inlet} \\ V_{i,j,k} &= V_{inlet} \\ W_{i,j,k} &= W_{inlet} \\ T_{i,j,k} &= T_{inlet} \\ ksgs_{i,j,k} &= ksgs_{inlet} \\ Y_k &= Y_{k,inlet} \\ DQ_{i,j,k,1} &= -\Delta t d(1) \end{aligned} \tag{207}$$

Where all the derivatives are calculated by forward differencing from the interior domain.

6.7.4 Subsonic Non-Reflecting Outflow

For subsonic outflow we have $(four + Ns)$ right running waves, which need numerical description and one physical boundary condition. The pressure at infinity P_∞ is imposed as a physical boundary condition to calculate the amplitude of the coming wave:

$$L_1 = K\left(P_{i,j,k} - P_\infty\right) \tag{208}$$

Where K is a constant described as:

$$K = \sigma\left(1 - Mach^2\right) a / \left(XLEN \rho\, C_p\right) \tag{209}$$

Here, $Mach$ is the maximum Mach number, XLEN is the characteristic size of the domain, σ is a constant taken as 0.15. The derivatives $\vec{d}$ is solved by an upwind backward differencing. Then, the change in the conservative variables $\vec{DQ}$ is described as follows:

$$\begin{aligned}
DQ_{i,j,k,1} &= -\Delta t d(1) \\
DQ_{i,j,k,2} &= -\Delta t \left(U d(1) + \rho d(3)\right) \\
DQ_{i,j,k,3} &= -\Delta t \left(V d(1) + \rho d(4)\right) \\
DQ_{i,j,k,4} &= -\Delta t \left(W d(1) + \rho d(5)\right) \\
DQ_{i,j,k,5} &= -\Delta t \left(\rho U d(3) + \rho V d(4) + \rho W d(5) + \left(E + \frac{P}{\rho}\right) d(1)\right) + d(2)/(\gamma - 1) \\
DK_{sgs} &= -\Delta t U \frac{\partial k_{sgs}}{\partial x1} \\
DQ_{i,j,k,6+k} &= -\Delta t \left(Y_k * d(1) + \rho U \frac{\partial Y_k}{\partial x1}\right) \cdot k = 1, Ns
\end{aligned} \tag{210}$$

Where all the derivatives $\frac{\partial k_{sgs}}{\partial x1}$ and $\frac{\partial Y_k}{\partial x1}$ are computed by backward differencing. For thermally perfect gas the above formulation is updated by [177].

6.7.5 Wall boundary Conditions

At the wall the variables are adjusted in the ghost cells to get a zero velocity and zero pressure derivative at the wall. The wall non-slip boundary conditions are set as follows:

$$\begin{aligned}
U_{iwall,j,k} &= -U_{iwall+1,j,k} \\
V_{iwall,j,k} &= -V_{iwall+1,j,k} \\
W_{iwall,j,k} &= -W_{iwall+1,j,k}
\end{aligned} \tag{211}$$

The other derivatives are computed as:

$$\begin{aligned}
\rho_{iwall,j,k} &= \rho_{iwall+1,j,k} \\
P_{iwall,j,k} &= P_{iwall+1,j,k} \\
T_{iwall,j,k} &= T_{iwall+1,j,k}
\end{aligned} \tag{212}$$

Another recommended boundary condition implementation that is named as the Sponge Buffer Absorbing Boundary condition is shown in Appendix (B).

6.7.6 Stability and LES Time Step and MacCormak's Limitations

As mentioned earlier, MacCormak's scheme is an explicit second order accurate in space and time. Since the T.E of the scheme is second order, it gives the numerical solution a more dissipative nature. However, the spatial central scheme is dispersive and non-monotonic. Earlier studies for MacCormak scheme for Euler computation ([178]) shows that for inviscid flows we still need to add artificial dissipation to compensate the lack of the natural one. MacCormak's scheme is more suited for low to moderate Reynolds number, where the grid doesn't have to be refined extensively to match the stability criteria. If the grid is refined, numerical oscillations will be produced and accentuated by the scheme dispersive nature. As a result, for very steep gradients, like shock waves, MacCormak's behaves poorly, due to its dispersive nature. The central differenced terms increase the numerical oscillations and can make the solution unstable. The solution for this is either to add source terms

to the scheme to act as a smoothing operator ([179]), or use other higher order upwind schemes, that naturally dissipate such oscillations. Another scheme that is used with highly supersonic flows is the Piecewise Parabolic method (PPM) ([180]). In the current work, all the problems involved are reactive and subsonic and MacCormak is found to be sufficient. Another limitation, as a space and time marching technique, is that the scheme is not suitable for solving pure elliptic PDEs, where the waves are propagating in all directions, like the poisson equation. However, the Navier stokes equations are mixed elliptic parabolic and the scheme is found appropriate. Based on the $Courant - Friedrichs - Lewy$ (CFL) condition, which states that for stability the numerical domain must include all the analytical domain. Hence, the speed of integration ($\frac{\Delta X}{\Delta t}$) is higher or equal to the mean flow files speed (U):

$$CFL = U\frac{\Delta t}{\Delta X} \leq 1 \tag{213}$$

Based on the CFL condition the Stability criteria is computed. For the Navier Stokes equations, since no analytical stability condition is known, the criteria is based on physical reasoning. The grid spacing is computed as $\Delta X = V_{i,j,k}/|\vec{A}|$. The velocity U is takes as the sum of the convective v_c, acoustic v_c, and diffusive velocity v_d, given as:

$$\begin{aligned} v_c &= U\vec{i} + V\vec{j} + W\vec{k} \\ v_a &= a \\ v_d &= \frac{2\gamma\mu}{\bar{\rho}Pr}\frac{|d\vec{A}|^2}{V_{i,j,k}} \end{aligned} \tag{214}$$

Where a is the speed of sound, Pr is the Prandtl number and ΔX is the characteristic grid spacing computed as $|d\vec{A}|^2/V_{i,j,k}$. Where:

$$d\vec{A} = (dA_x, dA_y, dA_z) \tag{215}$$

Finally the time step is expressed as ([181]):

$$\Delta t = min\left[\frac{CFL}{\frac{|u|}{\Delta x} + \frac{|v|}{\Delta y} + \frac{|w|}{\Delta z} + a\sqrt{\frac{1}{(\Delta x)^2} + \frac{1}{(\Delta y)^2} + \frac{1}{(\Delta z)^2}} + \frac{2\gamma\nu}{\bar{\rho}Pr}\left(\frac{1}{(\Delta x)^2} + \frac{1}{(\Delta y)^2} + \frac{1}{(\Delta z)^2}\right)}\right] \tag{216}$$

6.7.7 Chemistry Time Step

The chemical time step in the LEM subgrid level has to be computed accurately to reflect the physics and the coupling with the flow dynamics. Since, we are using a reduced mechanism with 19 species, the mechanism is expected to be stiff and the source terms have to be integrated with a time step adapted to the reaction diffusion. There are three main ways used in this thesis to integrate the chemistry source term. The most accurate way is to use the ODE integration package DVODE that is designed to integrate set of stiff ordinary differential equations. However, this method is expensive and is not suitable for detailed and reduced mechanisms, especially for high numbers of grid points. The two other methods are described below.

6.7.8 In Situ Adaptive Tabulation (ISAT)

In Situ Adaptive Tabulation (ISAT) is a very successful method to speed up the highly expensive reactive three dimensional problems. ISAT is most convenient with LES methods, where the source terms are computationally splitted from the main governing equations. With operator splitting method, the problem is finally decomposed into solving a set of ordinary differential equations that represents the source terms in the governing equations. ISAT is a substitute to solve this set of Ordinary Differential Equations (ODEs), which minimizing the need for a stiff ODE solver. A good discussion of ISAT and how it works can be found in [163]. ISAT retrieves pre-stored values of the scalars (species and temperature) within a prespecified ellipsoid error of tolerance ([163]). In this way, the need to solve the stiff ODEs every time step is minimized. ISAT provides a significant reduction of computational time with the increase in the number of scalars ([111]).

However, ISAT has some drawbacks:

- First we define the tree as the table that ISAT uses to retrieve data for a certain portion of the computational domain. This tree is composed of nodes, each corresponds to a certain realization or solution. As the tree grows up with time, if the number of tree nodes increases beyond the maximum allowable size, the tree will not be able to store new information (or create new nodes), if data is outside the ellipsoid error.

- As the number of nodes increases significantly, the memory storage requirement increases as well.

- Some studies are conducted to test the tree sensitivity to the integration time. It was found that reducing the integration time step will reduce the rate of tree growth significantly. A threshold value for the chemisty integration of $4X10E-8$ is found to be always a limit after which the tree growth will be exponential. However, this limit might change from one simulation to another and is not universal. In other words, for each simulated case this threshold value has to be recalculated.

- The ISAT subroutine is set such that each processor has its own tree. Hence, the distribution of the processors with respect to the flame location will affect greatly the tree behavior. If the flame is vertical, the processors have to be arranged as a horizontal slaps.

  Three important factors are examined here for an isotropic box.

- The effect of the number of processors used on the ISAT calculation is tested. Figure 16 shows the efficiency gain between ISAT and direct integration (DI) for a certain number of processors. The test case is for an ethylene 19 species reduced mechanism. The grid size is 64^3 grid points aligned across the box axis. It was found that as the number of processors increases the percentage gain decreases between ISAT and DI. In addition, no further gain if we increase the number of processors beyond 16, which is the total number of grid points divided by 4. This is attributed to the increase in the communication time as we increase the number of processors, which in this case will be the governing factor, rather than the chemistry computational time.

- The second factor is the tolerance for the accuracy of the retrieval ellipsoid. As this value increases retrieval rate increases (less need to creat new nodes) but on the account of losing accuracy. The current reduced mechanism with the values of 1E-4 gives accurate comparison to the DI values. Figure 17 shows the methane reaction rate comparison between DI and ISAT for two different error values (1E-3 and 1E-4), which shows that 1E-4 almost coincide with the DI results.

- The last factor that we studied is the optimum weighting values for the error tolerance that control local tabulation. Initially, this value was fixed during the whole simulation. In the current work this value is treated as floating and dynamic for every time step. With that the spatial and temporal distribution of the scalars vary and is not fixed and so does the tabulation error. This criteria is found to be more efficient and cause a more accurate results. The error weights are computed inside each LEM cells as the maximum scalar value in the current cell for local tabulation:

$$Wtmax_i = Max(Gsgs(1 : Isgs, I, J, K)_i)...i = 1, nspeci + 1.. \tag{217}$$

$$Wtmax_{N_s+2} = 0.1DT_{LES} \tag{218}$$

After that, the local error is computed inside the tree subroutine according to the following criteria:

$$X = ABS(\frac{Ynew_i - Yoldi}{WTMAX_i}) \tag{219}$$

where Ynew is the new scalar value computed from the direct integration and Yold is the inquiry point value.

6.7.9 Time splitting

The last method used here, is to compute the chemistry integration time step by dividing the LES time step. Then simply calling the mechanism to compute the reaction rates. The chosen value should match the direct integration results, with at most 5 % error. We chose to match the acetylene reaction rate with the DI value, since it is extremely important for us in the soot calculations. Figure 18 shows the reaction rate along the centerline for the non-premixed soot described in section VII. Fifteen steps are found to be sufficient per LES time step, which saved about 50% of the computational time.

The next three sections will show the application of the model to premixed and non-premixed flames. The validation case is chosen for a sooting non-premixed ethylene-flame in section VI. The conclusion will be in chapter VII.

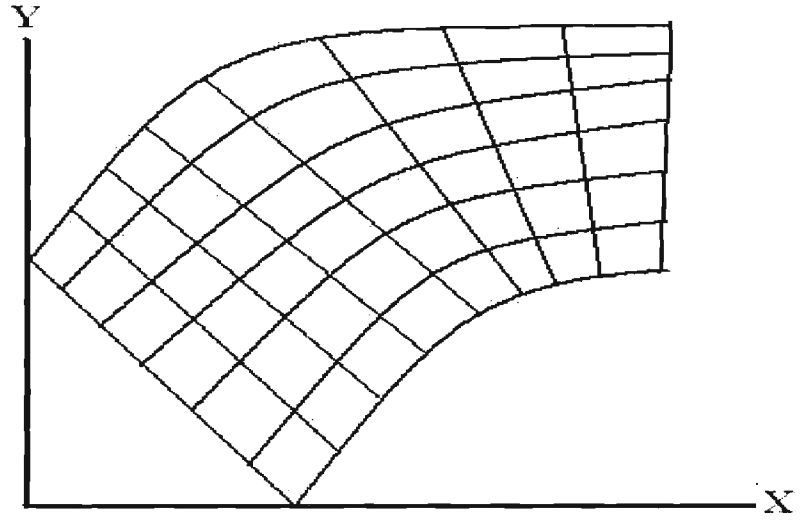

Figure 10: A two dimensional physical domain.

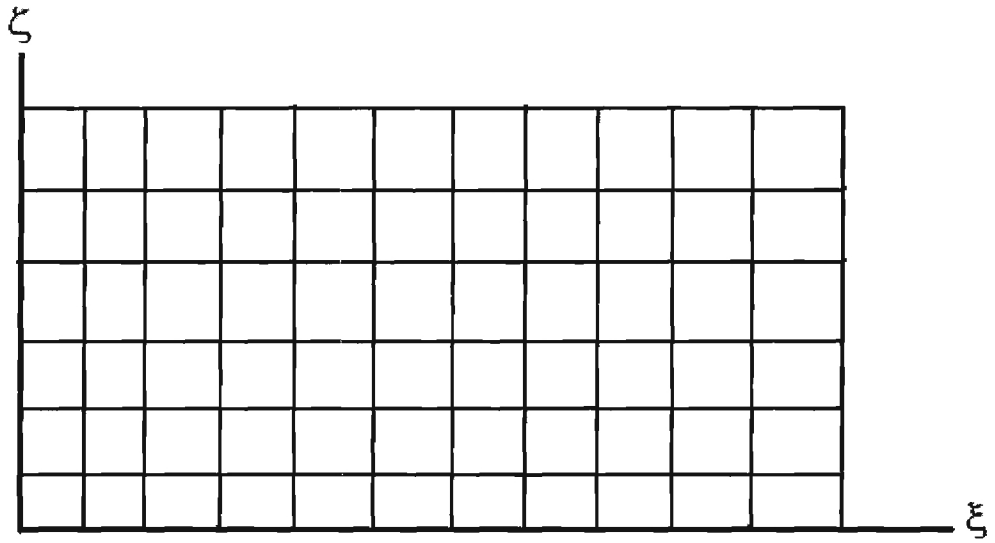

Figure 11: The corresponding computational domain

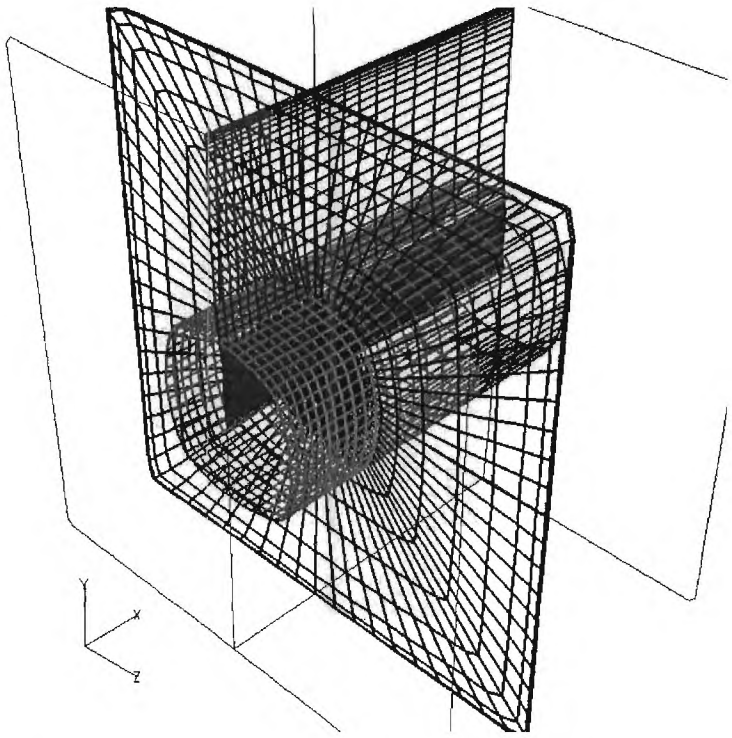

Figure 12: The outer cylindrical domain, five grid points are skipped in each direction

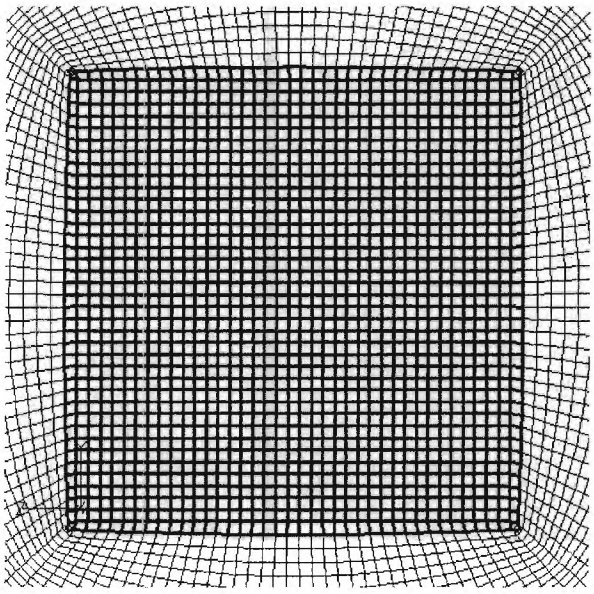

Figure 13: Inner cartesian grid

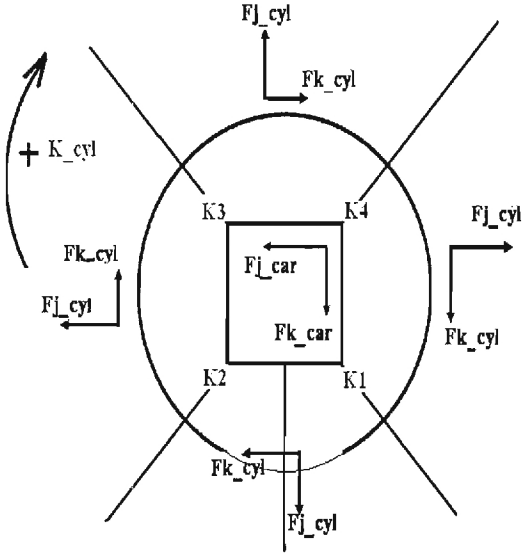

Figure 14: The axis arrangement and the fluxes interchange between the cylindrical (outer) and the cartesian (inner) grids for the two butterfly grid

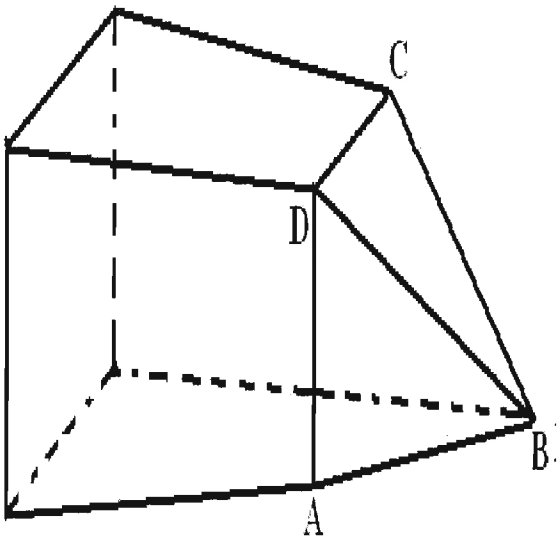

Figure 15: An arbitrary finite volume cell

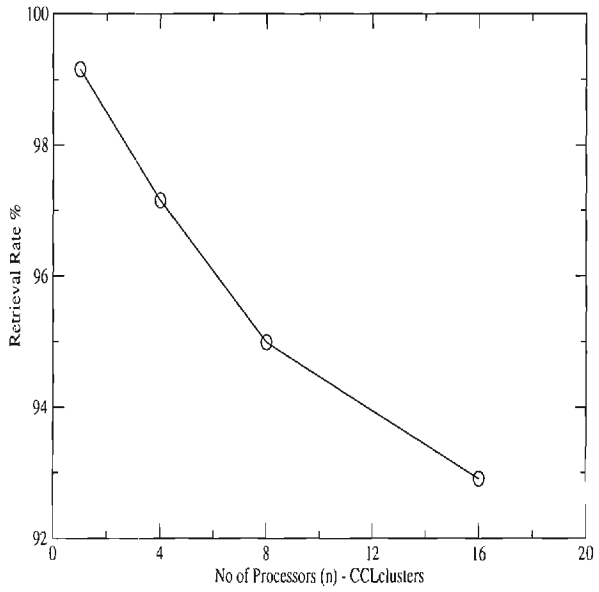

Figure 16: The effect of number of Processors on ISAT performance

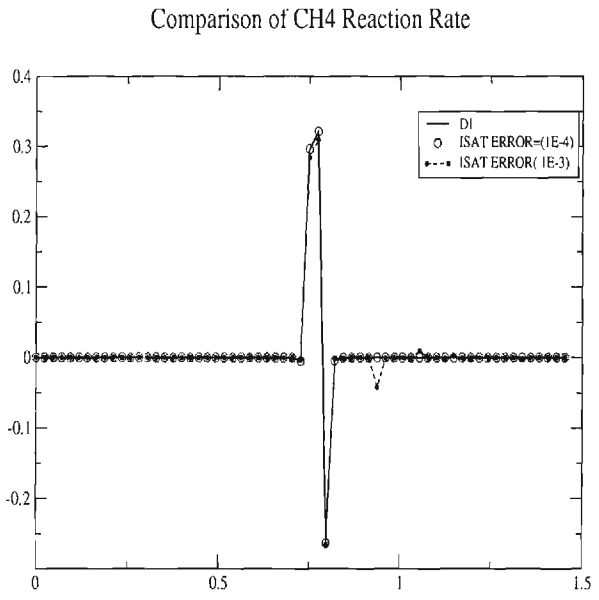

Figure 17: Effect of ellipsoid tolerance on final results

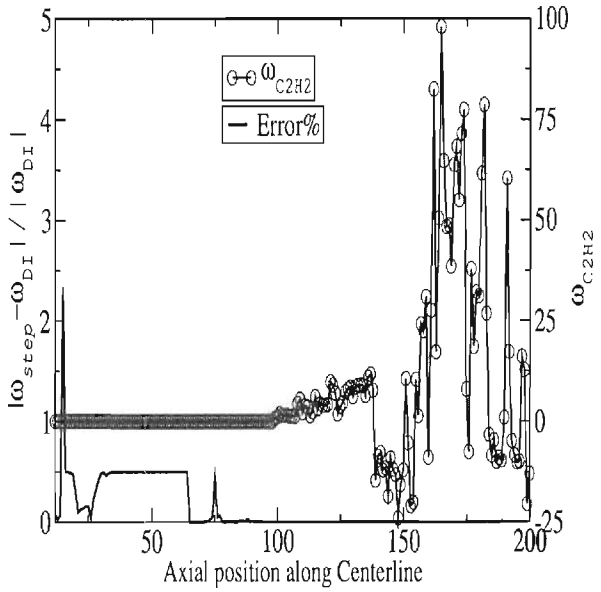

Figure 18: Comparison between the time splitting method and the direct integration

7 Premixed Sooting Flames

We study premixed flame turbulence interaction for various flame conditions. The configuration and numerical approach has been well established in many past studies ([182]) and comparison of LEMLES and DNS in the past for non-sooting flames ([110]) has demonstrated the validity of the LES approach used here.

The flame test conditions for these cases are summarized in Table (1). Four cases are simulated here using MECH-A to investigate the effect of (a) C/O ratio, (b) turbulence level, and (c) the species binary diffusivity on soot production in ethylene-air premixed flames. The critical C/O ratio for ethylene/air premixed flames is around 0.6 ([25]). Therefore, we study soot production for C/O ratios of 0.33 and 0.93. For the second case study, the C/O ratio is fixed at 0.67, and the turbulence level is varied. The F1 flame is in the thin reaction zone (TRZ) regime and the B3 flame is in the corrugated flamelet regime. One F1 case for $C/O = 0.67$ is repeated with MECH-B, with detailed binary diffusion coefficients and with constant species Schmidt number.

In Table (1), $Re = \left(u^{'} l\right)/\nu$, $Da = \left(S_F l\right)/\left(u^{'}\delta_F\right)$, $Ka = \left(\delta_F^2\right)/\left(\eta^2\right)$ are the turbulent Reynolds number, Damkoler number, and Karlovitz number, respectively, $u^{'}$ is the turbulent intensity, l is the integral length scale, and η is the Kolmogorov length scale. Also, S_F and δ_F are respectively, the laminar flame speed and the laminar flame thickness.

The LES grid resolution is 64x64x64 cube in a physical domain of 15x15x15 mm with 18 LEM cells per LES cell for the low C/O ratio case and 12 LEM cells per LES cell for the higher one. The LEM resolution is chosen to capture the flame thickness and to resolve close to the Kolmogorov length scale (1-2 η) ([182]). Characteristic inflow-outflow conditions are used in the axial direction, and periodic conditions in the other two direction. Inflow turbulence that is superimposed on the mean inflow velocity is assumed to satisfy the von Karman-Pao energy spectrum for isotropic turbulence ([183]).

The current approach requires solution of 20 species equations in every LEM domain in every LES cell. Thus, the evaluation of the kinetics is the limiting cost of these simulations. To enhance the computational efficiency, efficient parallel implementation is carried out and in addition, ISAT is employed in every LES cell to reduce the cost of the chemistry evaluation. The simulations are performed on a dual Intel Xeon (3.4 GHZ) PC cluster. A turn over time for the F1 low (high) C/O flame defined as $t_{flow} = l/u^{'}$, takes around 580 (1280) single-processor hours. The results reported here are averaged over 12 turnover times after the initial transients.

In the following section the validation of the reduced ethylene/air mechanism is first discussed briefly, followed by the validation of the stand-alone LEM-MOMIC model. After that, the effect of the C/O ratio is investigated and the conclusions are compared (albeit qualitatively) with past observations. The effect of turbulence is then analyzed for two different turbulent flames (i.e, F1 and B3) using MECH-A. Finally, the effect of using a variable binary diffusivity coefficients against constant Schmidt number is explored with the MECH-B for the F1 flame.

7.1 Evaluation of the Reduced Mechanisms

The reduced mechanisms are validated for homogeneous applications of a Perfectly Stirred Reactor (PSR) and auto-ignition, and for diffusive applications of premixed and non-premixed flames ([143]). Validation of MECH-A were reported earlier ([146]) and therefore not repeated here. [146] and [143] reported good agreement with the worst-case error for C_2H_2, approximately 30% on the fuel side. Considering the uncertainty in the present soot model, the reduction error in C_2H_2 can be considered to be acceptable, particularly in view of the gain in the computational capability in the simulation.

7.2 Evaluation of the stand-alone LEM-MOMIC model

Two test cases used by [24] are chosen for these studies. The first test case (Case A) accounts for coagulation only, and compares the discrete method results for a mono-disperse case with MOMIC. The second test case (Case B) accounts for simultaneous nucleation, surface growth, and coagulation. Stirring, combustion and diffusion are switched off and only a single scalar is considered. The results are compared to results extracted from [24]. The operating conditions for the two case studies are shown in Table 2.

Test case A is for a mono-disperse case with one class size. The results shows good agreement, as shown in Fig. 19 (a). The mean particle diameter increases with time by coagulation, while the number density decreases due to the decrease of the initial number of particles. The standard deviation of the PSDF computed from $\sigma = \sqrt{(\mu_3/\mu_2)^2 - 1}$ is also shown. As time is advanced, the deviation from the initial zero mean diameter increases linearly.

Figure 19 (b) shows the number density N_s predicted by the MOMIC and the discrete method for the test case B. The surface growth rate is taken from [56] as $k_s = 1x10^{-4} g/cm^2$, while the nucleation rate is calculated from [24]. The MOMIC curve shows a slight deviation at late times. This is might be a result of the interpolation error at the higher moments, since we are solving only up to the third moment ([141]). In addition, the soot oxidation process is not included here. Regardless, the above study demonstrates the acceptable ability of the stand alone LEM-MOMIC model.

7.3 Effect of C/O ratio

Figure 20 shows an instantaneous iso-surface for T = 1400 K, C/O ratio of 0.33, and the axial vorticity magnitude contour at the inflow and outflow plane. Due to flame-turbulence interaction the flame surface is wrinkled and its surface area is increased significantly from the initially laminar flame sheet ([184]). Heat release dissipates the smaller eddies leaving only larger structures behind the flame. The qualitative features of this flow structure and the flame surface are quite similar to the non-sooting cases studied in the past using LEMLES ([182]).

Figures 22 and 21 show respectively, contour plots for soot mass fraction at a median cross-sectional plane, with nucleation reaction rate contours and with soot oxidation rate. As shown in the figures, soot starts to form at the end of the flame reaction zone (to the right of the flame), and is then oxidized by the OH and O_2 mechanism, according to the

Lindstedt model ([52]). The amount of soot produced depends on many factors including fuel type, the residence time and flame type. Accordingly, either all the soot will be oxidized in the destruction zone or some trace will be emitted at the outflow depending on the aging process and the residence time. Generally, for premixed flames all the soot processes occur simultaneously, but the strength of each step varies according to the local conditions and species concentration. The formed particles start to grow by absorbing hydrocarbon gaseous species, and with collision particles start to coagulate or aggregate downstream of the flame front. As we will discuss in the next section the flame structure affects greatly the soot production as well. In the following, we focus primarily on the soot related properties obtained by statistical time averaging of the simulated cases.

Figure 23(a) shows the streamwise profile of the time averaged soot nucleation, surface growth and oxidation rates, and Fig. 23(b) shows the profiles for mean temperature, acetylene mass fraction, and soot volume fraction for C/O ratio of 0.33. Both nucleation and surface growth begin simultaneously around 1000 K prior to oxidation by OH and O_2, which starts around 1800 K. These results agree with past observations ([185]) that surface growth rate is negligible (three orders of magnitude less than nucleation) for ethylene-air premixed flames with C/O ratio below 0.75. Figure 23(a) also shows that for this C/O ratio, OH oxidation is more dominant than O_2 oxidation due to the abundance of OH, which also agrees with experimental observations ([186]) in atmospheric pressure flames. It can be seen that the soot peak coincides with the nucleation rate and the acetylene mass fraction peaks.

The corresponding figures for the high $C/O = 0.93$ case are shown in Figs. 24(a) and (b). The surface growth rate is higher (when compared to the low C/O flame) due to an abundance of C_2H_2. On the other hand, the OH and O_2 oxidation rates are much smaller, since O_2 and OH exist in very small proportions in this fuel-rich flame. These observations agree quite well with earlier results ([187]). Oxidation rate in the post flame zone is very low and soot formation by surface growth by acetylene addition is high enough to overcome the destruction by O_2 and OH. Finally, soot peak corresponds with the nucleation peak, similar to the lower C/O flame, and its formation also begins at approximately the same location. This observation shows that the soot inception location is independent of the equivalence ratio, but the magnitude and post flame variation depends on the concentration of acetylene and the other soot formation rates.

In summary, these studies for different C/O flames show results consistent with past observations in similar flames ([186, 187]). For ethylene/air flames the critical ratio is around C/O = 0.667. Soot inception location and conditions are mainly dependent on the fuel type rather than the C/O ratio. In addition, the oxidation of soot by OH is more dominant than O_2 at the post flame region for the current conditions. All the computed results agree with experimental observations and provide confidence in the simulation approach.

7.4 Turbulence Effect on Soot Formation

Figure 25(a) shows the averaged soot volume fraction and the temperature profile for two flames (F1 flames and B3 flame using MECH-A). The corrugated flamelet (B3) flame shows higher soot peak volume fraction than the TRZ (F1) flame. This suggests that the turbulence effect is to decrease the soot production level in premixed flames. This behavior is expected as turbulence increases stirring and mixing in the subgrid level in our LEM approach, which

is physically consistent. In the corrugated flamelet regime, the turbulent eddies are larger than the flame thickness and the residence time inside the flame is larger for the B3. Hence, more soot is produced. In the TRZ regime turbulent eddies penetrate the preheat zone, and as a result, fuel and oxidizer are more mixed and complete combustion is achieved.

Near the outflow, the B3 flame shows more complete combustion than that of the F1 flame. This is attributed to two main reasons. From Fig. 20 and the discussion following it, the effect of heat release is to dissipate the small scale structures and to reduce the turbulence effect leaving the larger vortices with higher residence time. In addition, the F1 flame has a wider turbulent flame brush as a turbulent flame. Hence, in an average sense the F1 flame has a wider preheat zone, and therefore, more chance to produce soot, which is not oxidized completely as it approaches the outflow.

The comparison of the mean acetylene mass fraction is shown in Fig. 25(b). Acetylene production level is found to be nearly the same for the F1 and B3, with minor changes at the peak location and elevated level for the F1 flame near the outflow. Since both flames have the same equivalence ratio the production level for acetylene will be comparable. However, since soot in the B3 case consumes most of the acetylene behind the flame, it shows lower levels than the F1 at the outflow. These results suggest a strong coupling between turbulence and chemistry.

The mean soot nucleation and surface growth rates are shown in Fig. 26. Turbulence is found to have a minor effect on the nucleation rate, with small differences attributed to the acetylene production level, as discussed above. However, the surface growth rate decreases with turbulence and is a direct consequence of the decrease in the average total surface area, which is shown in Fig. 27. Analysis shows that as the turbulence level increases the collision frequency increases, and the coagulation rate increases as well, which means that more particles coalesce together to give a larger diameter particle. For nearly the same nucleation rate the number density will decrease and the average surface area of the soot particle will decrease as well. Since, the B3 flame has larger average total surface area, the probability of collision of the acetylene as well as the oxidative species with the soot particles will be higher than in the F1 flame, which causes more reaction deposition and abstraction on the surface. As a result, the higher turbulent flame shows lower number of particles per unit volume, lower number density, and larger individual particle diameter than the B3 flame. Consequently, the total average mass (computed from the first moment) and the surface area of soot per unit volume are larger for the B3 flame.

7.5 Effect of binary diffusion

The effect of binary diffusivity on the subgrid level is studied here using MECH-B. The test case considered is the F1 flame with a C/O ratio of 0.667. Ethylene and air have nearly the same molecular weight and hence, both molecules diffuse equally in the mixture. Recent studies for laminar flame indicate that ethylene/air mixture has a neutral behavior, since the thermal and molecular diffusivity neutralize each other for a unity Lewis number ([188, 189]). However, in the turbulence case the flame is highly strained and the curvature effect changes the scalars profiles according to the ratio of the thermal to the molecular diffusivity. The flame stretch is induced by the flow nonuniformity (strain effect) and the curvature due to the wrinkling of the flame surface area, which increases its reaction front.

When the flame has negative curvature (concave towards the reactants), the mass is focused towards the products side and the heat is focused inwards to the reactants side. If the Lewis number (Le) is greater than unity, the thermal diffusivity will increase the temperature in the preheat zone and the flame burns strongly with a higher flame temperature ([188]). These observations are confirmed in Fig. 28, where the C_2H_4 reaction rate and temperature profile across a concave and a convex flame elements are plotted. The flame shows higher temperature and reaction rate across the concave element.

The fact that the thermal diffusivity focusing effect overcomes the molecular diffusivity defocusing effect indicates that Le > 1. Since, the definition of the indicative Lewis number is not clear, we show the mean mixture Lewis number across the flame combined with the mean temperature profile for both cases studied in Fig. 29. Both test cases predict a Lewis number bigger than unity, which coincide with the current observations. However, the constant Schmidt number case predicts a higher Lewis number, and hence higher thermal diffusivity effect. The closer to unity Lewis number in the variable diffusion case agrees with the literature observations ([188]).

Figure 30 shows the pdf of mean curvature for both test cases. The curvature tensor is computed using the following expression ([110]):

$$h_{ij} = -\frac{\partial^2 c}{\partial x_i \partial x_j}\frac{1}{g} + \frac{1}{g^3}\sum_{k=1}^{3}\frac{\partial c}{\partial x_i}\frac{\partial c}{\partial x_k}\frac{\partial^2 c}{\partial x_j \partial x_k} \tag{220}$$

where $g = |\nabla c|$, and c is the progress variable. The flame surface curvature is computed as the mean of the two principle radii of curvature computed from the eigenvalues of Eq. (220). The figure shows that the constant diffusion flame is skewed towards the positive curvature (convex towards reactants), while the variable diffusion case is more symmetric with higher probabilities in the negative curvature side. The wide range of curvature indicates the high turbulence effect on the flame structure and the surface area. In addition, the variable diffusivity case shows wider tails and no sharp peaks in the middle. The wider tails indicates the presence of more flames close to the spherical and saddle shapes. The mean in both cases is around zero. These observations are consistent with the past work in non-sooting premixed flames ([190, 191]) and suggested that the presence of soot particles have little effect on the flame curvature.

For Le > 1, the burning rate increases for a concave (negative curvature) surface due to the concentration of heat in the preheat zone, which consequently leads to a higher burning rate and a higher turbulent flame speed (estimated by integration of the burning rate). A comparison of the PDF of the mean turbulent flame speed non-dimensionalized by the laminar unstrained flame speed $\frac{S_T}{S_L} = (1 + \beta\frac{u'^{\alpha}}{S_L^{\alpha}})^{1/\alpha}$ is shown in Fig. 31. Here, $\alpha = 2$ and β is the minimum of 0.8165 $\frac{u'}{S_L}$ and 16.56 based on past studies ([192]). The mean value of the turbulent flame speed is around 12 for the variable diffusivity, while for the constant Schmidt number case it is around 10, with less skewness towards the higher values. This observation is consistent with the curvature PDF shown in Fig. 30.

The effect of the multi-species diffusion on soot formation is investigated. The mean mass fraction profiles of OH and C_2H_2 are shown in Fig. 32. The higher burning rate produces more hydroxyl for the variable diffusivity case, which increases the rate of soot oxidation, as shown in Fig. 33. Minor effect is found on acetylene, with slightly lower peak value for the

variable diffusivity case, probably due to higher consumption by the soot, as shown later. The difference in the acetylene mass fraction is reflected in the soot nucleation rate shown in Fig. 34. However, Fig. 35 shows that the variable diffusivity case has higher soot surface growth rate. The higher surface growth rate indicates larger average soot particles surface area (shown in Fig. 36) and higher soot number density (larger amount of particles) and soot average mass per unit volume (first moment) (shown in Fig. 37). As discussed previously, the higher Lewis number for the constant diffusivity case allows more heat to diffuse into the preheat zone, and this in turn, increases the collision frequency. Since collision frequency is proportional to the temperature, more coagulation occur, which results in a smaller number density, and is confirmed in Fig. 37, which shows the mean first (number density) and second moment (average soot mass per unit volume) spatial distribution. The variable diffusivity case shows higher number density, hence smaller coagulation rate.

Finally, Fig. 38 shows that the variable diffusion case predicts around double the peak value of the soot volume fraction of the other case. However, the constant diffusivity case shows a slightly wider profile for the temperature and the soot volume fraction. The wider profile is a direct consequence of the higher Le (higher thermal diffusivity) and the higher soot production is a direct result of the higher surface growth rate (shown earlier in Fig. 35).

Flame	C/O	Re	Da	Ka	S_F	δ_F	$u^{'}$	l	$\frac{u^{'}}{S_F}$	$\frac{l}{\delta_F}$	η
F1	0.33	164	1.152	91	0.66	0.039	7.85	0.535	11.90	13.71	0.012
F1	0.93	272	0.75	22	0.07	0.355	0.833	5.07	11.90	13.71	0.076
F1	0.67	271	1.152	23.76	0.24	0.108	2.86	1.474	11.90	13.71	0.022
B3	0.67	40	7.910	1.32	0.24	0.108	0.416	1.474	1.733	13.71	0.094

Table 1: Simulated turbulent flames. Where, δ_F, η, l dimensions are in mm. $u^{'}$ and S_F are in m/sec

Case	Mo(cm^{-3})	T (K)	$\rho_{soot} g/cm^3$	m_1(g)
A	10^{12}	1800	1.8	3.18X 10^{-12}
B	0.0	1800	1.86	4.784X10^{-22}

Table 2: Parameters for test case A (Coagulation Only) and case B (nucleation, coagulation and surface growth). Here, Mo is the number of initial molecules per unit volume, m_1 is the initial soot particle mass, ρ_{soot} is the soot particle density.

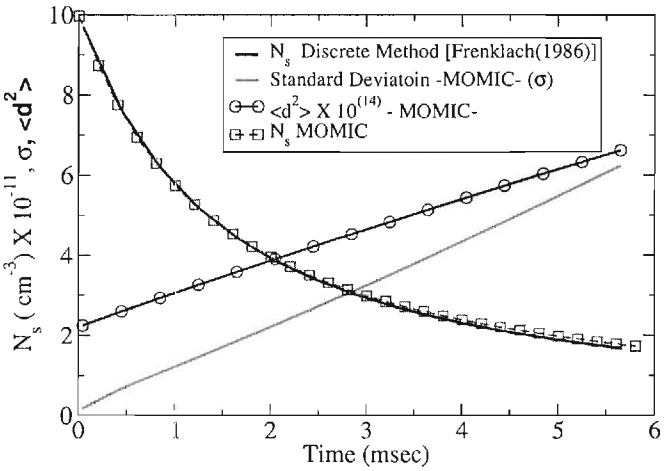

(a) Test case A. (coagulation only)

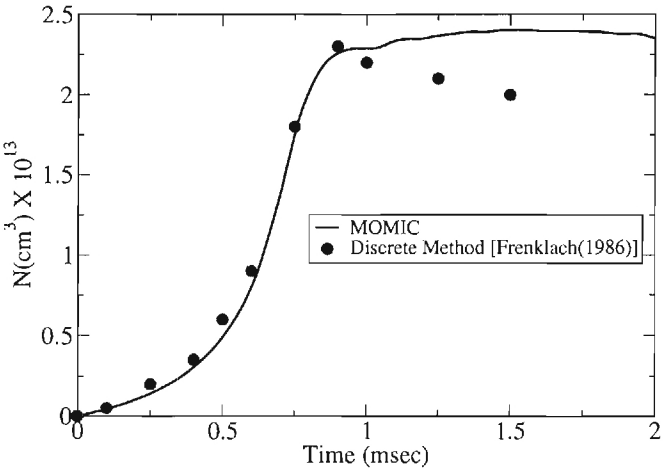

(b) Test case B. (simultaneous nucleation, surface growth and coagulation)

Figure 19: Comparison of method of moments and discrete method.

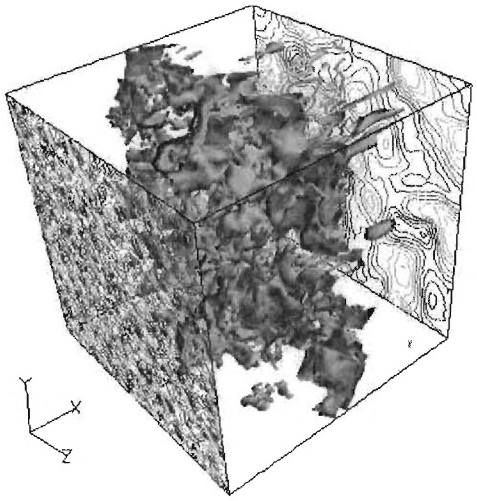

Figure 20: Soot and temperature iso-surface with vorticity contours for $C/O = 0.333$

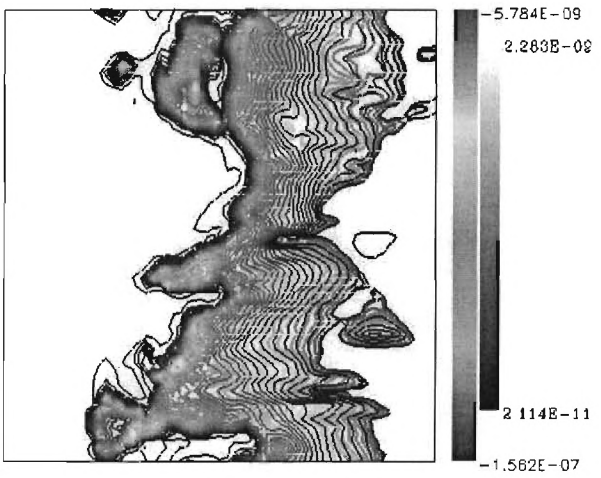

Figure 21: Contours of soot (grey) and oxidation rate (spectrum) for $\Phi = 1.0$

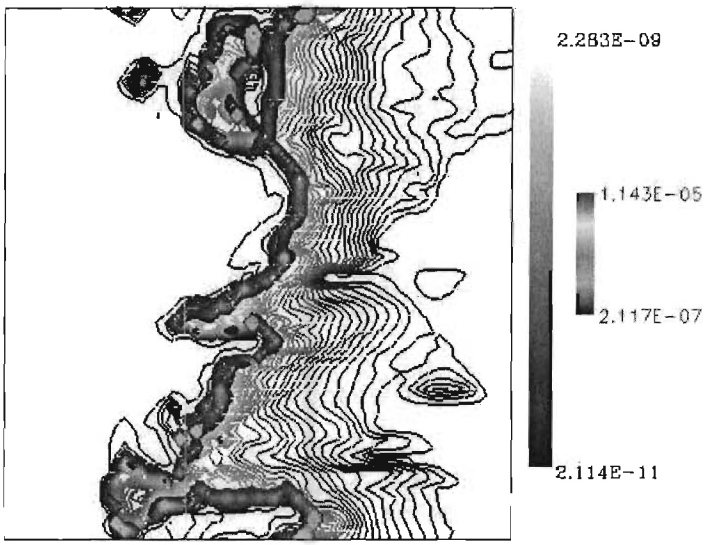

Figure 22: Contours of soot (grey) and nucleation rate (spectrum) for $\Phi = 1.0$

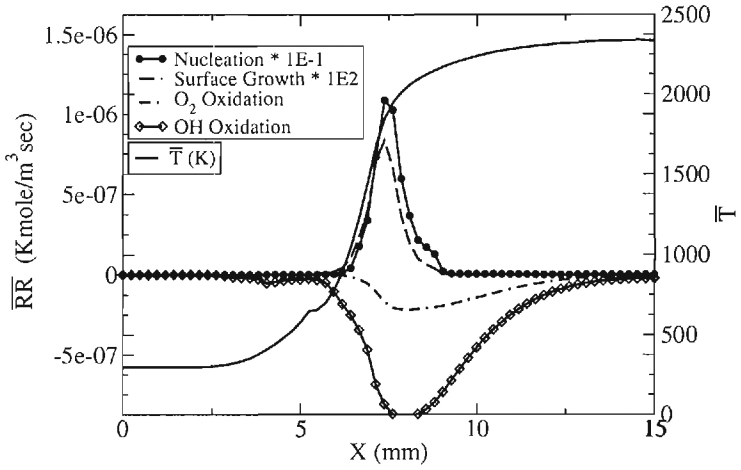

(a) Soot formation and oxidation rates

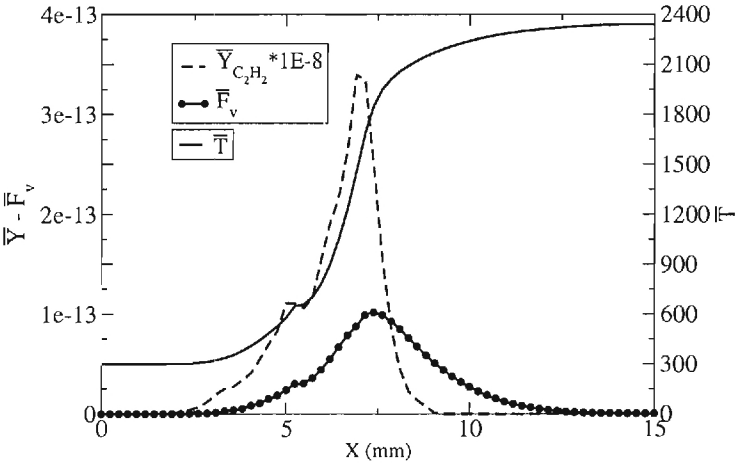

(b) Temperature, soot volume fraction, and acetylene mass fraction

Figure 23: Mean profiles for $C/O = 0.33$.

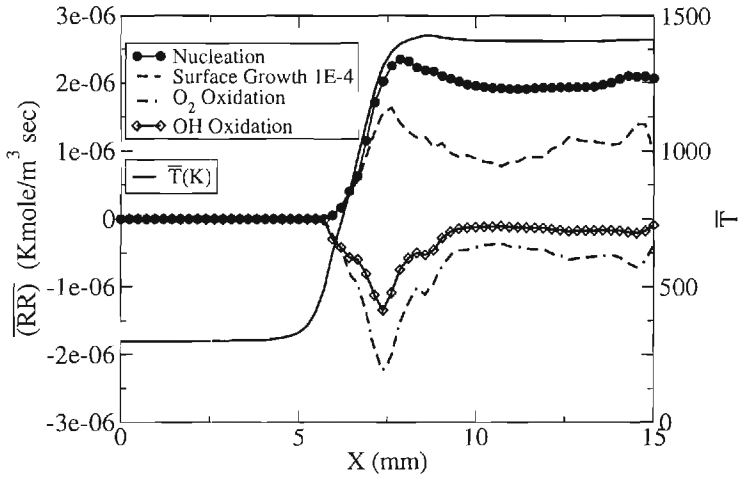

(a) Soot formation and oxidation rates

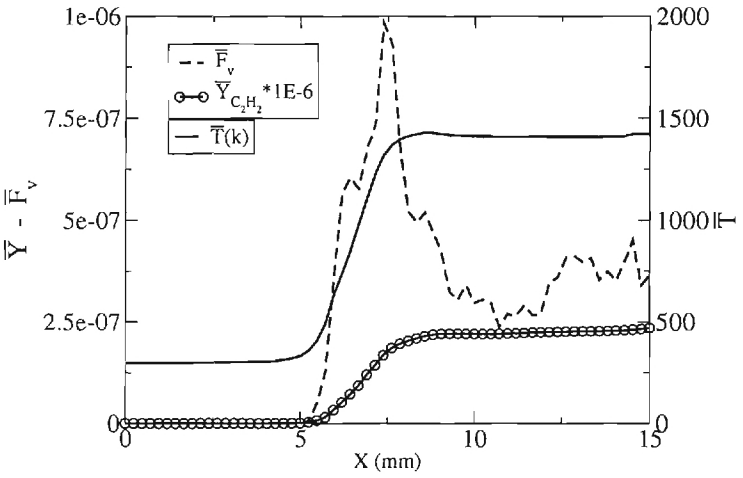

(b) Temperature, soot volume fraction, and acetylene mass fraction

Figure 24: Mean profiles for $C/O = 0.93$.

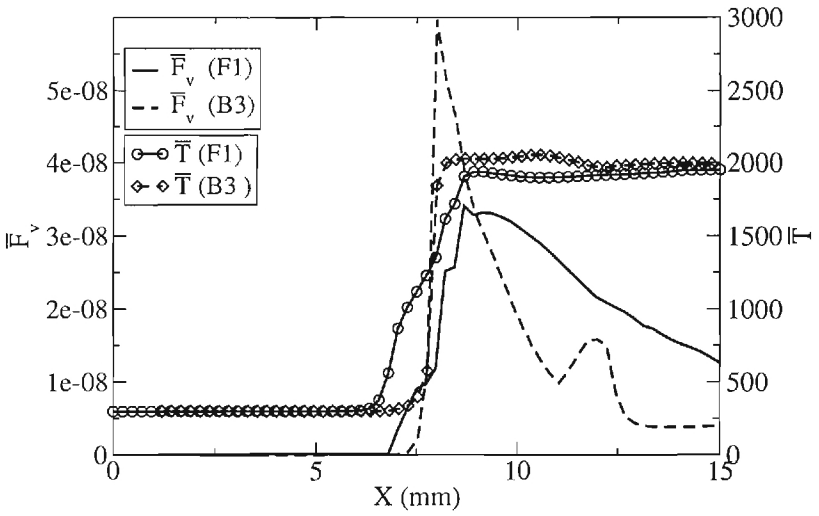

(a) $\overline{F}_v and \overline{T}$

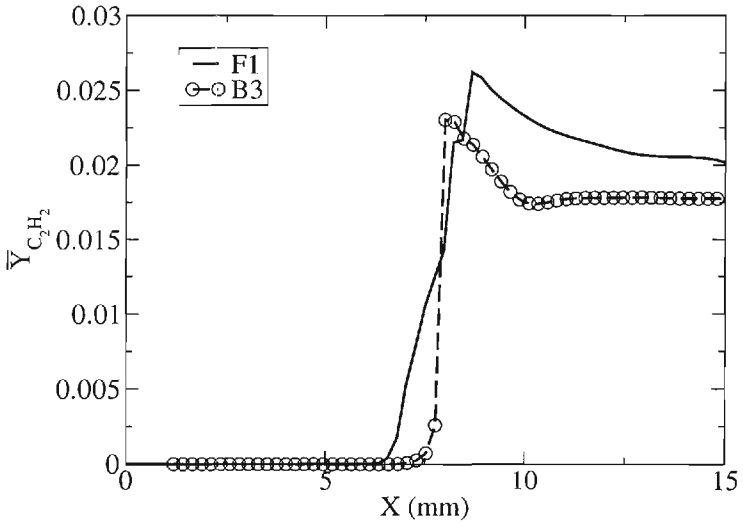

(b) $\overline{C_2H_2}$

Figure 25: Mean soot volume fraction, acetylene mass fraction and temperature profile at $C/O = 0.667$

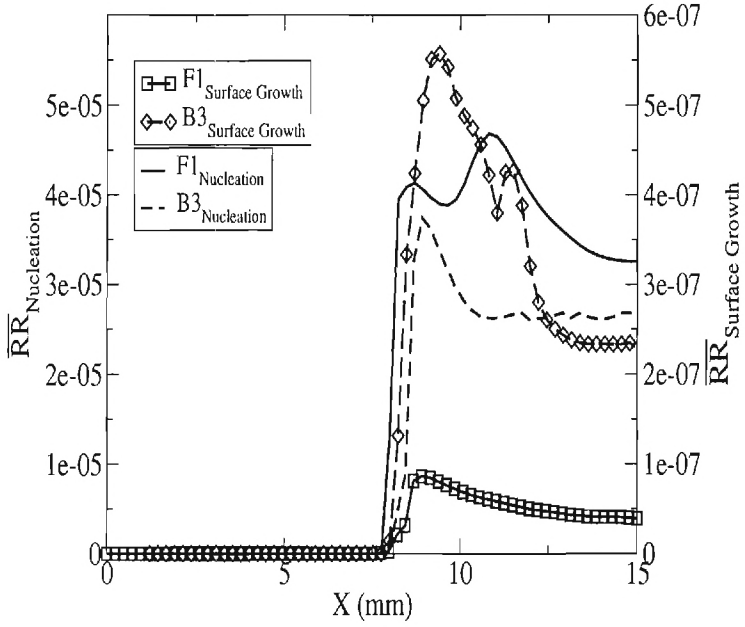

Figure 26: Mean nucleation and surface growth rates at $C/O = 0.667$

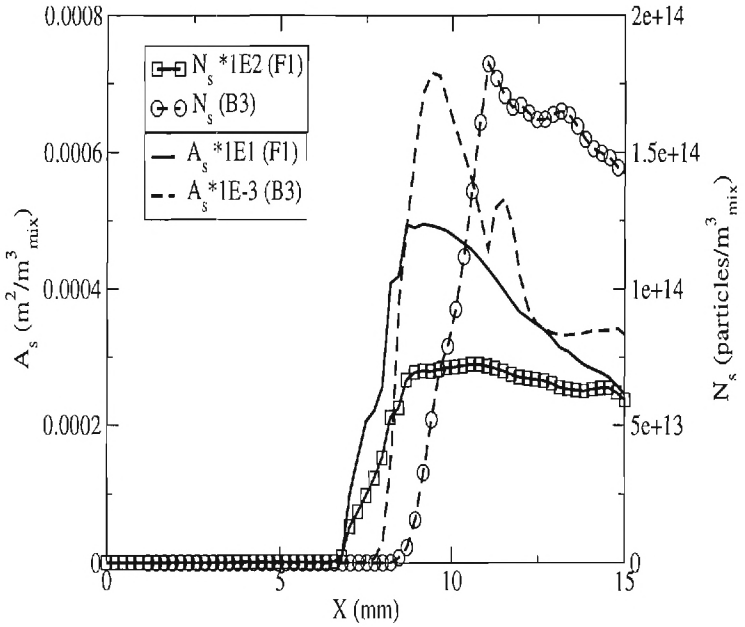

Figure 27: Mean average surface area per unit volume and soot number density at $C/O = 0.667$

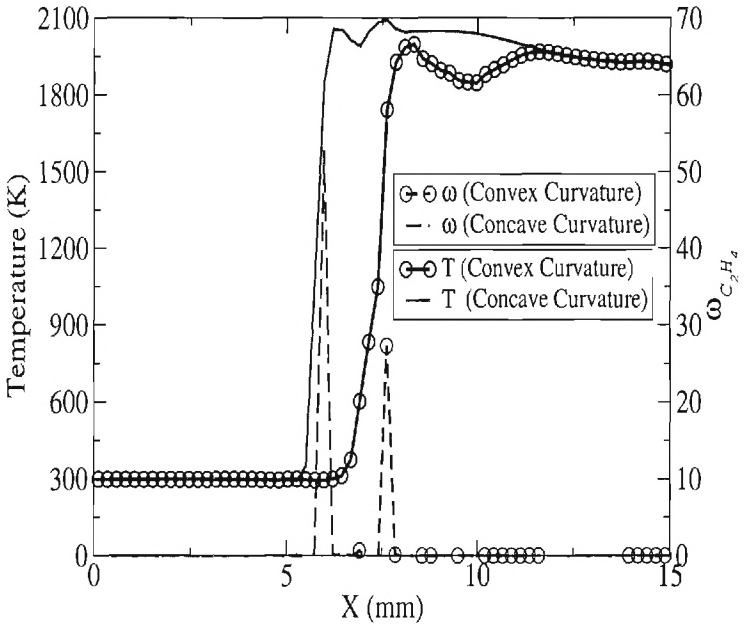

Figure 28: Instantaneous temperature and C_2H_4 reaction rate at a convex and concave flame segments with variable diffusion coefficients

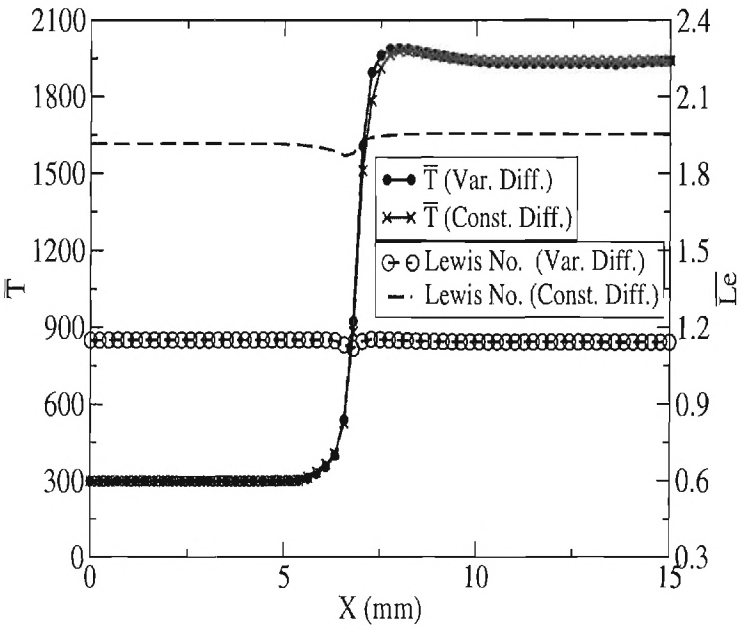

Figure 29: Mixture mean Lewis number and mean temperature profile comparison

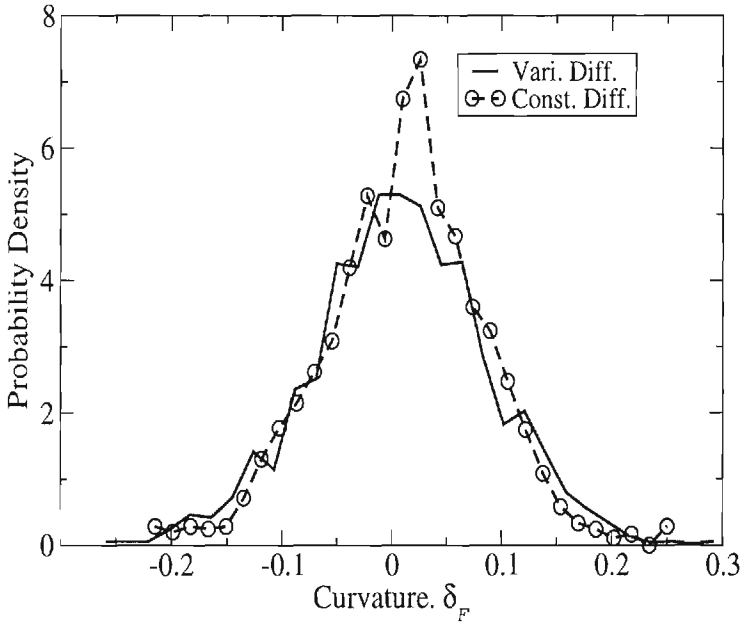

Figure 30: Mean Curvature probability density function (PDF)

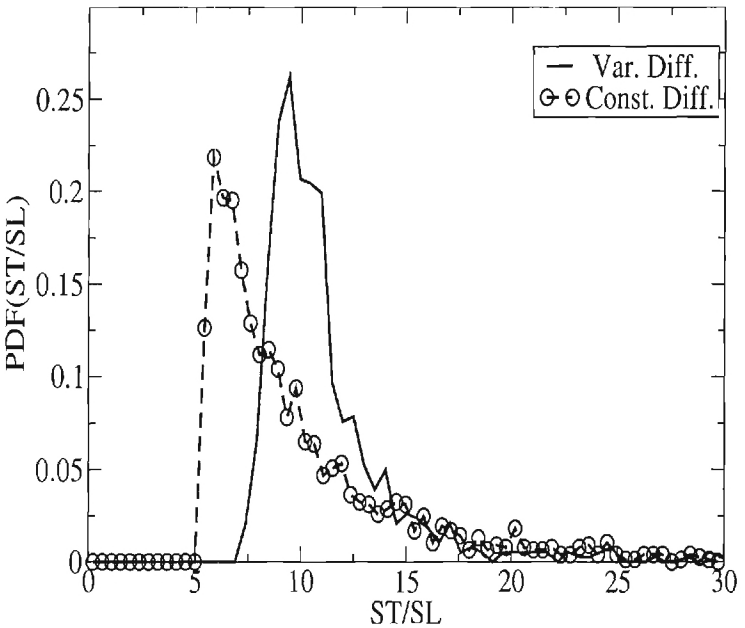

Figure 31: Mean normalized turbulent flame speed probability density function (PDF)

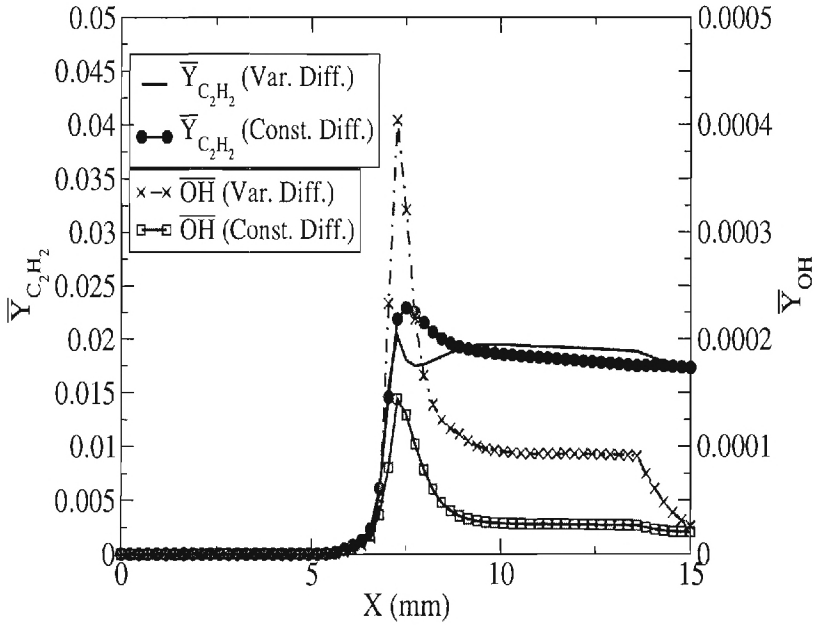

Figure 32: Mean mass fraction of acetylene C_2H_2 and hydroxyl OH

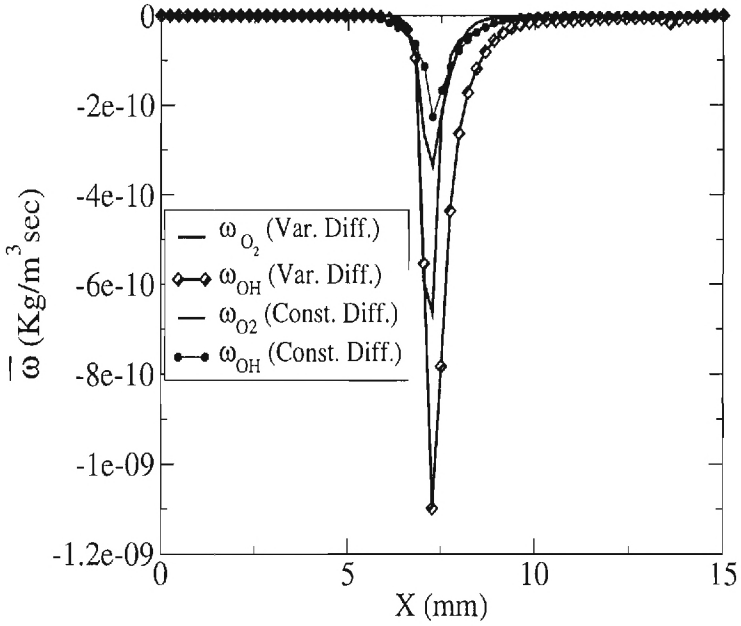

Figure 33: Soot oxidation rates

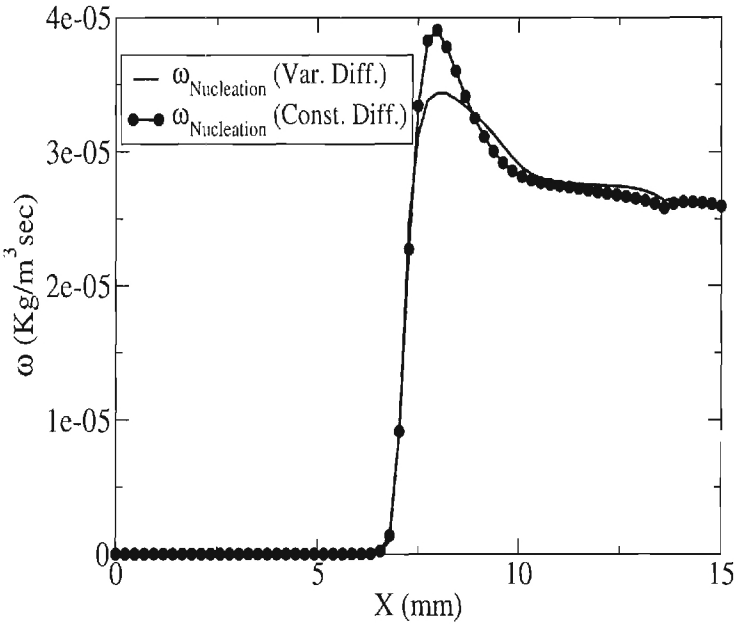

Figure 34: Soot nucleation rate

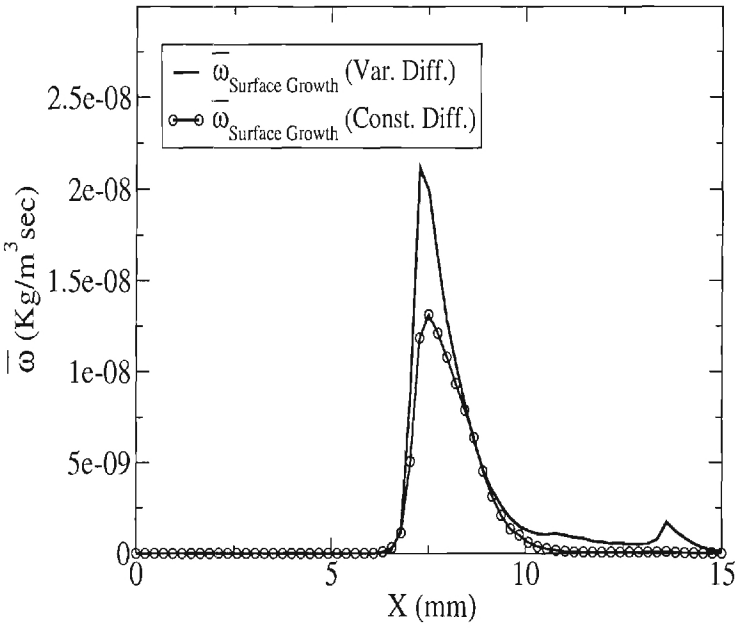

Figure 35: Soot surface growth

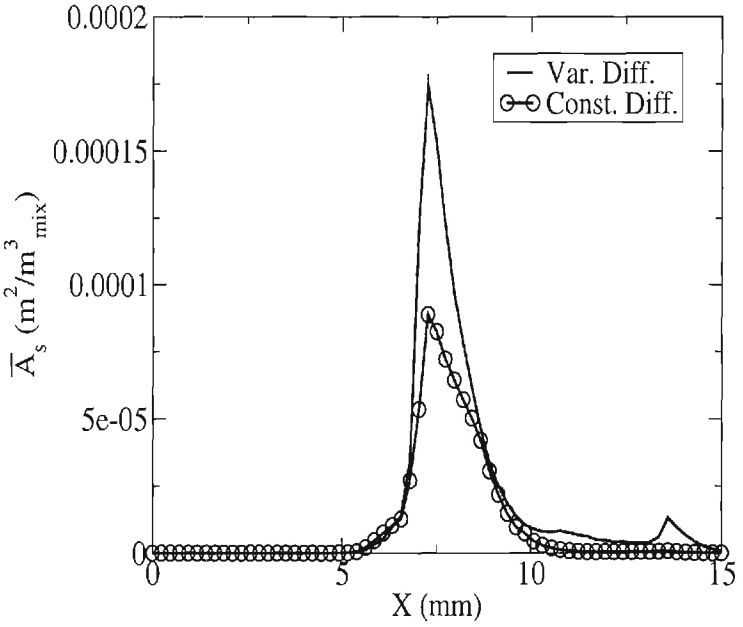

Figure 36: Mean soot surface area per unit mixture volume

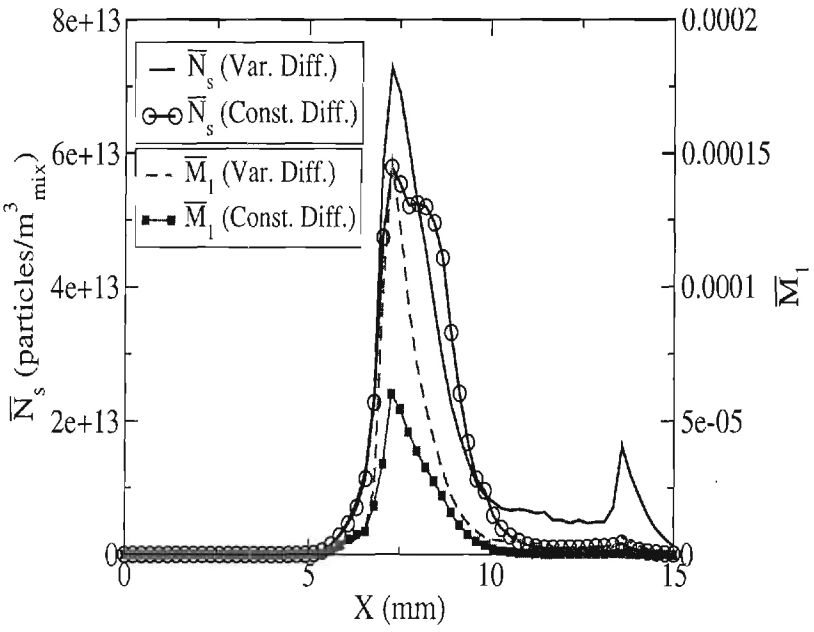

Figure 37: Mean soot number density and average mass per unit mixture volume

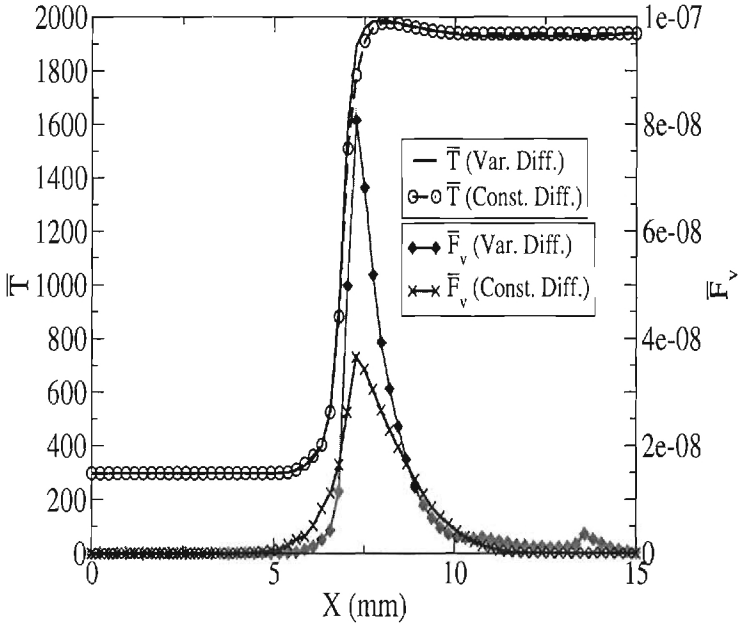

Figure 38: Mean soot volume fraction and temperature profile

8 Non-Premixed Non-sooting Flames

In the current section, two non-premixed flames are studied and compared to the experimental results. The case studies act as a precursor for the next sooting non-premixed flame.

Fuel-air mixing is a fundamental phenomenon that must occur prior to combustion in non-premixed systems. Efficient mixing and stable combustion over a wide range of operating conditions are essential for a successful combustor design. In most practical non-premixed systems, fuel is injected into regions of high turbulence to enhance mixing and flame is stabilized using either a geometrical or an aerodynamic flame holding mechanism. Classical examples of geometrical flame holders are the rearward facing step and the bluff body. The recirculating flow behind geometrical flame holders creates upstream transport of the burnt hot products, which in turn, can re-ignite and sustain the flame. In the aerodynamic flame holding approach, the flame is stabilized by creating a recirculation bubble, often called the vortex breakdown bubble (VBB), using inflow swirl. In some devices, both bluff body and swirl can be used in a coordinated manner to enhance fuel-air mixing and flame stability. An experimental device that combines swirling flow around a bluff body with centerline fuel injection has been well characterized in a series of experiments ([193, 194]), and is studied here using a large eddy simulation (LES) approach. A brief survey of the current experimental setup is given in the next section.

The first effort done on the current setup was by [195]. The experimental setup was for a bluff-body stabilized turbulent diffusion methane flames. For bluff body configurations, three controlling parameters exist. The strength of the circulating vortex controlled by the external coflow air velocity $\bar{u}_e$, the fuel jet momentum controlled by the jet velocity $\bar{u}_j$ and the diameter of the bluff body. By fixing the first and the last and increasing the jet velocity the peak mean temperature at the radial profile decreases in the regions of intense mixing. These regions extend for two bluff body diameters downstream of the recirculation zone. They designed the experiment such that no extinction occurs near the nozzle. In otherwords, the intense mixing and the turbulence-finite rate chemistry interaction will take place in the fully turbulent regions away from the nozzle exit. The flame is stabilized by a double toroidal recirculation zones formed on the bluff body base. By changing the u_e/u_j three type of flames are observed. The first is controlled by the external air stream, where all the jet fuel is consumed at the bluff body face and never penetrate the RZ region. The second, is a transient flame, where the fuel jet intermittently penetrate the RZ. The third flame type is a long flame, controlled by the fuel jet velocity, where the jet penetrates the RZ. For the last flame type, as the jet velocity increases a blue neck starts to form downstream the RZ. By increasing u_j further the flame starts puffing (they define the blow off limit by that), then blow-off from the blue neck region.

They also investigated the effect of mixing N_2 with the fuel, which shorten the flame and reduces the blow-off limits. They concluded also that the flame-turbulence interaction is largest in the neck region, where the temperature profiles are affected by changing the u_e/u_j ratio. The same configuration mean and instantaneous scalars composition was shown in [196] for a variety of flame conditions and jet fuel composition, [197] and [198]. They observed three mixing layers in the RZ, one between the air stream and the outer vortex, another between the fuel jet and the inner vortex, and one between the inner and outer vortex. As the fuel jet momentum increases the stoichiometric contours come closer to the centerline

to conserve continuity. In addition, [199] reported that the NOx production depends on the structure of the RZ. From the numerical work conducted in simulating bluff body stabilized flames, [200] using k-ϵ model, [106] using LEM-LES, and PDF methods by [201] and [193]. The RANS models shows discrepancy in the length of the RZ, the spreading and the decay rate. On the other hand, LEM-LES shows good comparison and adequate capturing of heat release and mixing. The PDF method shows good centerline and radial predictions, with slight over-prediction of some major species. However, still the main difficulty lies in the RZ on the face of the bluff body, where the velocity, mixing of the scalar fields are very complex and the residence time is rather too low and need more computational efforts to converge to the steady state situation. A summary for most of the experimental data and numerical results for bluff body stabilized flames on this configuration can be found in [202].

[193] introduced the next level of complexity by adding the swirl component to the above bluff body stabilized flame geometry. In this paper represents the first experimental results for the swirl burner velocity field. In the same work, they used a Monte Carlo-based PDF method combined with a flamelet library to represent chemistry. The method used the simplest type of models for closure of the molecular mixing (IEM), velocity (SLM), and the turbulent frequency (JPM). The computations reproduced the flame structure, with reasonable agreement of the velocity field. They designed the swirl burner to match the following requirements:

- The burner can provide strong enough swirl to cause vortex breakdown and recirculation.
- The burner still has a simple well defined boundary conditions.
- It should be amenable to laser diagnostic methods.
- Have flame regions, where the interaction between turbulence and chemistry is significant.

The configuration of this burner is the same as used here and will be described later. Fixing the geometry (the bluff body diameter) three other factors will control the flame stability and structure, which are:

- The jet central velocity U_j.
- The axial and tangential components of the swirling flow.
- The co-flow secondary air velocity.

They also discussed the stability curve for this burner. As the swirl number increases (increasing the tangential swirl component, or decreasing the axial swirl component) the stability of the flame (before blow off) increases then suddenly decrease (lower than the bluff body value) and then increase sharply again. The region where the stability decrease is the transient period of the vortex breakdown establishment. The flame length was found to be 5 times shorter than the zero swirl (bluff body) flame at swirl numbers beyond the vortex breakdown.

[203] introduced the compositional structure and flow field of two flames on the same burner. The two flames have the same swirl number with different jet velocities. They defined two main asymptotes, the burning asymptote, where the temperature and composition refer to a burned mixture, and the mixing asymptote, where the mixture temperature is moderate or contain combustion products due to mixing but is unburned.

[204] expanded these experimental results and tabulated all the possible type of flames that is produced by this burner under different swirl, jet and fuel (CH_4, $CH_4 - air$, and $CH_4 - H_2$) conditions. They observed two general blow off locations, one at the neck region and the other, where the flame beels off from the base at higher swirl numbers. On the other hand the $CH_4 - air$ flames only undergoes base blow-off. While only the velocity field data is represented in this paper, the detailed composition measurements are represented in other paper by [194]. All results are tabulated online [205]. They observed that for the same configuration changing one of the above parameters will change the flame structure. Nine flame shapes are identified. The transition swirl number between the low and the high stability regimes is identified between $0.3 - 0.4$, beyond which vortex break down is established and the flame is more stable. However, increasing the primary axial air velocity, while the geometrical swirl is above $0.3-0.4$ improves the flame stability. Below this threshold the SMA ($CH_4 - air$) flames cannot be stabilized, while the SM (CH_4) flames is vulnerable to neck then base blow off.

The corresponding non-reactive test cases were published by [206]. Five cold flow test cases were examined with the same jet velocity and co-flow secondary air speed. The swirl number is varied by variation of the axial and tangential components of the primary air flow. This paper is important since, it eliminates the combustion effect and focuses on the swirl and aerodynamic one. The vortex breakdown onset was found to depend not only on the swirl number but also on the axial momentum of the swirled flow. For instance, the higher swirl number $N16S159$ shows no (VBB), while the lower swirl number case $N29S054$ shows vortex break down bubble at the centerline, although it has half the swirl number but double the axial momentum. The shear stresses are highest inside the recirculation zones and the rotating structures due to the high velocity gradients at such locations. The presence of these recirculation zone enhances mixing between the inner fuel jet and the outer air primary and secondary streams. the fuel parcels are engulfed inside the recirculation zone to the outer stream and then engulfed inside again at the end of the recirculation zone. Also, in comparison with the bluff body case the recirculation zone is larger in the $N16S159$ case but smaller in the $N29S054$ case due to the onset of the vortex break down that compresses the bluff body recirculation zone.

The bluff body stabilized flames have been simulated by many groups. For instance using LES by [207] and [208], PDF methods by [209]. On the other hand few works (including the current work) attempt to simulate the swirling flow case. [210] simulated the SMH2 CH_4/H_2 flame using RANS methods. In the past, LES has been applied with reasonable success to relatively simple, non-swirling laboratory non-premixed flames ([127, 209]) and more recently, to more complex bluff body stabilized (but still non-swirling) non-premixed flames ([207, 89]). However, so far, no one (at least to the authors knowledge) have simulated the swirling, bluff-body stabilized non-premixed flame ([193, 194]) chosen for the current study. They concluded that RANS failed to predict any transient phenomena as flame instabilities. In addition, by using a simple eddy breakup model, as they increase the heat

of reaction the flow precession and instability diminishes.

The most recent work published for these series of swirling flame was by [211]. The flame instability modes are investigated by using two experimental methods. In general, two modes of instability are recognized for this burner. The precession mode in the center fuel jet and the puffing mode that is characterized by an expansion and collapse of the recirculation zone on the face of the bluff body. For the swirl burner isothermal flow shows that the two controlling parameters for the instabilities associated with isothermal flows are the Strouhal and the swirl numbers ([212, 210]). As the swirl increase beyond S_g=0.2 the jet starts precessing. The precession increases with the swirl number increase then starts to decline after a second limit S_g=0.5. The disappearance of this precision coincide with the vortex breakdown. This instability mode is named Mode *I*. Another mode of instability is added to Mode *I* with combustion and heat release. The first experimental technique (Mie scattering) reveals no Mode *I* instability for the SM1 and SMA2 flames. However, the SM1 jet was observed to alternate above and below the centerline. Since, this behavior is not periodic it couldn't be depicted as an instability mode. The SMA3, SMH2 and SMH1 show Mode *I* instability. Puffing was observed for the SM2 and the SMH3 flames, where the recirculation zone collapse and expand periodically. However, the shadowgraph shows that the SMA2 has Mode *I* instability.

Many LES approaches, with their respective subgrid closure approaches have been developed. There are advantages and disadvantages for every method ([213, 68]). Here, we apply a subgrid mixing and combustion approach developed earlier to this flame. Past studies have demonstrated the ability of this model for scalar mixing ([127, 214, 110]), premixed combustion ([100, 113, 182]), non-premixed mixing and combustion ([127]) and spray combustion ([215, 216]).

In the next section, a brief review on swirl flows and vortex breakdown literature will be presented. Next, the numerical set up and conditions are described and then, results for the non-reacting and reacting studies are reported. Finally, we conclude this study and note some future research issues.

8.1 Swirling Flows and Vortex Breakdown

One of the first major reviews on swirl flows is by [217]. The main effects of introducing swirl in a combustor are summarized as:

- Reduction in the mixing length needed to consume the fuel. Hence, the flame length is reduced.
- Improving the flame stability by allowing a longer residence time for mixing of the fuel and fresh air with products in the recirculation zones. In addition, the jet velocity requirements for flame stability will be much more relaxed.
- Reduces the flame impingement with the injector are by creating an aerodynamic blockage.

Generally, the swirl flow can be achieved either by a swirling guide vanes in an axial cylinder or injecting the flow tangential to the cylinder surface. In the swirl vane burner,

dome important observations are represented. The swirl number is found ro correlate with the recirculated mass in the recirculation zone. If S is the swirl number and M_r is the non-dimensional recirculated mass, then a data fitted equation is given as:

$$S = 0.5608 + 5.66M_r - 6.25M_r^2 + 2.28M_r^3$$

Although the critical swirl number for onset of a recirculation zone was set to 0.6, the shape of the injecting nozzle (divergent or straight) affects this number. For instance, Syred mentioned that using a divergent nozzle will reduce the critical value, increase the size of the reverse flow zone, and reduce the pressure losses across the nozzle. In other words the geometry of the injection nozzle and the swirl generation method can change the swirl flow characteristics. Increasing the swirl number further will lead naturally to the vortex breakdown phenomenon, where a central recirculation zone is established at the centerline. The three main forms of the vortex breakdown are the antisymmetric, spiral, and double helix. The occurrence and location of the second vortex breakdown is found to be a function of both the swirl number and the Reynolds number. The vortex breakdown phenomena can be considered either as an instability process, or a transition between a regime that can easily change by small perturbation of Reynolds number (the first generation of the toroidal recirculation zone) and a second more stable regime. However, occupance of the vortex breakdown may lead to the occurrence of another form of three dimensional instability known as the precessing vortex core (PVC).

In PVC the central vortex region becomes unstable and starts to precess about the axis of symmetry. The PVC usually lies between the inner boundary of reversed flow and the zero velocity streamline, where the turbulent kinetic energy is maximum. The core of the PVC usually is accompanied by high tangential velocity fluctuations. The sinusoidal action of the PVC is usually transmitted to the outgoing flow. The effect of combustion is found either to damp or excite the PVC formation. The flame type and the injection geometry affects this behavior as well. [217] found that premixed flames behave like isothermal flow, where a PVC with a similar precision frequency shows up, while non-premixed flames damp the PVC. For low Reynolds number as the mixture fraction is reduced the PVC is more damped. The intensity of the PVC recirculation also is found to increase significantly with the Reynolds number and slightly with the mixture ratio. The PVC can be controlled by reducing the drop in the total pressure in the axial and tangential directions.

Considering the blow-off limits, the effect of increasing the swirl number increases the rich blow off limits and reduces the lean one. However, the swirl number increases so much the recirculation zones will be long enough to withdraw cold air outside of the burned gases and the efficiency of the combustor is reduced.

8.2 Chemistry Closure

Although multi-step reaction kinetics can be included within LEM , in the current study, since we are not interested in soot formation, a global one-step mechanism for methane-air combustion ([218]) is used:

$$CH_4 + 2O_2 + 3.76N_2 \longrightarrow CO_2 + 2H_2O + 3.76N_2 \tag{221}$$

with a reaction rate given by:

$$k = 2.4E16exp^{-24358.3/T}[CH_4][O_2] \tag{222}$$

This five-species mechanism is not expected to capture all the features seen in the experiment but is considered reasonable (and obviously, computationally "cheap") to predict the global features, especially the effect of heat release on the velocity field.

8.3 Configuration and Numerical Setup

Figures 39, 40, and 41 show respectively, the Sydney swirl burner ([194]), a schematic of the computational domain simulated in the current study and a representative grid distribution. The burner has a bluff body of diameter $50mm$ with a central 3.6 mm diameter fuel injector. The primary air stream is injected from an annulus that surrounds the bluff body, with an outer diameter of 60 mm. The blockage ratio, $(2r_b^2/2r_s^2)$, is equal to 0.69 where r_s is the outer radius of the annulus and r_b is the bluff body radius ([204]). The burner assembly is placed in a SNL wind tunnel with a square cross sectional area of 305 mm x 305 mm. The wind tunnel provides a secondary air co-flow with a free stream turbulence level of 2%.

The flow conditions are extracted from the Sydney university web-page ([205]) for swirl and bluff body stabilized flame configurations. Table 3 shows the different inflow parameters for both the cold and the hot test cases simulated here ([204]).

Here, U_j is the central jet velocity, U_s is the axial velocity component of the primary air flow, U_e is the secondary axial wind tunnel co-flow velocity and Re is the Reynolds number based on U_s and the bluff body diameter. The geometrical swirl number S_g is defined as the ratio of the mean bulk tangential to axial velocity ([194]), $S_g = \frac{\overline{W_s}}{\overline{U_s}}$ and the flow swirl number S is defined as the ratio of the axial flux of tangential momentum divided by the axial flux of axial momentum ([219]) as:

$$S = \frac{\int_0^R \rho u_x W_\theta r^2 dr}{R \int_0^R \rho U_x U_x r} \tag{223}$$

For the flow conditions reported here, a value of $S = 0.61$ is obtained. This value is close to the critical swirl number (typically, around 0.6) and therefore, is high enough to create the classical vortex breakdown bubble ([217]) downstream of the dump plane. For the reacting case, this bubble, along with the base recirculation zones are expected to provide the stabilizing mechanism for the flame, as discussed later.

Ideally, the LES computational domain should include the entire swirl burner assembly (including the upstream swirl assembly) in order to capture the proper inflow into the combustor. However, this is an expensive approach and is not adopted at present. Instead, as shown in the schematic diagram in Fig. 40, the simulation starts at the injector outlet cross section. Since there is no data available at this location (the first location available is 6.8 mm downstream of this location ([205]), prescribing proper inflow profiles at this location is difficult, but not impossible if proper care is taken. In our study, the profiles at the inlet were adjusted to match the global flow rate and also the near-field profiles at 6.8 mm as best as possible. Figure 42 shows the three component of the velocity used at the inlet of the computational domain.

The computational domain is 210 mm in length with 305 mm x 305 mm cross sectional area. Thus, in this study, the complete SNL wind tunnel facility is included in the computational domain. A two-domain butterfly type grid is used with the centerline region resolved using a Cartesian grid, while the rest of the domain is resolved using a cylindrical grid. The choice of the grid resolution is dictated in part by the need to resolve the critical large-scale features and by the limitation of the subgrid closure. In LEMLES, the 3D LES grid resolution constraint is determined more by the need to resolve the important large-scale transport simulated on the LES grid than by the subgrid LEM needs. The localized, dynamic k_{sgs} model allows for non-equilibrium between production and dissipation of kinetic energy in the subgrid scales ([122]) and therefore, allows a relatively coarser grid (when compared to the Smagorinsky's algebraic model, which requires an equilibrium assumption and hence, ideally requires a finer grid) without compromising accuracy. Nevertheless, the shear layer around the fuel injector and around the bluff body still needs to be resolved adequately in order to capture the dynamics of large-scale mixing.

Preliminary simulations were conducted to determine the impact of grid resolution on the resolved features. For all the results reported here the inner Cartesian grid resolution is $210 \times 38 \times 38$ in axial, horizontal and vertical directions, respectively, while the outer cylindrical grid is $210 \times 110 \times 153$ points in the axial, radial and circumferential directions, respectively. We employ the same grid for both the cold and the hot flow test cases so as to make a direct comparison. The grid is clustered in the regions of high shear, especially in the swirling annular flow. It is estimated that the shear layer between the primary and the secondary air flow is resolved by over 10-15 points, which is considered reasonable. The fuel injector cross-section, which is 3.6 mm in diameter, and its shear layer are well resolved inside the Cartesian grid with nearly 38×38 grid points. Although an immersed boundary approach is available to resolve the circular boundary on a Cartesian grid ([220]), at this time, we decided to approximate the wall on the Cartesian grid due to the high resolution available in this region. Analysis shows that the jet shear layer evolves rapidly and shows very little boundary influence within 2-3 mm downstream of the inlet.

Using this LES grid and the analysis of the non-reacting simulation (discussed below), it is determined that $\eta = 0.044mm$ in the swirling shear layer region (based on maximum observable rms value = 6 m/sec), where $\overline{\Delta} \approx 0.5mm$. However, the Kolmogorov scale is $\eta = 0.025\ mm$ for the SM1 flame, and $\eta = 0.02\ mm$ for the SMA2. This implies that approximately 12 LEM cells are needed to fully resolve η. For computational expediency, we use 9 LEM cells within each LES cell and thus, the subgrid LEM resolution is capable of resolving $3 - 4\eta$ within these LES cells for the reactive case.

The solver is highly optimized and highly scalable for simulation on all parallel systems (including of-the-shelf PC clusters), and in particular, the subgrid LEM is optimal on such systems since the LEM simulations are conducted locally within each LES cell. Therefore, although LEMLES is computationally expensive (as per single processor hour estimate), on a parallel system, such simulations are becoming quite routine, especially if reduced kinetics are employed ([132]). This is emphasized here since, in the past, a major criticism of LEMLES has been the perceived computational cost. However, it is argued here that with proper parallel implementation and with the availability of cheap PC clusters, LEMLES of full-scale gas turbine sector simulations have started to become feasible with a reasonable turn-around time ([164]). With the rapid increase in computer technology and the scalability

of the LEMLES approach, future simulations of realistic devices, even with relatively detailed kinetics, may become practical.

For the present study, a typical flow through time (based on the bluff body diameter and the primary air flow inlet velocity) takes around 400 single-processor hours for the non-reacting LES case and 4483 single processor hours for the LEMLES on a Intel Xeon (3.44 GHz) PC cluster employing an Infiniband switched network. For all the results reported here, LES results are averaged around 6 flow through times after the initial transients.

8.4 Results and Discussion

In this section, we discuss the LEMLES results by comparing the time averaged velocity and some scalar statistics with the measurements. We begin this discussion by first briefly analyzing the non-reacting LES results and then focusing on the reacting case. Additionally, discussion will highlight the main differences between the SM1 and the SMA2 flames, as observed in the simulations.

8.4.1 Non-Reacting Flow Results

For the non-reacting simulation, an air jet is injected from the fuel injector and all conditions are chosen to match the test conditions, as best as possible. The overall time-averaged flow features show that there are two regions of recirculation or reverse flow. A region just behind the bluff body contains a toroidal recirculation zone (RZ) that is characteristic of base flow and extends about half the bluff body diameter downstream of the dump plane. There is another region further downstream approximately between $x = 50$ mm and $x = 120$ mm that is characteristic of the vortex breakdown bubble (VBB) associated with swirl flow ([206].)

Figures 43(a) and (b), show respectively the velocity vector field in the RZ and VBB regions. The positive axial velocity contour are superimposed on the velocity vector plot to clarify the flow features. The inner black line represents the zero-velocity contour. Figure 43 (a) shows that the toroidal RZ extends approximately half diameter downstream of the bluff body and surrounds the central air jet. The shape is highly 3D and converges towards the centerline. The fluid in-between the RZ and the central jet contains fluid that has very little motion near the base but further downstream, near the end of the RZ, the high speed central jet entrains this fluid and the flow is more aligned in the stream-wise direction.

Figure 43 (b) shows that the VBB region is an elongated structure approximately 70 mm in axial extent at the centerline beginning at around $x = 50$ mm with a width approximately 10 mm at this central plane. The peak reverse velocity in this bubble is around 4 m/s and turbulence intensity is around 8 m/s.

Figures 44 (a) and (b) show respectively, the iso-surface of the mean and instantaneous axial vorticity component. In the near field of the dump plane the flow is relative more azimuthally coherent, but further downstream, a wide range of scales is created as the swirling shear layer breaks down into more randomly oriented small scale structures.

We will revisit these non-reacting mean and instantaneous flow dynamics when discussing the reacting data to highlight the similarities and differences. To summarize the observed mean flow features, a schematic diagram is shown in Fig. 45 that identifies the shape and size of the RZ and VBB and the flow in-between them. As shown, surrounding the RZ

toroidal structure there exists a collar like structure as shown by the contour lines of the azimuthal velocity component. These structures are non-circulating with a high rotational speed. They are mainly established due to compression of the flow field between the outside nearly stagnant flow and the edge of the toroidal recirculation zone.

These observations are quantified by comparison with the data. The centerline mean axial velocity comparison is shown in Fig. 46. The extent of the VBB is clearly observable and is located in the LES between around $x = 50$ mm and $x = 120$ mm, while the experimental data suggests that the streamwise extent is between $x = 50$ mm and $x = 110$ mm. The over-prediction of the downstream end of the VBB is attributed to the coarsening of the grid beyond $x = 100$ mm. Nevertheless, the overall agreement with data ([212]) is considered acceptable.

The radial time-averaged mean axial, azimuthal and radial velocity profiles at four upstream locations, between 6.8 mm and 30 mm (before the VBB) are shown in Figs. 47 (a)-(c), respectively. The corresponding profiles at three locations in the region between 40 mm to 100 mm (downstream of the RZ primarily in the VBB) are shown in Figs. 48 (a)-(c). The agreement is considered reasonable at all locations. In the near-field, the mean axial velocity shows a peak around R = 28 mm in the shear layer between the primary and the secondary flow. This peak decays axially as the shear layer spreads so that, by around 70 mm, there is no longer any discernible peak. The radius of the RZ ahead of the injector starts with 23 mm and shrinks to 13 mm at x = 30 mm. The radial spread of the flow field at each axial location is indicated by the location where the mean azimuthal velocity $\overline{W_\theta}$ is zero. This location is shown to be around $R = 30$ mm. The mean azimuthal velocity component peaks at $x = 28$ mm due to the formation of the highly rotational collar-like structures. This peak starts to diminish after $x = 50$ mm, where the VBB starts to form.

The three-component root-mean-square (RMS) velocity fluctuation radial profiles at the first four upstream locations are shown in Fig. 49 and the corresponding profiles in the three locations further downstream are shown in Fig. 50. Overall, there is reasonable agreement at all locations. The axial component shows a bimodal behavior at $x = 6.8$ mm. This bimodal behavior is related to the location of the jet and the shear layer. The radial and azimuthal components also show two peaks at the same locations. There are some discrepancy in the peak value in the centerline region, especially for the azimuthal component, but overall, the agreement is considered acceptable.

An encouraging aspect of this cold flow LES study is that many of the finer details typically needed for LES inflow setup (inflow turbulence spectrum, turbulence profiles, etc.) may not be that important (at least for this setup) since most of the features are captured with reasonable accuracy without this knowledge, as demonstrated in the above figures. The key seems to be in providing a reasonably accurate mean profiles. It is, however, noted that based on past observations ([221]) the accuracy of the current LES is partly due to the k_{sgs} localized dynamic subgrid closure that has shown an ability to capture flow physics even when the grid is not highly refined. As discussed in the next section, this ability also plays a fundamental role in the reacting flow simulation since k_{sgs} is used to determine some of the key parameters of the subgrid mixing model.

8.4.2 Reacting Flow Results

The flow features for the SM1 flame are fairly conventional for swirl flow past a bluff body. Due to flow separation from the circular bluff body, there is a toroidal recirculation zone (RZ) in the base of the bluff body, and further downstream there is a VBB around the centerline due to the swirl effect. For the SM1 case, the base recirculation region extends to around $x = 32$ mm. The toroidal RZ shape is due to the presence of the central circular fuel jet. The VBB is observed downstream between $x = 76$ mm and $x = 96$ mm, and is about 16 mm in diameter in the $y - z$ plane at its maximum thickness. Overall, these two recirculation zones agree quite well with the experimental observations ([204]).

Figures 51 (a) and (b) show respectively, the velocity vector plot in the RZ and VBB region for the SM1 case. The region is similar to the non-reacting zones shown earlier in Figs. 43 (a) and (b). Again, the positive axial velocity contours are superimposed to visualize the flow field. Figure 51 (a) shows that the toroidal recirculation zone is again established downstream of the bluff body and extends to around $x = 32$ mm. The toroid is about 10 mm radius in the spanwise direction. The overall shape is not the same as in the non-reacting case. The toroidal zone is more elongated than the cold flow case and more open in the radial direction. In addition to the different jet and swirl velocities for both cases, the rate of decay of the axial velocity is different, which will be discussed later when discussing the centerline velocity.

The mean SM1 flame and flow structures show these observations model clearly. Figure 52 (a) shows a iso-surface of the temperature at T = 1800 K surrounded by the axial vorticity iso-surface. The flame is shrouded by the vortical structures and is anchored at two locations, one close to the bluff body, and the another downstream the centerline. The flame necking is again seen around $x = 50$ mm. Figure 52 (b) shows another view of the same flow features except that the axial vorticity is shown inside surrounded by the axial velocity iso-contours. Coherent flow structures are shown close to the bluff body. Since the velocity gradient is high at the shear layer, high axial vorticity magnitude structures are generated in-between the primary and the secondary flow field.

To visualize the swirl effect, few representative streamlines are traced from the injector and shown in Fig. 53, which shows the mean velocity streamlines from the central jet (inside) and the primary air flow (outside). The azimuthal velocity component at the primary air injector generates a pressure gradient in the axial (adverse) and radial directions, the balance between the axial momentum and the adverse pressure gradient generates the VBB downstream, which is showed by the twist of the jet streamlines at the centerline in Fig. 53.

Figure 54a shows a visualization extracted from the SM1 simulation that highlights all the key features and characteristic scales. In-between the base RZ and the swirl-induced VBB, there exists a collar-like vortical shear region with high rotational (azimuthal) velocity as the separated shear layer first turns towards the centerline and then diverges around the VBB. The contour plots of constant mean ϕ are superimposed to show the flame structure. The black boundary is the stoichiometric line (the scalar features are discussed in the next section).

In comparison, the SMA2 flame (Fig. 54b) shows only a single elongated RZ downstream of the bluff body. The recirculation zone extends axially to $x = 99.2$ mm, which is comparable to the 100 mm in the experiment. No VBB is observed for the SMA2 flame and this is

attributed to the higher fuel jet axial velocity in the SMA2 flame, which is nearly double the SM1 value. The swirl effect is also much lower for the SMA2 flame, and as a result, the adverse pressure gradient generated by the swirl component is not strong enough to overcome the axial momentum generated by the central jet.

8.4.3 Scalar Features of SM1 and SMA2 Flames

The flame length is predicted to be around 107 mm for the SM1 flame while it is 120 mm in the experiments ([194]). The estimation for the flame length is based on the mean stoichiometry equivalence ratio. This discrepancy is primarily in the downstream extent since, as shown later, the leading edge region is predicted quite accurately. Analysis shows that the coarser downstream grid resolution is the major culprit for this under-prediction. As observed in the experiments ([204]), a necking region is observed around $x = 50$ mm, where the flame cross sectional area decreases, and then increases at the tail region.

A qualitative visualization of the experimental image and the numerical shadowgraph, defined as $\nabla(\nabla\rho)$ are given in Figs. 55a and 55b, respectively. As shown, the flame is compressed by the collar-like structure and the inner jet, resulting in the necking feature. Clearly, the current simulation has been successful in capturing all these features of the experimental flame quite well. Similar conclusions can be drawn for the SMA2 flame and omitted here for brevity.

8.4.4 Time-Averaged Velocity Statistics

Figure 56 shows the centerline variation of the axial velocity for the SM1 and the SMA2 flames. For comparison, the cold flow result (for CASE N29S054 [205]) is also included. Overall, there is reasonable agreement with data for all cases, although there are some deviations near the VBB region, as noted earlier. The VBB is smaller for the SM1 case, between $x = 76$ mm and $x = 96$ mm with larger negative velocity motion when compared to the non-reactive case. For the SMA2 flame, reverse flow is not observed at the centerline, and the rate of decay of the centerline velocity is much lower than the SM1 case.

Figures 57a and 57b show respectively, the time-averaged axial and azimuthal velocity components at various axial locations for the SM1 flame. The agreement is generally good. The axial velocity peaks in the shear layer, between the primary and secondary flow field. This peak decays axially and moves inward. The azimuthal velocity peak is located above the axial velocity peak inside the collar structure region, and decays inward and in the radial direction.

The time-averaged axial and azimuthal velocity profiles for the SMA2 flame are shown in Figs. 58a and 58b, respectively. The peak location and magnitude in the shear layer are captured reasonably. In comparison to the SM1 flame, the peak in the shear layer is much lower. The mean azimuthal velocity profiles show that the peak location and magnitude are captured reasonably as well. This peak decays axially and inward to vanish nearly around $x = 50$ mm.

Figures 59a and 59b show respectively, the radial profiles of the RMS axial and the azimuthal velocity fluctuations. Overall agreement is reasonable in the near field. The RMS values show a peak near the edge of the bluff body in the shear layer. There are, however,

some discrepancies near the centerline. Analysis suggests that one possibility is that the low velocity recirculation in the VBB region requires a longer time to reach stationary state than the simulation time used here for statistical analysis. This slow convergence is a typical computational problem for practical systems. However, the size and extent of the VBB settles down quite rapidly.

Figures 60a and 60b show respectively, the SMA2 flame's RMS profiles of the axial and the azimuthal velocity components. The axial velocity RMS shows two peaks, one at the interface between the RZ and the jet outer boundary, and another in the shear layer between the primary and secondary flow field. The shear layer peak smears out by $x = 30$ mm. Again, there are some discrepancies near the centerline, especially for the azimuthal velocity component.

8.4.5 Time-Averaged Scalar Statistics

Figure 61 shows that there is overall good agreement with data for the centerline mean temperature profiles for both flames. For the SM1 flame, the peak in the centerline temperature is predicted at around $x = 88.5$ mm. However, no data is available at or near this location to determine if this correct. The SMA2 centerline profile shows that the centerline temperature peak occurs around $x = 100$ mm. This is slightly over-predicted but the overall trend is captured reasonably well.

The time-averaged radial profiles of temperature at various axial locations for SM1 and SMA2 flames are given in Figs. 62a and 62b, respectively. At locations $x = 10$ mm and $x = 20$ mm for the SM1 flame (that are inside the RZ), the temperature peaks in the shear layer separating from the bluff body corner. Further downstream, as the shear layer spreads the temperature goes down and the peak moves toward the centerline. The radial profiles show overall good agreement with some local regions of over prediction. Considering that we are using a highly simplified reduced kinetics model these results are considered reasonable. The SMA2 temperature profiles also show generally good agreement, especially in the width.

Finally, the time-averaged H_2O mass fraction profiles for the SM1 and SMA2 flames are shown in Figs. 63a and 63b, respectively. The overall agreement is reasonable and consistent with temperature prediction. Again, under prediction is observed in the shear layer and close to center line at $x = 30$ mm. It is anticipated that these discrepancies may be eliminated if a more detailed kinetics is utilized.

Table 3: Cold and hot flow test case parameters

Flow Case	Jet	S_g	U_j	U_s	U_e	Re
N29S054	Air	0.54	66	29.74	20.0	59000
SM1	CH_4	0.5	32.7	38.2	20.0	76000
SMA2	CH_4/Air	0.5	32.7	38.2	20.0	76000

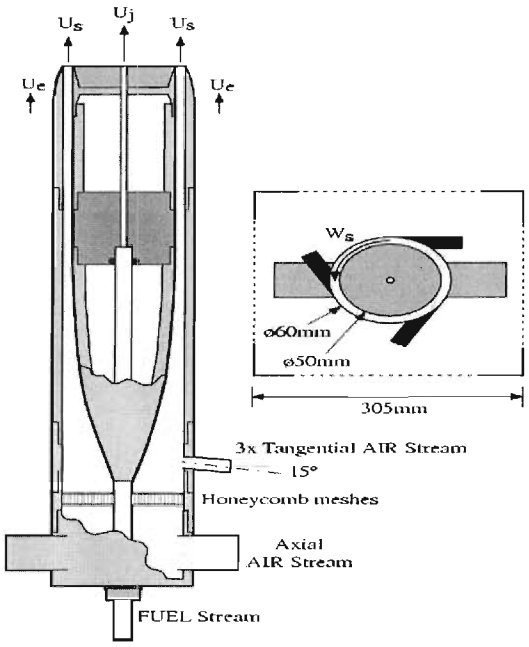

Figure 40: Injector setup.

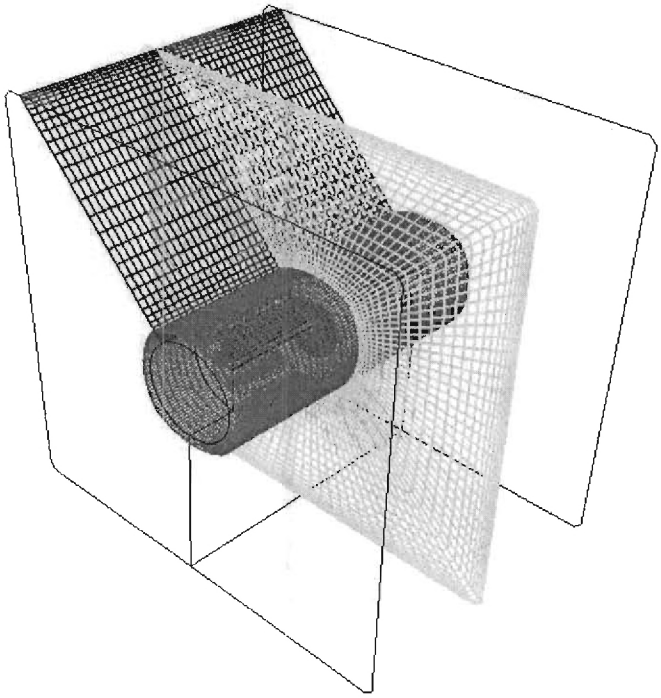

Figure 41: Grid

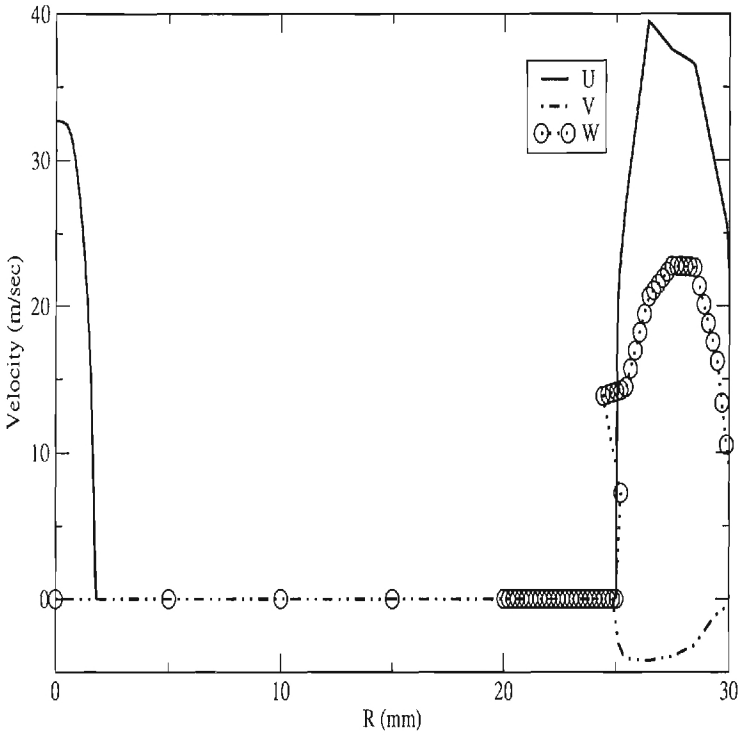

Figure 42: The inlet profile for the SM1 flame setup for the three velocity components

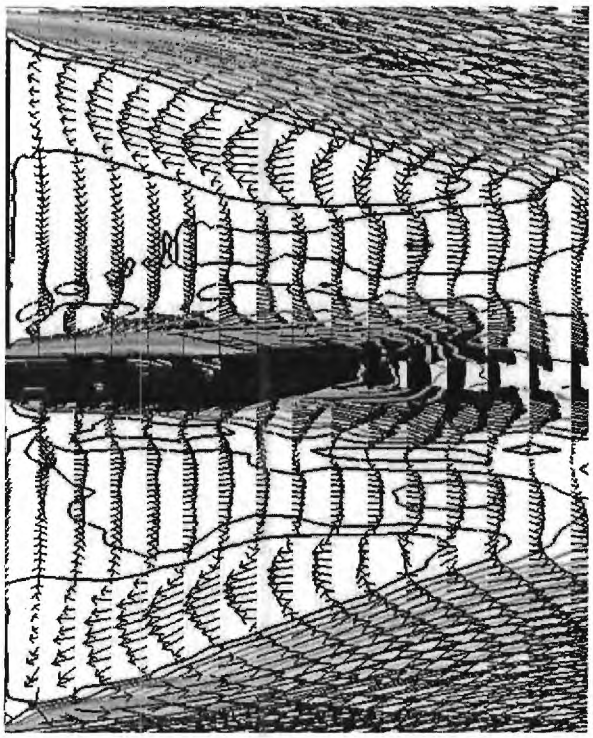

(a) Vector plot for RZ.

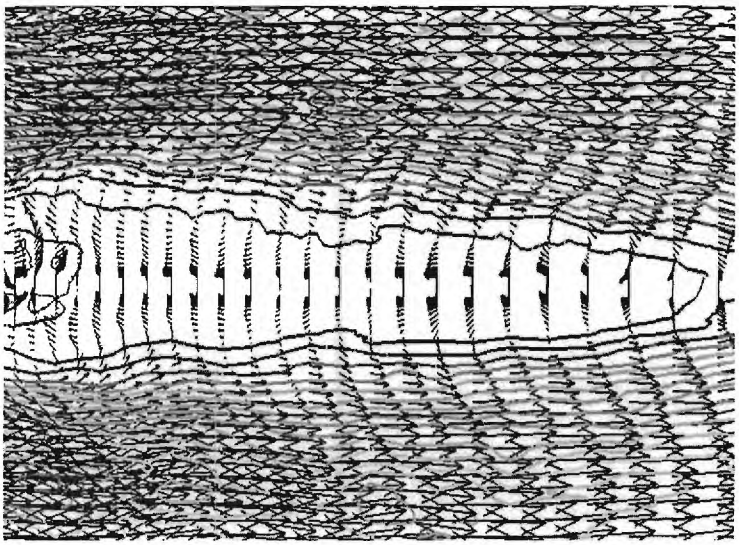

(b) Vector plot for VBB at the centerline.

Figure 43: Mean velocity vector plot in the x-y central plane combined with the positive axial mean velocity contours

(a) Mean axial vorticity iso-surface.

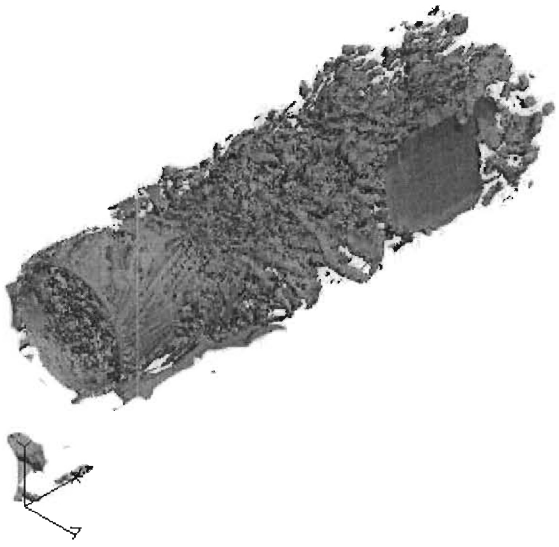

(b) Instantaneous axial vorticity iso-surface.

Figure 44: Axial vorticity iso-surface

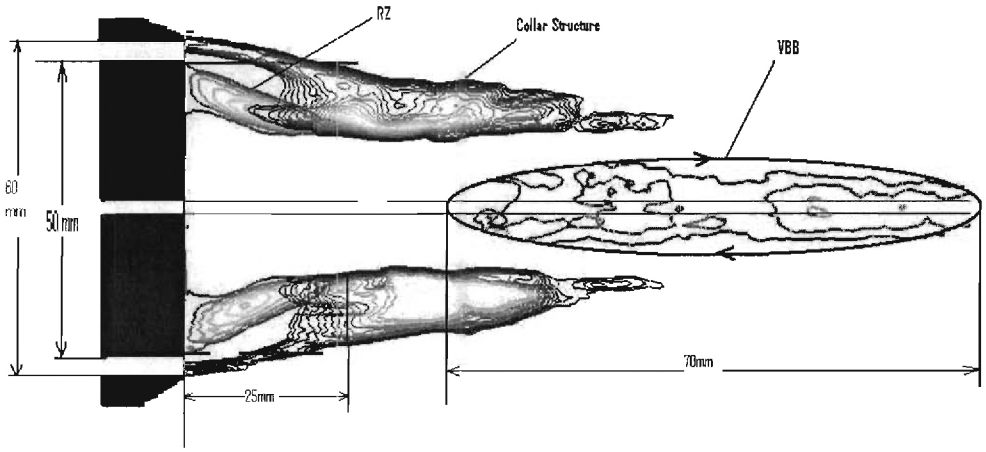

Figure 45: Flow field structure for the cold flow test case

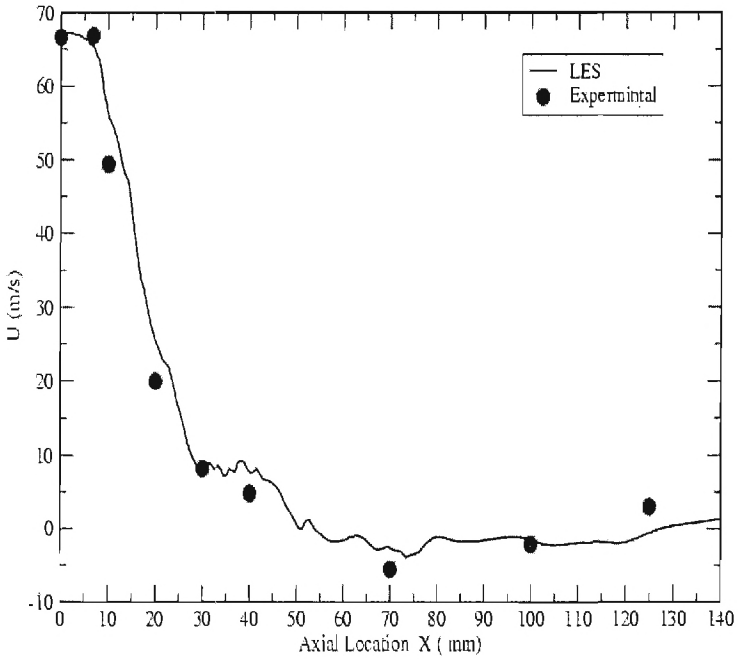

Figure 46: Centerline mean axial velocity profile

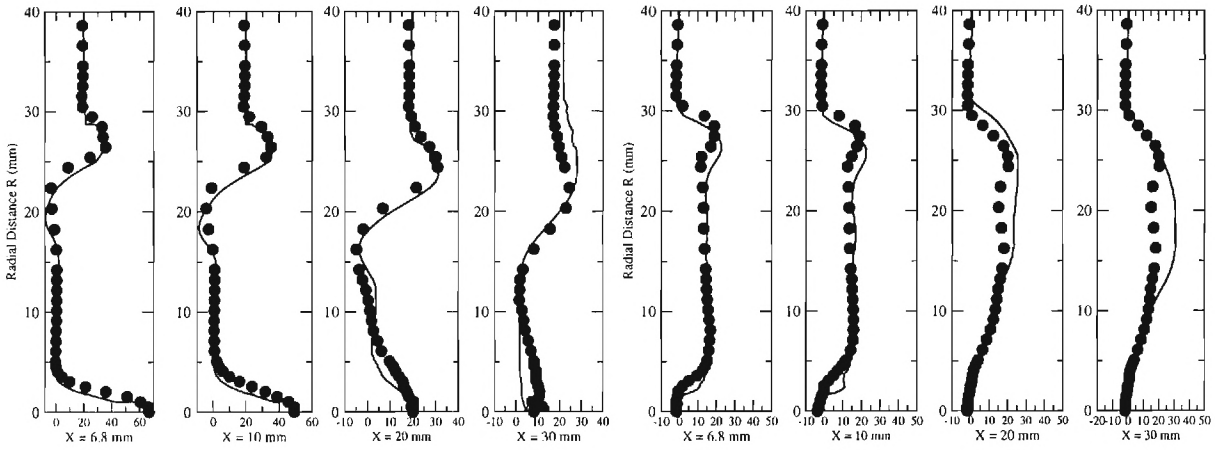

(a) $\overline{U_x}$(m/sec). (b) $\overline{W_\theta}$(m/sec).

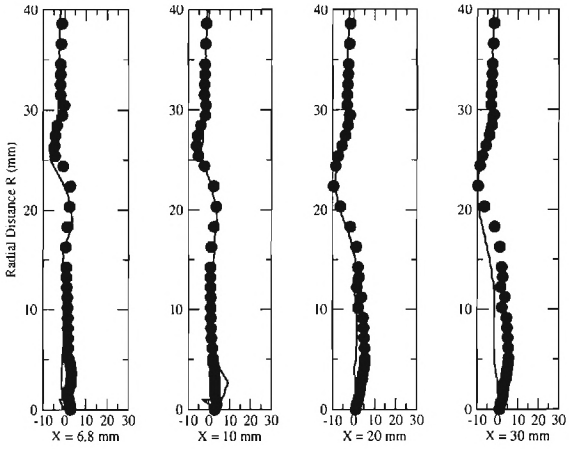

(c) $\overline{V_r}$(m/sec).

Figure 47: Radial mean velocity profiles, (LDV -•-, LES −) at $x = 6.8$ mm, 10 mm, 20 mm and 30 mm

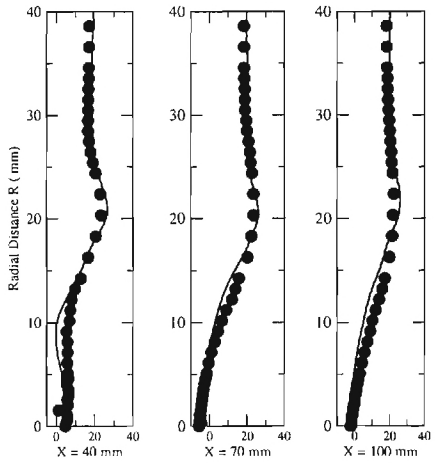

(a) $\overline{U_x}$(m/sec).

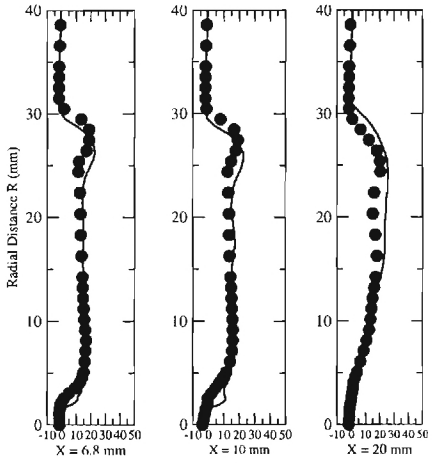

(b) $\overline{W_\theta}$(m/sec).

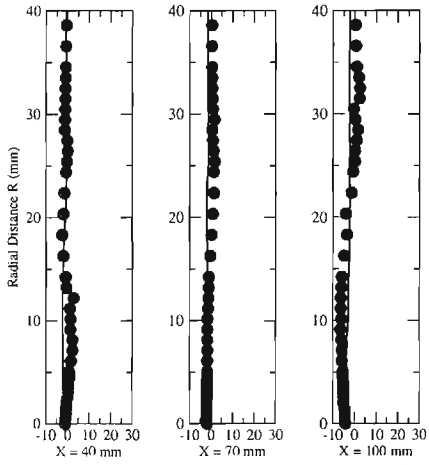

(c) $\overline{V_r}$(m/sec).

Figure 48: Radial mean velocity profiles, (LDV -•-, LES −) at $x = 40$ mm, 70 mm, and 100 mm

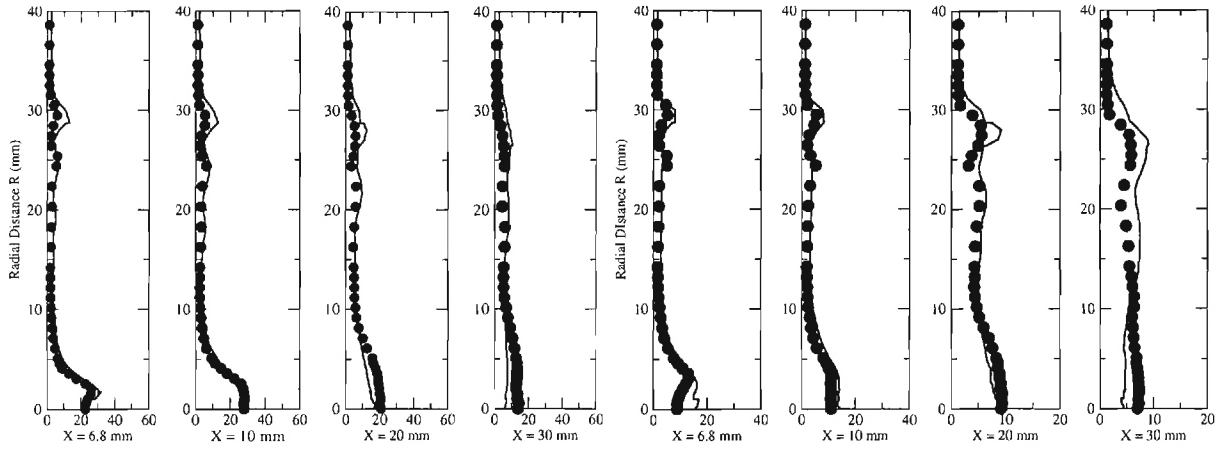

(a) U_{rms}(m/sec). (b) $W_{\theta}rms$(m/sec).

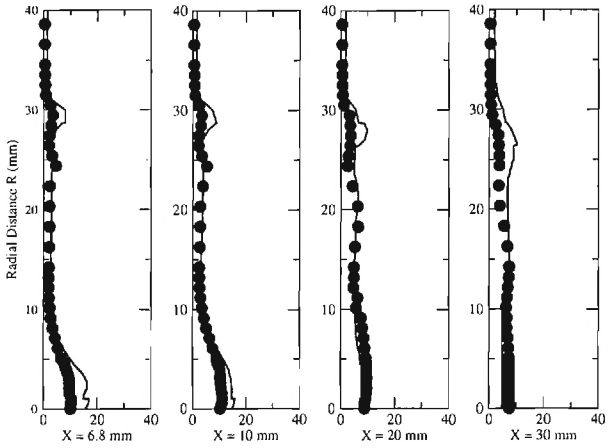

(c) $V_{r}rms$(m/sec).

Figure 49: Radial RMS velocity profiles, (LDV -●-, LES −) at x = 6.8mm, 10 mm, 20 mm and 30 mm

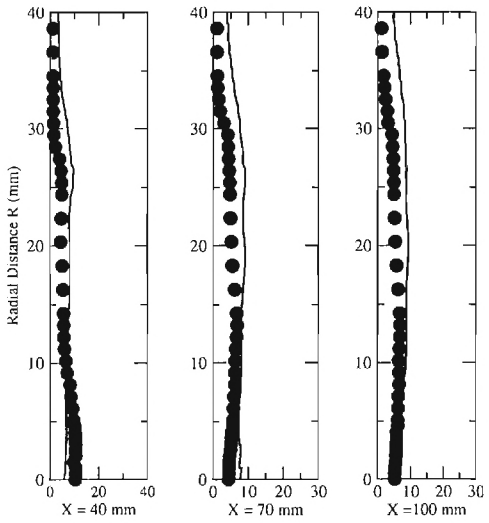

(a) U_{rms}(m/sec).

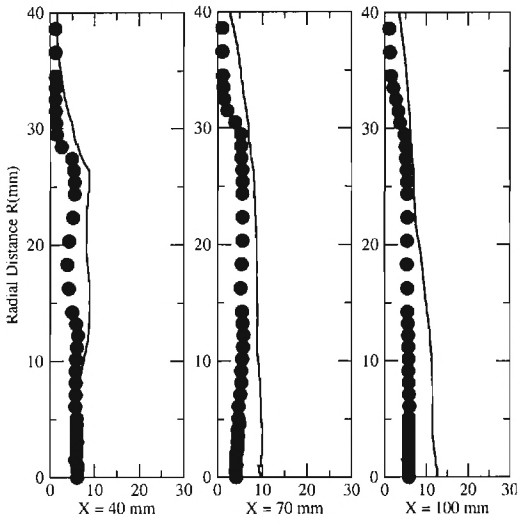

(b) $W_\theta rms$(m/sec).

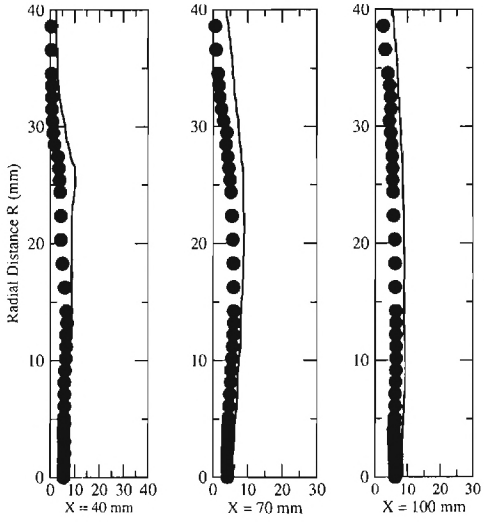

(c) $V_r rms$(m/sec).

Figure 50: Radial RMS velocity profiles, (LDV -•-, LES −) at x = 40mm, 70 mm, and 100 mm

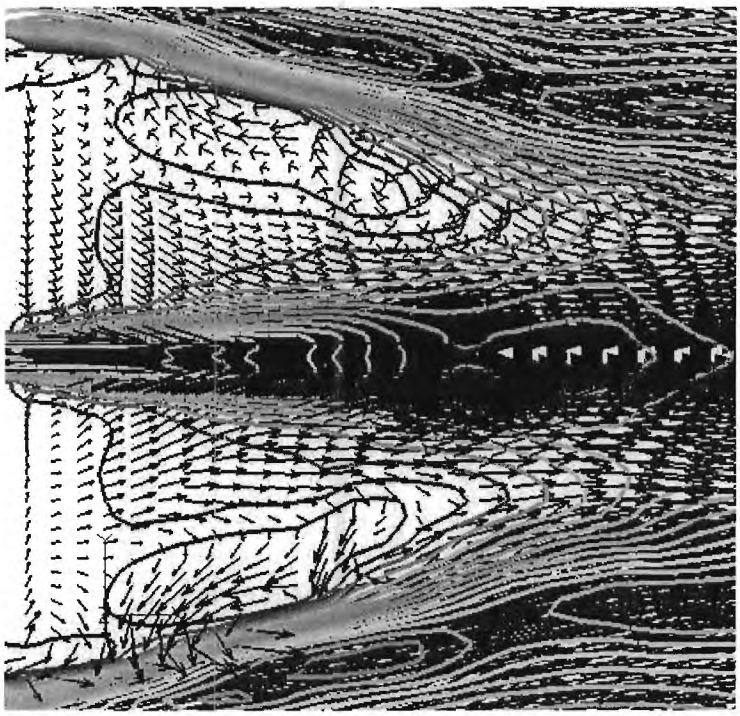

(a) Vector plot for RZ.

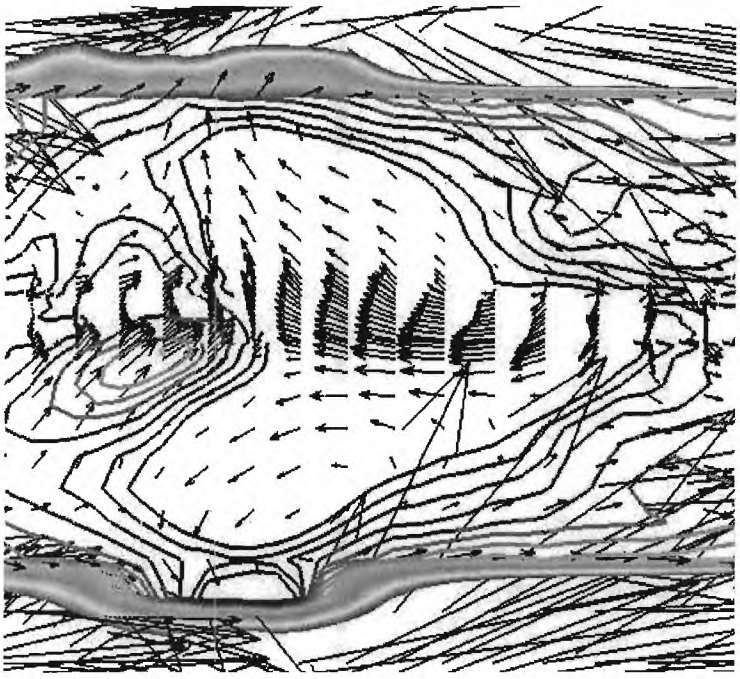

(b) Vector plot for VBB at the centerline.

Figure 51: Mean velocity vector plot in the x-y central plane combined with the positive axial mean velocity contours

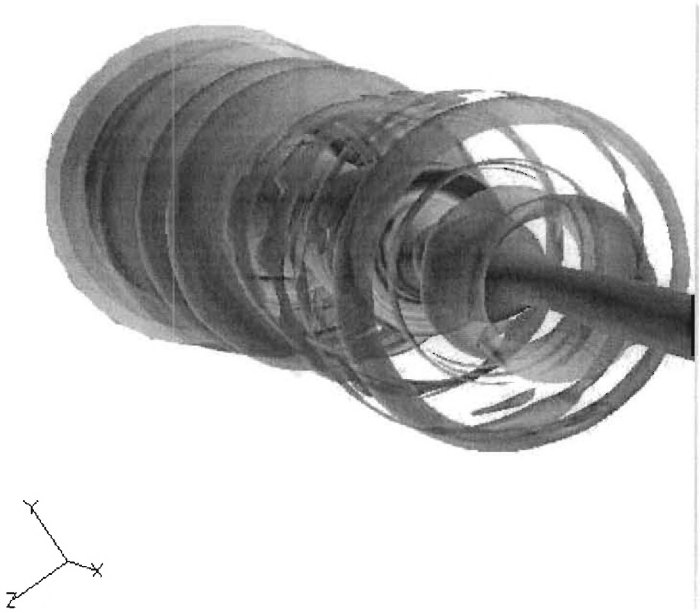

(a) Temperature iso-surface (inside) and Vorticity iso-surface (outside)

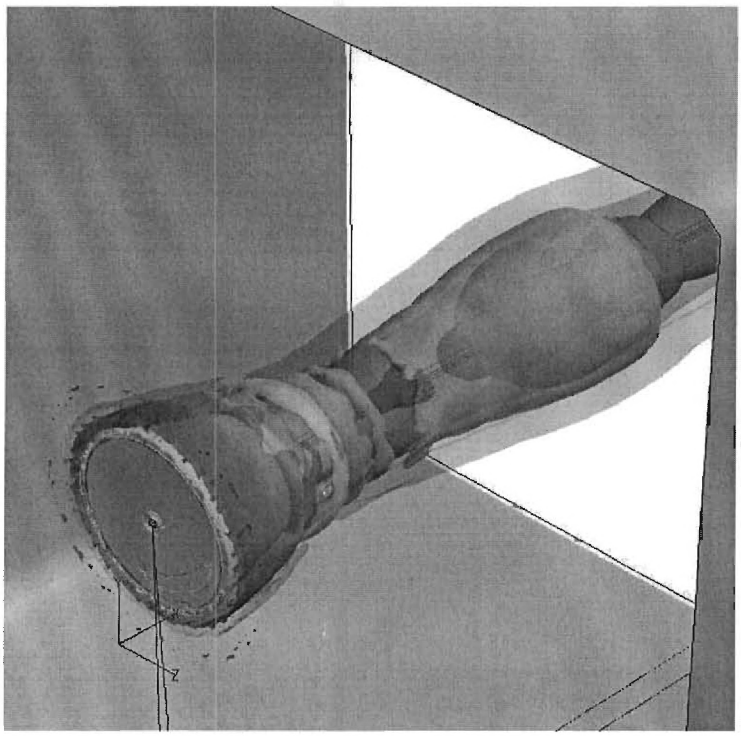

(b) Axial vorticity iso-surface (inside) - axial velocity iso-surface (outside)

Figure 52: Mean vorticity, temperature and axial velocity iso-surface for SM1 flame.

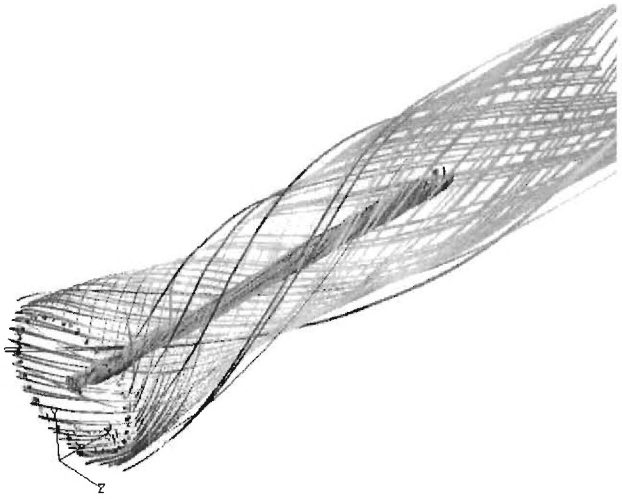

Figure 53: The mean velocity streamlines

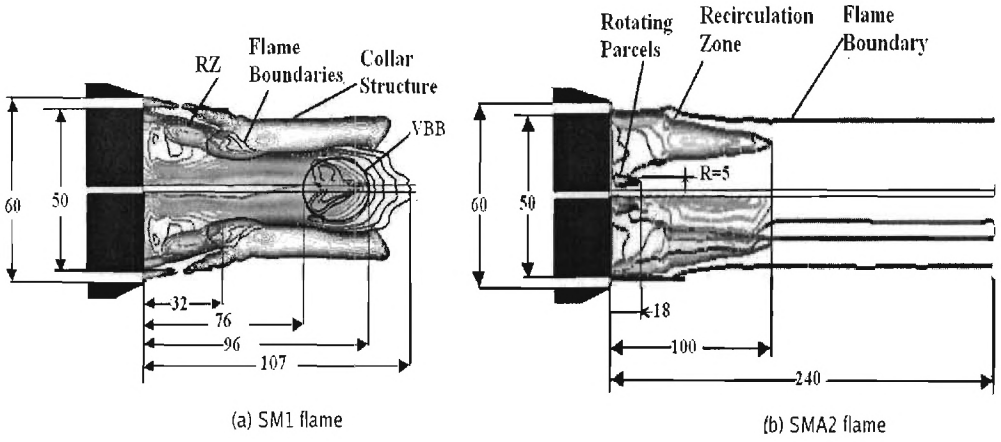

Figure 54: Flow field and flame structure downstream of the bluff body. Predicted dimensions of the critical features are shown in both figures in mm.

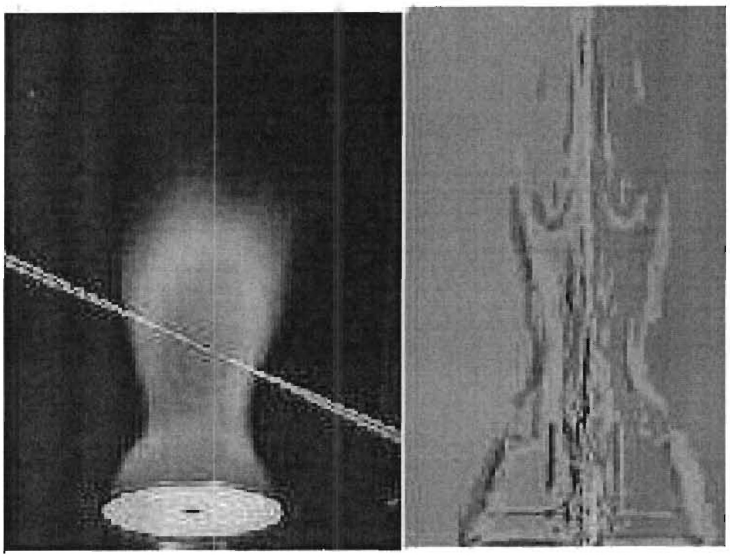

Figure 55: Comparison of SM1 flame structure. (a) experimental [205] and (b) numerical.

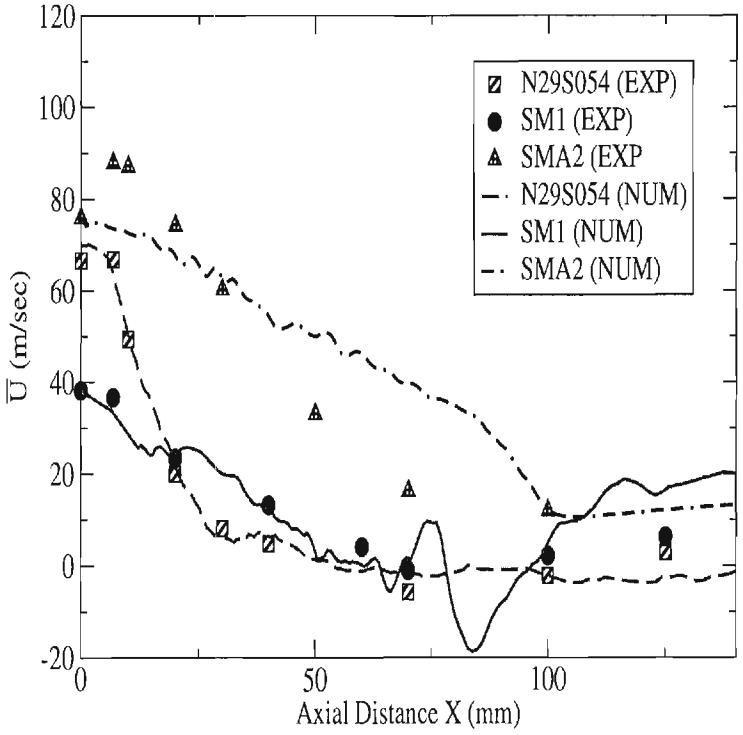

Figure 56: Centerline variation of the time-averaged axial velocity $\overline{U}$.

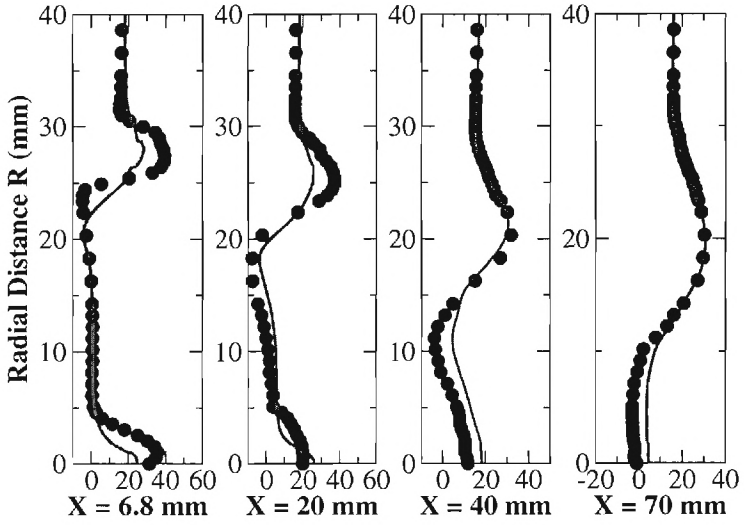

(a) Axial velocity, $\overline{U}$.

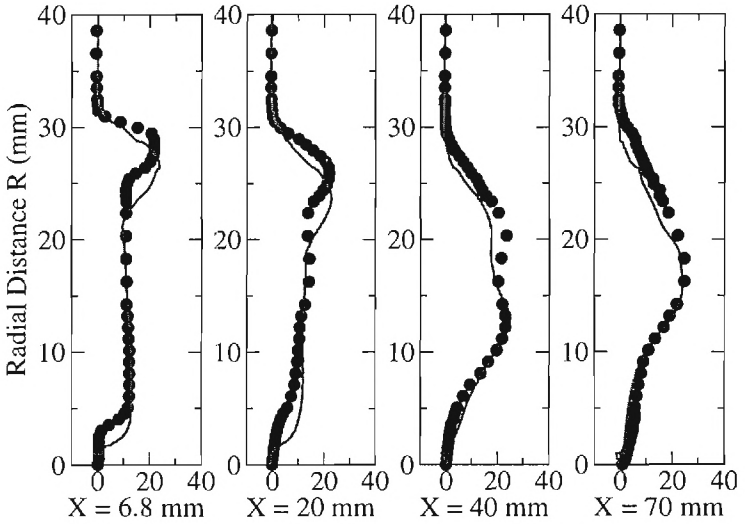

(b) Azimuthal velocity, $\overline{W_\theta}$.

Figure 57: Radial profiles of the time-averaged axial and azimuthal velocity at various axial locations for the SM1 flame. Symbols : experiments and lines : LEMLES.

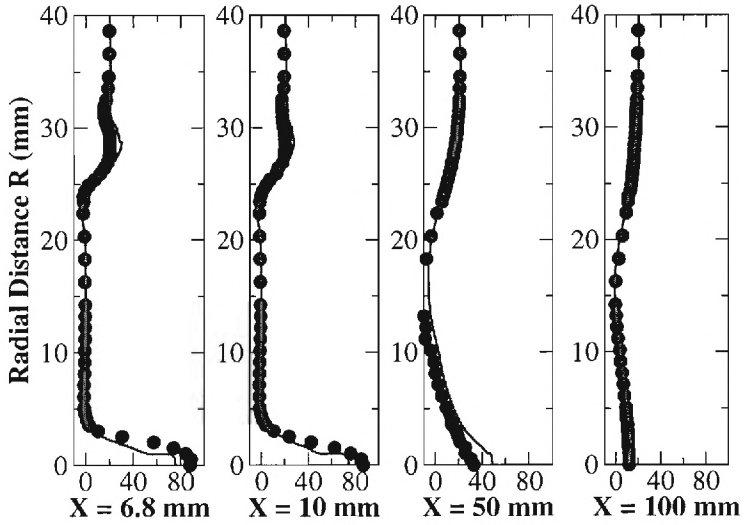

(a) Axial velocity, $\overline{U}$.

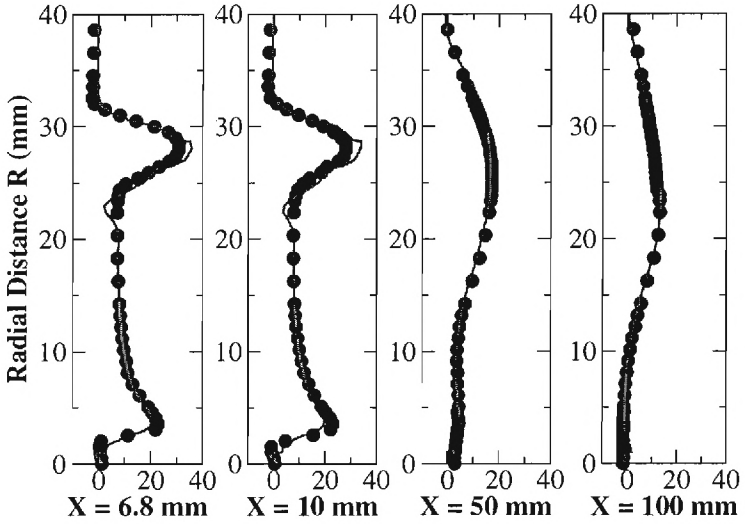

(b) Azimuthal velocity, $\overline{W_\theta}$.

Figure 58: Radial profiles of the time-averaged axial and azimuthal velocity at various axial locations for the SMA2 flame. Symbols : experiments and lines : LEMLES.

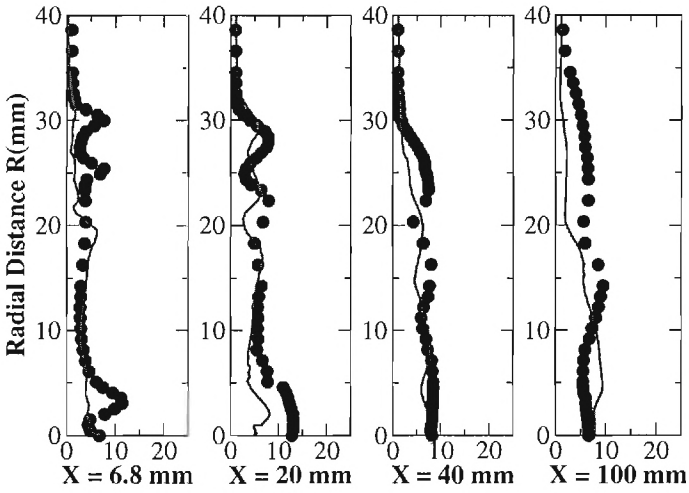

(a) Axial RMS, U_{rms}.

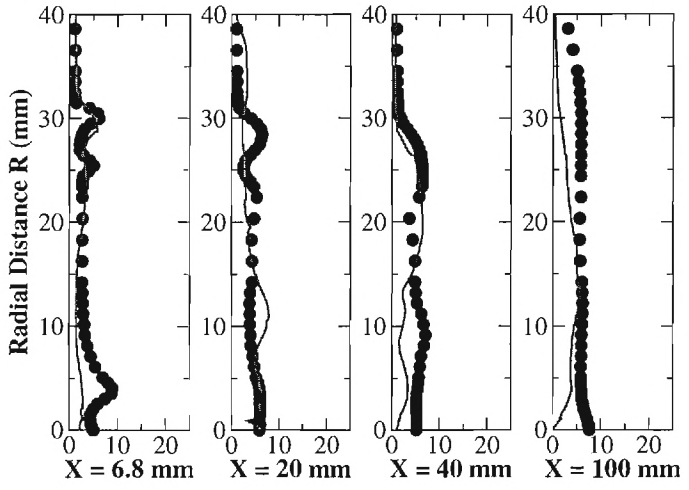

(b) Azimuthal RMS, $W_{\theta,rms}$.

Figure 59: Radial profiles of the RMS axial and azimuthal velocity fluctuation at various axial locations for the SM1 flame. Symbols : experiments and lines : LEMLES.

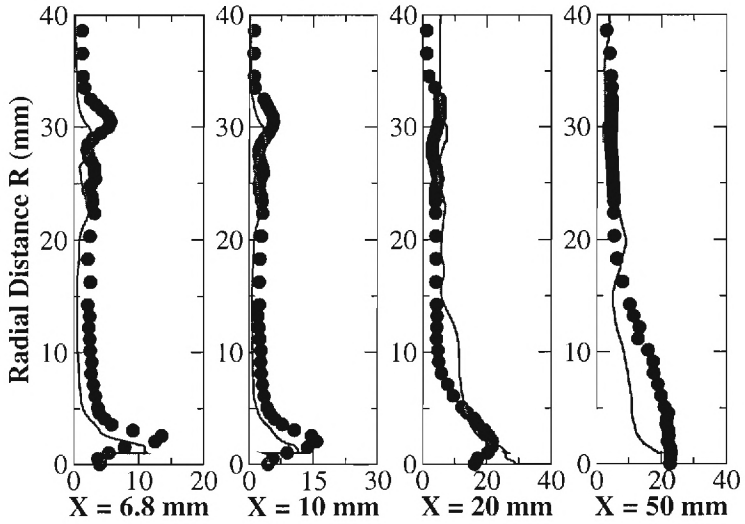

(a) Axial RMS, U_{rms}.

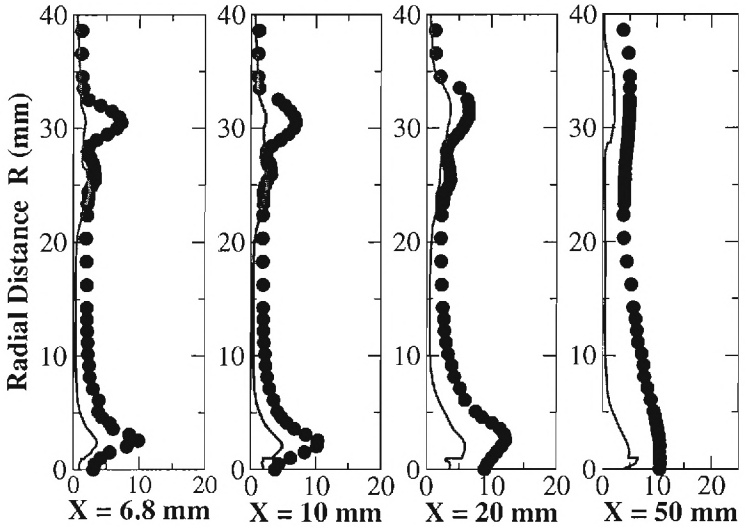

(b) Azimuthal RMS, $W_{\theta,rms}$.

Figure 60: Radial profiles of the RMS axial and azimuthal velocity fluctuation at various axial locations for the SMA2 flame. Symbols : experiments and lines : LEMLES.

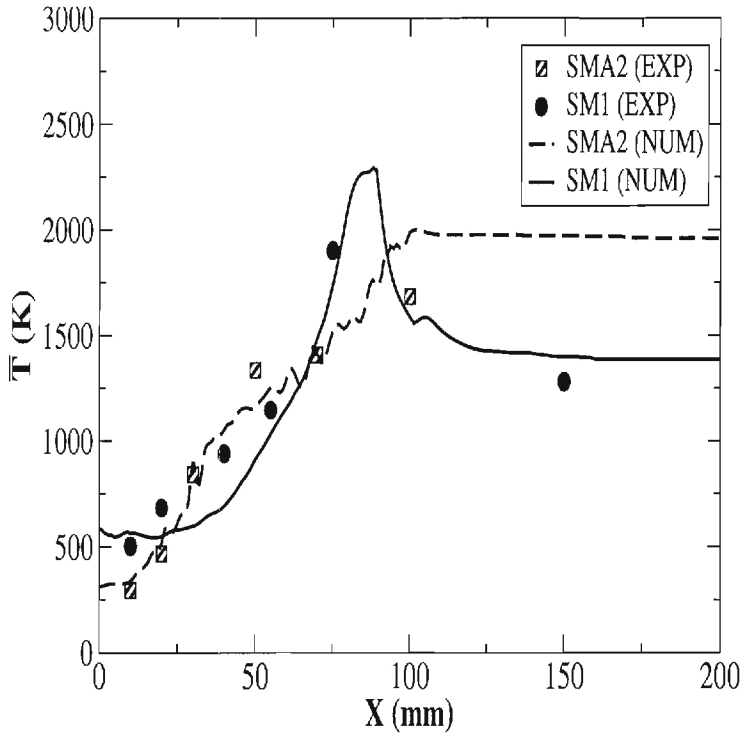

Figure 61: Centerline variation of the time-averaged temperature.

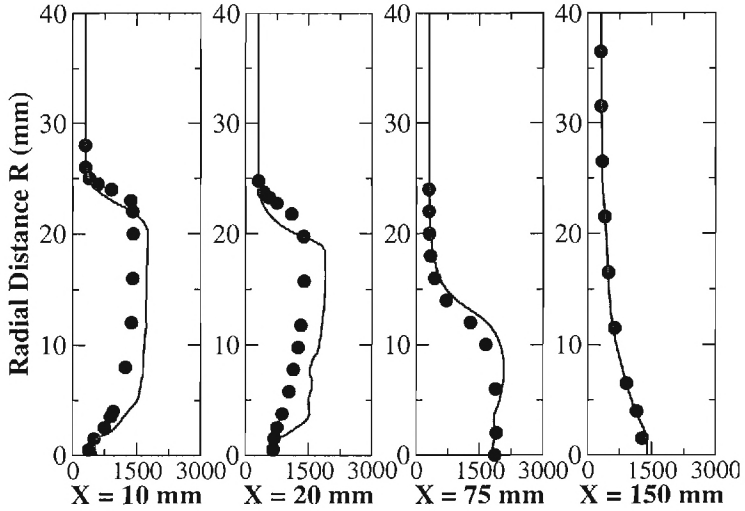

(a) SM1 flame

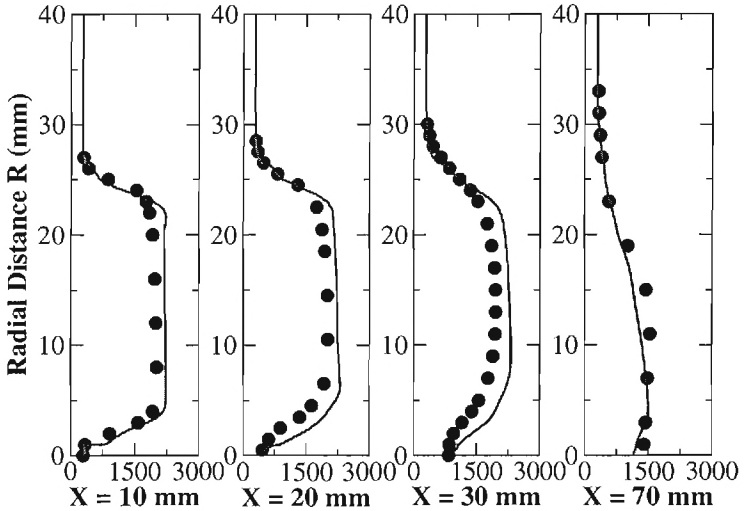

(b) SMA2 flame

Figure 62: Radial profiles of the time-averaged temperature $\overline{T}$ at various locations.

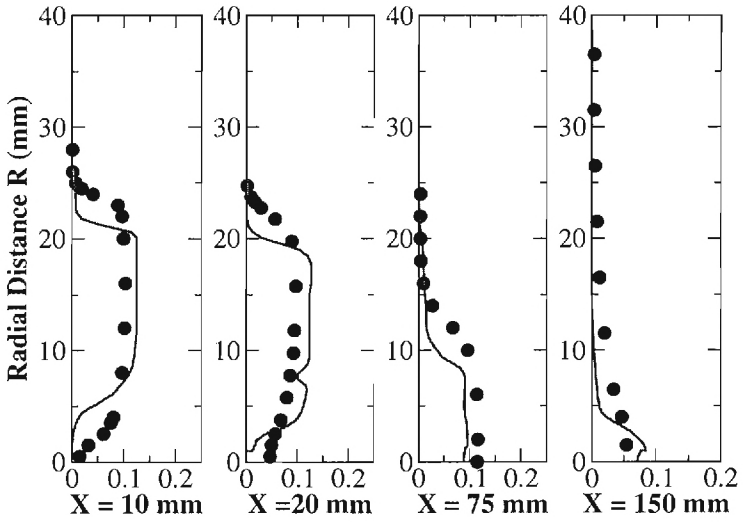

(a) SM1 flame.

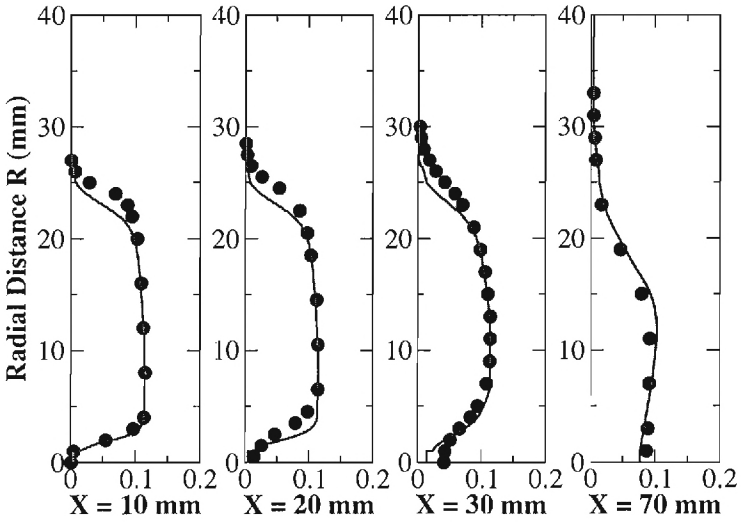

(b) SMA2 flame.

Figure 63: Radial profiles of the time-averaged $\overline{Y_{H_2O}}$ mass fraction at various axial locations.

9 Non-Premixed Sooting Flames

In this section, a sooting non-premixed jet turbulent flame is simulated and compared with experiments. The case is used as a validation for the model proposed earlier. The soot volume fraction, the number density, the size distribution, and the PSDF properties are studied. The results are explained in the context of soot formation processes at different locations inside the flame. Overall, good agreement is achieved considering the limitations of the model and measurements uncertainties. The soot volume fraction order of magnitude, the location of its maxima, and the soot particle size distribution, are all captured reasonably. Along the centerline, an initial region dominated by nucleation and surface growth is observed followed by an oxidation region. A possible initial log-normal distribution followed by a more Gaussian distribution downstream the centerline is predicted. Limitations of the current approach and possible solution strategies are also discussed. Few experimental and theoretical data for sooting turbulent flames exist in the literature. Further, only fraction of them are for ethylene flames. The earliest experimental data for ethylene turbulent jet flames was reported by [222]. They measured soot volume fraction in a vertical turbulent diffusion flame burning in a stagnant air. Different flames were studied by varying the jet velocity. The technique used to measure soot volume fraction was optical extinction of an argon-ion laser, while a platinum-rhodium thermocouple was used for temperature measurement. The setup also was simulated numerically with a two dimensional k - ϵ model with infinite rate equilibrium chemistry. A state relation between the mixture fraction and the temperature, derived from the experimental data, was used for closure of the source terms. Very good agreement was reported for the centerline temperature and soot volume fraction. They concluded that soot cannot be expressed as a single function of mixture fraction and other effects have to be included as species concentrations, temperature and residence time. For instance, for a given mixture fraction different soot volume fraction values can be found at different radii. In the early soot stages, residence time is found to be an important factor and finite rate chemistry has to be employed. The maximum soot volume fraction was found to be independent of the residence time.

[38] also conducted experimental measurement for soot volume fraction and temperature for an ethylene turbulent jet flame. Mean and root mean square values were measured and they showed that the soot production rate is influenced by turbulent mixing, whereas, buoyancy effect reduces soot formation. This flame has also been simulated by [46] using a joint-scalar transported PDF method. Overall good agreement was achieved.

[223] and [224] performed experimental and numerical studies of a non-premixed jet ethylene turbulent flame. The experimental setup is a 5 mm diameter vertical pipe that injects fuel into stagnant air. They reported mean and fluctuating velocity field data, species mean concentration, as well as the soot volume fraction. The numerical simulation was done using a k-ϵ turbulence model and the laminar flamelet approximation, together with a narrow band radiation model. They found that predicting the radiation effect without including the turbulence/radition interaction can induce $50-300$ percent error in the results. Contrary to [222] work they suggested the possibility of a universal function of soot in terms of mixture fraction. As a result, direct measurements of scalars in laminar flames can be used to provide state relationships for soot in turbulent flames. However, [20] suggests that the soot volume fraction is a strong function of the nozzle exit velocity, which reflects the flame residence

D (mm)	$\dot{m}$(g/sec)	V (m/sec)	Re	H_f (m)
4.56	0.48	25.4	13500	0.84

Table 4: Jet flow test conditions. [36]

time. Although, this assumption may be useful in low turbulent flames, where the flame can be considered as a wrinkled laminar flame, it may not hold in highly turbulent flames. However, other studies by [225, 222] suggest that for a long residence time the soot volume fraction is independent of residence time for wrinkled flames as well.

9.1 Configuration and Numerical Setup

The current configuration is extracted from the experimental work done by [36, 37, 226]. To this author's best knowledge this is the most recent experimental data for sooting ethylene/air turbulent diffusion flames. Additionally, the current work is one of the first LES of this experiment. The experimental measurements provide mean temperature, mean soot volume fraction at the centerline and at a few radial locations. The first work by [36] used thermophoretic sampling followed by transmission electron microscope (TEM) and laser extinction (LE) techniques to provide mean soot volume fraction. The primary particle spherule is found to be in-between 19 to 35 nm with experimental uncertainty around 35 %. The test conditions are summarized in table 4.

Here, D is the inner nozzle diameter, $\dot{m}$ is the inlet mass flow rate, $V(m/sec)$ is the jet velocity, $Re = \frac{VD}{\nu}$ is the Reynolds number, $\nu = 8.7X10^{-6}m^2/sec$, and H_f are the observed flame length. [37] using Laser Scattering and Extinction Technique (LSET) to obtain data on soot processes. A difference of about 35% in the soot centerline volume fraction is observed between the TEM/LE by [36] and the ISLE. The centerline temperature distribution was also measured in [226].

Due to the computational cost we simulate only $0.5m$ from the flame visible length, which is about 0.84 m long. This creates a source of ambiguity of the exit pressure. For the full length flame the exit pressure should be atmospheric. So the domain was extended by 0.05 m to avoid the direct influence of the back pressure on the collected statistics at the outflow locations. In addition, a co-flow of about 10% of the mean central jet is added to avoid adverse pressure gradient at the outflow section. This treatment may affect the results but is important to ensure global flow instability ([227]). For statistics collection, a characteristic flow through time has to be determined. Two characteristic residence times are identified in literature, the flame residence time (τ_f) and the soot integral time scale τ_s. The flame residence time is based on the location of maximum extension, which is found from the experiment by [37] as $x_m/D = 80$. Hence, $\tau_f = 14$ msec.

The other time scale is based on the soot integral length scale identified in the experiment by [38] and [36] as 7.5 mm. Therefore, the integral soot time scale $\tau_s = 3$ msec. Here, we first run the jet flame for a full flow characteristic time using a single step (five species) ethylene mechanism ([218]) to achieve an initial flow field. Afterwards, the flame is run for 10 soot characteristic time scales scales using the 15-step, 19 species ethylene/air mechanism ([143]).

The grid employed here is a butterfly grid similar to the one used in the previous section

with cylindrical grid resolution of 201x45x49 and Cartesian inner grid of 201x13x13 grid points. The total number of grid points is around 0.5 million grid points. Twelve LEM cells were used in the subgrid. To minimize the cost, the chemistry integration is done by a fractional step algorithm to avoid solving by the more expensive direct integration as described in section III. The time step was adjusted such that the acetylene mass fraction error at the centerline between the direct integration and the fractional step method is less than 5 %. The resolution in the shear layer at the nozzle exit is 0.08032 mm on the LES level and 0.007 mm on the subgrid level. The Kolmogorov length scale η is estimated to be 0.0036 mm in the shear layer just downstream the nozzle exit plane. Thus, the LEM resolution is of the order of 2η. The initial simulation cost is 4044 single processor hours on a Zion Intel cluster. The statistics collection done on 10 soot-moment characteristic flow times cost is 25000 single processor hours on the same machine.

9.2 Results and Discussion

Very little unsteady data is available and even the steady state data is rather sparse. Therefore, we focus primarily on making some direct comparison with measured quantities, and then make some observations about the model behavior. The conclusions will be connected at some points to the premixed data shown earlier.

The flame structure averaged in time is shown in Fig. 64 on the left compared to an instantaneous snapshot on the right. The flame structure and spread rate are captured reasonably compared to other similar flames. It is noticed that the instantaneous snapshot shows higher temperature than the averaged one at some instants. This observation is also seen in the experimental results as well ([38]). The adiabatic flame temperature for ethylne/air diffusion flames is estimated to be around 2400 K by [222].

Figure 65 shows the axial mean temperature along the centerline. The temperature rises monotonically, consistent with experimental observation and with good agreement with data for $X/D \leq 60$. Further downstream the predicted temperature is higher than the measured values. An over-prediction of about 250 K is observed at X/D = 120. Overall, the higher prediction is attributed to the high grid stretching downstream the centerline and possible outflow subsonic boundary condition feedback effect. In addition, the simplified empirical radiation model (originally calibrated for methane flames) may have an effect on the predicted values as well. Past studies have suggested that radiation may result in an over-prediction of $\pm$ 100 – 500 K ([37, 222]).

Regardless, given the uncertainty in the measurements (about 30 % [37]), the overall agreement is considered quite reasonable. The temperature increases up around X/D = 10, which reflects the high mixing and entrainment rate. The temperature starts to decrease at location X/D = 110, where the stoichiometric conditions are reached. This decrease may be attributed to the heat loss by soot radiation and the entrainment of fresh air from the outside.

The radial temperature profiles are shown in Fig. 66 at various axial locations (there is no data for comparison). At the first two radial locations the radial profile shows a peak in the reaction zone that moves radially outwards as the jet spreads.

By comparison of the temperature profiles of the premixed (studied earlier) and non-premixed flames we have the following observations. In the premixed case we have three

main regions: the preheat zone, the reaction zone and the post flame region, which are aligned sequentially across the flame. In the non-premixed case, the combustion is mixing controlled rather than kinetically controlled. However, the mixing can occur at any point by air entrainment from the outside to mix with the fuel and the products and the sequence seen in the premixed flame can occur locally in the jet flame with the fuel and oxidizer separated by the reaction zone. For instance, in the non-premixed case the sequence radially from the centerline will be fuel and burned gases, followed by the reaction zone, then air and burned gases. The burned gases are usually mixed by the effect of turbulence and entrainment with the unburned gases.

The above flame structure affects the soot formation process as well. In premixed flames, the nucleation, the surface growth and the oxidation all take place at the same time and at comparable temperatures. Therefore, at high temperatures the oxidation rate is higher than the pyrolysis rate of acetylene to produce soot. As a result, the premixed flames has low soot tendency. On the contrary, at the early spatial stages of the jet flame, the temperature is relatively low and the oxidative attack by O_2 and OH is very small due to the high fuel concentration (specially at the centerline). This leads to the existence of rich regimes, with relatively low temperatures (800-1200) K, which accelerates the pyrolysis rate, the formation of precursors and nucleation. As the jet spreads, and the centerline velocity decay, more air is entrained, which lowers the temperature at location $X/D = 110$, and increases the oxidation rate.

Figure 67 shows the soot contribution to the radiation effect is about 99% of the total radiation. The difference in temperature when using a detailed radiation model is expected to be an order of $100 - 500$ K less if no radiation is included ([222]). The current radiation model neglects soot absorption and scattering, as well as radiation of other optical species such as CO and CH_4. In addition, the empirical constants used are for methane/air sooting flames ([120]), which is a lightly sooting flame and may be unsuitable for the current ethylene flame. However, it is noted that there are two competing processes: the over-prediction in temperature increases the nucleation rate as well as the surface growth rate (as shown later) and thus, over-predicts the soot production, which in turn should reduce the temperature by the increase in thermal radiation. It is apparent that in our results the first effect is more dominant. This is attributed to the grid stretching effect, which is equivalent to an artificial increase in the local cell residence time.

Figure 68 shows the centerline mean soot volume fraction distribution. The trend and peak location is captured quite reasonably. However, an over prediction by nearly 90% at the peak location is observed. This is probably due to the over prediction of the temperature, as noted above. Another important factor may be the inclusion of the agglomeration effect. In a recent study ([228]), the soot volume fraction at the centerline with agglomeration (particles are assumed to become chain like structure) were compared to a case with coagulation (all the particles are assumed spherical) only. The agglomeration case showed an over-prediction by 400% that may be due to an over-prediction of the first moment, which controls the soot average mass. In the agglomeration case, the total surface area is affected by the number of primary particles in the aggregate in addition to the individual particle surface area, which increases the predicted soot mass fraction.

To illustrate the above argument, a one-dimensional study is conducted with only coagulation and compared with another case with agglomeration included. The initialization

of the problem is taken as the centerline of the jet case. Figure 69 shows the rate of time evolution of the first moment, which mainly controls the soot volume fraction, for the two cases. Agglomeration over-predicts the rate significantly than just the coagulation limit.

The soot peak location at X/D = 92 is shifted to the left of the stoichiometric temperature peak location at X/D = 110, as shown in Fig. 65. This observation coincide with the literature observations for sooting turbulent jet flames ([222]). The decrease in the soot mass faction is due to the carbon burnout and the decrease in the nucleation and surface growth rates as will be shown later. In addition, the over-prediction in temperature at the center line causes higher rate of inception, soot nucleation, and surface growth, which raises the soot mass fraction as well. This is also due to very low O_2 and OH mass fractions at the centerline. The radial soot profiles at three consecutive axial locations are shown in Figure 70 for X/D = 30, 50, and 100, respectively. The profiles show a nearly constant soot volume fraction towards the centerline due to the high turbulent transport rate, the soot diffusivity and the thermophretic forces produced by the high temperature gradient, which transport the soot produced in the reaction zone to the centerline. These factors, in addition to the soot production at the centerline itself controls the soot level at the centerline. The over-prediction at the downstream location is attributed to the grid stretching and the outflow boundary condition effect.

To estimate the soot diffusion effect, Fig. 71 shows a comparison of the soot diffusion coefficient with three species. At the initial nucleation and surface growth region, up to X/D = 65, soot diffusion is found to be important and comparable to other heavy species as CH_4 and CO_2. However, further downstream, the soot particles are heavy and diffusion is of less importance. On the other hand, the effect of thermophoresis is more important as we go downstream, where the temperature gradients are higher. Figure 72 shows the centerline thermophoretic velocity normalized by the temperature gradient. These values is expected to be higher radially, since the temperature gradient is more steep in the radial direction. On the right of Fig. 72 the mean free path along the centerline is shown. By combining this figure with the mean soot diameter data, we can know the regime of operation of the soot particles. However, knowing that the soot particles diameter is in the order of nm, the particles will spent most of its lifetime in the free molecular regime.

The radial profiles shows good agreement with the experimental data with over-prediction at the centerline and at X/D = 100. At far field locations there are many factors that affect the prediction accuracy. The domain width is not wide enough to reduce the boundary conditions effect on the numerical data. In addition, the radial and axial grid stretching rate is high as well.

The axial variation of the soot number density, shown in Fig. 73, suggests that the number of particles per unit mixture volume increases rapidly in the beginning due to nucleation. At around X/D = 100, the number density starts to decrease by the coagulation and agglomeration effect. There is an over-prediction (note the scale in the figure), which reflects either higher nucleation rate or lower coagulation rate. Another possibility is the under-prediction of the average soot diameter, which is shown in Fig. 74. The average diameter is under-predicted by a factor of 4, which may be a result of the under-prediction of the coagulation rate. As a result, having larger number of particles will make the average surface area per unit volume larger, as shown in Fig. 75. This will lead to higher surface growth rate and consequently higher soot mass fraction, as shown in Fig. 68.

The coagulation process is mainly controlled by the collision frequency between the soot particles. Figure 76 shows the axial variation of the mean collision frequency along the centerline. The expression is normalized in such a way to make it a function of temperature only. The figure shows that in general, the collision frequency is a strong function of temperature and follows the mean temperature trend. In addition, the frequency of collision in the free molecular regime is more sensitive to the temperature variations at lower values, where soot is still in its inception and nucleation period, and the particles are small with their diameters much smaller than the mean free path. These observations are in good agreement with past results ([150]).

Figure 77 shows the PSDF properties computed form the first three moments. The average mass per unit volume increases along the centerline and starts to decrease around X/D = 100 by the effect of oxidation. The maximum mean is around 3E-4 Kg/m^3. The standard deviation is around 2E-4 at the peak location. However, the standard deviation and the mean usually doesn't give enough information on the PSDF shape. Therefore, the dispersion is shown to increase along the axial direction, which indicates that the PDF became wider as we go downstream, having more size classes. Finally, the skewness shows that the PDF has wide tails towards the right of the mean or the bigger values. Immediately downstream of the nozzle the mean value is close to zero, at the same time as nucleation is activated and more particles are created, the skewness show very high positive values at these location, which corresponds to wide tails. Afterwards, as we go further downstream, this wide tails starts to decrease and the shape of the PDF become closer to the Gaussian distribution, or more symmetrical around the mean value. These observations indicate that the size distribution is highly polydisperse and simplified analysis, like an assumed PDF is not recommended for such highly turbulent sooting flames.

The centerline species concentrations are shown in Fig. 78. The major species are plotted along with some radicals. The fuel concentration approaches zero around X/D = 90. Acetylene concentration reaches its peak around X/D = 100, which coincide with the nucleation, and soot volume fraction peak. The H_2O starts to dissociate to give OH around X/D = 60. The O_2 level is in general small along the centerline. The high levels of CO_2 and CO indicate that the flame is highly rich along the centerline.

The soot formation and destruction rates along the centerline are shown in Fig. 79. In agreement with the experimental observation the soot nucleation and surface growth increases until X/D = 100, where the soot volume fraction is maximum. However, the nucleation peak is slightly shifted to the right of the surface growth rate. This is due to the reduction of the soot surface area by the oxidative attack by OH and O_2, which starts around X/D = 80 and reach its peak around X/D = 100. The decrease in the nucleation, as well as the surface growth rate afterwards are due to the reduction in the available acetylene concentration, since fuel is consumed around this location. This decline in the nucleation rate also causes the decline in the number density shown earlier in Fig. 73. Analysis shows that the surface growth rate starts around X/D = 32, while the nucleation starts earlier around X/D = 10. Thus, there is an overlap region where surface growth, nucleation and oxidation processes all occur. This is due to the fact that diffusion flames are mixing controlled, rather than kinetics controlled.

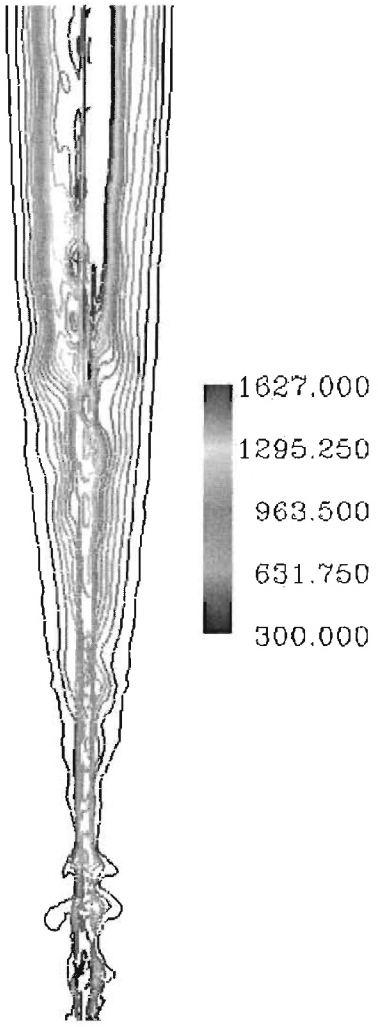

(a) Average temperature contours, $\overline{T}$.

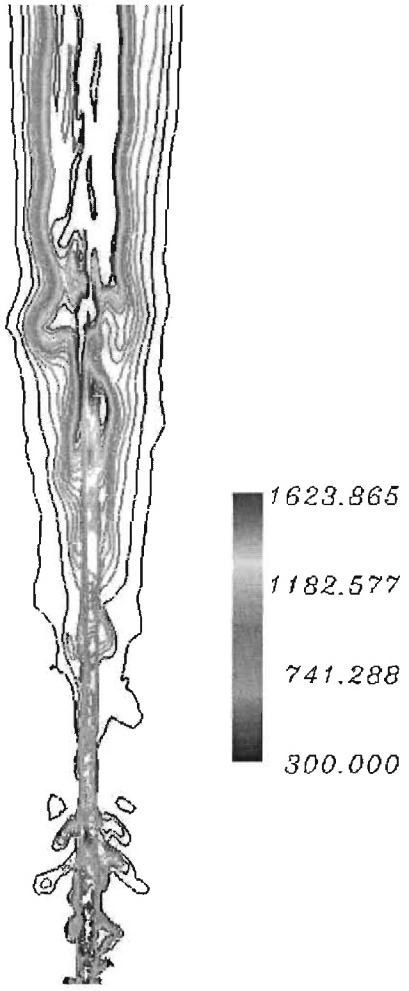

(b) Instantaneous temperature contours.

Figure 64: Comparison between average and instantaneous temperature contours

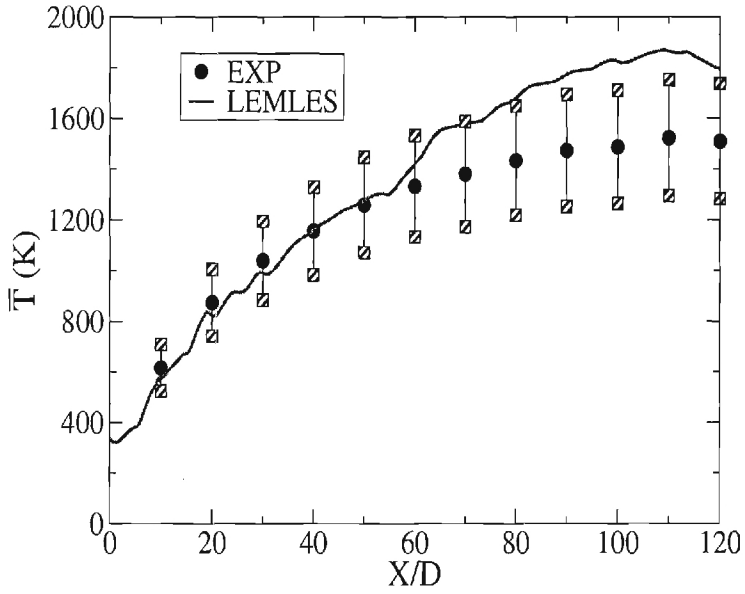

Figure 65: Mean axial temperature with error bars superimposed

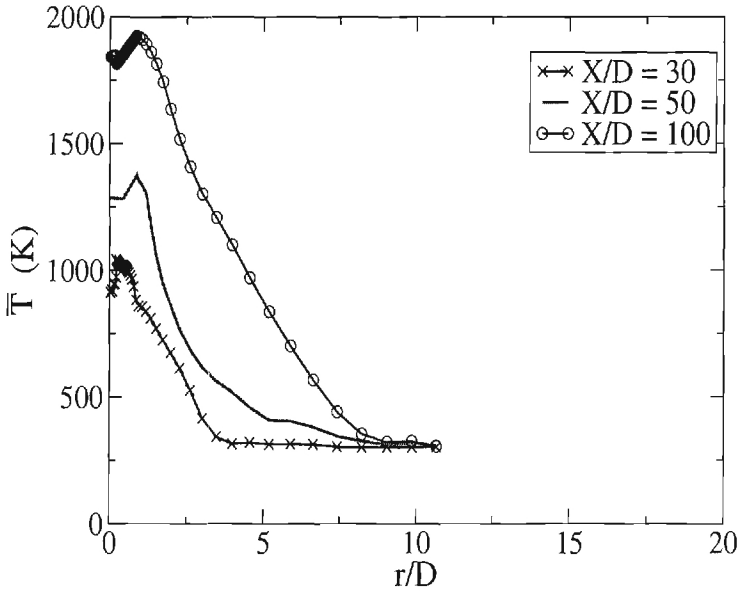

Figure 66: Mean radial soot temperature profiles

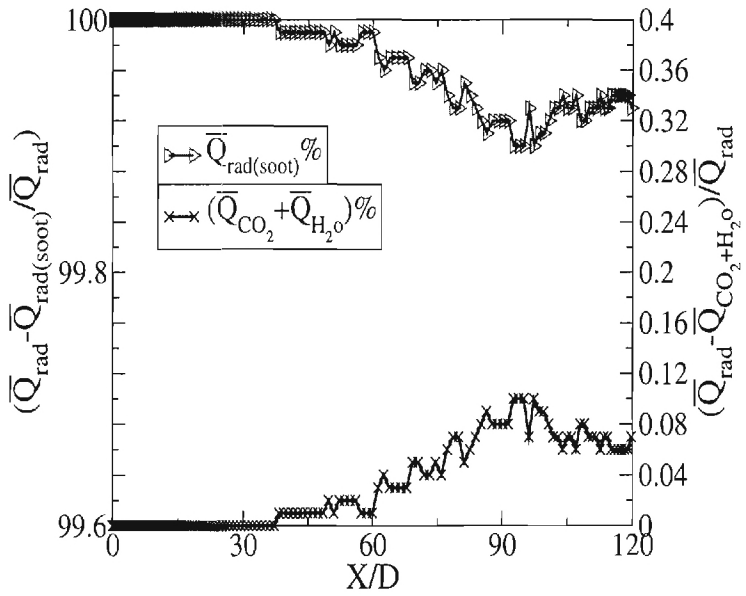

Figure 67: Percentage of soot radiation and CO_2 and H_2O along the centerline

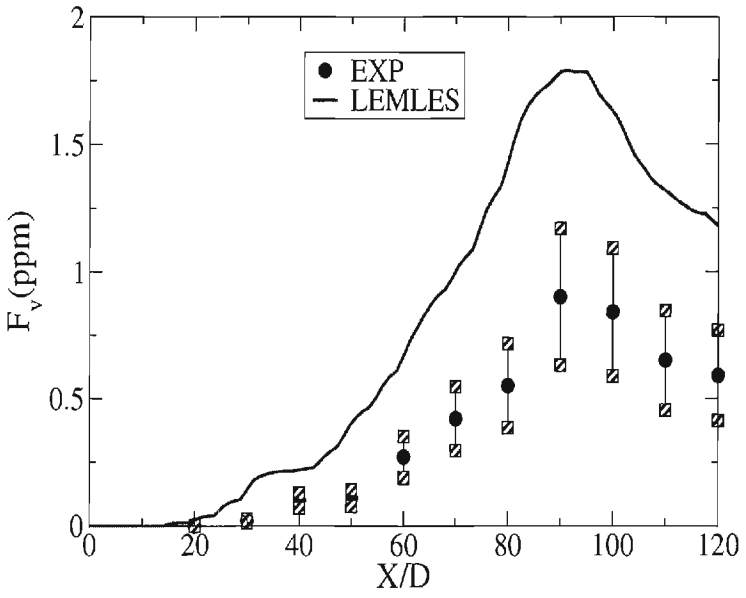

Figure 68: Mean axial soot volume fraction in ppm

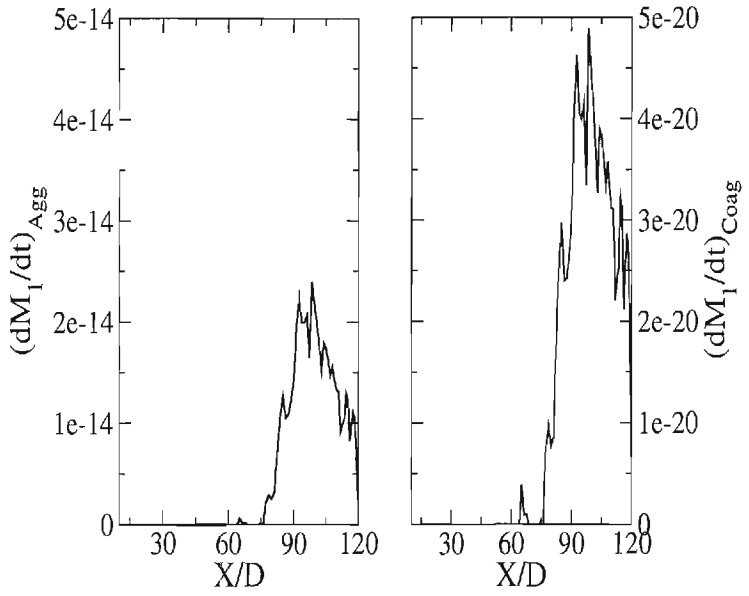

Figure 69: Comparison of the first moment rate with aggregation (left) and coagulation (right)

.

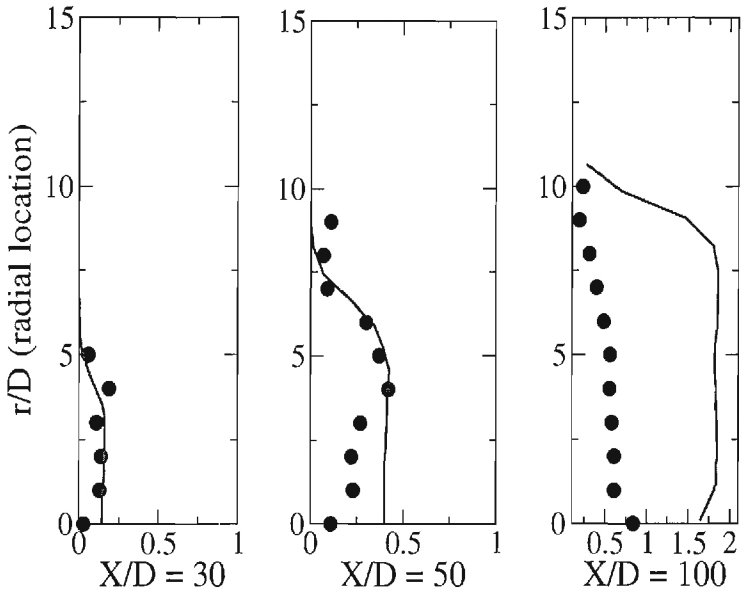

Figure 70: Mean radial soot volume fraction profiles

.

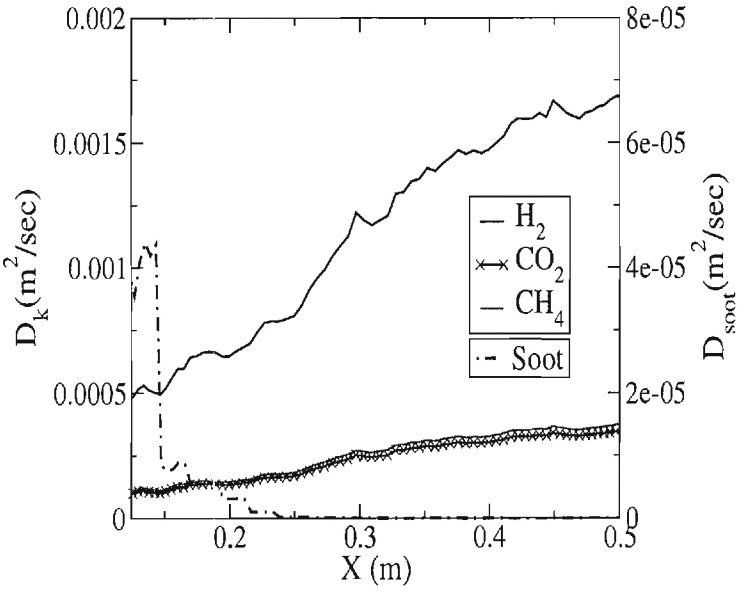

Figure 71: Comparison of soot diffusion with H_2, CO_2, and CH_4 diffusion along the centerline

.

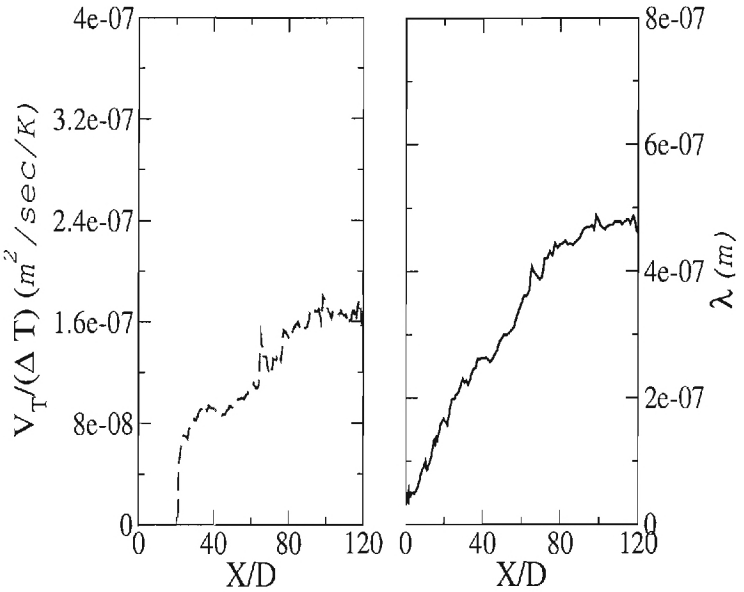

Figure 72: The thermophoretic velocity normalized by the temperature gradient and the mean free path along the centerline

.

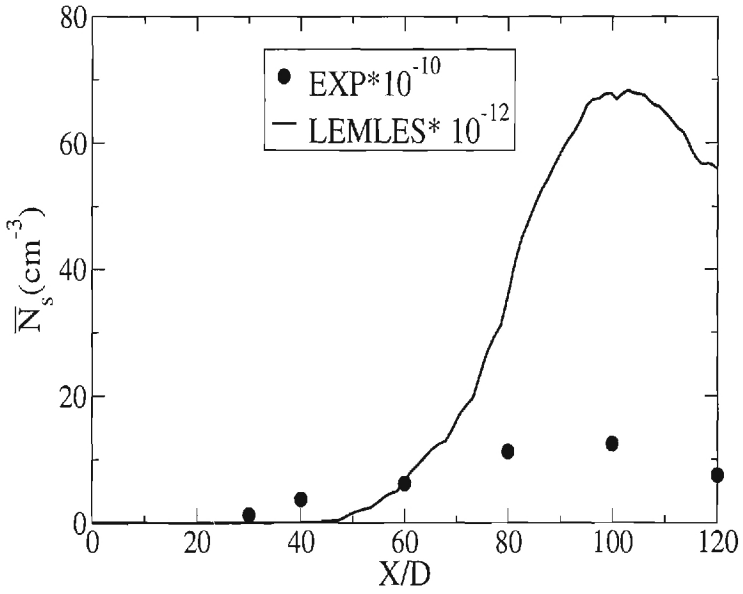

Figure 73: Mean axial number density

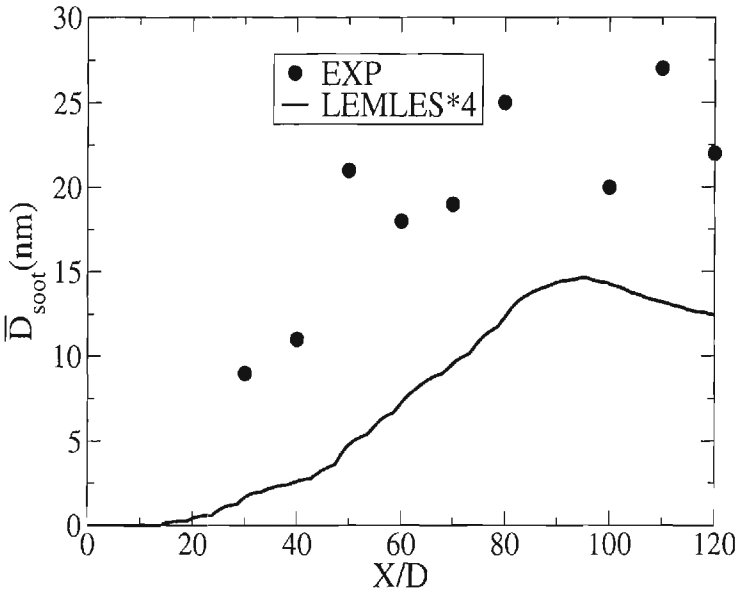

Figure 74: Mean axial soot diameter

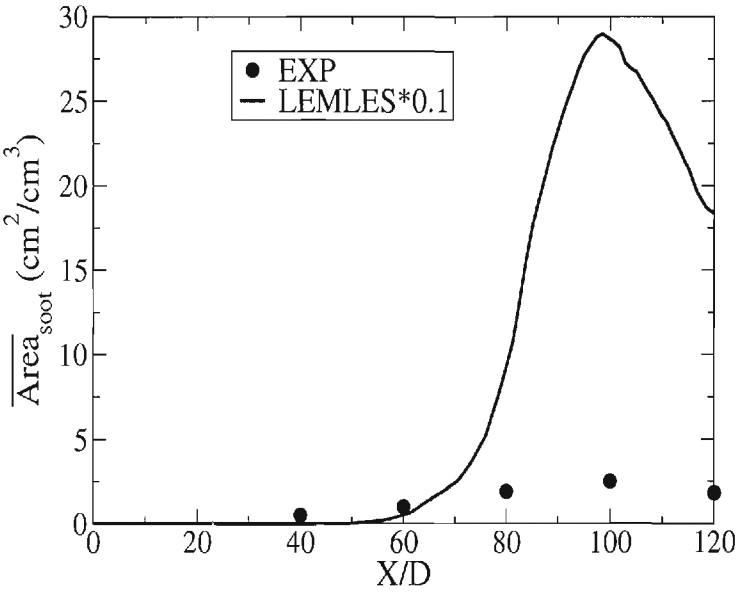

Figure 75: Mean axial average soot surface area per unit mixture volume

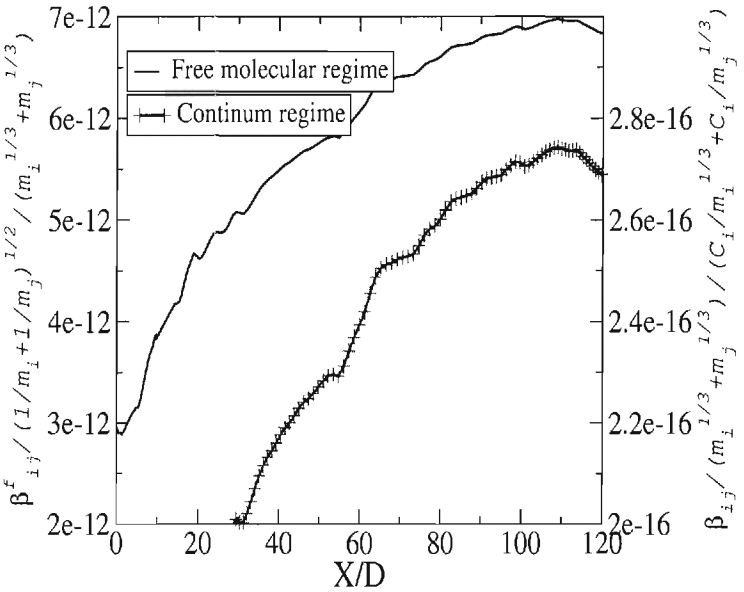

Figure 76: Mean axial variation of the collision frequency as function of temperature in the free and continuum regimes

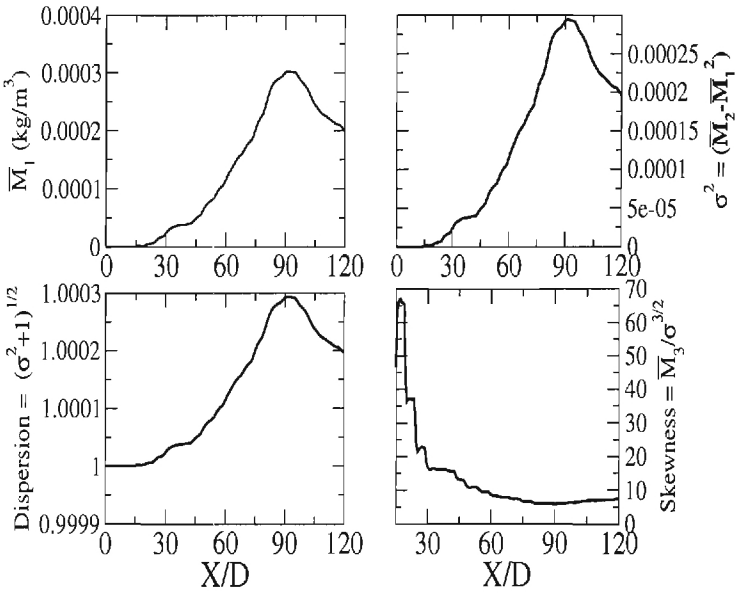

Figure 77: Mean , standard deviation, dispersion and skewness of the PSDF at the centerline
.

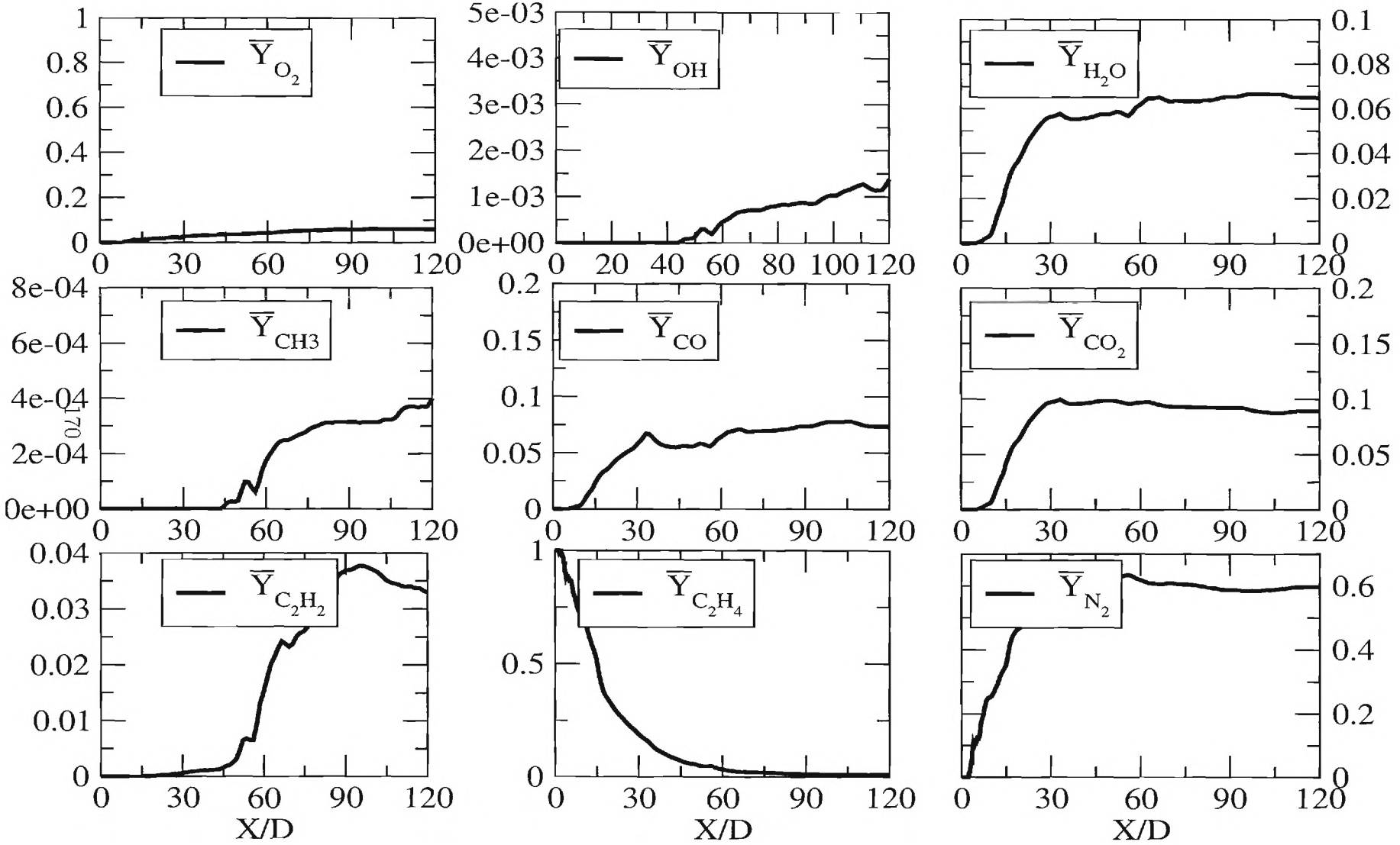
$\overline{Y}_{O_2}$
$\overline{Y}_{OH}$
$\overline{Y}_{H_2O}$
$\overline{Y}_{CH3}$
$\overline{Y}_{CO}$
$\overline{Y}_{CO_2}$
$\overline{Y}_{C_2H_2}$
$\overline{Y}_{C_2H_4}$
$\overline{Y}_{N_2}$
X/D
X/D
X/D

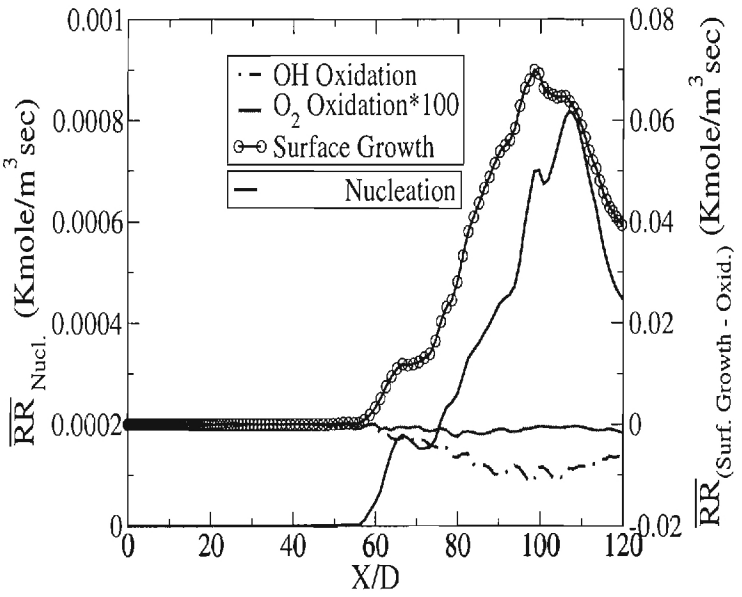

Figure 79: Mean centerline soot formation and destruction rates

10 Conclusions

- A new LES subgrid model for soot prediction is developed and validated against experiment. The model comprises most of the physical phenomena that contribute to the soot formation. The gas phase chemistry is modeled by a semi-empirical reduced ethylene-air mechanism, combined with a four step soot formation model, to account for the soot kinetics processes as nucleation, surface growth and soot destruction by oxidative attack. The soot initial nucleus is assumed to be composed of two carbon atoms, while the coagulation starts with a soot particle composed of 30 nuclei. The model is generic and can be applied for any combustion mode, (i.e. premixed, non-premixed and partially premixed).

- The MOMIC incorporated with an existing and previously validated subgrid mixing and combustion model solves for the PSDF first few moments. The subgrid model requires no ad hoc filtering and allows exact estimate of the diffusion and kinetics processes within the small scales. This allows for a generic solution that needs no priori assumption of the particle size distribution. In addition, it allows for the treatment of the soot particles physically in the free molecular regime, where the soot particles are much smaller than the fluid mean free path, the transition regime and the continuum regime.

- The collision of the soot particles with each other undergoes two phases. The coagulation phase, where the spherical soot particles coalesce together to form a larger spherical particle, and the aggregation phase, where the large soot particles for chain like structure. A detailed soot diffusion model that covers the soot diffusivity in the three regimes is used. Finally, the soot transport by the effect of thermophretic forces is accounted for as well.

- A set of canonically premixed flames have been simulated using the developed model to study the effect of turbulence and C/O ratio on soot production in turbulent premixed flames. The results show that soot formation occurs only when C/O ratio is above the critical value and this observation agrees with past results. It is also shown that turbulence increases the collision frequency between the soot particles, and as a result, the coagulation rate increases and the total average surface area of the soot particles per unit volume decreases. Consequently, the surface growth rate decreases with the increase in turbulence intensity.

- The assumption of a fixed Schmidt number (molecular diffusion coefficients) is found to affect the results. The variable diffusivity case shows a more symmetric curvature PDF with wider tails and more concave elements. The relatively higher thermal diffusivity, when compared to molecular diffusivity in the constant diffusion coefficients, increases the collision frequency and the coagulation rate, and that in turn reduces the number density and the soot surface growth rate. The above results show consistency with the physics reported in past observations in a similar non-sooting flames.

- As mentioned earlier LEMLES has been validated extensively for premixed and non-premixed flames. In the current work, this is extended to simulate a partially premixed

as well as a non-premixed flames. Overall good agreement is achieved for both flames, considering that a simplified one-step kinetics is employed in the subgrid model.

- The flame structure (whether premixed or non-premixed) is found to affect the soot production and formation rates significantly. The diffusion flame shows higher levels of soot for two reasons. Firstly, in diffusion flames, the centerline is usually highly rich, and the abundance of carbon atoms allow for higher nucleation rates. Secondly, in non-premixed jet flames, there is an initial region dominated by the nucleation and the surface growth processes, followed by a region downstream, where the oxidative attacks are activated. While in premixed flames, there is a simultaneous oxidative attack, with nucleation and surface growth at relatively high temperatures. At this elevated temperature level the oxidation rate is higher than the surface growth rate, which reduced the soot level. As a result, it is to be concluded that diffusion flames tendency to soot is significantly affected by the fuel structure and the mixing processes, where in premixed flames the chemical kinetics is the main controller, since the fuel and oxidizer are already premixed.

- The soot particles diffusivity (neglected in most of the currently published models) is found to be significant, especially in the initial nucleation and surface growth region, where the particles mass is still light enough to be diffused by the flow eddies.

- The thermophoretic forces included here affects the soot diffusivity in the radial and axial direction. This effect in non-premixed flames is more important due to the nature if the flame structure. In the radial direction the reaction zone is surrounded by a mixture of air and products from above and a mixture of fuel and burned gases from below. This temperature gradients generate thermal diffusivity effect in the radial direction.

11 Future Work and Recommendations

- The MOMIC is based on a double interpolation scheme, which is done using the Lagrangian method here. However, the error produced by the interpolation process need to be evaluated for different interpolation schemes to pick the most accurate.

- Based on the above results, it is highly recommended to incorporate a more detailed and accurate radiation model. Soot formation and destruction is found to be very sensitive to the radiation model used and a study should be conducted to evaluate and compare different radiation models.

- One of the problems faced the current study was the availability of computational resources. It is recommended to apply the current model with small modifications (regarding the radiation model) to gas turbine or internal combustion engines to asses the ability to predict soot in complex configurations.

- Nucleation, is one of the most important phases in soot formation. With the future expected advancement in chemical kinetics, it is recommended to incorporate a more

detailed mechanisms that account for PAHs formation, together with a suitable four step soot formation model that is based on PAHs. Once, this step is achieved, with the suitable radiation model the model generality will be broadened greatly.

- For most combustion processes, the flow is usually subsonic and compressible. It is recommended to use the sponge boundary condition method (described in Appendix B) coupled with the NSCBC to reduce the effect of the outflow boundary conditions on the results.
- Finally, other methods, like the sectional method, need to be compared with the MOMIC method in terms of accuracy and computational cost.

References

[1] G. M. Faeth, G. Roth, and M. Gundersen. *Combustion Emission and Control.* Taylor and Francis, 1998.

[2] L Zhigang and H. Wang. Drag force, diffusion coefficient and electric mobility of small particles. i. theory applicable to a free-molecule regime. *Phys. Review E*, 68:061206–1–061206–9, 2003.

[3] A. H. Lefebvre. *Gas Turbine Combustion.* Taylor and Francis, second edition, 1999.

[4] R. J. Hall, M. D. Smooke, and M. B Colket. Prediction of soot dynamic in opposed jet diffusion flames. In *Physical and Chemical Aspects of Combustion*, pages 189–230. Gordon and Breach Science, 1987.

[5] S. Bhattacharjee and W. L. Grosshandler. Effect of radiative heat transfer on combustion chamber flows. *Western States Sectional Meeting of Combust. Institute*, 1988.

[6] G. H. Markstein. Relationship between smoke point and radiant emission from buoyant turbulent and laminar diffusion flames. *Proc. Combust. Inst.*, 20:1055–1061, 1994.

[7] M. Sato, J. Hansen, D. Koch, A. Lacis, Reto Ruedy, O. Dubovik, B. Holben, M. Chin, and T. Novakov. Global atmospheric black carbon inferred. *Appl. Biological Sci.*, 100(11):6319–6324, 2003.

[8] R. E. Ferguson. An isotopic tracer study of carbon formation in hydrocarbon flames. *Combust. Flame*, 1:431–437, 1957.

[9] N. Nishiwaki, M. Hirata, and R. Echigo. A study on the radiation of luminous flames. *Proc. Combust. Inst.*, 11:381–389, 1967.

[10] C. F. Cullis, A. I. Read, and L. D. Trimm. The role of acetylenic hydrocarbons in the formation of carbon from gases. *Proc. Combust. Inst.*, 11:391–397, 1967.

[11] B. B. Chakraborty and R. Long. The formation of soot and polycyclic aromatic hydrocarbons in diffusion flames-part iii- effect of additions of oxygen to ethylene and ethane respectively as fuels. *Combst. and Flame*, 12(3):469–467, 1968.

[12] B. B. Chakraborty and R. Long. The formation of soot and polycyclic aromatic hydrocarbons in diffusion flames-part one. *Combst. and Flame*, 12(3):226–236, 1968.

[13] B. B. Chakraborty and R. Long. The formation of soot and polycyclic aromatic hydrocarbons in diffusion flames-part two. *Combst. and Flame*, 12(3):237–242, 1968.

[14] B. B. Chakraborty and R. Long. The formation of soot and polycyclic aromatic hydrocarbons in ethylene diffusion flames with methanol as an additive. *Combst. and Flame*, 12(3):168–170, 1968.

[15] F. Wright. The formation of carbon under well stirred conditions. *Proc. Combust. Inst.*, 12:867–875, 1969.

[16] J. B. Howard. On the mechanism of carbon formation in flames. *Proc. Combust. Inst.*, 12:877–887, 1969.

[17] A. Sjogren. Soot formation by combustion of an atomized liquid fuel. *Proc. Combust. Inst.*, 14:919–927, 1973.

[18] B. L. Wersborg, J. B. Howard, and G. C. Williams. Physical mechanisms in carbon formation in flames. *Proc. Combust. Inst.*, 14:929–940, 1973.

[19] B. F. Magnussen. An investigation into the behavior of soot in a turbulent free jet c_2h_2 flame. *Proc. Combust. Inst.*, 15:1415–1425, 1975.

[20] B. F. Magnussen and B. H. Hjertager. On mathematical modeling of turbulent combustion with special emphasis on soot formation and combustion. *Proc. Combust. Inst.*, 16:719–729, 1977.

[21] P. A. Tesner, E. I. Tsygankova, V. P. Guilazetdinov, L. P. Zuyev, and G. V. Loshakova. The formation of soot from aromatic hydrocarbons in diffusion flames of hydrocarbon-hydrogen mixtures. *Combust. Flame*, 17(3):279–285, 1971.

[22] B. F. Magnussen, B. H. Hjertager, G. J. Olsen, and D. Bhaduri. Effects of turbulent structure and local concentrations on soot formation and combustion in c_2h_2. *Proc. Combust. Inst.*, 17:1383–1393, 1979.

[23] A. D'Alessio, A. D. Lorenzo, A. F. Sarofim, F. Beretta, S. Masi, and C. Venitozzi. Soot formation in methane-oxygen flames. *Proc. Combust. Inst.*, 15:1427–1438, 1975.

[24] M. Frenklach and J. S. Harris. Aerosol dynamics modeling using the method of moments. *Journal of Colloid and Interface Science*, 118:252–261, 1986.

[25] H. Gg. Wagner. Soot formation in combustion. *Proc. Combust. Inst.*, 17:3–19, 1979.

[26] B. S. Haynes and H. G. Wagner. Soot formation. *Prog. in Energy and Combust. Sci.*, 7:229–273, 1981.

[27] A. Levy. Unresolved problems in sox, nox, soot control in combustion. *Proc. Combust. Inst.*, 19:1223–1242, 1982.

[28] H. F. Calcote. Mechanisms of soot nucleation in flames - a critical review. *Combust. Flame*, 42:215, 1981.

[29] O. I. Smith. Fundamentals of soot formation in flames with application to diesel engine particulate emissions. *Prog. Energy Combust. Sci.*, 7(4):275–291, 1981.

[30] I. Glassman and P. Yaccarino. The temperature effect in sooting diffusion flames. *Proc. Combust. Inst.*, 18:1175 – 1981, 1981.

[31] S. Nagle and R. F. Strickland-Constable. Effect of oxidation on the physical structure of soot. *Fifth Carbon Conference*, 1:154, 1962.

[32] I Glassman. Soot formation in combustion processes. *Proc. Combust. Inst.*, 22:195 – 311, 1988.

[33] H. Bockhorn. *Soot Formation in Combustion.* Springer Verlag, Heidelberg, 1994.

[34] J. B. Moss. Simultaneous measurements of concentration and velocity in an open premixed turbulent flame. *Combust. Sci. Tech.*, 22:119–129, 1980.

[35] J. B. Moss and S. J. Brookes. Measurements of soot production and thermal radiation from confined turbulent jet diffusion flames of methane. *Combust. Flame*, 116:49–61, 1999.

[36] B. Hu, B. Yang, and U. O. Koylu. Soot measurments at the axis of an ethylene/air non-premixed turbulent jet flame. *Combust. Flame*, 134:93–106, 2003.

[37] B. Yang and U. O. Koylu. Detailes soot field in a turbulent non-premixed ethylene/air flame from laser scattering and extinction experiments. *Combust. Flame*, 141:55–65, 2005.

[38] A. Coppalle and D. Joyeux. Temperature and soot volume fraction in turbulent diffusion flames: Measurements of mean and fluctuating values. *Combust. Flame*, 96:275–285, 1994.

[39] A. Kronenburg, R. W. Bilger, and J. H. Kent. Modeling soot formation in turbulent methane - air jet diffusion flames. *Combust. Flame*, 121:24 – 40, 2000.

[40] S. Menon and J. Wu. Effects of micro- and macro-scale turbulent mixing on the chemical processes in engine exhaust plumes. *J. of Applied Meteorology*, 37:639–654, 1998.

[41] L. Wang, S. R. Haworth, D. C. Turns, and M. F. Modest. Interactions among soot, thermal radiation, and no x emissions in oxygen-enriched turbulent nonpremixed flames: A computational fluid dynamics modeling study. *Combust. Flame.*, 141:170–179, 2005.

[42] I. M. Kennedy. Models of soot formation and oxidation. *Prog. Energy Combust. Sci*, 23:95 – 132, 1997.

[43] K.J Young and J. B. Moss. Laminar diffusion flames burning and oxygen-rnriched flames. *Combust. Sci. and Tech.*, 105:33–53, 1995.

[44] K. J. Syed, D. C. Stewart, and B. J. Moss. Modelling soot formation and thermal radiation in buoyant turbulent diffusion flames. *Proc. Combust. Inst.*, 23:1533–1541, 1990.

[45] M. Fairweather, W. P. Jones, and R. P. Lindstedt. Prediction of radiative transfer from a turbulent reacting jet in a cross-wind. *Combust. Flame*, 82:45–63, 1992.

[46] P. R. Lindstedt and S. A. Louloudi. Joint-scalar transported pdf modeling of soot formation and oxidation. *Proc. Combust. Inst.*, 30:775 – 783, 2005.

[47] D. Andrea, A. D'Alessio, and M. Patrizia. *Soot Formation in Combustion.* Springer Verlag, Heidelberg, 1994.

[48] S. E Setin. On the high temperature chemical equilibria of polycyclic aromatic hydrocarbons. *J. Phys. Chem.*, 83:566–571, 1978.

[49] M. Frenklach, D. W. Clary, W. C. Gardiner, and S. E. Stein. Detailed kinetic modeling of soot formation in shock-tube pyrolysis of acetylene. *Proc. Combt. Inst.*, 20:887, 1985.

[50] M. Frenklach and H. Wang. *Detailed Mechanism and Modeling of Soot Particle Formation.* Springer Verlag, Heidelberg, 1994.

[51] J. A. Miller, R. J. Kee, and C. K. Westbrook. Chemical kinetics and combustion modeling. *Annu. Rev. Phys. Chem.*, 41:345–387, 1990.

[52] P. R. Lindstedt. *Soot Formation in Combust.* Springer Verlag, Heidelberg, 1994.

[53] U. Vandsburger, I. Kennedy, and I. Glassman. Sooting counter-flow diffusion flames with varying velocity gradients. *Proc. Combust. Inst.*, 20:1105–1112, 1984.

[54] P. R. Lindstedt. Soot formation in combustion. *IUTAM Symposium on Aerothermodynamics in Combustion*, pages 1 – 21, 1991.

[55] P. R. Lindstedt and F. Mauss. *Reduced Kinetic Mechanisms for Acetylene Diffusion Flames.* Springer-Verlag, Berlin, 1992.

[56] S. J. Harris and A. M. Weiner. Determination of the rate constant for soot surface growth. *Combust. Sci. Tech.*, 32(5):267–275, 1983.

[57] T.J. Poinsot and D. Veynante. *Theoretical and Numerical Combustion.* Edwards, Inc., second edition, 2005.

[58] R. Hilbert, F. Tap, H. El-Rabii, and D. Thevenin. Impact of detailed chemistry and transport models on turbulent combustion simulations. *Prog. in Energy and Combust. Sci.*, 30:61–117, 2003.

[59] D. Veynante and L. Vervisch. Turbulent combustion modeling. *Prog. in Energy and Combust. Sci.*, 28:193–266, 2002.

[60] A. M. Eaton, L. D. Smoot, S. C. Hill, and C. N. Eatough. Components, formulations, solutions, evaluations, and application of comprehensive combustion models. *Prog. Energy and Combust. Sci.*, 25:387–436, 1999.

[61] N. Peters. The turbulent burning velocity for large-scale and small scale turbulence. *Journal of Fluid Mechanics*, 384:107–132, 1999.

[62] S. R. Turns. *An Introduction to Combustion.* McGraw-Hill, 2000.

[63] N. Peters. *Turbulent Combustion.* Cambridge Monographs on Mechanics, 2000.

[64] D. B. Spalding. Concentration fluctuations in a round turbulent free jet. *Chem. Eng. Sci.*, 26:95, 1971.

[65] R. W. Bilger. The structure of diffusion flames. *Combust. Sci. and Tech.*, 13:155–170, 1976.

[66] F. A. Williams. A review of some theoretical considerations of turbulent flame structure. In *Analytical and Numerical Methods for Investigation of Flow Fields with Chemical Reactions, Especially Related to Combustion*, volume 164 of *AGARD Conference Proc.* North Atlantic Treaty Organization, 1974.

[67] N. Peters. Laminar flamelet concepts in turbulent combustion. *Proc. Combust. Inst.*, 21:1231–1250, 1986.

[68] H. Pitsch. Large eddy simulation of turbulent flames. *Ann. Rev. Fluid Mech.*, 38:233–266, 2006.

[69] N. Peters. Laminar diffusion flamelet models in non-premixed turbulent combustion. *Prog. Energy Combust. Sci.*, 10:319–339, 1984.

[70] H. Pitsch and N. Peters. Unsteady flamelet modeling of turbulent hydrogen-air diffusion flames. *Proc. Combust. Inst.*, 27:1057–1064, 1998.

[71] H. Pitsch and L. Duchamp De Lageneste. Large-eddy simulation of premixed turbulent combustion using a level-set approach. *Proc. Combust. Inst.*, 29:2001–2008, 2002.

[72] CD. Pierce and P. Moin. Progress variable approach for large eddy simulation of turbulent combustion. *J. Fluid Mech.*, 504:73–97, 2004.

[73] F. A. Williams. Turbulent combust. In J. D. Buckmaster, editor, *The Mathematics of Combustion*. Society for Industrial and Applied Mathematics, 1985.

[74] W.-W. Kim and S. Menon. Numerical simulations of turbulent premixed flames in the thin-reaction-zones regime. *Combust. Sci. Tech.*, 160:119–150, 2000.

[75] T. M. Smith and S. Menon. The structure of premixed flames in a spatially evolving turbulent flow. *Combust. Sci. Tech.*, 119(1-6):77–106, 1996.

[76] H. Pitsch. A consistent level set formulation for large eddy simulation of premixed turbulent combustion. *Combust. Flame*, 2005. In press.

[77] T. D. Butler and P. J. O'Rourke. A numerical method for two dimensional unsteady reactive flows. *Proc. Combust. Instit.*, 16:1503–1515, 1977.

[78] R. W. Bilger. Conditional moment closure for turbulent reacting flows. *Phys. Fluids*, A5:436–444, 1993.

[79] A. Kronenburg, R. W. Bilger, and J. H. Kent. Modeling soot formation in turbulent methane - air jet diffusion flames. *Combust. Flame*, 121:24 – 40, 2000.

[80] SH. Kim and H. Pitsch. Conditional filtering method for large eddy simulation of turbulent nonpremixed combustion. *Phys. Fluid*, 2005. in press.

[81] R. W. Bilger, SB. Pope, and JF. Driscoll. Paradigms in turbulent combustion research. *Proc. Combust. Inst.*, 30:21–42, 2005.

[82] S. B. Pope. Pdf methods for turbulent reactive flows. *Prog. Energy Combust. Sci.*, pages 119–192, 1985.

[83] P. Givi. Subgrid scale modeling in turbulent combustion: A review. *AIAA-2003-5081*, 2003.

[84] R. R. Cao, H. Wang, and S. B. Pope. The effect of mixing models in pdf calculations of piloted jet flames. *Proc. Combust. inst.*, 31, 2006. in press.

[85] S. B. Pope. Computations of turbulent combustion:progress and challenges. *Proc. Combust. Inst.*, 23:591–612, 1990.

[86] P. J. Colucci, F. A. Jaberi, P. Givi, and S. B. Pope. Filtered density function of large eddy simulation of turbulent reacting flows. *Phys. Fluids*, 10(2):499–515, 1998.

[87] F. A. Jaberi, P. Colucci, P. Givi, and S. B. Pope. Filtered density function of large eddy simulation of turbulent reacting flows. *J. Fluid Mech.*, 401, 1999.

[88] P. Givi. Filtered density function for subgrid scale modeling of turbulent combustion. *AIAA Journal*, 1:16–23, 2006.

[89] V. Raman and H. Pitsch. Les/filtered-density function simulation of turbulent combustion with detailed chemistry. *Center of Turbulence Research*, pages 297–309, 2005.

[90] V. Raman, H. Pitsch, and R. O. Fox. A consistent hyprid les-pdf scheme for the simulation of turbulent reactive flows. *Combust. Flame*, 143:297–309, 2005.

[91] S. B. Pope. *Turbulenct Flow*. Cambridge Book Company, first edition, 2000.

[92] A. R. Kerstein. Linear-eddy model of turbulent scalar transport and mixing. *Combust. Sci. Tech.*, 60:391–421, 1988.

[93] A. R. Kerstein. Linear-eddy model of turbulent transport ii. *Combust. Flame*, 75:397–413, 1989.

[94] A. R. Kerstein. Linear-eddy model of turbulent transport iii. *Journal of Fluid Mechanics*, 216:411–435, 1990.

[95] A. R. Kerstein. Linear-eddy modeling of turbulent transport. part 6. microstructure of diffusive scalar mixing fields. *Journal of Fluid Mechanics*, 231:361–394, 1991.

[96] A. R. Kerstein. Linear-eddy modeling of turbulent transport. part v: Geometry of scalar interfaces. *Physics of Fluids A*, 3(5):1110–1114, 1991.

[97] A. R. Kerstein. Linear-eddy modeling of turbulent transport. part 4. structure of diffusion-flames. *Combust. Sci. Tech.*, 81:75–86, 1992.

[98] A. R. Kerstein. Linear-eddy modeling of turbulent transport. 7. finite-rate chemistry and multi-stream mixing. *Journal of Fluid Mech.*, 240:289–313, 1992.

[99] V.K. Chakravarthy and S. Menon. Subgrid modeling of premixed flames in the flamelet regime. *Flow, Turbulance and Combust.*, 65:23–45, 2000.

[100] V.K. Chakravarthy and S. Menon. Large-eddy simulations of turbulent premixed flames in the flamelet regime. *Combust. Sci. and Tech.*, 162:175–222, 2000.

[101] S. Menon and V. Sankaran. Subgrid combustion modeling of two-phase reacting flows. In *IUTAM Symposium on Turbulent Mixing and Combustion*, pages 415–425. Kluwer Press, 2001.

[102] S. Menon and A. R. Kerstein. Stochastic simulation of the structure and propagation rate of turbulent premixed flames. *Proc. Combust. Inst.*, 24:443–450, 1992.

[103] S. Menon, P. A. McMurtry, A. R. Kerstein, and J. Y. Chen. A new mixing to predict nox production in turbulent hydrogen-air jet flame. *J. Prop. and Power*, 10:161–168, 1994.

[104] P. A. McMurtry, S. Menon, and A. R. Kerstein. A new subgrid model for turbulent combustion :application to hydrogen-air combustion. *Proc. Combust. Inst.*, 23:271–278, 1993.

[105] W. H. Calhoon, S. Menon, and G. Goldin. Comparison of reduced and full chemical mechanisms for nonpremixed turbulent h2-air het flames. *Combust. Sci. Tech.*, 104:115–141, 1995.

[106] S. Menon, W. H. Calhoon, J. R. Goldin, and A. R. Kerstein. Effects of molecular transport on turbulent-chemistry interactions in hydrogen-argon-air jet diffusion flame. *Proc. Combust. Inst.*, 25:1125–1131, 1994.

[107] G. Goldin and S. Menon. Scalar pdf construction model for turbulent non-premixed combustion. *Combust. Sci. Tech.*, 125:47 – 72, 1997.

[108] T. M. Smith and S. Menon. Large-eddy simulations of turbulent reacting stagnation point flows. *AIAA-97-0372*, 1997.

[109] V. Sankaran and S. Menon. Structure of premixed flame in the thin-reaction-zones regime. *Proc. Combust. Inst.*, 28:203–210, 2000.

[110] V. Sankaran and S. Menon. Subgrid combustion modeling of 3-d premixed flames in the thin-reaction-zone regime. *Proc. Combust. Inst.*, 30(1):575–582, 2005.

[111] G. Eggenspieler. *Numerical Simulation of Pollutant Emission and Flame Extinction in Lean Premixed Systems.* PhD thesis, Gerogia Institute of Technology, Atlanta, USA, July 2005.

[112] H. El-Asrag and Menon. Large eddy simulation of a bluff body stabilized swirling non-premixed flames. *Proc. Combust. Inst.*, 31:inpress, 2007.

[113] G. Eggenspieler and S. Menon. Numerical simulation of flame extinction in the broken-reaction zone regime. *AIAA-2006-158*, 2006.

[114] H. El-Asrag, S. Menon, T. Lu, and C.K Law. Large eddy simulation of soot formation in turbulent premixed flame. *AIAA-2006-153*, 2006.

[115] D. A. Anderson, J. C. Tannehill, and R. H. Pletcher. *Computational Fluid Mechanics and Heat Transfer.* McGraw-Hill Book Company, 1997.

[116] J. R. Andrews and O. Biblarz. *Temperature Dependence of Gas Properties in Polynomial Form.* Naval Postgraduate School, 1981.

[117] S. B. Pope. Ten questions regarding the large eddy simulation of turbulent flows. *New Journal of Physics*, 35(6):1–24, 2004.

[118] G. Erlebacher, M. Y. Hussaini, C. G. Speziale, and T. A. Zang. Toward the large-eddy simulation of compressible turbulent flows. *Journal of Fluid Mech.*, 238:155–185, 1992.

[119] W.-W. Kim, S. Menon, and H. C. Mongia. Large-eddy simulation of a gas turbine combustor flow. *Combust. Sci. Tech.*, 143:25–62, 1999.

[120] C. R. Kaplan, C. R. Shaddix, and K. C. Smyth. Computations of enhanced soot production in time-varying ch4/air diffusion flames. *Combust. Flame*, 106:392–404, 1996.

[121] J. Smagorinsky. General circulation experiments with the primitive equations. *Monthly Weather Review*, 91(3):99–164, 1993.

[122] S. Menon, P.-K. Yeung, and W.-W. Kim. Effect of subgrid models on the computed interscale energy transfer in isotropic turbulence. *Computers and Fluids*, 25(2):165–180, 1996.

[123] W.-W. Kim and S. Menon. A new incompressible solver for large-eddy simulations. *International Journal of Numerical Fluid Mech.*, 31:983–1017, 1999.

[124] S. Liu, C. Meneveau, and J. Katz. On the properties of similarity subgrid-scale models as deduced from measurements in a turbulent jet. *Journal of Fluid Mechanics*, 275:83–119, 1994.

[125] D. K. Lilly. A proposed modification of the germano subgrid-scale closure method. *Physics of Fluids A*, 4(3):633–635, 1992.

[126] C. Fureby and S.-I. Möller. Large-eddy simulation of reacting flows applied to bluff body stabilized flames. *AIAA Journal*, 33(12):2339–2347, 1995.

[127] S. Menon and W. H. Calhoon. Subgrid mixing and molecular transport modeling for large-eddy simulations of turbulent reacting flows. *Proc. Combust. Inst.*, 26:59–66, 1996.

[128] H. Tennekes and J. L. Lumley. *A First Course in Turbulence.* MIT Press, 1992.

[129] A. R. Kerstein and Wm. T. Ashurst. Propagation rate of growing interfaces in stirred fluids. *Physical Review*, 68(7):934–937, 1992.

[130] T. M. Smith and S. Menon. Simulations of freely propagating turbulent premixed flows. *AIAA-96-3031*, 1996.

[131] S. B. Pope. Turbulent premixed flames. *Ann. Rev. of Fluid Mech.*, pages 237–270, 1987.

[132] V. Sankaran and S. Menon. Alignment statistics and small-scale structures in swirling spray combustion. *Proc. Combust. Inst.*, 29:577–584, 2002.

[133] T. M. Smith and S. Menon. Model simulations of freely propagating turbulent premixed flames. *Proc. Combust. Inst.*, 26:299–306, 1996.

[134] S. Menon, P.A. McMurtry, and A. R. Kerstein. A linear eddy mixing model for large eddy simulation of turbulent combustion. In B. Galperin and S. Orszag, editors, *LES of Complex Engineering and Geophysical Flows*, pages 287–314. Cambridge University Press, 1993.

[135] J. S. Brookes and J. B. Moss. Predictions of soot and thermal radiation properties in confined turbulent jet diffusion flames. *Combust. Flame*, 116:486–503, 1999.

[136] W. Kollmann, I. M. Kennedy, M. Metternich, and J.-Y. Chen. *Soot Formation in Combustion: Mechanisms and Models.* Springer Verlag, Berlin, 1994.

[137] M. I. Aksit and J. B. Moss. A hybrid scalar model for sooting turbulent flames. *Combust. Flame*, 145:231 - 244, 2006.

[138] Z. Wen, S. Yun, M.J. Thomson, and M.F. Lightstone. Modeling soot formation in turbulent kerosene/air jet diffusion flames. *Combust. Flame*, 135:323–340, 2003.

[139] S. Hong, S. W. Margaret, G. I. Hong, N. A. Dennis, and H. Pitsch. Development and application of a comprehensive soot model for 3d cfd reacting flow studeis in diesel engine. *Combust. Flame*, 143:11–26, 2005.

[140] D. J. Hudson. Lectures on elementary statistics and probability. *CERN*, 1963.

[141] M. Frenklach. Method of moments with interpolative closure. *Chem. Eng. Sci.*, 57:2229–2239, 2002.

[142] M. Frenklach. Reaction mechanism of soot formation in flames. *Phys. Chem. Chem. Phys.*, 4:2028–2037, 2002.

[143] T. Lu and C. K. Law. A directed relation graph method for mechanism reduction. *Proc. Combust. Inst.*, 30:1333 – 1341, 2005.

[144] K. M. Leung and P. R Lindstedt. A simplified reaction mechanism for soot formation in nonpremixed flames. *Combust. Flame*, 87:289 – 305, 1991.

[145] S. J. Harris and A. M. Weiner. Chemical kinetics of soot particle growth. *Ann. Rev. of Phys. Chem.*, pages 31–52, 1985.

[146] T. Lu, Y. Ju, and C. K. Law. Complex csp for chemistry reduction and analysis. *Combust. Flame*, 126:1445–1455, 2001.

[147] M. V. Smoluchowski. Versuch einer mathematischen theorie der koagulationskinetik kolloider losungen. *Z. Physical Chemistry*, 92:129–139, 1917.

[148] M. Frenklach. Dynamics of discrete distribution for smoluchowski coagulation mode. *Journal of Colloid and Interface Science*, 108:237–242, 1985.

[149] J. H. Seinfeld and S. N. Pandis. *Atmosperic Chemistry and Physics. From Air Pollution to Climate Change.* New York: Willy, 1998.

[150] A. Kazakov and M Frenklach. Dynamic modeling of soot particle coagulation and aggregation:implementation with the method of moments and application to high-pressure laminar premixed flames. *Combust. Flame*, 114:484–501, 1998.

[151] S. K. Friedlander. *Smoke, Dust, and Haze Fundamentals of Aerosol Dynamics.* Oxford University Press, 2000.

[152] J.H. Stephen and I. M. Kennedy. Soot particle aerosol dynamics at high pressure. *Combust. Flame*, 78:390–397, 1989.

[153] S. E Pratsinis. Simultaneous nucleation, condensation, and coagulation in aerosol reactors. *Journal of Collide and Interface Science*, 124:416–427, 1988.

[154] P Mitchell and M. Frenklach. Particle aggregation with simultaneous surface growth. *Phys. Review E*, 67:061407–1–061407–11, 2003.

[155] L Zhigang and H. Wang. Thermophoretic force and velocity of nanoparticles in the free molecular regime. *Phys. Review E*, 70:021205–1–021205–11, 2004.

[156] C. N. Davies. *Aerosol Science.* Acadamic Press, New York, 1966.

[157] A. Knudsen and S. Weber. *Ann. Phys. (Leipzig)*, 36:981–987, 1911.

[158] L Zhigang and H. Wang. Drag force, diffusion coefficient and electric mobility of small particles. ii. application. *Phys. Review E*, 68:061207–1–061206–13, 2003.

[159] A. Einstein. On the motion of small particles suspended in liquids at rest required by the molecular-kinetic theory of heat. *Annalen der Physik.*, 17:549–560, 1905.

[160] M. B. Colket and R. J. Hall. *Success and Uncertainties in Modelling Soot Formation in Laminar, Premixed Flames.* Springer Verlag, Heidelberg, 1994.

[161] M. Balthasar and M. Mauss. A stochastic approach to calculate the particle size distribution function of soot particles in laminar premixed flames. *Combust. Flame*, 133:289 – 298, 2003.

[162] M. Smith and T. Matsoukas. Constant-number monte carlo simulation of population balances. *Chem. Eng. Sci.*, 53(9):1777–1786, 1998.

[163] S. B. Pope. Computationally efficient implementation of combustion chemistry using in situ adaptive tabulation. *Combust. Theory Modelling*, 1:41–63, 1997.

[164] G. Eggenspieler and S. Menon. Les of premixed combustion and pollutant emission in a doe-hat combustor. *J. Prop. Power*, 20:1076–1086, 2004.

[165] O. U. Koylu, G. M. Faeth, T. L. Farias, and M. G. Carvalho. Fractal and projected structure properties of soot aggregates. *Combust. Flame*, 100:621–633, 1995.

[166] S. J. Harris and A. M. Weiner. Some constraints on soot particle inception in premixed ethylene flames. *Proc. Combust. Inst.*, 20:969–978, 1984.

[167] F. Xu, P. B. Sunderland, and G. M. Faeth. Soot formation in laminar premixed ethylene/air flames at atmospheric pressure. *Combust. Flame*, 108:471 – 493, 1997.

[168] Z. Qin, V. V. Lissianski, W. C. Gardiner, S. G. Davis, and H. Wang. A directed relation graph method for mechanism reduction. *Proc. Combust. Inst.*, 28:1663 – 1669, 2000.

[169] K. B. Lee, M. W Thring, and J. M. Beer. On the rate of combustion of soot in a laminar soot flame. *Combust. Flame*, 6:137 – 145, 1962.

[170] D. Bradley, G. Dixon-Lewis, S. El-Din Habik, and E. M. J. Mushi. The oxidation of graphite powder in flame reaction zone. *Proc. Combust. Inst.*, 20:931 – 940, 1984.

[171] G. Eggenspieler and S. Menon. Combustion and emission modeling near lean blow-out in gas turbine engines. *Prog. Comp. Fluid Dyn.*, 5(6):281–297, 2005.

[172] K. A. Hoffman and S. T. Chiang. *Computational Fluid Dynamics for Engineers: Volume II.* Engineering Education System, Wichita, Kansas, USA, 1993.

[173] R. W. MacCormack. The effects of viscosity in hyper-velocity impact cratering. *AIAA Paper 69–354*, 1969.

[174] C. C. Nelson. *Simulations of spatially evolving compressible turbulence using a local dynamic subgrid model.* PhD thesis, Georgia Institute of Technology, 1997.

[175] D. A. Anderson, J. C. Tannehill, and R. H. Pletcher. *Computational Fluid Mechanics and Heat Transfer.* McGraw-Hill Book Company, 1984.

[176] T.J. Poinsot and S.K. Lele. Boundary conditions for direct simulations of compressible viscous flow. *Journal of Computational Phys.*, 101:104–129, 1992.

[177] T. Baum, M. Poinsot and D. Thevenin. Accurate boundary conditions for multicomponent reactive flows. *J. Comp. Phys.*, 116:247 – 261, 1994.

[178] H. El-Asrag. Inviscid chemically reacting flow model using a fractional step method. Master's thesis, Cairo university - Aerospace Department, Cairo, Egypt, 2002.

[179] J. D. Anderson. *Computational Fluid Dynamics.* McGraw-Hill Book Company, 1997.

[180] P. Colella and P. R. Woodward. The piecewise parabolic method (ppm) for gas-dynamical simulation. *J. Comp. Phys.*, 541(1):174–200, 1984.

[181] J. C. Tannehill, T. L. Holst, and J. V. Rakich. Numerical computation of two dimensional blunt body flows with an impinging schock. *AIAA-1975-78-1209*, 1975.

[182] V. Sankaran and S. Menon. Les of scalar mixing in supersonic shear layers. *Proc. Combust. Inst.*, 30(2):2835–2842, 2005.

[183] M. Billson, L. Eriksson, and L. Davidson. Jet noise prediction using stochastic turbulence modeling. *AIAA 2003-3282*, 2003.

[184] A. Trouvé and T. Poinsot. The evolution equation for the flame surface density in turbulent premixed combustion. *Journal of Fluid Mech.*, 278:1–31, 1994.

[185] A. D'Alessio, A. D'Anna, L. A. Sgro, and A. Violi. On the relevance of surface growth in soot formation in premixed flames. *Proc. Combust. Inst.*, 28:2547–2554, 2000.

[186] K. G. Neoh, J. B. Howard, and A. F. Saforim. Effect of oxidation on the physical structure of soot. *Proc. Combust. Inst.*, 20:951 – 957, 1984.

[187] A. Kazakov, H. Wang, and M. Frenklach. Detailed modeling of soot formation in laminar premixed ethylene flames at a pressure of 10 bar. *Combust. Flame*, 100:111–120, 1992.

[188] C. K. Law, P. Cho, M. Mizomoto, and H. Yoshida. Flame curvature and preferential diffusion in the burning intensity of bunsen flames. *Proc. Combust. Inst.*, 21:1803–1809, 1986.

[189] M. Mizomoto, Y. Asaka, S. Ikai, and C. K. Law. Effects of preferential diffusion on the burning intensity of curved flames. *Proc. Combust. Inst.*, 20:1933–1939, 1984.

[190] T. Echekki and J. H. Chen. Unsteady strain rate and curvature effects in turbulent premixed methane-air flames. *Combust. Flame*, 106(1):184–202, 1996.

[191] D. Beadley, P. H. Gaskell, X. J. Sedaghat, and X. J. Gu. Generation of pdfs for flame curvature and for flame stretch rate in premixed turbulent combustion. *Combust. Flame*, 135:503 – 523, 2003.

[192] A. Pocheau. Scale invariance in turbulent front propagation. *Phys. Rev. E*, 49:1109–1122, 1994.

[193] A. R. Masri, S. B. Pope, and B. B. Dally. Propability density function computations of a strongly swirling nonpremixed flame stabilized on a new burner. *Proc. Combust. Inst.*, 28:123 - 131, 2000.

[194] A. R. Masri, P. A. Kalt, and R. S. Barlow. The compositional structure of swirl-stabilized turbulent non-premixed flame. *Combust. Flame*, 137:1 - 37, 2004.

[195] A. R. Masri and R. W. Bilger. Turbulent diffusion flames of hydrocarbon fuels stabilized on a bluff body. *Proc. Combust. Inst.*, 20:319 - 326, 1984.

[196] B. B. Dally, A. R. Masri, R. S. Barlow, and G. J. Fiechtner. Instantaneous and mean compositional structure of bluff-body stabilized nonpremixed flames. *Combust. Flame*, 114:119 - 148, 1998.

[197] A. R. Masri, B. B. Dally, R. S. Barlow, and C. D. Carter. The structure of the recirculation zone of a bluff-body combustor. *Proc. Combust. Inst.*, 25:1301 - 1308, 1994.

[198] J. B. Kelman, A. R. Masri, and R. W. Bilger. Wide-field conserved scalar imaging in turbulent diffusion flames by a raman and rayleight method. *Proc. Combust. Inst.*, 25:1141–1147, 1994.

[199] B. B. Dally, A. R. Masri, R. S. Barlow, and G. J. Fiechtner. Instantaneous and mean compositional structure of bluff-body stabilized nonpremixed flames. *Proc. Combust. Inst.*, 26(2):2191 - 2197, 1996.

[200] S. M. Correa and S. B. Pope. Comparison of a monte carlo pdf/finite-volume mean flow model with bluff-body raman data. *Proc. Combust. Inst.*, 24:279–285, 1992.

[201] S. M. Correa and A. Gulati. Measurments and modeling of a bluff body stabilized flame. *Combust. Flame*, 89:195–213, 1992.

[202] R. W. Masri, A. R. Dibble and R. S. Barlow. The structure of the turbulent non-premixed flames revealed by raman-rayleigh-lif measurments. *Prog. Energy. Combust. Sci.*, 22:307 - 362, 1996.

[203] P. A. M. Kalt, Y. M. Al-Abdeli, A. R. Masri, and R. S. Barlow. Swirling turbulent non-premixed flames of methane: Flow field and compositional structure. *Proc. Combust. Inst.*, 29:1913–1919, 2002.

[204] Y. M. Al-Abdeli and A. R. Masri. Stability characteristics and flowfields of turbulent non-premixed swirling flames. *Combust. theory and Modeling*, 7:731 - 766, 2003.

[205] A. R. Masri. *Swirl Flame Web Database.* University of Sydney, 2005. http://www.aeromech.usyd.edu.au/thermofluids/swirl.html.

[206] Y. M. Al-Abdeli and A. R. Masri. Recirculation and flowfield regimes of unconfined non-reacting swirling flows. *Exp. Therm. Fluid. Sci.*, 27:655 – 665, 2003.

[207] A. Kempf, R. P. Lindstedt, and J. Janicka. Large-eddy simulation of a bluff-body stabilized non-premixed flame. *Combust. Flame*, 144:170–189, 2006.

[208] V. Raman and H. Pitsch. Large eddy simulation of a bluff-body-stabilized non-premixed flame using a recursive filter-refinement procedure. *Combust. Flame*, 142:329–347, 2005.

[209] R. R. Cao, S. B. Pope, and A. R. Masri. Turbulent lifted flames in a vitiated coflow investigated using joint pdf calculations. *Combust. Flame*, 142:438–453, 2005.

[210] B. Guo, D. F. Fletcher, G. Marquez, Y. M. Al-Abdeli, S. H. Starner, and A. R. Masri. Rans calcualtions and measurments of instabilities in swirl-stabilized jets and flames. *Proceedings of the 2003 Australian Symposium on Combustion and the 8th Australian Flame Days, Melbourne Australia*, 2003.

[211] Y. M. Al-Abdeli, A. R. Masri, G. R. Marquez, and S. H. Starner. Time-varying behavior of turbulent swirling nonpremixed flames. *Combust. Sci. Tech.*, 176(5-6):645 – 664, 2004.

[212] Y. M. Al-Abdeli and A. R. Masri. Precession and recirculation in turbulent swirling isothermal jets. *Combust. Sci. Tech.*, 176(5-6):645 – 664, 2004.

[213] J. Janicka and A. Sadiki. Large eddy simulation of turbulent combustion systems. *Proc. Combust. Inst.*, 30(1):537–548, 2005.

[214] V.K. Chakravarthy and S. Menon. Linear-eddy simulations of reynolds and schmidt number dependencies in turbulent scalar mixing. *Physics of Fluids*, 13:488–499, 2001.

[215] S. Menon. Co emission and combustion dynamics near lean blow-out in gas turbine engines. *ASME-GT2004-53290*, 2004.

[216] S. Menon and N. Patel. Subgrid modeling for les of spray combustion in large-scale combustors. *AIAA Journal)*, 44(4):709–723, 2006.

[217] N. Syred and J. M. Beer. Combustion in swirling flows. *Combust. Flame*, 23:143–201, 1974.

[218] C. K. Westbrook and F. L. Dryer. Simplified reaction mechanisms for the oxidation of hydrocarbon fuels in flames. *Combust. Sci. Tech.*, 27:31–43, 1981.

[219] G. Lilley. Swirl flows in combustion: A review. *AIAA Journal*, 15(8):1063–1078, 1977.

[220] C. Peskin. The immersed boundary method. *Acta Numerica*, 11:479–517, 2002.

[221] W.-W. Kim and S. Menon. Numerical modeling of turbulent premixed flames in the thin-reaction-zones regime. *Combust. Sci. Tech.*, 160:119–150, 2000.

[222] J. H. Kent and D. Honnery. Soot and mixture fraction in turbulent diffusion flames. *Combust. Sci. and Tech.*, 54:383 – 397, 1987.

[223] J. P. Gore and G. M. Faeth. Structure and spectral radiation properties of turbulent ethylene/air diffusion flames. *Proc. Combust. Inst.*, 21:1521 – 1531, 1986.

[224] Y. R. Sivathanu, J. P. Gore, and G. M. Faeth. Scalar properties in the overfire region of sooting turbulent diffusion flames. *Combust. Sci. and Tech.*, 73:315–329, 1988.

[225] J. H. Kent and S. J. Bastin. Parametric effects on sooting in turbulent acetylene diffusion flames. *Combust. Flame*, 56:29, 1984.

[226] B. Yang and U. O. Koylu. Mean soot volume fraction in turbulent hydrocarbon flames: A comparison of sampling and laser measurments. *Combust. Sci. Tech.*, 177:1603–1626, 2005.

[227] H. Guy and B. Carlo. Large eddy simulation of planar co-flowing jet. In *Direct and Large Eddy Simulation*, volume II, pages 11 – 22. Kluwer Academic, 1997.

[228] F. Mauss, K. Netzell, and Harry. Lehtiniemi. Aspects of modelling soot formation in turbulent diffusion flames. *Combust. Sci. Tech.*, 178:1871 – 1884, 2006.

[229] C. Le Ribault, S. Sarkar, and S. A. Stanley. Large eddy simulaiton of a plane jet. *Phys. Fluid*, 11:3069, 1999.

[230] Q. Hu. Fang. Absorbing boundary conditions. *Int. J. of Comp. Fluid Dynaimcs*, 18(6):513–532, 2004.

[231] C. A. Kennedy and M. H. Carpenter. Several new numerical methods for compressible shear-layer simulations. *App. Num. Math.*, 14:397 – 433, 1994.

[232] T. Colonius, S. K. Lele, and P. Moin. Boundary conditions for direct computation of aerodynamic sound generation. *AIAA J.*, 31(9):1574–1582, 1993.

[233] M.R. Visbal and D.V. Gaitonde. Very high order spatially implicit scheme for computational acoustics on curvilinear meshs. *J. Comput. Acoust.*, 9:1259–1286, 2001.

[234] J. B. Freund. Proposed inflow/outflow boundary condition for direct computation of aerodymainc sound. *AIAA J.*, 35(2):740–742, 1997.

[235] L. J. S. Bradbury. The structure of a self-preserving turbulent plane jet. *J. Fluid Mech.*, 23:31 – 64, 1965.

NADV	IADD	JADD	KADD
n	1	1	1
n+1	0	1	1
n+2	1	0	1
n+3	0	0	1
n+4	1	1	0
n+5	0	1	0
n+6	1	0	0
n+7	0	0	0

Table 5: The switch parameters for the forward backward differencing sequence

A Coding Application

As mentioned in section (6.7.1) the order of differencing should be reversed to eliminate any bias of one sided operations. In the code the order of differencing is alternated in space and time. If $NADV$ is the time advancement parameter, three switches are identified one for each spatial direction $IADD$, $JADD$, and $KADD$. These three switches are computed from:

$$\begin{aligned} IADD &= mod(NADV, 2) \\ JADD &= mod((NADV + IADD)/2, 2) \\ KADD &= mod((NADV + IADD + 2JADD)/4, 2) \end{aligned} \tag{224}$$

Then the direction of flux being forward + or backward − is identified for each step based on the above combination. If the switch is equal to 1 the sequence will be forward backward and the reverse if the switcher value is equal to 0. Table 5 summarizes one loop before the sequence repeats itself. Now we will follow up the algorithm of computing the flux in the i direction (F):

- Reading the input parameters, such as the grid dimension, the number of processors and other reference values.
- Reading the grid physical coordinates x, y, z.
- Specify type and location of boundaries.
- Initialize the flow field.
- Set the physical boundary conditions.
- Start the time integration loop

  Compute the LES time step.
- Specify the sequence of differencing in each direction according to Table 5.
- Start the predictor step

- Compute the flux in the $i-th$ direction as follows:
- If the sequence is forward, $n, n+2, n+4, n+6$ then shift all the Q (conservative variables) by one cell to the right and store them in Q_{AV}. If the sequence is backward the same I, J, K location will be stored in Q_{AV} without any shift. For instance for I ranges for $(0 - Imax)$ in the forward step Q_{AV} will be:

$$Q_{AV}(0 : Imax, J, K) = Q_{AV}(1 : Imax + 1, J, K)$$

- The primitive variables are computed based on the new Q_{AV} values.
- The contravarient velocity $\tilde{U}$ is computed and stored in a variable called QS as:

$$Q_S(0 : Imax) = (\zeta_x U + \zeta_y V + \zeta_z W)/J$$

- The contravarient velocity Q_S is then multiplied by Q_{AV} and stored in $\vec{F_{SI}}$ to give.

$$\vec{F_{SI}} = \begin{bmatrix} \rho\tilde{U} \\ \rho\tilde{U}U \\ \rho\tilde{U}V \\ \rho\tilde{U}W \\ \rho\tilde{U}E \\ \rho\tilde{U}Y_k \end{bmatrix}$$

- The pressure terms are then added to F as:

$$\vec{F_{SI}} = \vec{F_{SI}} + \begin{bmatrix} 0 \\ PAV\zeta_x \\ PAV\zeta_y \\ PAV\zeta_z \\ PAV\tilde{U} \\ 0 \end{bmatrix}$$

- The viscous terms are added according to Eq. (178) as follows:
- The primitive variables derivatives (U,V,W,T,Y_K) are computed. For instance $DUDX$ will be computed as:

$$\frac{dU}{dX} = \zeta_x \frac{dU}{d\zeta} + \eta_x \frac{dU}{d\eta} + \xi_x \frac{dU}{d\xi}$$

where ζ_x, η_x, ξ_x are the metrics computed as in Eq. (172). The cross-stream derivatives ($\frac{dU}{d\eta}$ and $\frac{dU}{d\xi}$) are differenced centrally, while $\frac{dU}{d\zeta}$ are done using a forward differencing to eliminate one-sided bias as explained before:

$$\frac{dU}{d\zeta} = U_{i+1,j,k} - U_{i,j,k} \quad \frac{dU}{d\eta} = U_{i,j+1,k} - U_{i,j-1,k} \quad \frac{dU}{d\xi} = U_{i,j,k+1} - U_{i,j,k-1}$$

At the boundaries a one-sided differencing (backward for outflow and forward for inflow) is done for all derivatives.

- Afer computing all the derivatives the average values at the cell face is computed and stored. For instance, $T_{av} = \frac{T_{i,j,k}+T_{i+1,j,k}}{2}$.

- Using, the above information, the shear stress components, the heat flux by conduction and diffusion are computed based on Eqs. (180,181).

- Finally, the viscous flux components are summed up together. For instance, the total energy flux will be:

$$\begin{aligned} FV(5) = &(\tau_{xx} * U_{av} + \tau_{xy} V_{av} + \tau_{xz} W_{av} + q_x)\,\zeta_x + \\ &(\tau_{yx} * U_{av} + \tau_{yy} V_{av} + \tau_{yz} W_{av} + q_y)\,\zeta_y + \\ &(\tau_{zx} * U_{av} + \tau_{zy} V_{av} + \tau_{zz} W_{av} + q_y)\,\zeta_z \end{aligned} \tag{225}$$

- The viscous and inviscid fluxes are summed up to give $\vec{F}$.

- Compute the change in the conservative variables due to the flux in the $i-th$ direction as (excluding the ghost cells):

$$D\vec{Q}_{i,j,k} = -\frac{\Delta t}{\Delta V}\left[\vec{F}_I - \vec{F}_{I-1}\right]$$

  In the forward step, this will be equivalent to $\vec{F}_{I+1} - \vec{F}_I$ and in the backward step that will be $\vec{F}_I - \vec{F}_{I-1}$. Summing up the predictor and corrector step will result in a central scheme.

- Store the mass fluxes F_{VEL} on the two faces (i, i-1)at constant i for the LEM splicing as:

$$FVEL_{i,j,k}(1) = FVEL_{i,j,k}(1) + \frac{\Delta t}{2} F(1)_{I-1}$$

$$FVEL_{i,j,k}(2) = FVEL_{i,j,k}(2) + \frac{\Delta t}{2} F(1)_{I}$$

  Summing up the predictor and corrector steps will be equivalent to:

$$FVEL_{i,j,k}(1) = \frac{\Delta t}{2}\left(F(1)_I + F(1)_{I-1}\right)$$

$$FVEL_{i,j,k}(2) = \frac{\Delta t}{2}\left(F(1)_{I+1} + F(1)_I\right)$$

  although, the equations are highly non-linear, from the linear point of view, it is equivalent to a central scheme for the face flux calculations.

- The characteristic boundary conditions are then applied in the $i-th$ direction.

- The same operations are repeated in the $j-th$ and $k-th$ directions. We will get finally six mass fluxes for each one of the cell faces.

- The source terms are calculated for the k_{sgs} equation.

- The subgrid processes are computed by LEM and splicing is performed.
- The conservative variables are updated based on the new DQs for the predictor step as:

$$\vec{Q^*}_{i,j,k} = \vec{Q}_{i,j,k} + D\vec{Q}_{i,j,k}$$

and for the corrector step as:

$$\vec{Q^{n+1}}_{i,j,k} = \frac{1}{2}\left(\vec{Q^*}_{i,j,k} + +\vec{Q}_{i,j,k} + 2D\vec{Q}_{i,j,k}\right)$$

- The primitive variables are decoded from the conservative variables.
- After the predictor-corrector step is finished the new sequence is computed for the new time step.

B Sponge Buffer Absorbing Boundary Condition

For most of the combustion applications the flow is subsonic and the outflow is usually non-uniform. In addition, the back pressure is usually unknown. At such case the NSCBC might be unstable, if the outflow is not aligned with the characteristic lines. This problem is observed in the literature ([227]),([229]), where chunks of back flow are observed at the outflow section due to the generation of an adverse pressure gradient. This problem is more specific and annoying for free jet problems, where the solution stability is usually tied up to the stability of the boundaries.

A methodology that is often used in these situations is the zonal buffer absorbing boundary conditions, where a set of actions is implemented either together or separately to ensure non-reflecting, absorbing boundary conditions, with no adverse back pressure. Usually, these methodologies are implemented in a buffer zone, where the solution is un-physical and the outgoing disturbance is attenuated by one way or another ([230]). This buffer zone is usually terminated with absorbing characteristic boundary conditions as described before.

The first methodology is to refilter the outflow section to make the solution under-resolved and to damp the numerical oscillations. There are many filtering procedures in the literature with different order. See for example [231] and [232] for explicit filtering and [233] for implicit filtering. Another technique is to stretch the grid at the outflow section to under-resolve the incoming waves. However, this has to be done gradually to avoid generation of numerical instabilities. Another, common method is to add a damping factor to the governing equations, that is zero at the buffer zone boundary and maximum at the outflow section. For instance for a general set of PDE, the damping viscosity μ can be added as ([230]):

$$\frac{\partial u}{\partial t} = L(u) - \mu\,(u - u_o) \tag{226}$$

Finally, another methodology, which is implemented here ([234]), is to add a convection term inside the buffer zone to the governing equations to accelerate the flow field supersonically at the outflow section. That way no back pressure is needed and the buffer layer acts as a sponge, where all the incoming waves are absorbed. If we assume that we have an artificial velocity with zero components in the transverse and spanwise directions, then the convection term are added to the fluxes as follows ([234]) (for example the flux in the $i-th$ direction:

$$\begin{aligned} F_{i,j,k} &= F_{i,j,k} + Q_{i,j,k} * Qs_{Buffer} \\ Qs_{Buffer} &= \zeta_x U_B + \zeta_y V_B + \zeta_z W_B \end{aligned} \tag{227}$$

Where the artificial buffer convection speed is calculated as ([234]):

$$\begin{aligned} U_B &= \alpha_1 * a(1 + \tanh(\phi(X_{i,j,k} - X_{max})))/2.0 \\ V_B &= 0.0D + 00 \\ W_B &= 0.0D + 00 \end{aligned} \tag{228}$$

Here, X_{max} is the domain length, X is the local axial location, α_1 is a value greater than 1 (typically 1.15) to accelerate the flow above the speed of sound, and (a) is the speed of sound. The parameter ϕ is calculated such that $U_B(X_{max} - X_{buffer}) = \alpha_2 a$, where X_{buffer}

is the length of the buffer zone, and α_2 is a very small value chosen to match the velocity at the buffer zone boundaries. Accordingly, ϕ will be given as:

$$\phi = -0.5(log(2(\alpha_2)/\alpha_1)/(2.0 - 2(\alpha_2)/\alpha_1))/X_{buffer} \tag{229}$$

The sponge boundary condition is applied to a travelling pressure wave in the axial direction, which is initialized as:

$$\begin{aligned} U_{i,j,k} &= U_{ref} + (0.5U_{ref} \exp(-(12.0(I - 0.5I_{max})/I_{max})^2)) \\ V_{i,j,k} &= 0.0D + 00 \\ W_{i,j,k} &= 0.0D + 00 \\ P_{i,j,k} &= P_{ref} - \rho_{ref} * a_{ref} * ABS(U_{i,j,k} - U_ref) \end{aligned} \tag{230}$$

Where, I_{max} is the maximum number of cell boundaries in the I direction, I is the local grid index, and all the values with the subscript ref is a pre-specified reference values that determine the peak of the pressure wave and its convection velocity. The results show good absorbtion of the pressure wave as shown in Fig. 80, where six successive snapshots with time are shown for the time advancement of the pressure wave. The linear plot on the upper left corner if for the pressure along the flow axis. Figure 80 (e) shows that the pressure wave is completely absorbed with very small reflections that is much smaller than the inflow values. A second test is performed on a travelling vortex. First, the center of the vortex (X_{cen}, Y_{cen}) and vortex strength are determined as:

$$\begin{aligned} &X_m = X_{i,j,k} - X_{cen} \; Y_m = Y_{i,j,k} - Y_{cen} \\ &R_m = \sqrt{X_m^2 + Y_m^2} \\ &C = a_{ref} * YLEN(-0.001) \\ &A = \exp \frac{-R_m}{0.5YLEN^2} \end{aligned} \tag{231}$$

Then the velocity field is initialized as:

$$\begin{aligned} U_{i,j,k} &= U_{ref} - 2 * C * Y_m(A)/\rho/YLEN^2 \\ V_{i,j,k} &= 2 * C * Y_m(A)/\rho/YLEN^2 \\ W_{i,j,k} &= 0.0D + 00 \\ P_{i,j,k} &= P_{i,j,k} - 4 * \rho_{ref} * C^2 * A/YLEN^2 \end{aligned} \tag{232}$$

Figure 81 (a-d) shows the contours of the vorticity in the span-wise direction (z-component). The vortex is completely absorbed inside the sponge layer with very small (almost negligible) reflections as shown in Fig. 81 (d).

A validation ([235]) case for a free planar jet is simulated and compared with experiment. The jet centerline decay in Fig. 82 and the spread rate in Fig. 83, show good agreement with the experiment. The radial velocity profiles are also shown in Fig. 84. The statistics were collected for 15 flow through times. The buffer zone outflow boundary conditions is used combined with NSCBC. The test case conditions are summarized in Table 6.

Where, h is the height between the plates and Re is the Reynolds number based on the jet velocity and height. The domain length is 30h x60h x5h in the axial, vertical and transverse directions. The grid used is 260x137x31.

h (mm)	V_{Jet} (m/sec)	Re	U1 (co-flow) (m)
9.525	54.0	30000	0.16 V_{jet}

Table 6: Free Jet flow test conditions. [235]

As shown in Fig. 82 an initial potential core exist, where the flow is inviscid, and the velocity field is uniform and constant. This potential core extends about $8-9\ h$. In order to conserve the initial jet momentum, as the jet grows downstream, momentum is transferred to the surrounding air and the axial velocity decays. At the same time, air is entrained inside the jet to compensate the loss in mass and to conserve the initial momentum. The rate of entrainment and momentum transfer to the surrounding air controls the jet spread rate as shown in Fig. 83.

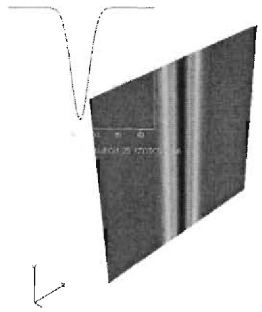

(a) Pressure wave t = 0.

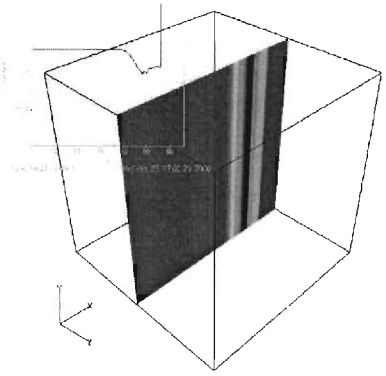

(b) Pressure wave t = t1.

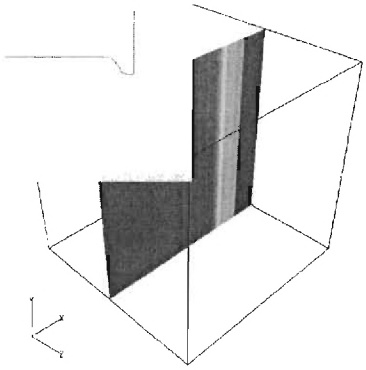

(c) Pressure wave t = t2.

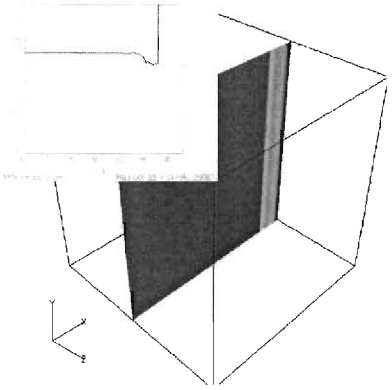

(d) Pressure wave t = t3.

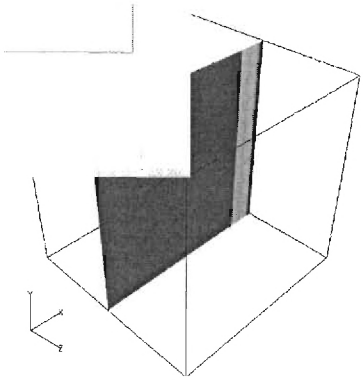

(e) Pressure wave t = t4.

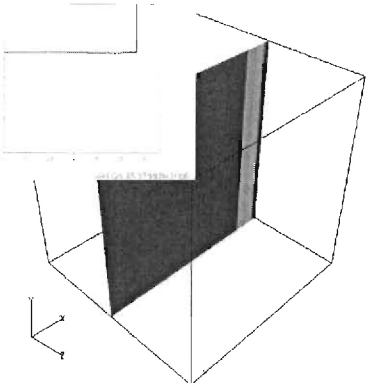

(f) Pressure wave t = t5.

Figure 80: Absorption of the pressure wave by the sponge layer.

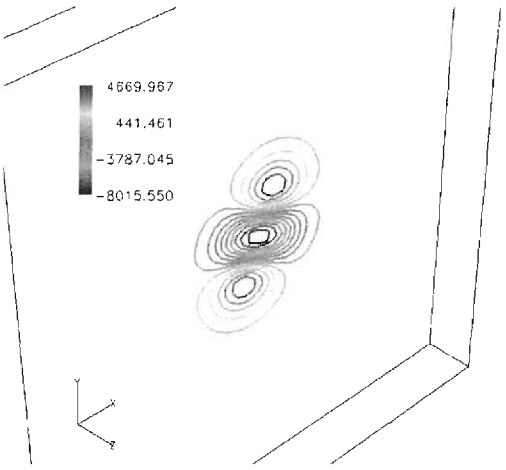

(a) Vortex propagation t = 0.

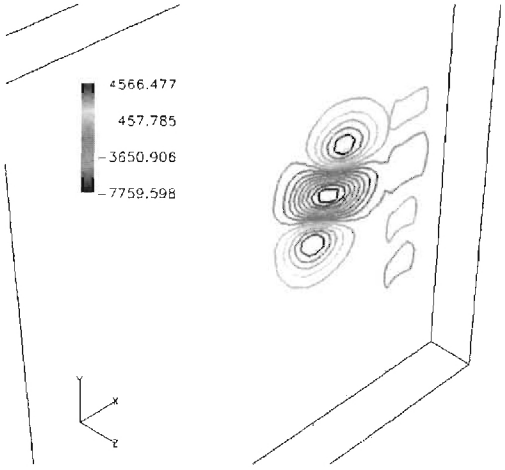

(b) Vortex propagation t = t1.

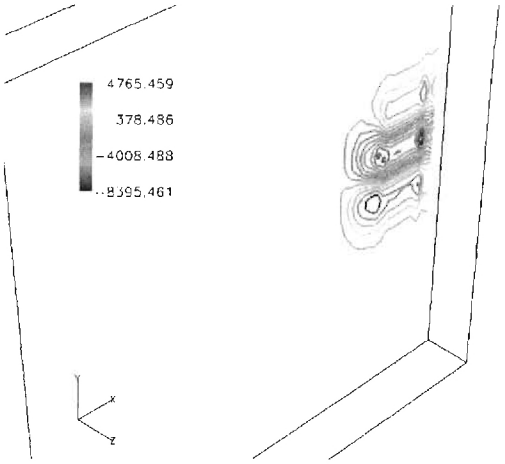

(c) Vortex propagation t = t2.

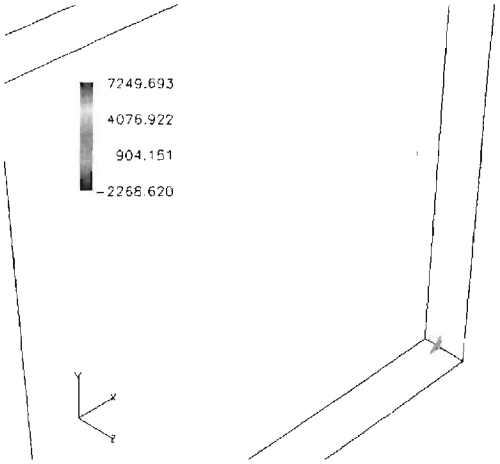

(d) Vortex propagation t = t3.

Figure 81: Absorption of a vortex by the sponge layer.

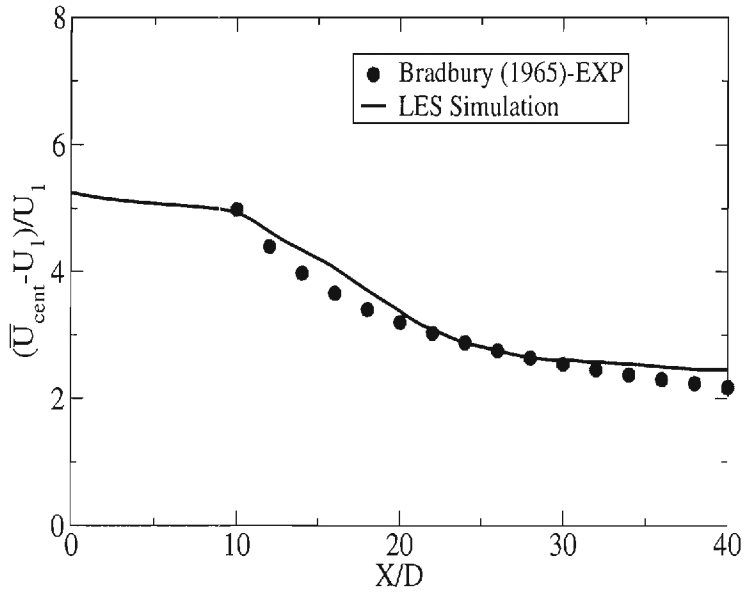

Figure 82: Mean centerline axial velocity (validation case)

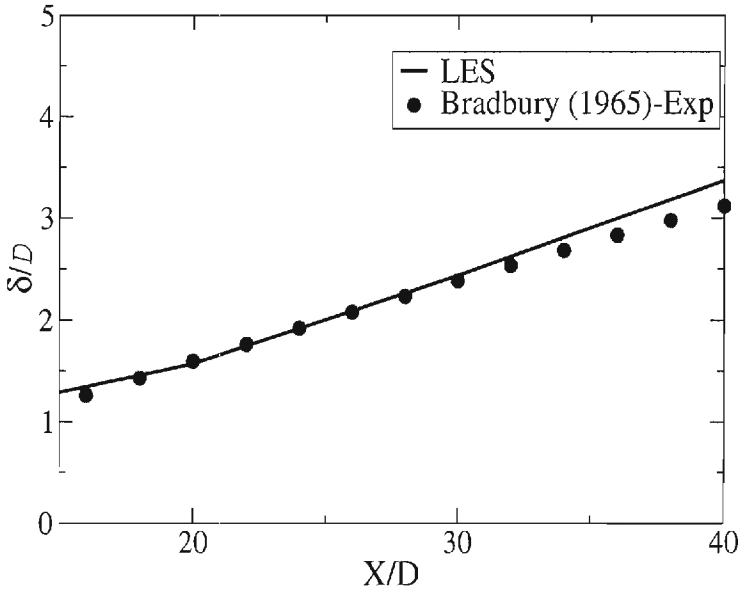

Figure 83: Jet spread rate (validation case)

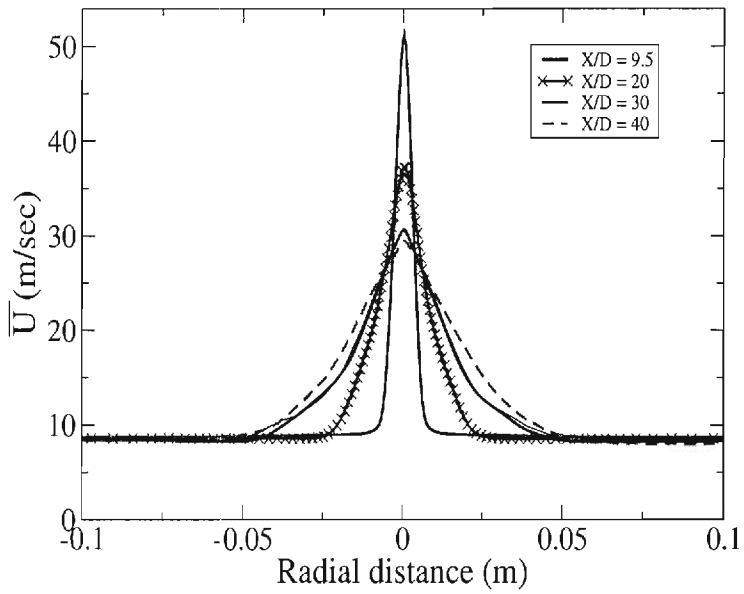

Figure 84: Mean radial velocity distribution (validation case)